The Dissertation Committee for Yixuan Yu Certifies that this is the approved version of the following dissertation:

Surface Functionalization and Self-Assembly of Ligand-Stabilized Silicon Nanocrystals

Committee:

Brian A. Korgel, Supervisor

Delia Milliron

John G. Ekerdt

Charles B. Mullins

Mike Downer

Surface Functionalization and Self-Assembly of Ligand-Stabilized Silicon Nanocrystals

by

Yixuan Yu, B.E. M.E.

Dissertation

Presented to the Faculty of the Graduate School of

The University of Texas at Austin

in Partial Fulfillment

of the Requirements

for the Degree of

Doctor of Philosophy

The University of Texas at Austin

May, 2015

Dedication

For my parents and family

Acknowledgements

It is not possible for me to achieve goals and dreams in my life without the help and encouragement of my family, friends, and colleagues. I am in permanent debt of the people around me, from who I learn my knowledge, gain my experience, build my character, and finally become the person who I am.

I would like to thank my advisor, Dr. Brian Korgel, for the gulidance, supports, and opportunities throughout my graduate career. Every time I look back, I am surprised by the progress I have made in the last five years, which is not possible without Brian's help. I would also like to thanks Dr. Truskett, Dr. Milliron, and Dr. Downer for insightful discussions, as well as Dr. Ekerdt and Dr. Mullins for serving in my committee.

I would like to especially express my gratuide to Colin Hessel and Daria Reid for teaching me silicon nanocrystal synthesis, Brian Goodfellow for teaching me nanocrystal superlattice fabrication and characterization, Detlef Smilgies for all the help with synchrotron and X-ray scattering, Micheal Rasch for his introducing me to nanobiotechnology. I would like to thank Xiaotang Lu for working closely with me, Christine Bosoy, Adrien Guillaussier, Vikas Reddy Voggu, and Avni Jain for all the time we have spent at synchrotron, Dorothy Silbaugh for helping me with silicon nanocrystal stability study, Timothy Bogart for the time spend on teaching me XPS and running XPS samples for me, and Jonathan Peck for organizing the group. I am also indebted to all of the current and past members of Korgel group, including Vahid Akhavan, Matthew Panthani, Vincent Holmberg, Aaron Chockla, Justin Harris, Chet Steinhagen, Taylor Harvey, Jackson Stolle, Emily Adkins, Dan Houck, Gang Fan, Hyun Gyung Kim, Taizhi Jiang, Philip Liu, Doug Pernik, Tim Siegler, Cherrelle Thomas, and Julian Villarreal.

I would also like to thank Hugo Celio for his support with XPS, TGA, and FTIR, Dwight Romanovicz for his help with TEM, Jingping Zhou and Karalee Jarvis for teaching me high resolution TEM, Vincet Lynch for his assiatance in XRD, Dr. Swinnea for providing access to SAXS on campus, and Yunping Fei for helping me with DSC.

I would also espcically like to thank my master advisor Dr. Qiang Cai at Tsinghua University for in introducing me into the academia.

Finally, I would like to thank my parents, siblings, and my wife, for the love, encouragement, and support in my life.

Surface Functionalization and Self-Assembly of Ligand-Stabilized Silicon Nanocrystals

Yixuan Yu, Ph.D.

The University of Texas at Austin, 2015

Supervisor: Brian A. Korgel

Silicon nanocrystals or quantum dots combine the abundance and nontoxicity of silicon with size-tunable energy band structure of quantum dots to form a new type of functional material that has applications in biomedical fluorescence imaging, photodynamic therapy, light-emitting devices, and solar cells.

The surface is the major concern for using silicon nanocrystals in bio-related applications. Room temperature hydrosilylation is introduced to functionalize silicon nanocrystals in the dark to minimize temperature/photon-induced side reactions that can potentially damage the nanocrystal surface and capping ligands. As a proof of concept, silicon nanocrystals are passivated with styrene at room temperature, without showing styrene polymerization. Silicon nanocrystals are also conjugated to iron oxide nanocrystals through room temperature hydrosilylation to generate fluorescent/magnetic cell labeling probes. Thermally-induced thiolation is used to generate silicon nanocrystals passivated with silicon-sulfur bond that is metastable and can turn to silicon-carbon bond through a ligand exchange.

The band gap and emission color of silicon nanocrystals depend on size. Monodisperse silicon nanocrystals and their self-assembly are of great importance for the applications in light-emitting devices and solar cells. Silicon nanocrystals are size-

selected through a modified size-selective precipitation. Face-centered cubic superlattices are formed with monodisperse silicon nanocrystals, and characterized by using grazing incidence small angle X-ray scattering. The structure of silicon nanocrystal superlattice is stable at temperatures up to 375^{o}C, due to the covalent Si-C bond on the nanocrystal surface. Silicon and gold nanocrystals are assembled to a simple hexagonal AlB_2 binary superlattice that shows interesting thermal behavior.

Finally, superlattices made with alkane thiol-capped sub-2 nm gold nanocrystals are used as model systems to study the superlattice phase transitions. Halide ions are found to be critical for order-to-order structural rearrangements in dodecanethiol-capped 1.9 nm gold nanocrystals superlattices at 190^{o}C. Reversible amorphous-to-crystalline transition upon heating is discovered for octadecanethiol capped 1.66 nm gold nanocrystal superlattices, which is attributed to the ligand melting transition.

Table of Contents

List of Figures

Figure 9.6: *In situ* GISAXS data obtained from a superlattice of 1.9 nm diameter dodecanthiol-capped Au nanocrystals formed with the addition of TOPB (TOPB : thiol=1:6) heated to 190^{o}C. (a) Contour plot of the radially integrated scattering intensity as a function of scattering vector *q* and time (30–450 sec) during *in situ* GISAXS measurement of the nanocrystal superlattice at 190^{o}C. (b) GISAXS pattern of the nanocrystal superlattice being heated at 190^{o}C for 40 sec, indexed to a BCC superlattice with a lattice constant of 3.96 nm, oriented with its $(110)_{SL}$ plane parallel to the substrate. (c) Radial integration of the GISAXS pattern in (b), showing $(110)_{SL}$, $(200)_{SL}$, and $(211)_{SL}$ diffraction peaks for BCC superlattice. (d) GISAXS pattern of the nanocrystal superlattice being heated at 190^{o}C for 65 sec, indexed to an ico-AB_{13} BSL, with a lattice constant of 15.6 nm. (e) Radial integration of the GISAXS pattern in (d), in which red dash lines labeled d_1 to d_9 are indexed to $(200)_{BSL}$, $(220)_{BSL}$, $(222)_{BSL}$, $(400)_{BSL}$, $(420)_{BSL}$, $(422)_{BSL}$, $(440)_{BSL}$, $(531)_{BSL}$, and $(600)_{BSL}$ diffraction peaks of an ico-AB_{13} BSL. (f) GISAXS pattern of the nanocrystal superlattice being heated at 190^{o}C for 150 sec, indexed to a FCC superlattice with a lattice constant of 14.2 nm, oriented with its $(111)_{SL}$ plane parallel to the substrate. (g) Radial integration of the GISAXS pattern in (f), in which red dash lines highlight the expected diffraction peaks of a FCC superlattice. (h) GISAXS pattern of the nanocrystal superlattice being heated at 190^{o}C for 440 sec, showing no diffraction features. (i) Radial integration of the GISAXS pattern in (h), showing no diffraction features 199

Figure 9.7: TEM images of nanocrystal superlattices of 1.9 nm diameter dodecanthiol-capped Au nanocrystals infiltrated with TOPB ([TOPB]:[thiol] mole ratio of 1:6) heated at 190^{o}C for various times. (a) 0 sec, Au nanocrystals formed BCC superlattice, with lattice constant of 3.95 nm, oriented with its $(110)_{SL}$ plane parallel to the substrate, and $[110]_{SL}$ direction perpendicular to the substrate. (b) Scheme of $(110)_{SL}$ planes of BCC superlattice and the Fast Fourier Transform (FFT) of the image in (a). (c) 20 sec, Au nanocrystal experienced Otswald ripening and the superlattice rearranged to an ico-AB_{13} BSL, oriented with its $(100)_{BSL}$ plane parallel to the substrate, and $[100]_{SL}$ direction perpendicular to the substrate.. (d) Scheme of $(100)_{BSL}$ planes of ico-AB_{13} BSL and the FFT of the image in (c). (e) 30 sec, the superlattice rearranged to sh-AB_2 BSL, oriented with its $(001)_{BSL}$ plane parallel to the substrate, and $[001]_{SL}$ direction perpendicular to the substrate. The $(100)_{BSL}$ *d*-spacing of 4.88 nm corresponds to a lattice constant of $a_{sh\text{-}AB2}$ (30 sec)= 5.64 nm. (f) Scheme of $(001)_{BSL}$ planes of sh-AB_2 BSL and the FFT of the image in (e). (g) 50 sec, Au nanocrystals formed a simple hexagonal (SH) superlattice, with lattice constant of 6.36 nm, oriented with its $(001)_{SL}$ plane parallel to the substrate, and $[001]_{SL}$ direction perpendicular to the substrate. (h) Scheme of $(001)_{SL}$ planes of SH superlattice and the FFT of the image in (g). (i) 50 sec, Au nanocrystals also formed a FCC superlattice, with lattice constant of 13.5 nm, oriented with its $(111)_{SL}$ plane parallel to the substrate, and $[111]_{SL}$ direction perpendicular to the substrate. (j) Scheme of

Chapter 1: Introduction

Silicon (Si) is the second most abundant element in the earth's crust (about 28% in mass), and exists as silicate minerals in nature. Pure silicon is a semiconductor with a band gap of 1.12 eV at 300K, and appears to be a crystal with a diamond cubic (space group: Fd3m) lattice and a lattice constant of 0.5431 nm. Silicon is of great importance because it is the fundamental material in semiconductor industry (over $300 billion revenue per year) and also dominates the photovoltaic market (over 90%). However, silicon performs poorly as a light absorber or emitter, due to its indirect band gap.

1.1 LIGHT EMISSION FROM SILICON NANOCRYSTAL

A semiconductor has an indirect band gap if the top of the valence band does not align with the bottom of the conduction band in the momentum space, as illustrated in Figure 1.1. Good examples of indirect band gap semiconductors are silicon and germanium. According to the momentum conservation law, the electron at the conduction band bottom and the hole on the valence band top can only recombine by absorbing or emiting a phonon, which compensates the momentum difference. As a result, light absorption / emission in an indirect band gap semiconductor are highly inefficient three-body processes (electron-hole-phonon).

In contrast to an indirect band gap semiconductor, a direct band gap semiconductor, i.e. GaAs, has an energy band structure in which the conduction band bottom aligns with valence band top in the momentum space, (Figure 1.2) and hence, the electron and hole can directly recombine and emit a photon.

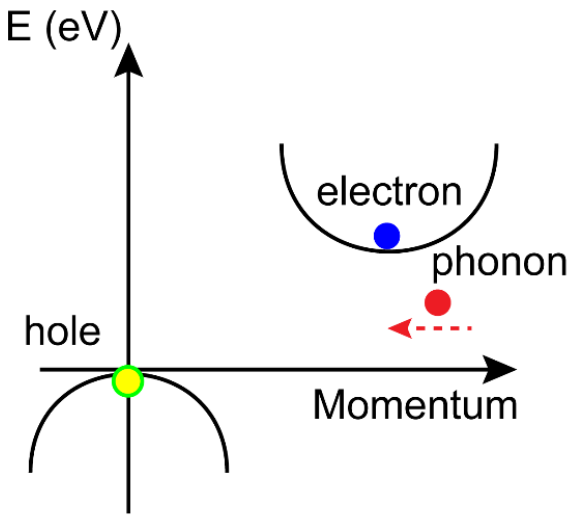

Figure 1.1: Electron-hole recombination in an indirect band gap semiconductor.

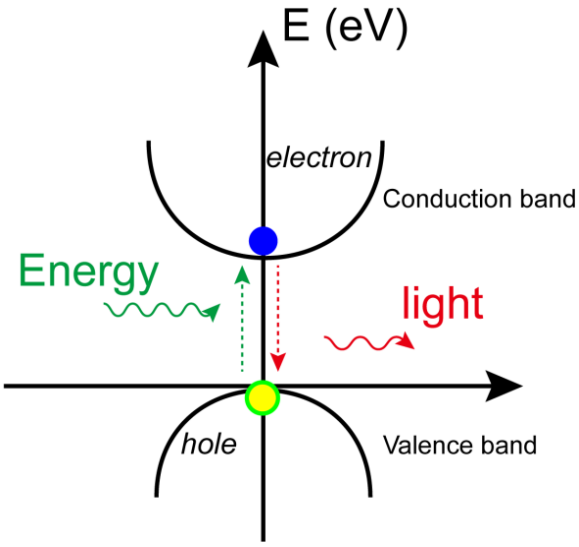

Figure 1.2: Electron-hole recombination in a direct band gap semiconductor.

An effective approach to achieve efficient light absorption / emission for an indirect band gap semiconductor like silicon is to shrink the size of the semiconductor crystal until it is smaller than its Bohr radius (about 4.5 nm for silicon). Such a small semiconductor crystal is called a nanocrystal or quantum dot. In a silicon nanocrystal, the

electron and hole are spatially confined in the nanocrystal, and consequently, their wave functions are delocalized in momentum space, leading to wavefunction overlap and direct electron-hole recombinations.[1,2] (Figure 1.3) Such an effect is called quantum confinement, which also makes silicon nanocrystals with smaller size have a wider band gap. Therefore, the light emission of silicon nanocrystals can be tuned from visible to near infraredwavelength. [1]

Silicon nanocrystals show bright photoluminescence (PL) upon excitation by UV light, as shown in Figure 1.4a. The light emission of a ligand-capped silicon nanocrystasl can be ultra-stable. Figure 1.4b shows a glowing phrase "silicon nanocrystal" that has been painted on a lab notebook cover for two years, by using 2.5 nm diameter 1-dodecene-capped silicon nanocrystals as ink.

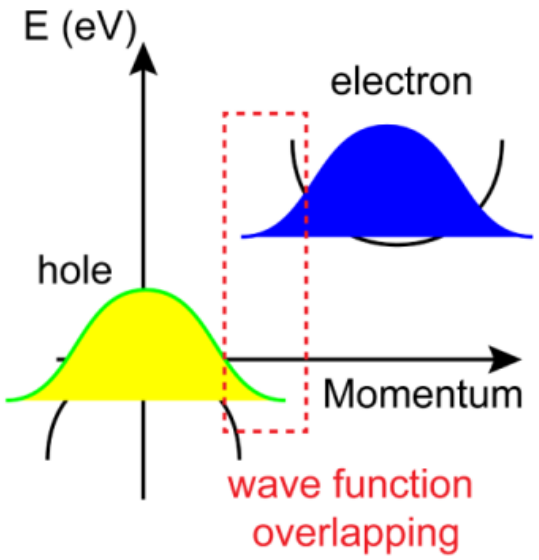

Figure 1.3: Electron-hole wave function overlap in a silicon nanocrystal owe to quantum confinement.

Figure 1.4c shows PL emission spectra for various size silicon nanocrystals, excited at 350 nm. The efficiency of PL can be described as quantum yield that is defined as the number ratio of emitted photons to absorbed photons. PL quantum yield of silicon nanocrystals is size-dependent, ranging from 1% for sub 2 nm nanocrystals to about 60% for 3.5 nm nanocrystal.[3] The origin of the size-dependent PL quantum yields in silicon nanocrystals is not completely clear.

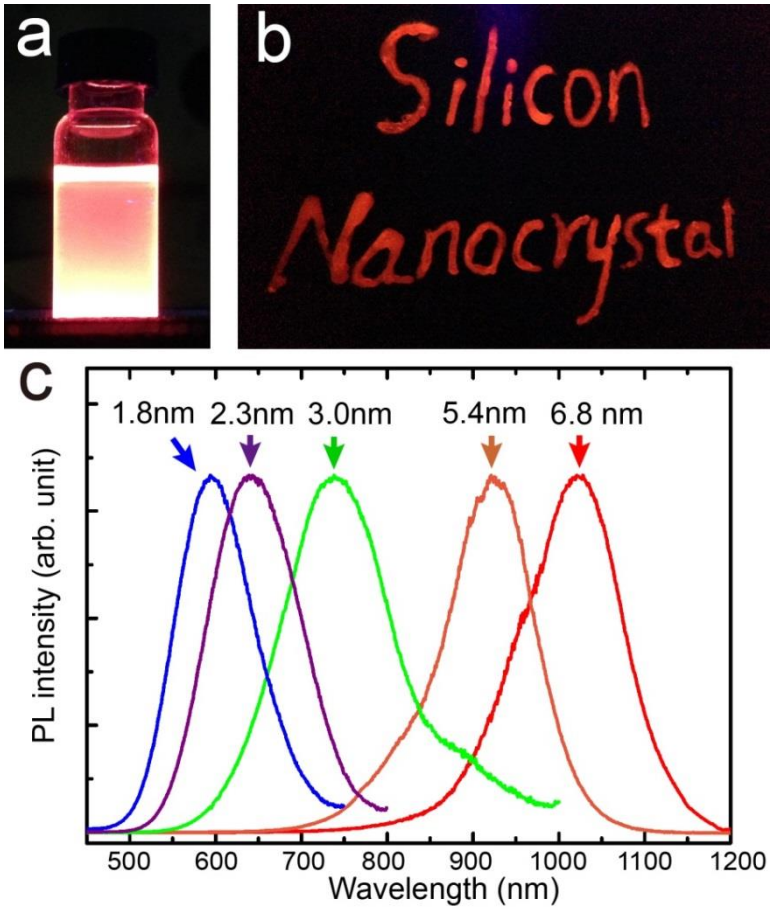

Figure 1.4: (a) A vial of 2.5 nm diameter silicon nanocrystals dispersed in toluene above a 365 nm UV light. (b) "silicon nanocrystal" painted with 2.5 nm diameter silicon nanocrystals as ink, glowing under 365 nm UV light. (c) Photoluminescence spectra showing size-dependent light emission from silicon nanocrystals excited by 400 nm light.

Excitons in silicon nanocrystals have slow radiative recombination channels, with lifetimes ranging from tens to hundreds of microseconds, due to the indirect band gap.[4] Time-resolved PL of silicon nanocrystal can be measured through a time-correlated single photon counting (TCSPC) technique, and the data can be fitted by a double-or triple-exponential decay. Figure 1.5 shows typical TCSPC data of silicon nanocrystal fitted by a double exponential decay, in which the fast decay has a life time of several nanoseconds, and is often interpreted as the nonradiative recombination, while the slow decay with a life time of about 50 μs is generally considered as radiative recombination.

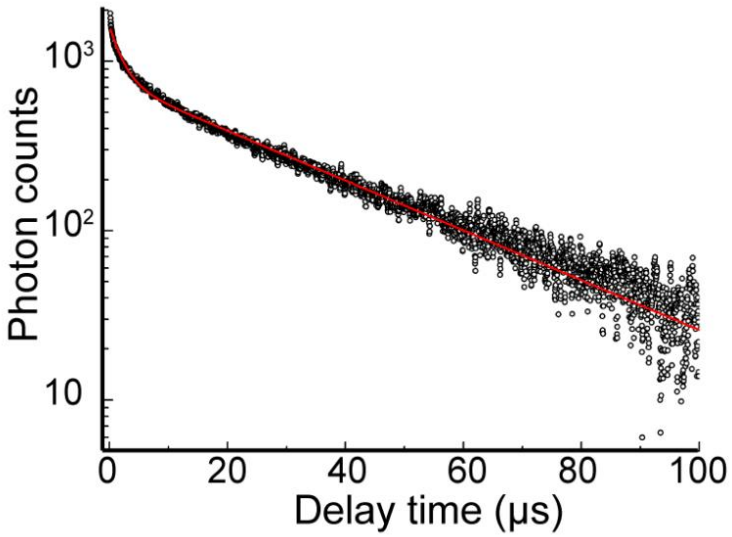

Figure 1.5: Time-resolved photoluminescence of 2.5 nm diameter silicon nanocrystal measured through time-correlated single photon counting technique.

1.2 SILICON NANOCRYSTAL APPLICATIONS

Silicon nanocrystals combine the abundance / nontoxicity, well-established fabrication / chemistry of silicon, with the nanocrystal properties including quantum

confinement, coulomb blockade, and solution processability. They have a wide range of applications, such as light emitting devices, solar cells, electronics, and bio-related applications.

1.2.1 Light Emitting Devices

Light emission from quantum confined silicon nanocrystals has opened up an exciting opportunity for all-silicon laser[5]: using silicon for both gain media and controlling electronics, which can greatly cut the cost of solid state laser fabrication and provide a solution for silicon photonics based integrated circuits. Pavesi[1] has demonstrated optical gain from silicon nanocrystals embedded in a silicon dioxide substrate with an optical-pumped design. Unfortunately, Pavesi has attributed the PL of silicon nanocrystal to oxide-related surface states, which is controversial. More and more evidences have been published, supporting that the PL is generated from the quantum confined silicon core. There are also very few follow-up work to this gain effect by other research groups. Lasing from silicon nanocrystals still requires further investigation.

Light emitting silicon nanocrystals are promising candidates for light sources in light emitting devices (LED), due to their high emission stability, low toxicity (at least in bulk form), and abundance in nature. The high emission stability will provide a long durability for the LED, and low toxicity will remove the environmental-related concerns in the commercialization process of devices. LEDs with silicon nanocrystals emitting at 800 nm has been shown by Cheng[6-7] *et al* to exhibit a power efficiency of 8.6%, which is the highest efficiency that has ever been reported for organic LEDs, including quantum

dots / organic LEDs. Ozin group[8-9] is also dedicated in developing light emitting devices with silicon nanocrystals. They have reported a device with an efficiency of 0.17%, and managed to improve it to 1.1%.

The current design for silicon nanocrystals-based LEDs basically involve a light-emitting layer made by ligand-stabilized silicon nanocrystals, electron transport layer and hole transport layer made by polymers, and top/back contacts. It is essentially an organic LED design but replace the light-emitting dye/polymer with silicon nanocrystals, and it is the reason why they are usually referred as quantum dot-OLEDs. The stability of the device with this design is limited by the least stable layer in the device, which is, currently, the hole transport layer. All-inorganic silicon nanocrystal LED would be the next step towards a commercial product.

There are also several issues related to using silicon nanocrystals in LED. First, the PL quantum yield of silicon nanocrystals can be as high as 60%, but the highest power efficiency of silicon nanocrystal LED emitting at a similar wavelength is only 8.6%. The low power efficiency of the LED is probably due to the low charge carrier injection efficiency to the silicon nanocrystal passivated with organic ligands that act as insulating barriers. Second, the slow radiative recombination rate of silicon nanocrystals put an upper limit for the on/off rate of LED. For instance, silicon nanocrystal with PL lifetime of 100 μs cannot support a LED switching at a rate faster than 10KHz. Coupling surface plasmon modes of metals to PL of silicon nanocrystals can accelerate the radiative recombination, but will also decrease the PL quantum yield because this

coupling opens up another nonradiative energy transfer channel from silicon nanocrystal to surface plasmon polaritons.

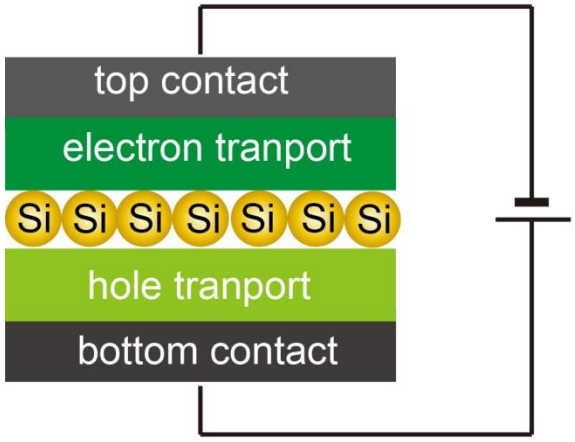

Figure 1.6: A general design for silicon nanocrystals-based organic light-emitting device.

1.2.2 Photovoltaic Devices

Silicon has currently occupied about 90% of the photovoltaic market. However, due to the poor light absorption of bulk silicon, those solar cells usually require a thick silicon layer to absorb the solar spectrum, leading to a significant amount of material cost. Silicon nanocrystal, exhibiting both high absorption coefficient, optimal band for utilizing solar spectrum, and low cost solution processability, can be a promising candidate for the third generation photovoltaic devices. The size-tunable band gap of silicon nanocrystal also provides an opportunity for generating a low cost silicon nanocrystal-based multi-junction solar cell, which can break the Shockley limit of the solar cell efficiency. Silicon nanocrystals also show efficient multiple exciton generation (MEG),[10] which can utilize hot carriers before they are thermalized to the band edge.

1.2.3 Biomedical-related applications

Silicon nanocrystals could be the next generation biomedical fluorescence imaging contrast agents to replace the current organic dyes because they have the following advantages:

1. Silicon nanocrystals have a high absorption coefficient, which is about two orders of magnitude higher than organic dyes, resulting in a much higher imaging sensitivity;
2. PL of silicon nanocrystals is resistant to photo-bleaching, proving a broader time window for bioimaging;
3. Silicon nanocrystals have broad absorption bands, size-tunable emission bands, and large stokes shifts, making it possible to perform multicolor imaging with a single excitation source.
4. PL of silicon nanocrystal has a long lifetime, up to hundreds of microseconds, enabling the filtration of short-lived cell / tissue auto-fluorescence through a time-gated imaging technique.
5. Silicon nanocrystals are biocompatible and biodegradable,[11,12] presenting low toxicity to biological systems.

The excitation energy in silicon nanocrystals can transfer to the triplet ground state oxygen ($^3O_2$) to excite the $^3O_2$ to singlet oxygen ($^1O_2$), which is highly cytotoxic. The diffusion length of singlet oxygen in tissue is less than 20nm, hence the cytotoxicity is highly localized to the photosensitizer. Photodynamic therapy (PDT) takes advantage of this effect to treat cancer. In order to have an efficient energy transfer, the life time of

the excitation state in the photosensitizer has to be comparable or longer than the energy transfer lifetime (several microseconds). The efficiency of energy transfer from silicon nanocrystals to triplet oxygen can achieve almost 100%,[13-14] due to the long PL lifetime of silicon nanocrystals. Silicon nanocrystal as a photosensitizer has another advantage over current molecular photosensitizers used in photodynamic therapy: silicon nanocrystal is biodegradable and causes no side effects related to the residual photosensitivity.

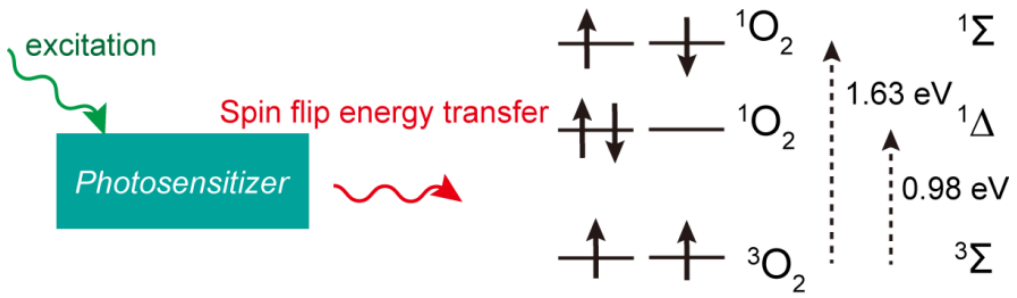

Figure 1.7: Scheme from energy transfer from a photosensitizer to triplet oxygen ground state.

The energy of photons absorbed by silicon nanocrystals can be harvested in different path ways towards biomedical applications: (1) hot carriers created by excitation quickly thermalize to the band edge, generating heat which can be used for photothermal therapy; (2) exciton radiative recombination, generating fluorescence for imaging application; (3) spin flip energy transfer to tripolet oxygen, generating singlet oxygen for photodynamic therapy.

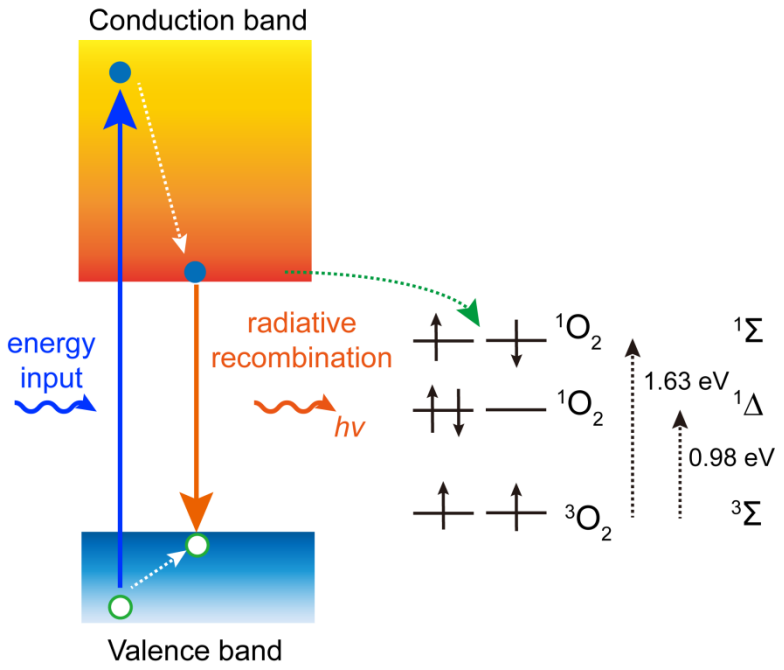

Figure 1.8: Scheme for various pathways to harvest the energy absorbed by silicon nanocrystal for biomedical related applications.

1.3 SILICON NANOCRYSTAL SYNTHESIS METHODS

1.3.1 Thermal Annealing of Substoichiometric Glass (SiO_x, x<2)

Thermal annealing of substoichiometric glass thin films as a synthesis method for silicon nanocrystals embedded in a silicon dioxide thin film has been reported in early 1990s. Such substoichiometric glass thin films can be made by ion implantation,[5] co-sputtering[15] or plasma enhance chemical vapor deposition[16] of silicon and silicon dioxide, or molecular beam epitaxy grow[17] of amorphous silicon and silicon dioxide superlattice. The thermal annealing takes place in inert atmosphere, such as nitrogen gas, argon gas, et al, at temperatures around 1100^{o}C.

The advantage of this method is the compatibility to the modern semiconductor industry, making it a good choice for synthesizing silicon nanocrystals towards device application. The yield of this method is very low, and nanocrystal size control is poor.

1.3.2 Laser Pyrolysis of Silane

Cannon[18,19] first demonstrated that 150 W continuous laser with 10.591 μm can be resonantly absorbed by silane molecules, leading to silane dissociation and the formation of silicon containing clusters. This method yields silicon nanocrystals at a rate of 1g/h with an 80%-100% precursor conversion. Silane molecules are injected in to the reaction zone of the reactor from a nozzle, where they are irradiated by infrared laser and heated to temperature exceeding 1000^{o}C. Silicon nanocrystals nucleate and grow in the reaction zone, and continue flow to the end of the reactor. The nanocrystals extracted directly from the reaction zone have small sizes; those extracted from the end of the reactor are usually larger than 15 nm and heavily agglomerated, probably due to the fusion in the downstream where the temperature are lower.

The size of silicon nanocrystals could be reduced by hydrofluoric acid (HF) wet etching. Swihart[20] et al have shown that HF etching can tune the PL of silicon nanocrystals synthesized by laser pyrolysis from red to green (580 nm). It is worthwhile to mention that 580 nm is the shortest emission wavelength has ever been achieved by silicon nanocrystals. “Blue emitting silicon nanocrystals” appears frequently in literature, but their PL lifetime is about tens of nanoseconds, three orders of magnitude shorter than other silicon nanocrystals. It is very likely that “blue emitting silicon nanocrystals” emit

light in a different manner rather than the band edge emission mediated by quantum confinement. Given the fact that "blue emitting silicon nanocrystals" papers either fail to show X-ray diffraction (XRD) data proving the existence of silicon nanocrystals (diffraction peaks indexed to crystalline silicon with proper peak width corresponding to nanocrystal size), or show XRD data proving there is no silicon nanocrystal, those "blue emitting silicon nanocrystals" may actually not be nanocrystalline silicon.

1.3.3 Nonthermal plasma synthesis

Nonthermal plasma synthesis is a popular synthesis method for silicon nanocrystal, which has been actively studied by Kortshagen group[21-22] in University of Minnesota. A general design of nonthermal plasms reaction consists of a glass tube wrapped by a set of copper rings which act as high voltage electrodes. The reactor is fed with a silane and argon mixture, and the silicon nanocrystals are collected by a filter in the downstream. The size of silicon nanocrystals is controlled by the flow rate of silane: higher flow rate leads to a shorter residual time and hence a smaller size. A 0.25 inch inner diameter tube can produce fluorescent silicon nanocrystals at a rate of 50 mg/h, with 50% silane conversion. As-synthesized silicon nanocrystals have hydride-terminated surface and can undergo hydrosilylation to form ligand stabilized silicon nanocrystals. Nonthermal plasma method yields silicon nanocrystals with a broad size distribution, which is a disadvantage for this method.

1.3.4 Thermal decomposition of hydrogen silsesquioxane (HSQ)

Hessel and Veinot[23] pioneered the synthesis of silicon nanocrystals through thermal decomposition of hydrogen silsesquioxane (HSQ). This method involves a commercially available precursor called flowable oxide (Fox-n), produced by Dow Corning, which contains HSQ dissolved in toluene and isobutylmethylketon. "n" stands for the weight concentration of HSQ, for example, Fox-16 means HSQ solution with 16% weight concentration. This synthesis method has been adopted by Korgel group in the University of Texas at Austin and Ozin group in Toronto University, and attracted more and more attention as the whole silicon nanocrystal community grows.

Figure 1.9 illustrates the typical synthesis of silicon nanocrystals.[24,25] HSQ is annealed in forming gas (93% nitrogen gas and 7% hydrogen gas) at temperature between 1000 and 1400^{o}C for 1 hour to form silicon nanocrystals embedded in silicon dioxide matrix, with nanocrystal size controlled by annealing temperature. The silicon dioxide embedded silicon nanocrystals are ground into a brown color fine powder that is etched in a mixture of hydrofluoric acid and hydrochloric acid to yield hydride-terminated silicon nanocrystals. Hydride-terminated surface can further be passivated with terminal alkenes through hydrosilylation to finally generate ligand stabilized silicon nanocrystals.

This method provides highly crystalline silicon nanocrystals with proper size control. However, FOx are pretty expensive, and the precursor conversion (HSQ) rate is only 10%, due to the stoichiometry of HSQ ($H_8Si_8O_{12}$). To apply this method for large scale production of silicon nanocrystals, a cheaper precursor is required.

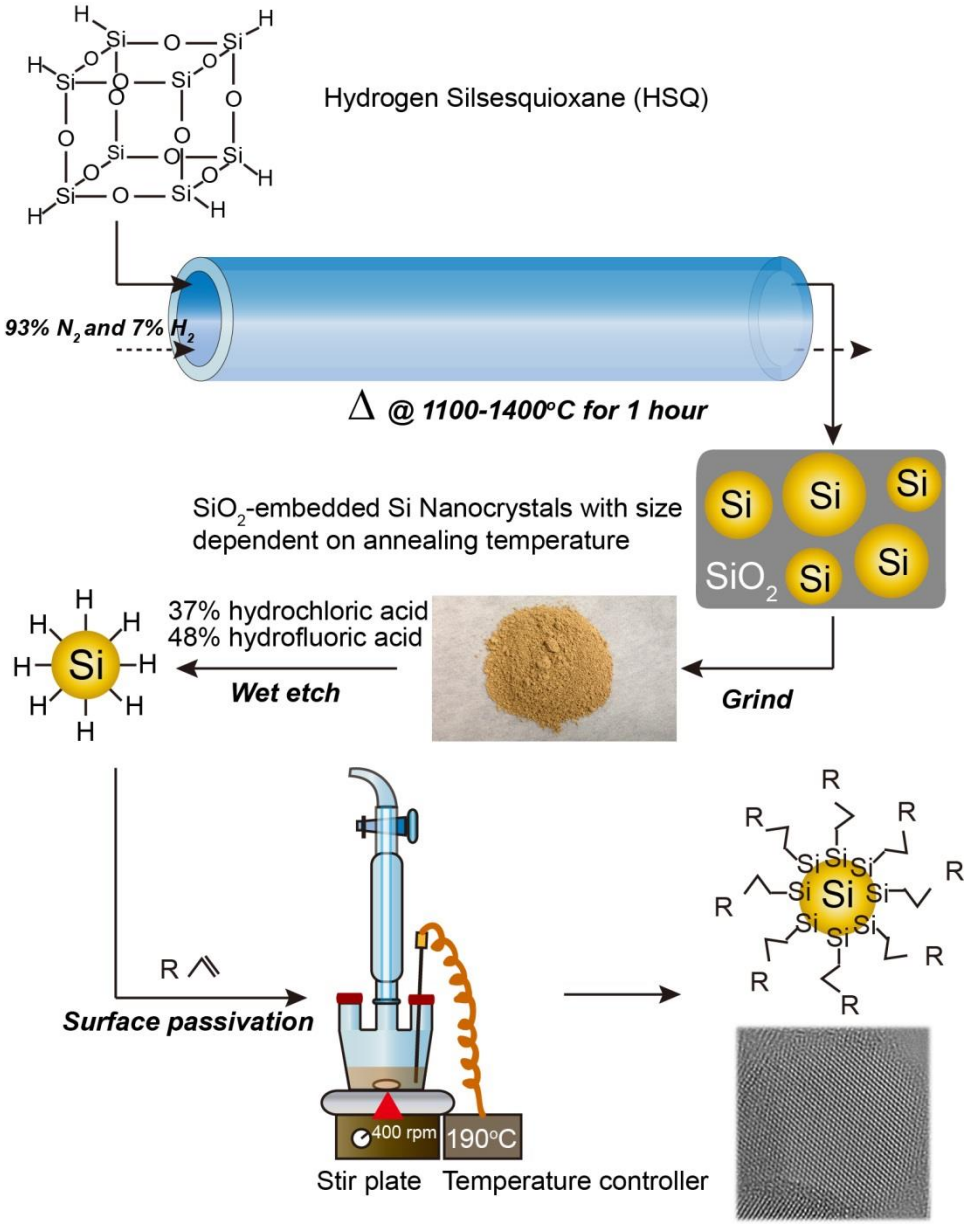

Figure 1.9: Scheme for synthesis of ligand stabilized silicon nanocrystals through thermal decomposition of HSQ.

1.4 Dissertation Overview

The surface functionalization of silicon nanocrystals by room temperature hydrosilylation will be presented in chapter 2. Chapter 3 presents styrene passivation on

silicon nanocrystals surface at room temperature as a proof of concept for room temperature hydrosilylation.

Chapter 4 focuses on undecenoic acid-functionalized silicon nanocrystal showing high water dispersibility. Silicon nanocrystal surface oxidation in water is studied by various characterization tools, including X-ray photoelectron spectroscopy, Fourier transform infrared spectroscopy, and photoluminescence spectroscopy.

Synthesis of covalently conjugated silicon/iron oxide nanocrystals is discussed in chapter 5. A thermally-induced thiolation on hydride-terminated silicon nanocrystal surface is presented in chapter 6, which also demonstrates the first example of ligand exchange on silicon surface.

Chapter 7 focuses on size-selection of silicon nanocrystals, self-assembly of silicon nanocrystal superlattice, and the superlattice thermal stability. Chapter 8 demonstrates the formation of a silicon/gold binary superlattice. Gold nanocrystal structural rearrangements mediated by halide ions are explored in chapter 9; reversible heating-induced ordering of gold nanocrystals is discussed in chapter 10.

Finally, chapter 11 summarizes the main conclusions of this dissertation and provides some suggestions for the future work.

1.5 REFERENCES

(1) Hessel, C. M.; Reid, D.; Panthani, M. G.; Rasch, M. R.; Goodfellow, B. W.; Wei, J.; Fujii, H.; Akhavan, V.; Korgel, B. A. Synthesis of Ligand-Stabilized Silicon Nanocrystals with Size-Dependent Photoluminescence Spanning Visible to Near-Infrared Wavelengths. *Chem. Mater.* **2012**, *24*, 393-401.

(2) Mastronardi, M. L.; Maier-Flaig, F.; Faulkner, D.; Henderson, E. J.; Kübel, C.; Lemmer, U.; Ozin, G. A. Size-Dependent Absolute Quantum Yield for Size-Separated Colloidally-Stable Silicon Nanocrystals. *Nano Lett.* **2012**, *12*, 337-342.
(3) Jurgergs, D.; Rogojina, E.; Mangolini, L.; Kortshagen, U. Silicon Nanocrystals with Ensemble Quantum Yields Exceeding 60%. *App. Phys. Lett.* **2006**, *23*, 233116.
(4) Vial, J. C.; Bsiesy, A.; Gaspard, F.; Hérino, R.; Ligeon, M.; Muller, F.; Romestain, R. Mechanisms of Visible-Light Emission from Electro-Oxidized Porous Silicon. Phys. Rev. B 1992, 45, 14171-14176.
(5) Pavesi, L.; Dal Negro, L.; Mazzoleni, C.; Franzò, G.; Priolo, F. Optical Gain in Silicon Nanocrystals. *Nature* **2000**, *408*, 440-444.
(6) Cheng, K.-Y.; Anthony, R.; Kortshagen, U. R.; Holmes, R. J. Hybride Silicon Nanocrystal-Organic Light-Emitting Devices for Infrared Electroluminescence. *Nano Lett.* **2010**, *10*, 1154-1157.
(7) Cheng, K.-Y.; Anthony, R.; Kortshagen, U. R.; Holmes, R. J. High-Efficiency Silicon Nanocrystal Light-Emitting Devices. *Nano Lett.* **2011**, *11*, 1952-1956.
(8) Puzzo, D. P.; Henderson, E. J.; Helander, M. G.; Wang, Z.; Ozin, G. A.; Lu, Z. Visiblle Colloidal Nanocrystal Silicon Light-Emitting Diode. *Nano Lett.* **2011**, *11*, 1585-1590.
(9) Maier-Flaig, F.; Rinck, J.; Stephan, M.; Bocksrocker, T.; Bruns, M.; Kübel, C.; Powell, A. K.; Ozin, G. A.; Lemmer, U. Multicolor Silicon Light-Emitting Diodes (SiLEDs). *Nano Lett.* **2013**, *13*, 475-480.
(10) Beard, M. C.; Knutsen, K. P.; Yu, P.; Luther, J. M.; Song, Q.; Metzger, W. K.; Ellingson, R. J. Nozik, A. J. Multiple Exciton Generation in Colloidal Silicon Nanocrystals. *Nano Lett.* **2007**, *7*, 2506-2512.
(11) Park, J.-H.; Gu, L.; von Maltzahn, G.; Ruoslahti, E.; Bhatia, S. N.; Sailor, M. J. Biodegradable luminescent porous silicon nanoparticles for in vivo applications *Nat. Mater.* **2009**, *8*, 331-336.
(12) Gu, L.; Hall, D. J.; Qin, Z.; Anglin, E.; Joo, J.; Mooney, D. J.; Howell, S. B.; Sailor, M. J. In vivo Time-Gated Fluorescence Imaging with Biodegradable Luminescent Porous Silicon Nanoparticles. Nat. Commun. 2012, 4, 2326.
(13) Kovalev, D.; Fujii, M. Silicon Nanocrystals: Photosensitizers for Oxygen Molecules. *Adv. Mater.* **2005**, *17*, 2531-2544.
(14) Xiao, L.; Gu, L.; Howell, S. B.; Sailor, M. J. Porous Silicon Nanoparticle Photosensitizers for Singlet Oxygen and Their Phototoxicity against Cancer Cells. *ACS Nano* **2011**, *5*, 3651-3659.
(15) Hayashi, S.; Nagareda, T.; Kanzawa, Y.; Yamamoto, K. Photoluminescence of Si-Rich SiO_2 Films: Si Cluster as Luminescent Centers. Jpn, J. Appl. Phys. 1993, 32, 3840.
(16) Tsybeskov, L.; Hirschman, K. D.; Duttagupta, S. P.; Zacharias, M.; Fauchet, P. M.; McCaffrey, J. P.; Lockwood, D. J. Nanocrystalline-Silicon Superlattice Produced by controlled recrystallization. App. Phys. Lett. 1998, 72, 43.
(17) Lu, Z. H.; Lockwood, D. J.; Baribeau, J.-M. Quantum Confinement and Light Emission in SiO_2/Si Superlattice. *Nature* **1995**, *378*, 258-260.

(18) Cannon, W. R.; Danforth, S. C.; Flint, J. H.; Haggerty, J. S.; Marra, R. A. Sinterable Ceramic Powders from Laser-Driven Reactions: I, Process Description and Modeling. *J. Am. Ceram. Soc.* **1982**, *65*, 324-330.
(19) Cannon, W. R.; Danforth, S. C.; Haggerty, J. S.; Marra, R. A. Sinterable Ceramic Powders from Laser-Driven Reactions: II, Powder Characteristics and Process Variables. *J. Am. Ceram. Soc.* **1982**, *65*, 330-335.
(20) Li, X.; He, Y.; Talukdar, S. S.; Swihart, M. T. Process for Preparing Macroscopic Quantities of Brightly Photoluminescent Silicon Nanoparticle with Emission Spanning the Visible Spectrum. *Langmuir* **2003**, *19*, 8490-8496.
(21) Mangolini, L.; Thimsen, E.; Kortshagen, U. High-Yield Plasma Synthesis of Luminescent Silicon Nanocrystals. *Nano Lett.* **2005**, *5*, 655-659.
(22) Mangolini L.; Kortshagen, U. Plasma-Assisted Synthesis of Silicon Nanocrystal Inks. *Adv. Mater.* **2007**, *18*, 2513-2519.
(23) Hessel, C. M.;.Henderson, E. J.; Veinot, J. G. C. Hydrogen Silsesquioxane: A Molecular Precursor for Nanocrystalline Si-SiO2 Composites and Freestanding Hydride Surface Terminated Silicon Nanoparticles. *Chem. Mater.* **2006**, *18*, 6139-6146.
(24) Yu, Y.; Hessel, C. M.; Bogart, T. D.; Panthani, M. G.; Rasch, M. R.; Korgel, B. A. Room Temperature Hydrosilylation of Silicon Nanocrystals with Bifunctional Terminal Alkenes. *Langmuir* **2013**, *29*, 1533-1540.
(25) Yu, Y.; Bosoy, C. A.; Hessel, C. M.; Smilgies, D.-M.; Korgel, B. A. Silicon Nanocrystal Superlattices ChemPhysChem 2013, 14, 84-87.

Chapter 2: Room Temperature Hydrosilylation on Silicon Nanocrystal Surface with Bifunctional Terminal Alkenes[§]

2.1 INTRODUCTION

Silicon (Si) nanocrystals exhibit bright photoluminescence (PL) with size-tunable color over much of the visible to near-infrared spectrum.[1-4] Since Si is susceptible to oxidation, surface passivation is needed to prevent corrosion and stabilize the PL, which can be provided by Si-C bonded organic capping ligands. One approach to obtain these is by synthesis of H-terminated Si nanocrystals followed by hydrosilylation.[1-7] Bifunctional alkenes can also be grafted by hydrosilylation to expose distal functional groups needed for aqueous dispersibility and for tethering biological molecules for medical applications,[6] such as propionic acid,[8] acrylic acid,[9] and allylamine.[10] Here, we report that H-coated Si nanocrystals undergo *room temperature* hydrosilylation in the presence of ω-ester-terminated and ω-acid-terminated alkenes without photoexcitation or added catalyst and that these nanocrystals can be dispersed in polar and aqueous solvents and retain their photoluminescence.[1]

Hydrosilylation reactions on silicon (Si) surfaces have been widely studied since 1993 when Linford and Chidsey showed that alkenes can insert into surface Si-H and yield Si-C bonded alkyl groups.[11] This reaction involves silyl radicals that can be created using a radical initiator, catalyst, heat, or light.[12,13] Hydrosilylation on Si surfaces can

[§] Portion of chapter appears in Yu, Y.; Hessel, C. M.; Bogart, T.; Panthani, M. G.; Rasch, M. R.; Korgel, B. A. *Langmuir*, 29, 1533-1540 (**2013**). Y. Yu performed the experiments, C. M. Hessel contributed to the mechanism discussion, T. Bogart did XPS characterization. All authors contributed to writing the text. B. A. Korgel provided funding through research grant.

also be promoted with Grignard[14] or alkylithium reagents,[15] or catalyzed with Lewis acid[16] or Pt complexes,[17] and direct nucleophilic attack of Si-H may also be possible.[18] Hydrosilylation with ω-ester-terminated alkenes has also been accomplished on Si (100) surfaces heated to 200°C[19] and on porous silicon heated to 85°C[20] or exposed to UV light.[21,22] Alkene esters[23] and 10-undecenoic acid[24] have also been attached to Si nanocrystals by heating to 135-140°C or stirring under intense white light (250 W). However, room temperature hydrosilylation of a Si surface without catalyst or photoinitiation has not been reported.

Room temperature hydrosilylation was carried out by exposing hydrogen-terminated Si nanocrystals to either ω-ester-terminated (alkene-COOR) or ω-acid-terminated alkenes (alkene-COOH). The nanocrystals, ranging between 2 and 8 nm in diameter, were obtained using methods initially developed by Hessel and Veinot[5] in which a wet HF etch is used to liberate Si nanocrystals from an oxide matrix material produced by hydrogen silsesquioxane (HSQ) decomposition. Both ester and carboxylic acid groups were found to facilitate direct nucleophilic attack by the alkene to yield Si-C bonded capping ligands. Neither the ester nor the acid form stable bonds to the surface but are needed to promote the hydrosilylation reaction.

2.2 EXPERIMENTAL DETAILS

2.2.1 Materials

Fox-16, 10-undecenoic acid (98%), methyl 10-undecenoate (96%), ethyl 10-undecenoate (97%), undecanoic acid (97%), and 1-octene (98%) were purchased from

Sigma-Aldrich. Ethanol, toluene, hexanes, chloroform, and Hydrochloric acid (HCl, 37.5%) were from Fisher Scientific. Hydrofluoric acid (HF, 48%) was obtained from EMD chemicals. Deionized (DI) water was obtained using a Barnstead Nanopure Filtration System (17 MΩ resistance).

2.2.2 Preparation of Hydride-Terminated Si Nanocrystals

Hydrogen-passivated nanocrystals were synthesized as described previously.[1] Hydrogen silsesquioxane (HSQ) was heated to 1100-1300^{o}C for 1 hour under forming gas flow. Higher temperature produces larger nanocrystals. The product was ground with agate mortar and pestle for 10 min and shaken in a wrist-action shaker for 10 hours with 3 mm borosilicate glass beads. 300 mg of the ground powder were etched in 1 ml 25% HCl and 10 ml 40% HF in dark for 4-6 hours. Nanocrystals were isolated by centrifugation at 8000 rpm for 5 minutes and rinsed once with DI water, twice with ethanol, and once with chloroform.

2.2.3 Passivation of Si Nanocrystals with ω-Ester-Terminated or ω-Acid-Terminated Alkenes

The Si nanocrystals isolated from the HF etching procedure were dispersed in 6 mL of methyl 10-undecenoate, ethyl 10-undecenoate, or 10-undecenoic acid. Methyl 10-undecenoate and ethyl 10-undecenoate dispersions were freeze-pump-thawed four times and then stirred under nitrogen flow for 20 hours at room temperature (~20^{o}C); 10-undecenoic acid dispersions were stirred at 30^{o}C since the melting point of 10-undecenoic acid is about 26^{o}C. Poorly capped nanocrystals were separated by

precipitation by centrifugation at 8000 rpm for 5 minutes and discarded. Ligand-stabilized nanocrystals that remained dispersed in the supernatant were then precipitated with hexanes and isolated by centrifugation.

Nanocrystals capped with methyl 10-undecenoate or ethyl 10-undecenoate were redispersed in 1:1 v/v ethanol:toluene and washed 3 times by solvent/antisolvent precipitation with 1:1 v/v ethanol:toluene and hexanes. Ester-terminated Si nanocrystals were typically dispersed in 1:1 v/v ethanol:toluene.

Nanocrystals capped with 10-undecenoic acid were redispersed in ethanol and purified by precipitation with hexanes. Acid-terminated nanocrystals were dispersed in ethanol.

Ester and acid-terminated nanocrystals could be redispersed in water by repeated dilution of ethanol dispersions using 50 kDa molecular weight cut off centrifugal filters, and pH 7 DI water.

2.2.4 Si Nanocrystal Passivation with Mixed Alkene and Acid/Ester at Room Temperature

Hydride-terminated Si nanocrystals (6 mg) were dispersed in 12 ml of 1-octene and 1 ml of undecanoic acid. Three freeze-pump-thaw cycles were applied to the dispersion. The dispersion was then stirred in N_2 flow for 12, 24, or 120 hours at room temperature. Poorly capped nanocrystals were precipitated by centrifugation at 8000 rpm for 5 minutes and discarded. The remaining nanocrystals in the supernatant were then precipitated with ethanol and isolated by centrifugation. The ligand-stabilized

nanocrystals were redispersed in toluene and purified three times by precipitation with ethanol.

2.2.5 Hydrosilylation Yield Determination

The yield of nanocrystals obtained after hydrosilylation was determined by measuring the weight fraction of starting H-terminated Si nanocrystals retained after purifying the hydrosilylated nanocrystals. Typically, 520 mg of oxide-embedded Si nanocystals were HF-etched and divided into four samples of equal weight. Three of the samples were passivated at 30^{o}C with 10-undecenoic acid, methyl 10-undecenoate, and ethyl 10-undecenoate and then purified and dried. The remaining sample was used to determine the mass of starting material. The weight fraction of capping ligand in the hydrosilylated samples was determined by thermal gravimetric analysis (TGA, Mettler Toledo TGA-1). TGA measurements were made using 1 mg of nanocrystals dried into a 70 μL alumina crucible (Mettler Toledo), heated from 40°C to 800°C at 20°C/minute under 50 mL/min air flow.

2.2.6 HF Etch of 10-undecenoic Acid-Capped Si Nanocrystals

2.5 mg of Si nanocrystals capped with 10-undecenoic acid were dispersed in 5 mL of 48% HF and 5 mL of ethanol, and stirred in the dark for 30 minutes. HF was removed by centrifugation at 3000 rpm with a 50 kDa molecular weight cut off centrifugal filter to collect the nanocrystals. During the centrifugation step, the volume of the retentate is reduced from 10 mL to 1 mL. DI-H_2O is then added to the retentate to a volume of 10 mL, followed by another centrifugation. This dilution/centrifugation process was

repeated five times. The nanocrystals were then redispersed in ethanol, transferred to a glass centrifuge tube, and purified by precipitation with hexanes.

2.2.7 Materials Characterization

Attenuated total reflectance Fourier transform infrared (ATR-FTIR) spectra were obtained on a Thermo Mattson Infinity Gold FTIR spectrometer equipped with a Spectra-Tech Thermal ARK attenuated total reflectance module. A background measurement was taken after purging with N_2 for 30 minutes before loading the sample into the ARK attenuated total reflectance module. Nanocrystals dispersed in a solvent (i.e. ethanol, toluene) with concentration of 1 mg/ml were drop cast onto the crystal plate of the ARK module and dried with N_2. Measurements were made by acquiring 128 scans at a resolution of 4 cm^{-1}. The average transmittance is reported with background subtraction.

For transmission electron microscopy, nanocrystals were drop cast onto 200 mesh carbon-coated copper grids (Electron Microsopy Science). TEM images were acquired digitally using either a FEI Tecnai Biotwin TEM operated at 80 kV accelerating voltage or with a JEOL 2010F TEM operated at 200kV. For highest resolution, nanocrystals were drop cast onto graphene substrates. Graphene TEM substrates were prepared by dropping 3 μL of ethanol dispersion of graphene (0.1 mg/mL) onto a lacey carbon-coated copper grid (Electron Microscopy Sciences) and dried in air for 1 hour. The grid was plasma-treated for 5 minutes to make it hydrophilic. Nanocrystals were deposited onto the TEM substrates by dropping 5 μL of a dilute dispersion of 10-undecenoic acid-

terminated Si nanocrystals in ethanol and then heating at 200 ^{o}C in flowing forming gas for 3 hours.

Photoluminescence (PL) and photoluminescence excitation (PLE) spectra of 2-3 nm diameter Si nanocrystals were acquired on a Varian Cary Eclipse fluorescence spectrophotometer, PL spectra of larger Si nanocrystals were acquired on a Fluorolog-3 spectrophotometer (Horiba Jobin Yvon) with an InGaAs photomultiplier tube for visible detection and a Hamamatsu H10330-45 detector for NIR detection. UV-vis absorbance spectroscopy was performed on a Varian Cary 50 Bio ultraviolet-visible (UV-vis) spectrophotometer. To make an optical measurement, 3 ml of Si nanocrystal dispersion was loaded into a quartz cuvette with 10 mm optical path length. Quantum yields for 2-3 nm diameter Si nanocrystals were measured relative to a Rhodamine 101 standard sample dissolved in anhydrous ethanol.

X-ray diffraction (XRD) was performed using a Rigaku R-Axis Spider Diffractometer with an image plate detector and a graphite monochromator using Cu Kα radiation (λ=0.15418 nm). The instrument was controlled by Rapid/XRD diffractometer control software (version 2.3.8, Rigaku Americas Corp.) Nanocrystals were placed onto a nylon loop and mineral oil was applied to secure the sample if necessary. Two-dimensional diffraction data were collected for 10 min while rotating the sample stage at 5^{o} per minute. 2D diffraction data were radially integrated with 2DP Spider software (version 1.0, Rigaku Americas Corp.)

Small angle X-ray scattering (SAXS) data were obtained for solvent-dispersed Si nanocrystals. Measurements were performed on a Molecular Metrology system using a

rotating copper anode X-ray source (Bruker Nonius FR591, λ=0.154 nm) operating at 3.0 kW, and a 2D multiwire gas-filled detector (Molecular Metrology, Inc.). Si nanocrystals passivated with methyl 10-undecenoate and 10-undecenoic acid were dispersed in 1:1 v/v ethanol:toluene and pure ethanol, respectively. Measurements were conducted using 200 μL of nanocrystal solution (5 mg Si nanocrystals/mL). Datasqueeze (JDK 1.6.0_21) was used to convert 2D intensity profile to 1D plot. SAXS data are reported with the solvent background subtracted.

X-ray photoelectron spectroscopy (XPS) was performed using a commercial X-ray photoelectron spectrometer (Kratos Axis Ultra), utilizing a monochromatic Al Kα X-ray source (hν=1486.5 eV), hybrid optics (employing a magnetic and electrostatic lens simultaneously) and a multi-channel plate detector coupled to a hemispherical analyzer. Si nanocrystal films were drop-cast onto indium tin oxide coated glass slides and were secured on the experimental tray using double-sided Cu tape. The photoelectron take-off angle was normal to the surface of the sample and 45° with respect to the X-ray beam. All spectra were recorded using a single sweep and an aperture slot of 300 μm by 700 μm. High-resolution spectra were collected with 20 eV pass energy. Spectra were collected at 0.1 eV intervals and 1500 ms integration time through a tungsten coil set at 4.8 V bias with respect to the sample. The pressure in the analysis chamber was typically $3 \cdot 10^{-9}$ Torr during data acquisition. Sample charging was corrected by shifting the Si^0 $2p^{3/2}$ to a binding energy of 99.3 eV. Background subtraction was done using a Shirley background model.[26] The Si^0 $2p^{3/2}$ and Si^0 $2p^{1/2}$ peaks were fit with Voigt profiles (30% Gaussian character) centered at 99.3 and 99.8 eV, respectively, maintaining the

appropriate intensity ratio of 2:1 corresponding to the spin-orbit splitting ratio for p-orbitals. Peak contributions from Si^{1+}, Si^{2+}, Si^{3+}, Si^{4+}, and Si-C were fit using Voigt profiles centered at 100.4 eV, 101.5 eV, 102.6 eV, and 103.7 eV, and 102.0 eV, respectively.

2.3 RESULTS AND DISCUSSION

2.3.1 Si Nanocrystal Passivation with Ethyl 10-Undecenoate

Room temperature addition of relatively size-monodisperse, freshly HF-etched Si nanocrystals to the ω-ester-terminated alkene, ethyl 10-undecenoate, under air-free conditions results in a yellow (or yellowish-brown, depending on the nanocrystal size) optically clear dispersion after about 20 hours. The nanocrystals can be precipitated by adding non-polar organic solvent and redispersed in a mixture of ethanol and toluene. TEM (Figure 2.1) showed that the nanocrystals are not aggregated and have similar size as the starting material. XRD (Figure 2.1) verified that the passivated nanocrystals remain crystalline, with diamond cubic Si peaks of width consistent with the sizes measured by TEM. Nanocrystals ranging from 2 to 8 nm in diameter can be capped with ethyl 10-undecenoate, but with a higher yield of passivated nanocrystals for smaller nanocrystals, indicating that there is a size dependence for the passivation reaction. The ligand-passivated nanocrystals were luminescent with size-dependent PL, as shown in Figure 1.

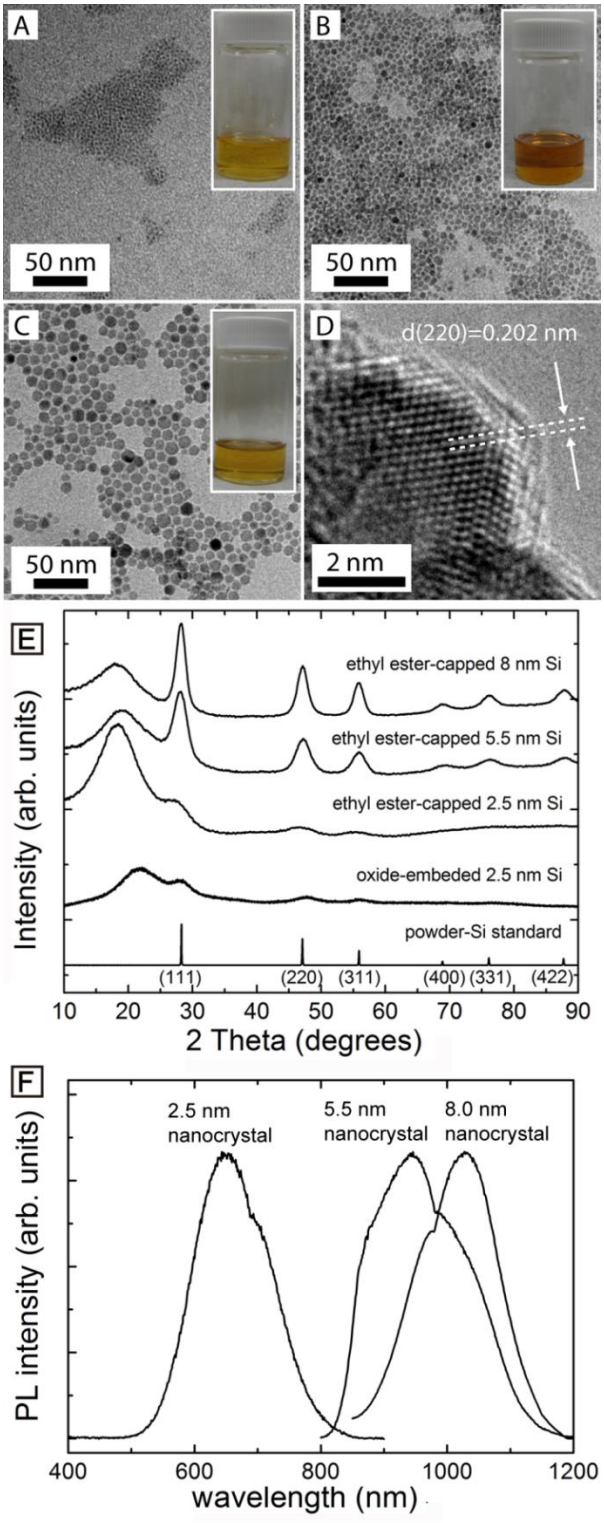
A
50 nm
B
50 nm
C
50 nm
D
d(220)=0.202 nm
2 nm
E
ethyl ester-capped 8 nm Si
ethyl ester-capped 5.5 nm Si
ethyl ester-capped 2.5 nm Si
oxide-embeded 2.5 nm Si
powder-Si standard
Intensity (arb. units)
(111)
(220)
(311)
(400)
(331)
(422)
10 20 30 40 50 60 70 80 90
2 Theta (degrees)
F
2.5 nm nanocrystal
5.5 nm nanocrystal
8.0 nm nanocrystal
PL intensity (arb. units)
400 600 800 1000 1200
wavelength (nm)

Figure 2.1

Figure 2.1: TEM images of Si nanocrystals with (A) 2.5 nm, (B) 5.5 nm, and (C) 8.0 nm diameter after room temperature passivation with ethyl 10-undecenoate. Insets: Photographs of nanocrystals dispersed in 1:1 v/v ethanol:toluene. (D) High resolution TEM image of a 10-undecenoic acid-capped Si nanocrystal. The 0.202 nm lattice spacing corresponds to the (220) d-spacing of diamond cubic Si. (E) XRD of the ethyl 10-undecenoate-capped Si nanocrystals imaged in (a-c). A diffraction pattern of 2.5 nm diameter Si nanocrystals embedded in oxide and a reference pattern for diamond cubic Si ((PDF # 027–1402, a=b=c=5.431 Å) are also provided. The diameters were determined by TEM. (F) PL ($_{exc}$=400 nm) from the ethyl 10-undecenoate-capped Si nanocrystals dispersed in1:1 v/v ethanol:toluene imaged in (a-c). The PL intensities are normalized—the larger nanocrystals have lower PL quantum yield.

2.3.2 Hydrosilylation With Other Bifunctional Ester and Acid Alkenes

Si nanocrystals could also be passivated at room temperature with the bifunctional methyl ester and carboxylic acid alkenes, methyl 10-undecenoate and 10-undecenoic acid. Figure 2.2 shows photographs of the nanocrystal dispersions before and after passivation. The nanocrystal dispersions were optically clear after passivation, and their absorbance, PLE and PL spectra are shown in Figure 2.2. When dispersed in polar solvents, the acid- and ester-terminated nanocrystals exhibited orange PL with quantum yields of about 7%, similar to hydrophobic hydrosilylated Si nanocrystals in this size range.[1,6,8,22] The polar functional groups do not appear to affect the light-emitting properties of the nanocrystals.

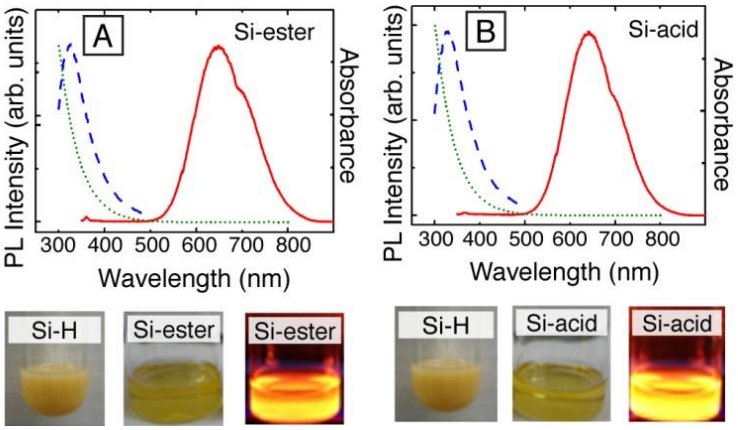

Figure 2.2: Absorbance (green curve), PLE (λ_{em}=650 nm; blue curve) and PL (λ_{exc}=325 nm; red curve) spectra of 2.3 nm diameter Si nanocrystals passivated at room temperature with (A) methyl 10-undecenoate ("Si-ester") dispersed in 1:1 v/v ethanol:toluene and (B) 10-undecenoic acid ("Si-acid") dispersed in ethanol. (Bottom) Photographs of nanocrystal dispersions before (turbid) and after (optically clear) ligand passivation under room and UV (365 nm) light.

Figure 2.3 shows TEM images and SAXS data for Si nanocrystals capped with methyl 10-undecenoate and 10-undecenoic acid. The average nanocrystal diameter was

determined from SAXS (Figures 3a and 3c) by assuming a dilute dispersion of non-interacting spherical particles:[27, 28]

$$\mathrm{I}(q) \propto \int_0^\infty N(R)P(qR)R^6 dR \quad . \tag{1}$$

q is the scattering vector, $q = (4\pi/\lambda)\sin(\theta/2)$, with scattering angle θ; $P(qR)$ is the form factor for a solid homogeneous sphere of radius R,

$$P(qR) = \left[3\frac{\sin(qR) - qR\cos(qR)}{(qR)^3} \right]^2 \quad ; \tag{2}$$

and the average radius $\overline{R}$, and standard deviation δ, of the dispersion are obtained by assuming a Gaussian size distribution,

$$N(R) = \frac{1}{\delta\sqrt{2\pi}} \exp\left[\frac{-(R-\overline{R})^2}{2\delta^2} \right] \tag{3}$$

Fits of Eqns (1-3) to the SAXS data in Figures 2.3b and 2.3d gave average diameters of 2.3±0.6 nm and 2.3±0.9 nm the Si nanocrystals passivated with methyl 10-undecenoate and 10-undecenoic acid, respectively. The nanocrystals used for these passivation experiments were obtained from the same batch of HF-etched nanocrystals. These data indicate that there is little change in size during the passivation reactions. The nanocrystals also remain crystalline diamond cubic Si—Figure 2.3e shows some high resolution TEM images of crystalline Si nanocrystals passivated with 10-undecenoic acid.

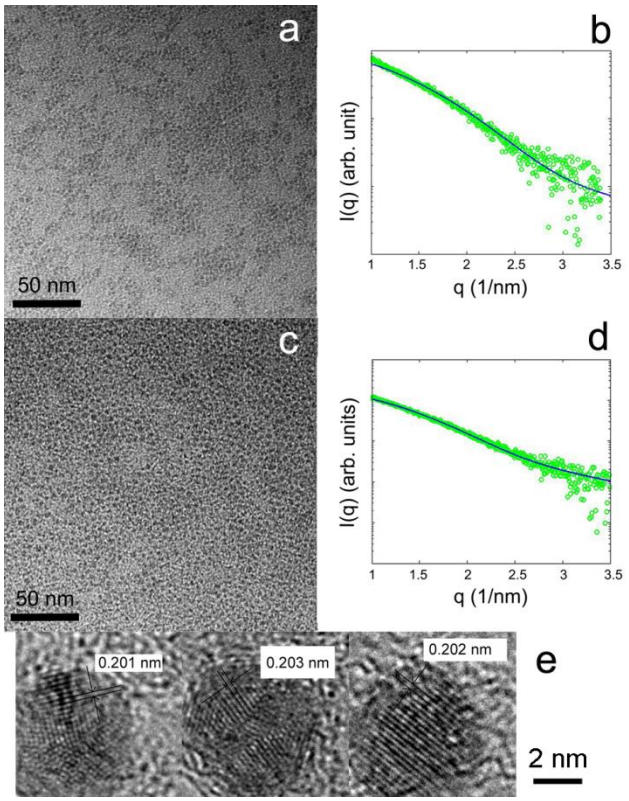

Figure 2.3: TEM images and SAXS measurements of Si nanocrystals passivated at room temperature with (a,b) methyl 10-undecenoate and (c,d) 10-undecenoic acid. In (b) and (d), the green circles are experimental data and the blue line is a fit of Eqns (1-3), which give average diameters of 2.3±0.6 nm and and 2.3±0.9 nm, respectively. (e) High resolution TEM images of the Si nanocrystals passivated with 10-undecenoic acid; 0.202 nm lattice spacing is consistent with (220) d-spacing of diamond cubic Si.

2.3.3 FTIR Analysis

FTIR spectra confirmed that passivation by the ω-ester-terminated (alkene-COOR) and ω-acid-terminated alkenes (alkene-COOH) occurs by hydrosilylation to create Si-C bonding an leave the polar functional groups (i.e., ester or acid) exposed on the nanocrystal periphery, which is consistent with their dispersibility in polar solvents. Figure 2.4 shows ATR-FTIR spectra of Si nanocrystals after passivation with methyl 10-

undecanoate, ethyl 10-undecenoate and 10-undecenoic acid. The characteristic signatures of the vinyl group (i.e., sp^2 C-H_x stretching at 3076 cm^{-1}, strong deformation vibrations of sp^2 C-H at 990 cm^{-1} and 907 cm^{-1}, and C=C stretching at 1640 cm^{-1}) disappear after hydrosilylation, while the peaks associated with C-H_x stretching,-CH_2- scissor vibration, C-O stretching, and C=O stretching remain. The polar functional groups remain intact and exposed to the solvent, as expected based on the observed dispersibility in polar solvents. Similar FTIR spectra have been reported for other Si substrates after thermal and photoinduced hydrosilylation of ω-ester-terminated and ω-acid-terminated olefins.[19-22]

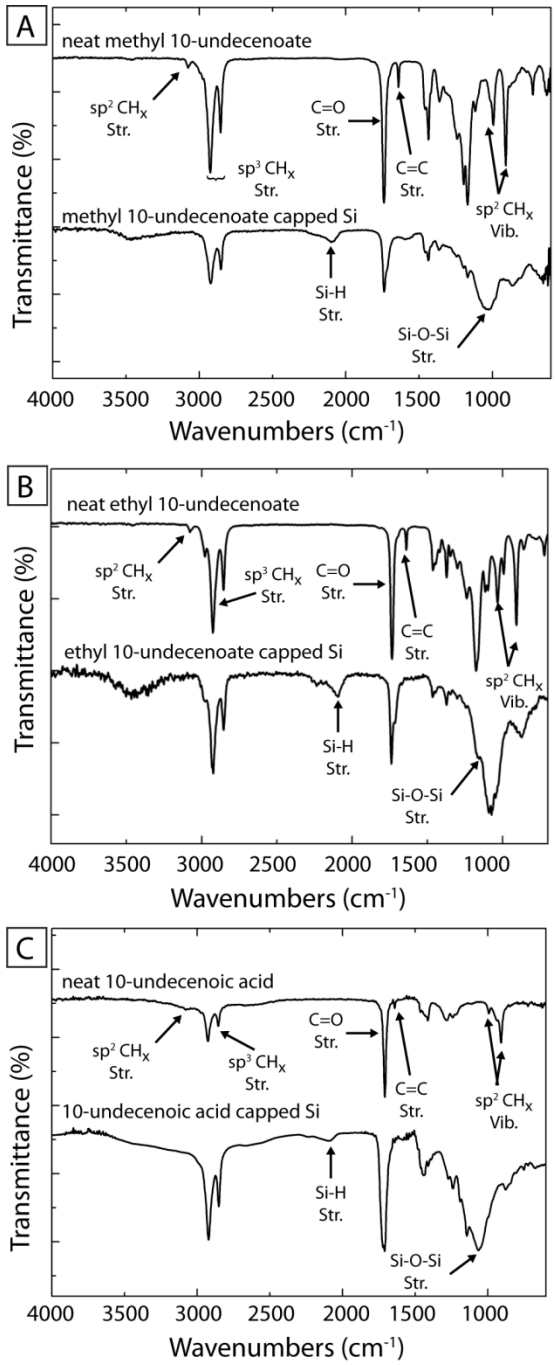

Figure 2.4: ATR-FTIR spectra of (A) methyl 10-undecenoate-capped, (B) ethyl 10-undecenoate-capped, and (C) 10-undecenoic acid-capped Si nanocrystals compared to pure "neat" methyl 10-undecenoate, ethyl 10-undecenoate, and 10-undecenoic acid.

2.3.4 Further Verification of Si-C Bonding of Ligands

A number of control experiments were performed that further verified that ligands bonded to the surface by Si-C and not Si-O-C bonding. For example, reaction between hydride-terminated Si nanocrystals and undecanoic acid (no terminal alkene) did not yield passivated nanocrystals, only resulting in a colorless transparent liquid (determined to be pure undecanoic acid, see support information) and a brown precipitate. FTIR spectra of the brown precipitate (Figure 2.5C) showed Si-H stretching at 2100 cm^{-1} and deformation at 910 cm^{-1}, and Si-O stretching between 1000 cm^{-1} and 1100 cm^{-1}, characteristic of unpassivated, hydride-terminated Si nanocrystals [6, ref]. The ester and carboxylic acid functional groups do not form stable bonds with the Si-H terminated surfaces.

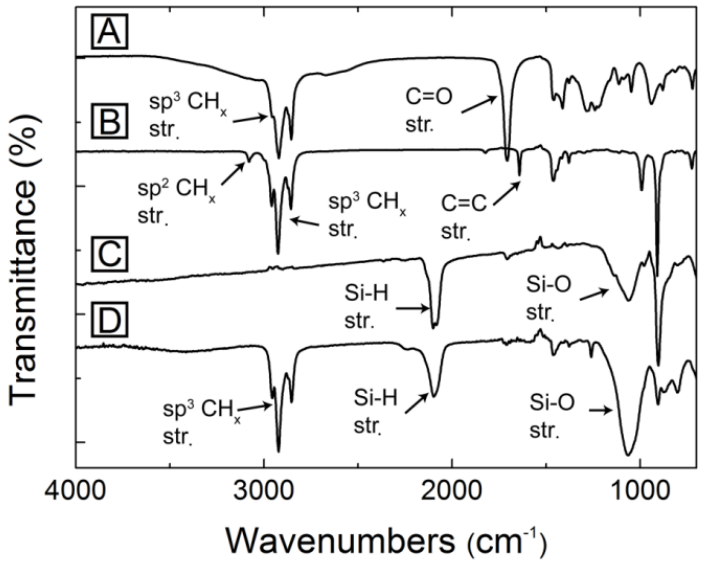

Figure 2.5: ATR-FTIR spectra of pure (A) undecanoic acid and (B) 1-octene compared to the (C) precipitate obtained after adding H-terminated Si nanocrystals to undecanoic acid, and the (D) Si nanocrystals that remained dispersed after passivation in a mixture of 1-octene and undecanoic acid.

Si-O-C bonding of the ligands to the nanocrystal surface was further ruled out by performing an HF etch on Si nanocrystals passivated with 10-undecenoic acid. If the ligands were bonded to the Si surface by Si-O-C linkages, the HF would cleave the Si-O bond and remove the capping ligands. After 30 minutes of exposure to HF the nanocrystals exhibited similar FTIR spectra (Figure 2.6B) as the material prior to etching. The only noticeable difference was a stronger Si-H stretch (2100 cm^{-1}) and weaker Si-O stretch (1000 cm^{-1}-1100 cm^{-1}), indicating that the ligands were still bound to the nanocrystals, but that the residual oxidized surface was partly transformed to hydride-terminated surface, due to HF. This is not unexpected, as all passivated nanocrystals had some oxidation and incomplete elimination of hydride species evident in the FTIR spectra (Figure 2.4 for example), that is probably due to steric hindrance between neighboring capping ligands that prevents Si-C termination of all surface Si atoms.

Etching the Si nanocrystals passivated with 10-undecenoic acid for even longer—for 6 hours—led to nanocrystals that no longer dispersed in ethanol. However, the ligands are still observed in the FTIR spectra (Figure 2.6C), with strong C-H stretch (2800 cm^{-1}-3000 cm^{-1}) and C=O stretch (1710 cm^{-1}). Furthermore, there is no Si-O stretch (1000 cm^{-1}-1100cm^{-1}). The C=O stretch of "neat" 10-undecenoic acid (Figure 2.6E) occurs as a single peak between 1690 cm^{-1} and 1720 cm^{-1}, while the C=O stretch of 10-undecenoic acid bound to the Si nanocrystals appeared as a doublet (Figure 2.6D). The C=C stretch at 1640 cm^{-1} of "neat" 10-undecenoic acid is also not present in the nanocrystal spectra, further indicating that the C-H and C=O signals in the FTIR spectra correspond to bound ligand. The change in dispersibility therefore appears to result

from increased surface hydrogenation or hydrogenation of the acid group, but FTIR shows that the ligands are clearly still attached to the nanocrystals after the long HF etch, confirming Si-C bonding to the surface.

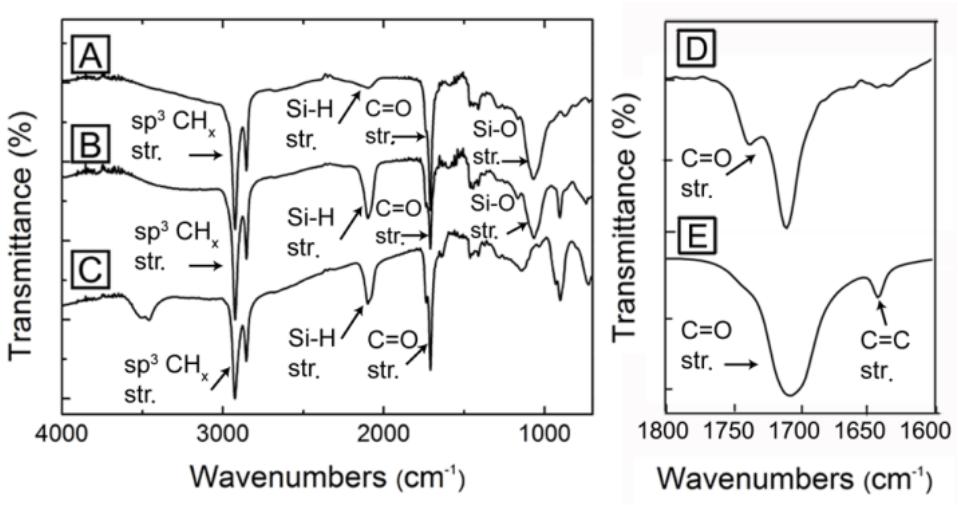

Figure 2.6: ATR-FTIR spectra of (A) 10-undecenoic acid-capped Si nanocrystal before HF etch, (B) 10-undecenoic acid-capped Si nanocrystal being etched in HF for 30 minutes, and (C) 10-undecenoic acid-capped Si nanocrystal being etched in HF for 6 hours, (D) zoomed-in spectra between 1800 cm^{-1} and 1600 cm^{-1} of 10-undecenoic acid-capped Si nanocrystal being etched in HF for 6 hours, (E) zoomed-in spectra between 1800 cm^{-1} and 1600 cm^{-1} of "neat" 10-undecenoic acid.

2.3.5 XPS Analysis

XPS was used to determine the binding of the capping ligand to the nanocrystals through the presence of the Si-C bonding signal. XPS data of ethyl 10-undecenoate, methyl 10-undecenoate, and 10-undecenoic acid-capped Si nanocrystals exhibit peak contributions of Si^0 $2p^{3/2}$ (99.8 eV) and Si^0 $2p^{1/2}$ (99.3 eV) corresponding to the Si core of nanocrystal and a strong signals from Si-C bonding (101.9 eV[6]). There are also contributions from Si^{4+} (103.7 eV), Si^{3+} (102.6 eV), and Si^{1+} (100.5 eV) due to some

surface oxidation prior to analysis. The contribution of Si-C bonding was verified by the XPS of Si nanocrystals freshly capped with 1-dodecene, which shows strong signal from Si^0 and Si-C bonding with minimal signal from surface oxidation. XPS of hydride-terminated Si nanocrystals dispersed in chloroform on the bench top for 5 days shows strong surface oxidation and no Si-C bonding. XPS of 1-dodecene-capped sample which had been on the bench top for 3 weeks retains the strong Si-C bonding signal with little oxidation signals demonstrating the ability of the capping ligand to inhibit oxidation of the nanocrystal surface. For oxide-embedded Si nanocrystal, XPS data is dominated by Si^{4+} corresponding to the large SiO_2 matrix the nanocrystals are embedded in.

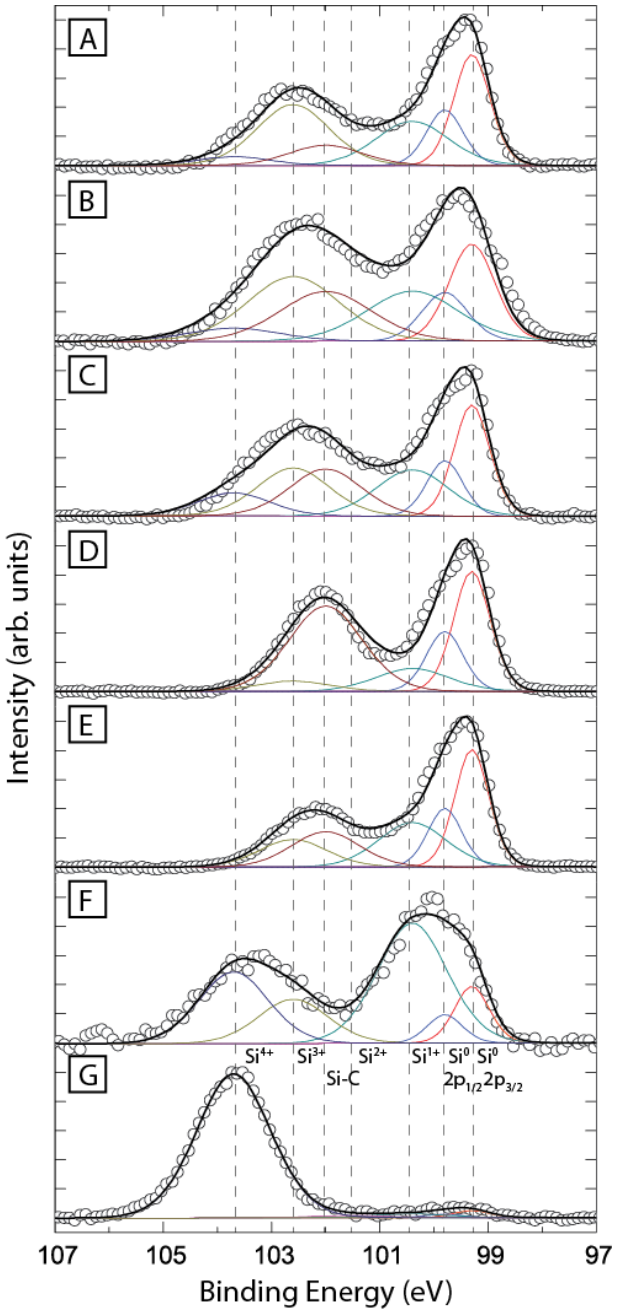

Figure 2.7: XPS of Si nanocrystals passivated with (A) ethyl 10-undecenoate, (B) methyl 10-undecenoate, (C) 10-undecenoic acid, and (D) 1-dodecene (at high temperature) along with (E) 1-dodecene passivated and (F) HF etched Si nanocrystals that were exposed to air on the benchtop in chloroform for 3 weeks and 5 days, respectively, and (G) oxide embedded nanocrystals. The data (o) were fit (black line) to the separate peak contributions from Si^0 $2p_{3/2}$, Si^0 $2p_{1/2}$, Si^{1+}, Si^{2+}, Si^{3+}, Si^{4+} , and Si-C signals shown in color.

2.3.6 Reaction Mechanism

Figure 2.8 shows TGA data of Si nanocrystals passivated with undecenoic acid, methyl 10-undecenoate and ethyl 10-undecenoate compared to pure undecenoic acid, methyl 10-undecenoate and ethyl 10-undecenoate. Ligand desorption leads to a net weight loss while Si oxidation produces an increase in mass. The relative mass of Si and organic in the passivated sample was determined from the remaining mass of SiO_2 and the total weight loss was due to the removal of the organic ligands. The following thermal events are observed: Si oxidation (40-170^{o}C), evaporation of free ligand (170-400^{o}C), loss of bound ligand (330-520^{o}C), and oxidation of remaining Si (520-800^{o}C) to fully oxidized particles (SiO_2).

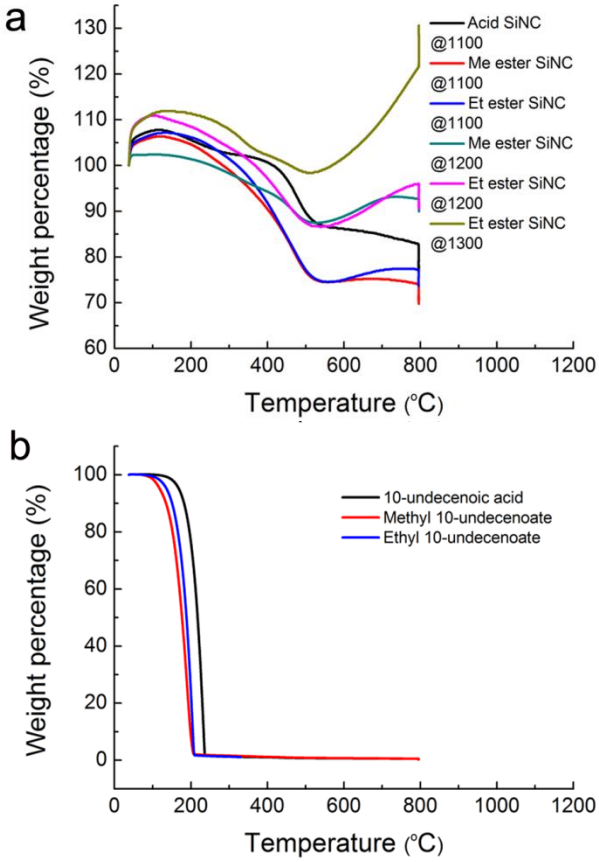

Figure 2.8: TGA of (a) Si nanocrystals: "Acid SiNC," "Me ester SiNC," and "Et ester SiNC" refers to nanocrystals passivated with 10-undecenoic acid, methyl 10-undecenoate, and ethyl 10-undecenoate, respectively. (b) shows TGA data for pure 10-undecenoic acid, methyl 10-undecenoate, and ethyl 10-undecenoate.

Hydrosilylation yields could be determined comparing the weight of final passivated nanocrystal, to the weight of initial hydride-terminated nanocrystal. The silicon content of the final nanocrystal was calculated with the TGA data. The passivation reaction was found to depend on nanocrystal size and the functional group. Figure 2.9 lists the yield of nanocrystals with three different sizes obtained after passivation with ethyl 10-undecenoate, methyl 10-undecenoate and 10-undecenoic acid. Ethyl 10-

undecenoate provided the most effective room temperature passivation, and the smallest nanocrystals were found to be most reactive.

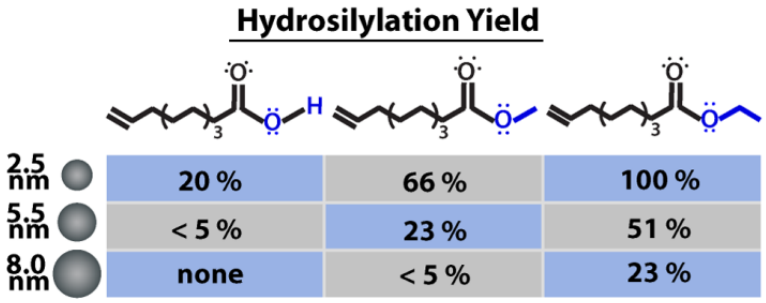

Figure 2.9: Yield of nanocrystals obtained after hydrosilylation with 10-undecenoic acid, methyl 10-undecenoate, and ethyl 10-undecenoate. Nanocrystals with three different average diameters were tested.

To gain a better understanding of the reaction mechanism and the role of the ester and acid functional groups in the hydrosilylation reaction, various control experiments were carried out. Room temperature passivation did not occur with alkene (dodecene), ester (methyl 10- undecanoate) or acid (10-undecanoic acid). Alkene-ketones also did not lead to passivation.

The ester (or carboxyl) segment of the bifunctional ligands catalyzes hydrosilylation, most likely by a mechanism in which the nucleophilic carbonyl group of the ester (acid) coordinates to the oxophilic Si surface and enhances the reactivity of the Si-H to the alkene end of another independent reactant molecule. Upon coordination, the Si-H bond lengthens, increases in hydridic character, and becomes more nucleophilic toward alkenes. When in close proximity, the electron deficient C=C accepts H- from surface to facilitate Si-C bond formation, as illustrated in Figure 2.10A. Unlike radical-initiated hydrosilylation that propagates across the Si surface,[11,12] this single-step reaction

must occur repeatedly for complete surface passivation, similar to Lewis acid catalyzed hydrosilylation reactions.

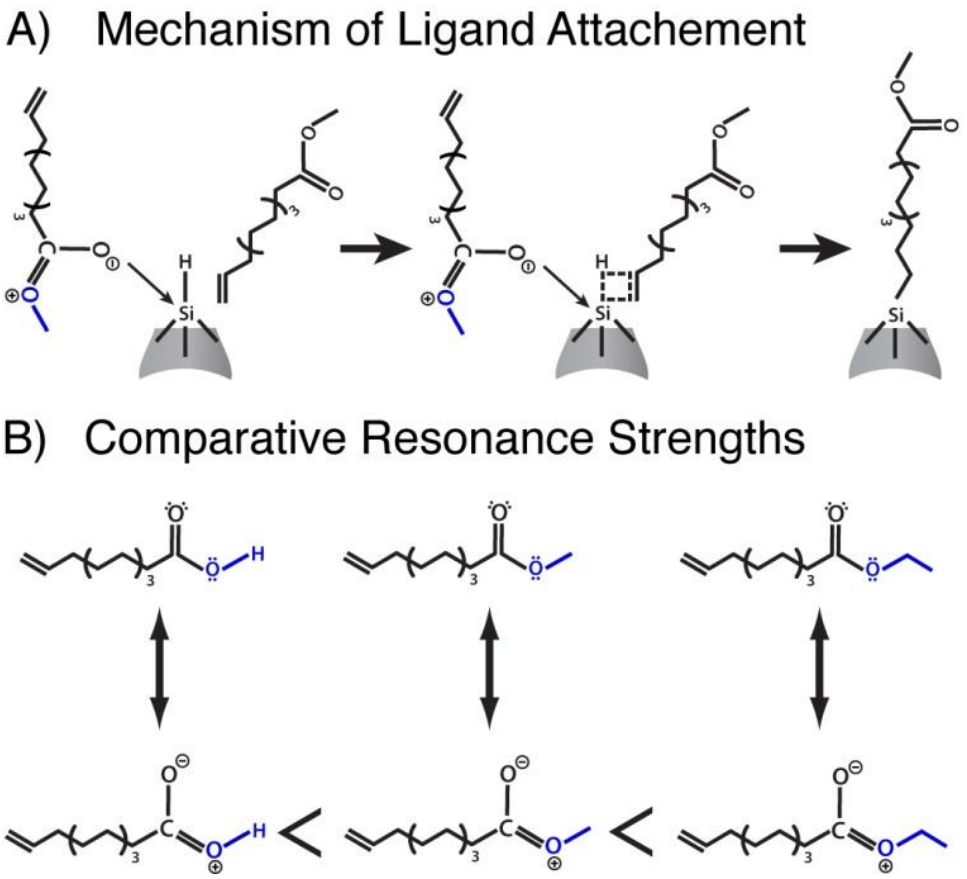

Figure 2.10: (A) Mechanistic illustration of methyl 10-undecenoate attachment to the Si nanocrystal surface. The catalyst molecule is shown in its resonance form to emphasize the regions of electrostatic interaction. (B) Relative resonance strengths of 10-undecenoic acid, methyl 10-undecenoate, and ethyl 10-undecenoate.

The mechanism of ligand attachment has similarities to Lewis acid (LA) catalyzed hydrosilylation Si-H surfaces with unsaturated carbon-carbon bonds.[16] Lewis acids such as Et_2AlCl catalyze hydrosilylation reactions[16,29] by forming electropositive adducts with alkenes or alkynes that readily inert into Si-H bonds via attack at the electropositive carbon by H^-. In other words, the Lewis acid makes the alkene a

stronger electrophile. In the case of the ester and carboxylic acid functional groups, the carbonyl activates the Si-H bond. Coordination of the electron rich carbonyl group to the Si surface enhances the nucleophilicity of the Si-H bond enough to facilitate H^- attack at the unsaturated carbon-carbon bond. Our observations show the extent of the catalytic effect increases with increasing electron density at the carbonyl oxygen (C=O). The hydrosilylation efficiency—evaluated by determining the weight fraction of passivated Si nanocrystals recovered after purification—was observed to follow the trend of alkene-ethyl ester > alkene-methyl ester > alkene-carboxylic acid. Light was also found to play no role, as reactions performed under room light and in the dark yielded similar results. These findings are consistent with the mechanism in Figure 1A. Illustrated in Figure 2.8B, esters have stronger resonance forms than carboxylic acids due to the electron donating character of alkyl groups and correspondingly have greater electron density on the carbonyl oxygen.[30] Also consistent with the proposed mechanism, attempts to add alkene-ketones to the surface led to no hydrosilylation and surface passivation. Without oxygen adjacent to the carbonyl to contribute to a resonance form, the ketone cannot activate Si-H bonds as needed for hydrosilylation.

Liu *et al.*[31,32] or Zaborovskiy *et al.*[33] recently proposed a mechanism for attachment of bifunctional alkyne-esters to tris(trimethylsilyl)silane involving a radical chain mechanism initiated by reaction of adventitious oxygen with Si-H bonds to form silyl and hydroperoxyl radicals. In the case of the Si nanocrystals, if adventitious oxygen created silyl radicals, then hydrosilylation would be expected with 1-octene at room temperature, which is not observed. On the other hand, through the exactly same

procedure, reaction in a mixture of undecanoic acid (no terminal alkene) and 1-octene, however, did lead to a yellow transparent solution with orange PL, indicating the existence of passivated Si nanocrystal. FTIR (Figure 2.5D) revealed strong C-H stretching at 2800 cm^{-1}-3000 cm^{-1}, but negligible C=O stretching (1710 cm^{-1}), indicating the Si nanocrystal was passivated with 1-octene at room temperature, with the presence of undecanoic acid.

2.4 CONCLUSIONS

Bifunctional alkenes with distal polar moieties—either ethyl-, methyl-ester or carboxylic acids—undergo room temperature hydrosilylation with 2-8 nm diameter H-terminated Si nanocrystals without photoexcitation or added catalyst. The polar ether or carboxylic acid functional group promotes addition across the terminal alkene to yield hydrophilic Si nanocrystals. The Si nanocrystals still exhibit bright PL when dispersed in polar solvents, including water.

2.5 REFERENCES

(1) Hessel, C. M.; Reid, D.; Panthani, M. G.; Rasch, M. R.; Goodfellow, B. W.; Wei, J.; Fujii, H.; Akhavan, V.; Korgel, B. A. Synthesis of Ligand-Stabilized Silicon Nanocrystals with Size-Dependent Photoluminescence Spanning Visible to Near-Infrared Wavelengths. *Chem. Mater.* **2012**, *24*, 393-401.

(2) Hua, F.; Mark T. Swihart, M. T.; Ruckenstein, E. Efficient Surface Grafting of Luminescent Silicon Quantum Dots by Photoinitiated Hydrosilylation. *Langumir* **2005**, *21*, 6054-6062.

(3) Mangolini, L.; Kortshagen, U. Plasma-Assisted Synthesis of Silicon Nanocrystal Inks. *Adv. Mater.* **2007**, *19*, 2513-2519.

(4) English, D. S.; Pell, L. E.; Yu, Z.; Barbara, P. F.; Korgel, B. A. Size Tunable Visible Luminescence from Individual Organic Monolayer Stabilized Silicon Nanocrystal Quantum Dots. *Nano Lett.* **2002**, *2*, 681-685.

(5) Hessel, C. M.;.Henderson, E. J.; Veinot, J. G. C. Hydrogen Silsesquioxane: A Molecular Precursor for Nanocrystalline Si-SiO2 Composites and Freestanding

Hydride Surface Terminated Silicon Nanoparticles. *Chem. Mater.* **2006**, *18*, 6139-6146.
(6) Hessel, C. M.; Rasch, M. R.; Hueso, J. L.; Goodfellow, B. W.; Akhavan, V. A.; Puvanakrishnan, P.; Tunnel, J. W.; Korgel, B. A. Alkyl Passivation and Amphiphilic Polymer Coating of Silicon Nanocrystals for Diagnostic Imaging. *Small* **2010**, *6*, 2026-2034.
(7) Bae, Y.; Lee, D. C.; Rhogojina, E. V.; Jurbergs, D. C.; Korgel, B. A.; Bard, A. J. Electrochemistry and Electrogenerated Chemiluminescence of Films of Silicon Nanoparticles in Aqueous Solution *Nanotechnology* **2006***, 17,* 3791-3797.
(8) Sato, S.; Swihart, M. T. Propionic-Acid-Terminated Silicon Nanoparticles: Synthesis and Optical Characterization. *Chem. Mater.* **2006**, *18*, 4083-4088.
(9) Li, Z. F.; Ruckenstein, E. Water-Soluble Poly(acrylic acid) Grafted Luminescent Silicon Nanoparticles and Their Use as Fluorescent Biological Staining Labels. *Nano Lett.* **2004**, *4*, 1463-1467.
(10) Warner, J. H.; Hoshino, A.; Yamamoto, K.; Tilley, R. D. Water-Soluble Photoluminescent Silicon Quantum Dots. *Angew. Chem. Int. ed.* **2005**, *44*, 4550-4554.
(11) Linford, M. R.; Chidsey, C. E. D. Alkyl Monolayers Covalently Bonded to Silicon Surfaces. *J. Am. Chem. Soc.* **1993**, *115*, 12631-12632.
(12) Buriak, J. M. Organometallic Chemistry on Silicon and Germanium Surfaces. *Chem. Rev.* **2002**, *102*, 1271-1308.
(13) Bateman, J. E.; Eagling, R. D.; Worrall, D. R.; Horrocks, B. R.; Houlton, A. *Angew. Chem. Intl. Ed.* **1998**, *37*, 2683-2685.
(14) Kim, N. Y.; Laibinis, P. E. Derivatization of Porous Silicon by Grignard Reagents at Room Temperature. *J. Am. Chem. Soc.* **1998**, *120*, 4516-4517.
(15) Song, J. H.; Sailor, M. J. Functionalization of Nanocrystalline Porous Silicon Surfaces with Aryllithium Reagents: Formation of Silicon-Carbon Bonds by Cleavage of Silicon-Silicon Bonds. *J. Am. Chem. Soc.* **1998**, *120*, 2376-2381.
(16) Buriak, J. M.; Allen, M. J. Lewis Acid Mediated Functionalization of Porous Silicon with Substituted Alkenes and Alkynes. *J. Am. Chem. Soc.* **1998**, *120*, 1339-1340.
(17) Zazzera, L. A.; Evans, J. F.; Deruelle, M.; Tirrell, M.; Kessel, C. R. Bonding Organic Molecules to Hydrogen-Terminated Silicon Wafers. *J. Electrochem. Soc.* **1997**, *144*, 2184-2189.
(18) Boukherroub, R.; Morin, S.; Wayner, D. D. M.; Bensebaa, F.; Sproule, G. I.; Baribeau, J.-M.; Lockwood, D. J. Ideal Passivation of Luminescent Porous Silicon by Thermal, Noncatalytic Reaction with Alkenes and Aldehydes. *Chem. Mater.* **2001**, *13*, 2002-2011.
(19) Sieval, A. B.; Demirel, A. L.; Nissink, J. W. M.; Linford, M. R.; Van der Maas, J. H.; de Jeu, W. H.; Zuilhof, H.; Sudholter, E. J. R. Highly Stable Si-C Linked Functionalized Monolayers on the Silicon (100) Surface. *Langmuir* **1998**, *14*, 1759-1768.

(20) Boukherroub, R.; Wayner, D. D. M.; Sproule, G. I.; Lockwood, D. J.; Canham, L. T. Stability Enhancement of Partially-Oxidized Porous Silicon Nanostructures Modified with Ethyl Undecylenate. *Nano Lett.* **2001**, *1*, 713-717.
(21) Boukherroub, R.; Wayner, D. D. M. Controlled Functionalization and Multistep Chemical Manipulation of Covalently Modified Si(111) Surfaces. *J. Am. Chem. Soc.* **1999**, *121*, 11513-11515.
(22) Li, X.; He, Y.; Swihart, M. T. Surface Functionalization of Silicon Nanoparticles Produced by Laser-Driven Pyrolysis of Silane Followed by HF-HNO_3 Etching. *Langmuir* **2004**, *20*, 4720-4727.
(23) Rogozhina, E. V.; Eckhoff, D. A.;Gratton, E.; Braun, P. V. Carboxyl Functionalization of Ultrasmall Luminescent Silicon Nanoparticles Through Thermal Hydrosilylation. *J. Mater. Chem*. **2006**, *16*, 1421-1430.
(24) Froner, E.; Amato, E. D.; Adamo, R.; Prtljaga, N.; Larcheri, S.; Pavesi, L.; Rigo, A.; Potrich, C.; Scarpa, M. Deoxycholate as an Efficient Coating Agent for Hydrophilic Silicon Nanocrystals. *J. Coll. Interf. Sci.* **2011**, *358*, 86-92.
(25) Boukherroub, R.; Morin, S.; Sharpe, P.; Wayner, D. D. M.; Allongue, P. Insights into the Formation Mechanisms of Si-OR Monolayers from the Thermal Reactions of Alcohols and Aldehydes with Si(111)-H. *Langmuir* **2000**, *16*, 7429-7434.
(26) Shirley, D. A. High-Resolution X-Ray Photoemission Spectrum of the Valence Bands of Gold. *Phy. Rev. B* **1972**, *5*, 4709-4714.
(27) Goodfellow B. W.; Patel R. N.; Panthani M. G.; Smilgies D. M.; Korgel B. A. Melting and Sintering of a Body-Centered Cubic Superlattice of PbSe Nanocrystals Followed by Small Angle X-ray Scattering. *J. Phy. Chem. C* **2011**, *115*, 6397-6404.
(28) Socrates, G. *Infrared Characteristic Group Frequencies: Tables and Charts.* John Wiley & Sons, New York, **1994**, 34-189.
(29) Zipoli, F.; Bernasconi, M. Ab initio Simulation of the Grafting of Phenylacetylene on Hydrogenated Surfaces of Crystalline Silicon Catalyzed by a Lewis Acid, *J. Phys. Chem. B* **2006**, *110*, 23403-23409.
(30) Peter, K.; Vollhardt, C.; Schore, N. E. *Organic Chemistry: Structure and Function*, W. H. Freeman and Company, New York, **2002**, 864-879.
(31) Liu, Y.; Yamazaki, S.; Yamaba, S.; Nakato, Y. A mild and efficient Si (111) Surface Modification via Hydrosilylation of Activated Alkynes. *J. Mater. Chem.* **2005**, *15*, 4906-4913.
(32) Liu, Y.; Yamazaki, S.; Yamabe, S. Modification and Chemical Transformation of Si(111) Surface. *J. Org. Chem.* **2005**, *70*, 556-561.
(33) Zaborovskiy, A. B.; Lutsyk, D. S.; Prystansky, R. E.;Kopylets, V. I.; Timokhin, V. I.; Chatgilialoglu, C. A Mechanistic Investigation of $(Me_3Si)_3SiH$ Oxidation *J. Organomet. Chem.* **2004**, *689*, 2912-2919.

Chapter 3: Styrene Capping of Silicon Nanocrystals by Room Temperature Hydrosilylation

3.1 INTRODUCTION

Silicon (Si) nanocrystals exhibit bright, size-tunable photoluminescence[1-4] and electroluminescence[5-8] covering much of the visible to near infrared spectrum, and hence have potential applications in fluorescent bio-imaging[9,10] and light-emitting devices (LEDs).[5-8] To protect Si from oxidation, it is necessary to passivate the surface and stabilize the unique optical properties that arise from quantum confinement.[1-4] One of the most common and effective approaches to colloidal Si nanocrystal surface passivation is to create organic ligand capping layers by alkene addition via hydrosilylation.[1-4,11-13]

Hydrosilylation typically involves radicals created using either a radical initiator, catalyst, heat, or UV light.[23.24] These approaches can induce intermolecular side-reactions for some capping ligands that make monolayer surface passivation impossible. This is the case with styrene, as it rapidly polymerizes in the presence of radicals, especially at the elevated temperatures that are typically used for thermally-promoted alkene addition to Si nanocrystals.[25] This does lead to styrene adsorption to the Si nanocrystals, but along with styrene polymerization, creating a composite material of Si nanocrystals embedded in a polystyrene matrix,[26] rather than free-standing styrene-terminated Si nanocrystals. For certain applications, this is not desirable. For example, when used as light emitters in light-emitting diodes (LEDs)[5-8] or light absorbers in photovoltaic (PV) devices,[14,15] Si nanocrystals need to have enough electrical

conductivity to allow charge carriers to transport through the layer of nanocrystals for either charge injection in LED or charge separation in PV device and a significant amount of intervening polymer matrix is usually undesirable. In the case of adsorbed chromophores designed to transfer charge to and from the Si nanocrystals[30], the intervening linker molecules need to be short with controlled surface coverage. There is a desire to explore aromatic capping ligands or organic linker molecules, as these might enhance charge transport from the Si nanocrystals.[18,19] Furthermore, styrene is commercially available and has been assembled on surface of bulk Si[20,21] and germanium[22] to study the electron transport through the interface.[21]

Our group discovered recently a non-radical, room temperature route to hydrosilylation that we demonstrate here can be applied to controlled styrene monolayer addition to Si nanocrystals without styrene co-polymerization. This method involves activation of Si-H bonds by the carbonyl oxygen in the resonance form of carboxylic acid or ester group.[27] Styrene adds to hydride-terminated Si nanocrystals at room temperature in the presence of undecanoic acid as a catalyst. This room temperature hydrosilylation yield free-standing styrene-terminated Si nanocrystals without additional styrene polymer.

3.2 EXPERIMENTAL DETAILS

3.2.1 Materials

FOx-16 was purchased from Dow Corning. %), undecanoic acid (97%), and styrene (>99%) were purchased from Sigma-Aldrich. Ethanol, toluene, chloroform, and

hydrochloric acid (HCl, 37.5%) were obtained from Fisher Scientific. Hydrofluoric acid (HF, 48%) was obtained from EMD chemicals.

3.2.2 Synthesis of Hydride-Terminated Si Nanocrystals

20 mL of flowable oxide (FOx-16) was evaporated in vacuum for 6 hours to yield hydrogen silsesquioxane (HSQ), which was decomposed at 1100^{o}C under forming gas (93% nitrogen and 7% hydrogen) for 1 hour, result in a brown glassy material which was SiO_2-embedded Si nanocrystal. The brown material was ground with an agate mortar and pestle to a powder, and shacked in a wrist-action shaker for 9 hours with 30 g of 3 mm diameter borosilicate glass beads to become a fine powder. Hydride-terminated Si nanocrystal was obtained by wet etching 300mg of fine powder with 10 mL of HF (48%) and 1 mL of HCl (37%) in dark for 4 hours. Then the hydride-terminated Si nanocrystals were isolated by centrifugation and rinsed once with DI water, twice with ethanol, and once with chloroform.

3.2.3 Passivation with Styrene at Room Temperature

In a typical synthesis, hydride-terminated Si nanocrystals were isolated from chloroform by centrifugation and dispersed in 3 mL of toluene, which was then mixed with 2 mL of styrene, 2 mL of undecanoic acid, and 2 mL of ethanol. The mixed solution was transferred into a 20 mL vial, and purged with nitrogen gas for 30 min, and finally the vial was sealed with a rubber septum. It took about 5-7 days for hydrosilylation to complete. (Figure 1)

3 mL of toluene was added to the raw reaction solution to fully disperse the passivated Si nanocrystal, while the unpassivated particles were removed by centrifugation. The passivated Si nanocrystal was cleaned by precipitation and centrifugation with toluene/ethanol solvents combination. The cleaned passivated nanocrystal was dispersed in toluene until further characterization.

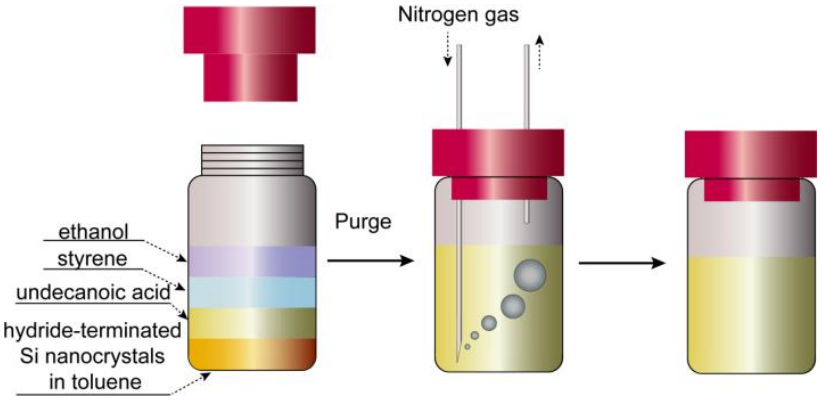

Figure 3.1: Experimental setup for free-standing styrene-capped Si nanocrystal synthesis at room temperature.

2.2.4 Passivation with Styrene at 190 °C

Hydride-terminated Si nanocrystals were isolated from chloroform by centrifugation and dispersed in 6 mL of styrene, which was transferred to a three-neck flask, and degased with three freeze-pump-thaw cycles. The Si nanocrystal styrene mixture was then heated to 190°C in nitrogen atmosphere for 1 hour.

2.2.5 Materials Characterization

Transmission Electron Microscopy was performed on a FEI Tecnai Biotwin TEM operated at 80 kV accelerating voltage. Nanocrystals were drop cast onto 200 mesh carbon-coated copper grids for imaging (Electron Microsopy Science).

Attenuated total reflectance Fourier transform infrared (ATR-FTIR) spectra were obtained on a Thermo Mattson Infinity Gold FTIR spectrometer with a Spectra-Tech Thermal ARK attenuated total reflectance module. The instrument was purged with nitrogen gas for more than 30 min to get rid of the signal from CO_2. A background measurement was taken before loading the sample into the ARK attenuated total reflectance module. Then, nanocrystals dispersed in toluene were drop cast onto the crystal plate of the ARK module and dried under N_2 flow. Measurements were made by acquiring 256 scans at a resolution of 4 cm^{-1}. The average transmittance is reported with background subtraction.

Thermal gravimetric analysis (TGA) was performed using a Mettler Toledo TGA-1, by adding Si nanocrystal dispersion (contains ~1 mg sample) to a 70 alumina crucible (Mettler Toledo), and allowing solvents to evaporate in a fume hood. Samples were heated from 40°C to 800°C, at rate of 20°C/min, and then held at 800°C for 30 min, under 50 mL/min air flow.

TGA data can be used to calculate the average number of ligand per nanocrystal by assuming spherical nanocrystal with density of bulk material.

$$N_{ligand\ per\ nanocrystal} = \frac{4}{3}\pi\overline{R}^3\rho_{Si} * {(1 - Si_{wt}\%)}/{Si_{wt}\%} * 6.02 * 10^{23}/M_{ligand} \quad (1)$$

In Eqn (1), $\overline{R}$ is average radius of Si nanocrystal determined by SAXS, ρ_{Si} is the bulk density of Si, $Si_{wt}\%$ is weight percentage of Si in the Si nanocrystal determined by TGA, and M_{ligand} is molecular weight of ligand.

Photoluminescence (PL) and photoluminescence excitation (PLE) spectra in the UV-visible wavelength range were acquired on a Varian Cary Eclipse fluorescence spectrophotometer with a 10 mm-path length quartz cuvette. UV-visible absorbance spectroscopy was performed on a Varian Cary 50 Bio ultraviolet-visible (UV-vis) spectrophotometer. PL quantum yields were estimated relative to Rhodamine 101 in anhydrous ethanol, which was assumed to have 100% quantum yield.

X-ray diffraction (XRD) was performed using a Rigaku R-Axis Spider Diffractometer with an image plate detector and a graphite monochromator using Cu Kα radiation (λ=0.15418 nm). The instrument was controlled by Rapid/XRD diffractometer control software (version 2.3.8, Rigaku Americas Corp.) Nanocrystals were placed onto a nylon loop and mineral oil was applied to secure the sample if necessary. Two-dimensional diffraction data were collected for 20 min while rotating the sample stage at 10^{o} per minute. 2D diffraction data were radially integrated with 2DP Spider software (version 1.0, Rigaku Americas Corp.)

Small angle X-ray scattering (SAXS) data obtained for Si nanocrystals dispersed in toluene was performed on D1 beam line of the Cornell High Energy Synchrotron Source (CHESS), using monochromatic X-ray with wavelength of 1.154 nm. A fiber coupled CCD camera with a total of 1024 × 1024 pixels was used to acquire the SAXS pattern image, which was integrated with Fit2D software (version: 12_077_i686_WXP).

SAXS data are reported with the solvent background subtracted, and fitted by assuming non-interacting solid spheres of mean radius$\bar{R}$, standard deviation , based on Gaussian size distribution $N(R)$:

$$I(q) \propto \int_0^\infty N(R)P(qR)R^6 dR \quad (2)$$

$$N(R) = {}^{1}/_{2\pi\delta} \exp\left[{}^{-(R-\bar{R})^2}/_{2\sigma^2}\right] \quad (3)$$

and homogeneous solid sphere's shape factor:

$$P(qR) = 9\left[{}^{(\sin(qR) - qR\cos(qR))}/_{(qR)^3}\right]^2 \quad (4)$$

The scattering vector is $q = (4\pi/\lambda)\sin(\theta/2)$ where λ is the X-ray wavelength and θ is the scattering angle.[1]

3.3 RESULTS AND DISCUSSION

Si nanocrystals were synthesized using the method of HSQ decomposition first described by Hessel and Veinot,[28] with some modifications, as described by Yu, *et al*.[27] Oxide-embedded Si nanocrystals are made by thermal decomposition of hydrogen silsesquioxane (HSQ) under forming gas (93% nitrogen gas and 7% hydrogen gas) at 1100°C and then liberated by HF-etching to obtain freely dispersible hydride-terminated Si nanocrystals. If the hydride-terminated Si nanocrystals are mixed with styrene and heated to 140°C under nitrogen, a yellow gel of polystyrene-embedded Si nanocrystals is obtained, similar to what has recently been reported by Veinot and coworkers.[26] For controlled styrene passivation of the nanocrystals without significant styrene polymerization, hydrosilylation was carried out at room temperature under nitrogen with H-terminated Si nanocrystals dispersed in toluene with added styrene, undecanoic acid, and ethanol. The hydrosilylation reaction is complete after 5 days. The majority of

styrene-terminated Si nanocrystals dispersed in the raw reaction solution, while the precipitate in the vial contained the rest of styrene-terminated Si nanocrystals and unpassivated particles. (Figure 3.2a, inset).

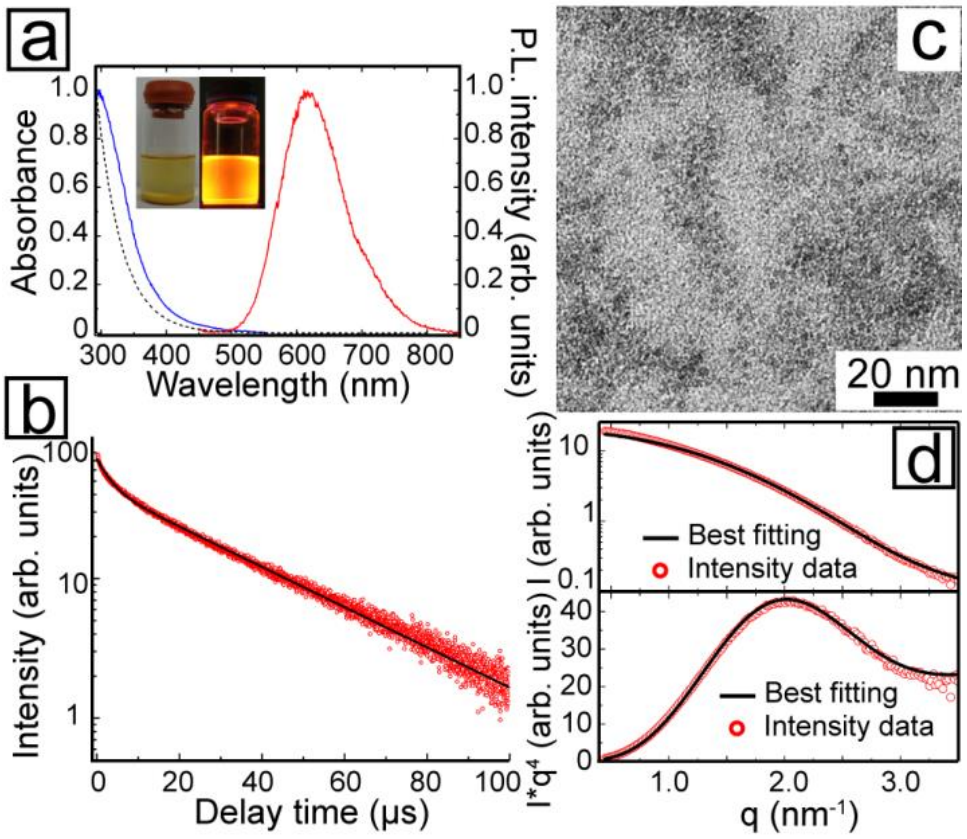

Figure 3.2: (a) Illustration of the room temperature hydrosilylation of Si nanocrystals with styrene. (b) PL (red solid curve, λ_{ex}=290 nm), PLE (blue solid curve, λ_{em}=620 nm), and absorbance (black dash curve) spectra of styrene-terminated Si nanocrystals dispersed in toluene. The inset in (B) shows a photograph of styrene-passivated Si nanocrystals dispersed in original mixed solution under (left) ambient light and (right) 365 nm UV light. (c) Time-correlated single photon counting PL decay spectrum of free-standing styrene-terminated Si nanorystals with λ_{det}=615 nm and λ_{ex}=290 nm (red circles) and biexponential decay fitting (black line), indicating average lifetime of 20.2 μs. (c) TEM image of free-standing styrene-terminated Si nanorystals; (d) solution SAXS of free-standing styrene-terminated Si nanorystals dispersed in toluene (red circles) and the best fit (black line), top: intensity logarithmic plot, bottom: porod plot.

The styrene-passivated Si nanocrystals disperse in toluene and bright exhibit orange PL. Figure 3.2a shows the PL spectra of styrene-terminated Si nanocrystals with quantum yield of 12%. Figure 3.2b shows time-correlated single photon counting (TCSPC) PL decay of Si nanocrystals with detection wavelength of 615 nm, excitation wavelength of 371 nm. The PL decay was fit to a biexponential decay:

$$I_{emission} = I_0(A_1 e^{-t/\tau_1} + A_2 e^{-t/\tau_2}) \quad (5)$$

to yield parameters, A_1=0.37, τ_1=3.3μs, A_2=0.63, and τ_2=30.1μs. The average lifetime (τ=$A_1\tau_1 + A_2\tau_2$) is 20.2 μs, which aligns with literature values for alkene-passivated Si nanocrystals.[29]

Figure 3.2c shows a transmission electron microscopy (TEM) image of styrene-terminated Si nanocrystals. The nanocrystal diameter in the sample ranges between 2-3 nm, which matches the average diameter of 2.2±0.66 nm determined by small angle X-ray scattering (SAXS, Fig. 3.2d). Figure 1d shows solution SAXS data of free-standing styrene-terminated Si nanocrystals dispersed in toluene, which was fitted by assuming non-interacting solid spheres with Gaussian size distribution.

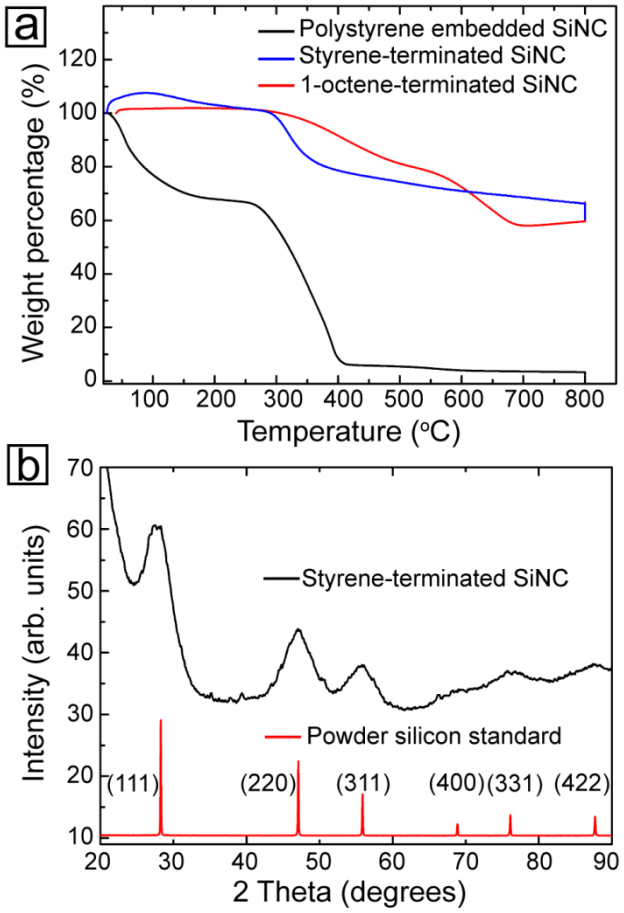

Figure 3.3: (a) TGA carried out in air for Si nanocrystals after high temperature (140°C) passivation with styrene (i.e., "polystyrene-embedded"), room temperature undecanoic acid-aided styrene passivation (blue curve), and 1-octene-terminated (red curve). The mass percentage of Si in the nanocrystals samples are 1.1%, 30%, and 31%, respectively. (b) XRD of styrene-terminated Si nanocrystals (black) compared to the standard diffraction pattern (red) for diamond cubic Si (PDF # 027–1402, a=b=c=5.43088 Å).

The relative amount of Si in the various nanocrystal samples after passivation was determined using thermal gravity analysis (TGA). (Figure 3.3a) During TGA, organic capping ligands are removed, leaving inorganic Si core oxidized to SiO_2. The mass percentage of Si could be calculated from the mass percentage of SiO_2. The polystyrene-embedded nanocrystals had 1.1 wt% Si, compared to the hydrosilylated styrene and

octane-capped nanocrystals, which were composed of 30 wt% Si and 31 wt%, respectively. The styrene surface coverage can be estimated from the TGA measurements. Taking a Si core diameter of 2.2 nm, approximately 6800 styrene molecules are contained in the sample embedded in polystyrene compared to 173 styrene molecules per nanocrystal in styrene-passivated sample. Based on the weight fraction of Si in the nanocrystals passivated with 1-octene (C_8H_{16}), there are 156 octene molecules per nanocrystal, close to the value of free-standing styrene sample. X-ray diffraction (XRD) of the styrene-capped Si nanocrystals also matches diamond cubic Si. (Figure 3.3b)

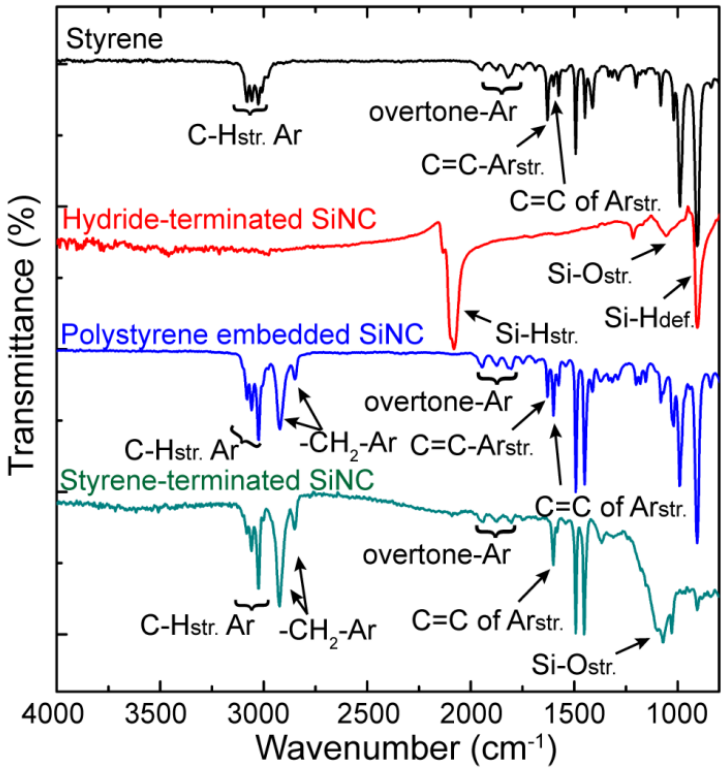

Figure 3.4: ATR-FTIR spectra of styrene (black curve), hydride-terminated Si nanocrystals (red curve), polystyrene-embedded Si nanocrystals (blue curve), and free-standing styrene-terminated Si nanocrystals (green curve).

Figure 3.4 shows attenuated total reflectance Fourier transform infrared (ATR-FTIR) spectra for styrene, hydride-terminated Si nanocrystals, polystyrene-embedded Si nanocrystals, and styrene-terminated Si nanocrystals. The styrene spectra show aromatic C-H stretching at 3010-3080 cm^{-1}, C-H out of plane bending overtone peaks of styrene at 1750-2000 cm^{-1}, aromatic C=C stretching at 1590 cm^{-1}, and stretching vibration of terminal C=C at 1628 cm^{-1};. The H-terminated Si nanocrystals show Si-H stretching at ~2100 cm^{-1}, Si-O stretching at ~1100 cm^{-1}, and Si-H deformation at 900 cm^{-1}, confirming the Si-H surface on Si nanocrystal.[31] Polystyrene-embedded Si nanocrystal only show signals corresponding to polystyrene (i.e. C-H stretching in aromatic ring and $-CH_2-$, aromatic C=C stretching, and aromatic overtone), and styrene monomer (stretching vibration of terminal C=C at 1628 cm^{-1}) because Si makes up such a small fraction of the total sample (0.5 vol% calculated from the mass percentage by TGA). On the other hand, the styrene-capped nanocrystals clearly show Si-O stretching due to the oxidation of surface Si that cannot bind to styrene because of steric repulsion of capping ligands. The stretching signal of terminal C=C disappeared, indicating there was no free styrene in the sample.

The Si nanocrystals could not be passivated with styrene at room temperature without the addition of undecanoic acid. Undecanoic acid itself also does not passivate the Si nanocrystals at room temperature. The room temperature styrene hydrosilylation appears to proceed by a similar reaction mechanism as recently discovered for bifunctional alkenes in which carboxylic acid group can promote the reaction between surface Si-H and terminal vinyl group of alkenes.[27] In this case, undecanoic acid appears

to activate the H-terminated Si surface to styrene addition to the Si surface, as illustrated in Figure 3.5a. Undecanoic acid has a resonance form where the oxygen atom next to the carbonyl group donates electron density to the carbonyl oxygen which can then coordinate to the oxophilic Si surface. The coordination increase the hydridic character of Si-H, enhance the nucleophilicity of Si-H enough to facilitate H^- attack at the electropositive carbon of terminal C=C of styrene.

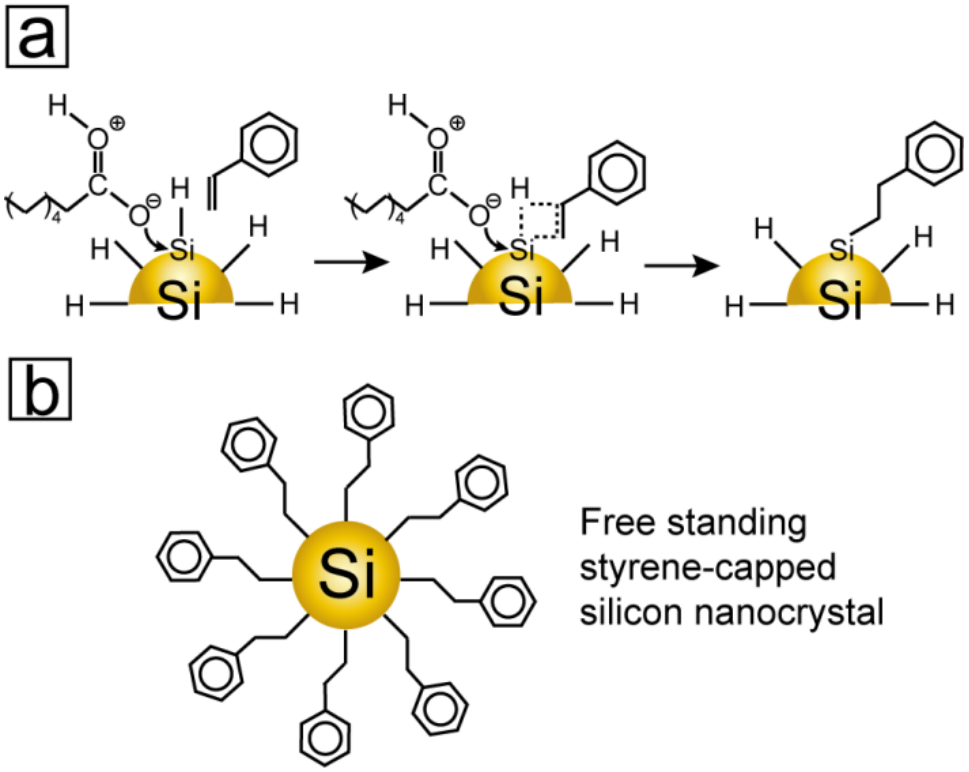

Figure 3.5: (a) Mechanistic illustration for the room temperature attachment of styrene to hydride-terminated Si nanocrystal, in which undecanoic acid is shown with its resonance form to emphasize the regions of electrostatic interaction[27]; (b) Schematic of free-standing styrene-terminated Si nanocrystal.

Room temperature hydrosilylation of hydride-terminated Si nanocrystal with styrene differs from thermal hyrosilylation in two ways: 1) in room temperature

hydrosilylation, coordination of carbonyl oxygen to surface silicon and H^- attacking at terminal C=C must occur repeatedly to complete surface passivation, temperature is also much lower than that of thermal hydrosilylation, leading to a slow reaction rate; thermal hydrosilylation is a radical reaction which quickly propagates across the Si surface once a radical is initiated on nanocrystal; 2) room temperature greatly reduces the radical concentration, and can yield styrene-terminated Si nanocrystals (Figure 3.5b); thermal hydrosilylation involves radicals, leading to polystyrene-embedded Si nanocrystals. Room temperature addition of styrene to silicon nanocrystal does have it limitation: this method is efficient for 2-3 nm silicon nanocrystal but works poorly for larger nanocrystals. It is because this chemistry requires surface Si-H bond, undecanoic acid, and styrene to cooperate simultaneously, which asks for a large space, in this case, a high surface curvature on nanocrystals. Room temperature hydrosilylation of bifunctional alkenes like ethyl 10-undecenoate shows highest passivation efficiency for smallest Si nanocrystals (2-3 nm diameter), but is still efficient for 4-10 nm nanocrystals.[27] In the case of styrene which has a bulky nature, the passivation is only efficient for 2-3 nm nanocrystals.

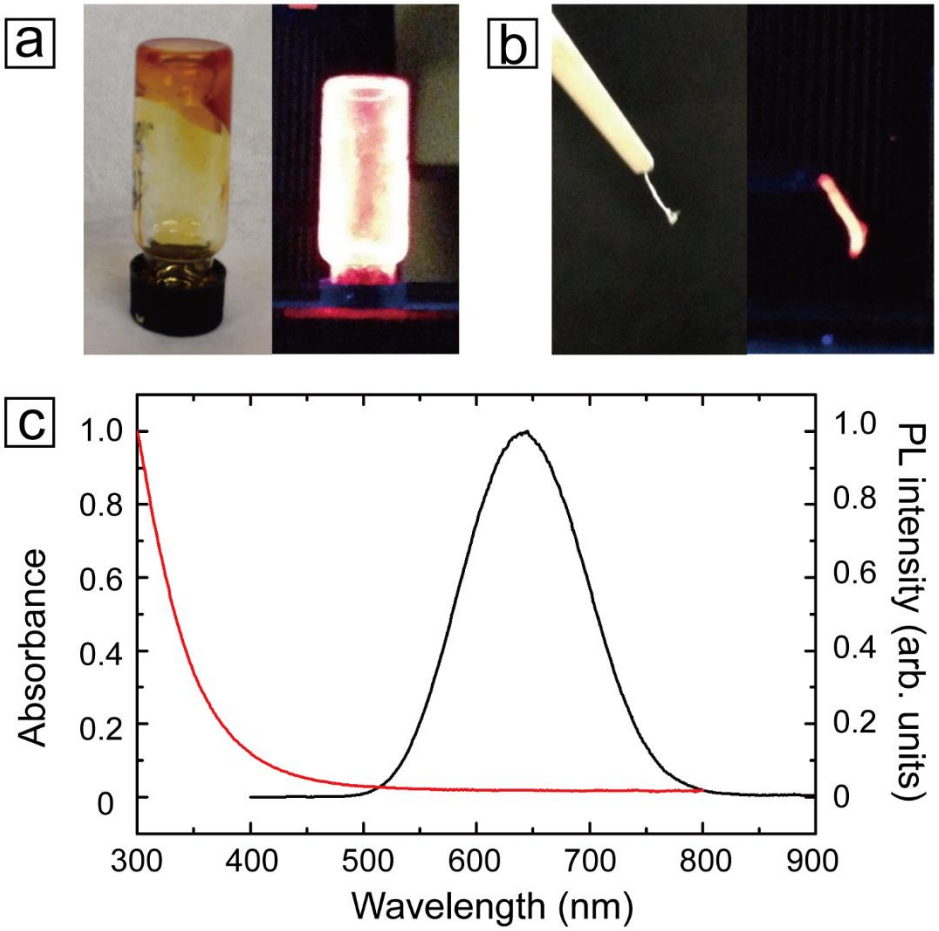

Figure 3.6: Optical property of polystyrene-embedded Si nanocrystal sample. (a) Polystyrene-embedded Si nanocrystals form a gel under ambient light (left), and 365 nm UV light (right). (b) Pictures of polystyrene-embedded Si nanocrystal got quickly dried and turn into fibers under ambient light (left), and 365 nm UV light (right). (c) Absorbance (red curve) and PL (black curve) of polystyrene-embedded Si nanocrystal.

Photoluminescent styrene-terminated Si nanocrystals were synthesized by acid-catalyzed room temperature hydrosilylation. The nanocrystals exhibit diamond cubic Si crystal structure. Controlled surface passivation of Si nanocrystals with styrene at elevated temperature is not possible because of rapid self-intiated thermal polymerization of styrene. To speed the hydrosilylation reaction relative to solution polymerization of

styrene, undecanoic acid is added as a promoter that induces hydrosilylation of the Si surface with styrene at room temperature. Under these conditions, the mass percentage of inorganic Si core in free-standing styrene-terminated Si nanocrystal is much higher than that in polystyrene-embedded Si nanocrystal. The ligand packing density of the Si nanocrystals passivated with styrene at room temperature is similar to the nanocrystals passivated with 1-octene at elevated temperature.

3.4 CONCLUSIONS

Photoluminescent styrene-terminated Si nanocrystals were synthesized by acid-catalyzed room temperature hydrosilylation. The nanocrystals exhibit diamond cubic Si crystal structure. Controlled surface passivation of Si nanocrystals with styrene at elevated temperature is not possible because of rapid self-intiated thermal polymerization of styrene. To speed the hydrosilylation reaction relative to solution polymerization of styrene, undecanoic acid is added as a promoter that induces hydrosilylation of the Si surface with styrene at room temperature. Under these conditions, the mass percentage of inorganic Si core in free-standing styrene-terminated Si nanocrystal is much higher than that in polystyrene-embedded Si nanocrystal. The ligand packing density of the Si nanocrystals passivated with styrene at room temperature is similar to the nanocrystals passivated with 1-octene at elevated temperature.

3.5 REFERENCES

(1) Hessel, C. M.; Reid, D.; Panthani, M. G.; Rasch, M. R.; Goodfellow, B. W.; Wei, J.; Fujii, H.; Akhavan, V.; Korgel, B. A. Synthesis of Ligand-Stabilized Silicon Nanocrystals with Size-Dependent Photoluminescence Spanning Visible to Near-Infrared Wavelengths. *Chem. Mater.* **2012**, *24*, 393-401.

(2) Hua, F.; Mark T. Swihart, M. T.; Ruckenstein, E. Efficient Surface Grafting of Luminescent Silicon Quantum Dots by Photoinitiated Hydrosilylation. *Langumir* **2005**, *21*, 6054-6062.
(3) Mangolini, L.; Kortshagen, U. Plasma-Assisted Synthesis of Silicon Nanocrystal Inks. *Adv. Mater.* **2007**, *19*, 2513-2519.
(4) English, D. S.; Pell, L. E.; Yu, Z.; Barbara, P. F.; Korgel, B. A. Size Tunable Visible Luminescence from Individual Organic Monolayer Stabilized Silicon Nanocrystal Quantum Dots. *Nano Lett.* **2002**, *2*, 681-685.
(5) Cheng, K.-Y.; Anthony, R.; Kortshagen, U. R.; Holmes, R. J. Hybride Silicon Nanocrystal-Organic Light-Emitting Devices for Infrared Electroluminescence. *Nano Lett.* **2010**, *10*, 1154-1157.
(6) Cheng, K.-Y.; Anthony, R.; Kortshagen, U. R.; Holmes, R. J. High-Efficiency Silicon Nanocrystal Light-Emitting Devices. *Nano Lett.* **2011**, *11*, 1952-1956.
(7) Puzzo, D. P.; Henderson, E. J.; Helander, M. G.; Wang, Z.; Ozin, G. A.; Lu, Z. Visiblle Colloidal Nanocrystal Silicon Light-Emitting Diode. *Nano Lett.* **2011**, *11*, 1585-1590.
(8) Maier-Flaig, F.; Rinck, J.; Stephan, M.; Bocksrocker, T.; Bruns, M.; Kübel, C.; Powell, A. K.; Ozin, G. A.; Lemmer, U. Multicolor Silicon Light-Emitting Diodes (SiLEDs). *Nano Lett.* **2013**, *13*, 475-480.
(9) Hessel, C. M.; Rasch, M. R.; Hueso, J. L.; Goodfellow, B. W.; Akhavan, V. A.; Puvanakrishnan, P.; Tunnel, J. W.; Korgel, B. A. Alkyl Passivation and Amphiphilic Polymer Coating of Silicon Nanocrystals for Diagnostic Imaging. *Small* **2010**, *6*, 2026-2034.
(10) Li, Z. F.; Ruckenstein, E. Water-Soluble Poly(acrylic acid) Grafted Luminescent Silicon Nanoparticles and Their Use as Fluorescent Biological Staining Labels. *Nano Lett.* **2004**, *4*, 1463-1467.
(11) Sieval, A. B.; Demirel, A. L.; Nissink, J. W. M.; Linford, M. R.; Van der Maas, J. H.; de Jeu, W. H.; Zuilhof, H.; Sudholter, E. J. R. Highly Stable Si-C Linked Functionalized Monolayers on the Silicon (100) Surface. *Langmuir* **1998**, *14*, 1759-1768.
(12) Linford, M. R.; Chidsey, C. E. D. Alkyl Monolayers Covalently Bonded to Silicon Surfaces. *J. Am. Chem. Soc.* **1993**, *115*, 12631-12632.
(13) Boukherroub, R.; Wayner, D. D. M. Controlled Functionalization and Multistep Chemical Manipulation of Covalently Modified Si(111) Surfaces. *J. Am. Chem. Soc.* **1999**, *121*, 11513-11515.
(14) Jiang, C.-W.; Green, M. A. Silicon Quantum Dots Superlattices: Modeling of Energy Bands, Densities of States, and Mobilities for Silicon Tandem Solar Cell Applications. *J. Appl. Phys.* **2006**, *99*, 114902.
(15) Beard, M. C.; Knutsen, K. P.; Yu, P.; Luther, J. M.; Song, Q.; Metzger, W. K.; Ellingson, R. J. Nozik, A. J. Multiple Exciton Generation in Colloidal Silicon Nanocrystals. *Nano Lett.* **2007**, *7*, 2506-2512.
(16) Porter, M. D.; Bright, T. B.; Allara, D. L.; Chidsey, C. E. D. Spontaneously Organized Molecular Assemblies. 4. Structural Characterization of n-Alkyl Thiol

Monolayers on Gold by Optical Ellipsometry, Infrared Spectrosopy, and Electrochemistry. *J. Am. Chem. Soc.* **1987**, *109*, 3559-3568
(17) Finklea, H. O.; Avery, S.; Lynch, M. Blocking Oriented Monolayer of Alkyl Mercaptans on Gold Electrodes. *Langmuir* **1987**, *3*, 409-413.
(18) Mastronardi, M. L.; Henderson, E. J.; Puzzo, D. P.; Chang, Y.; Wang, Z. B.; Helander, M. G.; Jeong, J.; Kherani, N. P.; Lu, Z.; Ozin, G. A. Silicon Nanocrystal OLEDs: Effect of Organic Capping Group on Performance. *Small* **2012**, *8*, 3647-3654.
(19) Feng, W.; Miller, B. Self-Assembly and Characterization of Fullerence Monolayers on Si(100) Surfaces. *Langmuir* **1999**, *15*, 3152-3156.
(20) Schwartz, M. P.; Ellison, M. D.; Coulter, S. K.; Hovis, J. S.; Hamers, R. J. Interaction of π-Conjugated Organic Molecules with π-Bonded semiconductor Surfaces: Structure, Selectivity, and Mechanistic Implications. *J. Am. Chem. Soc.* **2000**, *122*, 8529-8538.
(21) Kirczenow, G. Linear Chains of Styrene and Methylstyrene Molecules and their Heterojunctions on Silicon: Theory and Experiment. *Phys. Rev. B* **2005**, *72*, 245306.
(22) Kim, D. H.; Hwang, Y. J.; Ryou, J.; Kim, S.; Hong, S. Atomic and Electronic Structure of Styrene on Ge(100). *Surf. Sci.* **2011**, *605*, 1438-1444.
(23) Buriak, J. M. Organometallic Chemistry on Silicon and Germanium Surfaces. *Chem. Rev.* **2002**, *102*, 1271-1308.
(24) Bateman, J. E.; Eagling, R. D.; Worrall, D. R.; Horrocks, B. R.; Houlton, A. Alkylation of Porous Silicon by Direct Reaction with Alkenes and Alkynes. *Angew. Chem. Int. Ed.* **1998**, *37*, 2683-2685.
(25) Khuong, K. S.; Jones, W. H.; Pryor, W. A.; Houk, K. N. The Mechanism of the Self-Initiated Thermal Polymerization of Styrene. Theoretical Solution of a Classic Problem. J. *Am. Chem. Soc.* **2005**, *127*, 1265-1277.
(26) Yang, Z.; Dasog, M.; Dobbie, A. R.; Lockwood, R.; Zhi, Y.; Meldrum, A.; Veinot, J. G. C. Highly Luminescent Covalently Linked Silicon Nanocrystal/Polystyrene Hybrid Functional Materials: Synthesis, Properties, and Processability. *Adv. Funct. Mater.* **2013,** DOI: 10.1002/adfm.201302091.
(27) Yu, Y.; Hessel, C. M.; Bogart, T. D.; Panthani, M. G.; Rasch, M. R.; Korgel, B. A. Room Temperature Hydrosilylation of Silicon Nanocrystals with Bifunctional Terminal Alkenes. *Langmuir* **2013**, *29*, 1533-1540.
(28) Hessel, Colin M.; Henderson Eric J.; Veinot, Jonathan G.C. Hydrogen Silsesquioxane: A Molecular Precursor for Nanocrystalline Si-SiO_2 Composites and Freestanding Hydride-Surface-Terminated Silicon Nanoparticles. Chem. Mater. **2006**, *18*, 6139-6146.
(29) Mastronardi, M. L.; Maier-Flaig, F.; Faulkner, D.; Henderson, E. J.; Kübel, C.; Lemmer, U.; Ozin, G. A. Size-Dependent Absolute Quantum Yield for Size-Separated Colloidally-Stable Silicon Nanocrystals. *Nano Lett.* **2012**, *12*, 337-342.
(30) Locritani, M.; Yu, Y.; Bergamini, G.; Baroncini, M.; Molloy, J. K.; Korgel, B. A.; Ceroni, P. Silicon Nanocrystals Functionalized with Pyrene Units: Efficient-

Harvesting Antennae with Bright Near-Infrared Emission. *J. Phys. Chem. Lett.* **2014**, *5*, 3325-3329.
(31) Lucovsky, G.; Nemanich, R. J.; Knights, J. C. Structural interpretation of the vibrational spectra of a-Si:H alloys. *Phys. Rev. B* **1979**, *19*, 2064-2073.

Chapter 4: 10-Undecenoic Acid Passivated Silicon Nanocrystals with High Aqueous Dispersibility and Emission Stability

4.1 INTRODUCTION

Silicon nanocrystals exhibit bright, size-tunable photoluminescence (PL),[1-6] and can be used as biomedical or diagnostic imaging contrast agents[7-9] or as photosensitizers for photodynamic therapy (PDT)[10-12]. The surface passivation layer plays a critical role in eliminating surface defects, protecting the silicon core from oxidization, and providing dispersibility in solvents. Silicon nanocrystals are typically passivated with terminal alkenes such as 1-dodecene through hydrosilylation that is promoted by heating or UV irradiation[13,14]. These nanocrystals can disperse in nonpolar organic solvents, including toluene, chloroform, and hexanes. Synthesis of silicon nanocrystals with high aqueous dispersibility and PL stability remains a challenge in using them for *in-vitro* or *in-vivo* biological applications.[9]

Silicon nanocrystals with hydrophobic surface can be dispersed in water by loading into lipid micelles[9] or coating them with amphiphilic polymers[8], however these methods significantly increase the particle size (50-120 nm). Considering that the optimal hydrodynamic diameter for nanoparticles to cross cellular membrane via receptor-mediated endocytosis is 25-30 nm,[15,16] it is desired that the starting passivated nanoparticle is small enough to give sufficient flexibility for protein adsorption[17] or bioconjugation[18,19] to bioactive molecules. Photodynamic therapy, in which silicon nanocrystals absorb light and transfer the energy to triplet O_2 to generate singlet O_2 which

can in turn damage targeted cells,[10] requires that silicon nanocrystals be in very close contact with target cells since the diffusion length for singlet O_2 in biological media is less than 70 nm.[20,21] Silicon nanocrystals encapsulated in micelles are expected to have a poor performance in PDT because the micelles would act as a diffusion barrier for singlet O_2.

An alternative approach is to directly passivate silicon nanocrystal surfaces with capping ligands terminated with carboxylic acids or amines. For example, Li and Ruckenstein[22] have grafted silicon nanocrystal surface with poly(acrylic acid) for biological staining, Sato and Swihart[23] have passivated silicon nanocrystal with propionic acid, and Clark and Veinot et al[24] have attached carboxylic acid with various chain lengths to the surface of silicon nanocrystals and used dialysis to disperse them in water. The previous examples of carboxylic acid passivation were typically promoted with UV irradiation, which yields poor aqueous dispersibility, i.e. low concentration for water dispersion,[24] and poor spectral stability.[22] Such poor aqueous dispersibility and spectral stability may possibly be attributed to the low ligand packing density on nanocrystal surface.

It is of great interest to study the surface oxidation and subsequent corrosion of silicon nanocrystals dispersed in water, which affects their colloidal and spectral stability. To date, very little work has been reported on this, mainly due to the difficulty in producing large quantity, highly stable water-dispersible silicon nanocrystals. Our group has recently reported that room temperature hydrosilylation can passivate hydride-terminated surface of silicon nanocrystal with bifunctional alkenes such as carboxylic

acids and esters at room temperature without photon irradiation, leading to a capping ligand packing density close to that of thermal hydrosilylation with terminal alkenes.[25] Here, we show that silicon nanocrystals with diameters ranging from 2.7 to over 10 nm passivated through room temperature hydrosilylation can be easily dispersed in water through a simple centrifugal filtration process. These silicon nanocrystals can form colloidal dispersions in water with very high concentrations up to10 mg/mL, and this fabrication process can be easily scaled up to produce high quality water-dispersible silicon nanocrystals at the gram scale. The nanocrystals exhibit a less than 10% PL intensity decrease over a month, suggesting high emission stability.

4.2 EXPERIMENTAL DETAILS

4.2.1 Materials

Flowable oxide (FOx®-16) was purchased from Dow Corning, 10-undecenoic acid (98%), ethyl 10-undecenoate (>97%), and sodium hydroxide (>98%) were purchased from Sigma-Aldrich. Ethanol, hexanes, hydrochloric acid (HCl, 37.5%), and amicon Ultra-15 centrifugal filters were purchased from Fisher Scientific. Hydrofluoric acid (HF, 48%) was obtained from EMD chemicals. Deionized (DI) water was obtained using a Barnstead Nanopure Filtration System (18.2 MΩ resistance).

4.2.2 Synthesis of Hydride-Terminated Si Nanocrystals

Silicon nanocrystals were synthesized through thermal decomposition of hydrogen silsesquioxane (HSQ) followed by hydrofluoric acid etching.[26] In a typical

synthesis, 20 mL of FOx®-16 was stirred under vacuum to form dry HSQ, which was transferred onto a quartz boat, loaded into a tube furnace, and heated to either 1100^{o}C, 1250^{o}C, or 1300^{o}C (to produce nanocrystals of 2.7nm, 7.4nm, or 10.6nm in diameter, respectively) at a heating rate of 18^{o}C/min under forming gas (93% N_2 and 7% H_2) flow. 1 hour of annealing turned HSQ into silicon dioxide (SiO_2)-embedded silicon nanocrystals, which was ground with an agate mortar and pestle for 30 min and shaken with 3 mm borosilicate glass beads in a wrist-action shaker (Burrell Corp., model: BB) for 9 hours to form a fine brown powder. 300 mg of powder was etched with 1 mL of 37.5% hydrochloric acid and 10 mL of 48% hydrofluoric acid (HF) in the dark for 3 hours to generate hydride-terminated silicon nanocrystals.

4.2.3 Passivation of Silicon Nanocrystals Through modified room temperature hydrosilylation

Silicon nanocrystals were passivated with either 10-undecenoic acid or ethyl 10-undecenoate through a modified room temperature hydrosilylation without heating or UV irradiation, which was described in detail in our previous publication.[25] In a typical functionalization, hydride-terminated silicon nanocrystals were isolated after HF etching by centrifuging at 8000 rpm for 5 min, then rinsed twice with ethanol and once with chloroform, and redispersed in 8 mL of 10-undecenoic acid (for 2.7 nm silicon nanocrystal), or 8 mL of ethyl 10-undecenoate (for larger silicon nanocrystals). The dispersion was transferred to a 3-neck flask, degassed through 3 freeze-pump-thaw cycles, and stirred at room temperature (~30^{o}C) for 12 hours in N_2 gas flow. 8 mL of

ethanol (for 2.7 nm 10-undecenoic acid passivated silicon nanocrystal) or 4 mL of ethanol and 4 mL of toluene (for larger ethyl 10-undecenoate passivated silicon nanocrystals) was added in to the flask, and the dispersion was transferred to a 20 mL vial which was then sealed with a septum. The sealed vial was left on the bench top for 10 days, during which time the dispersion slowly turned from turbid to transparent. The hydrosilylation yields,[25] defined as the percentage of nanocrystals that are passivated and colloidally dispersed, are typically higher than 95% for this reaction.

4.2.4 Purification of Silicon Nanocrystals

The clear dispersion was transferred to a 30 mL glass centrifuge tube and centrifuged at 8000 rpm for 5 min to precipitate the unpassivated silicon nanocrystals. In the case of silicon nanocrystal passivated with 10-undecenoic acid, the supernatant, containing the passivated silicon nanocrystals, was mixed with 12 mL of hexanes and centrifuged at 8000 rpm for 5 min. The precipitate was dispersed in 5 mL of ethanol and cleaned three times through centrifugation / precipitation using hexanes as the anti-solvent. Ethyl 10-undecenoate passivated silicon nanocrystals were cleaned in a similar manner, using a 1/1 volume ratio of an ethanol and toluene mixture as the solvent and hexanes as the anti-solvent. The nanocrystal weight was determined on a scale after evaporating the solvent in a rotary evaporator, and the nanocrystals were finally dispersed in ethanol or ethanol/toluene at a concentration of 10 mg/mL.

4.2.5 Dispersing 10-Undecenoic Acid Capped Silicon Nanocrystals in Water

1 mL of 10-undecenoic acid capped silicon nanocrystal solution (at a concentration of 10 mg/mL) was diluted with 4 mL of ethanol, and diluted again with 5 mL of DI water with pH adjusted to 7.4 with sodium hydroxide. The diluted dispersion (1 mg/mL) was transferred to a 50 KDa cutoff centrifugal filter and centrifuged at 1100 G (centrifugal force, corresponding to 2925 rpm) for 7 min. Approximately 9 mL of ethanol water mixture went through the filter, while 1mL of the nanocrystal dispersion concentrated at 10 mg/mL remained above the filter. 9 mL of DI water (pH 7.4) was added to dilute the dispersion back to a total volume of 10ml, and the solution was then centrifuged again at 1100 G for 7 min. The centrifugal filtration process was repeated 5 times to completely remove ethanol from the dispersion, and the silicon nanocrystals were eventually dispersed in DI water (pH 7.4) at a concentration of 10 mg/mL until further use.

4.2.6 Hydrolysis of Ethyl 10-Undecenoate Capped Silicon Nanocrystals

The ester groups on ethyl 10-undecenoate capped silicon nanocrystals can be hydrolyzed to carboxylic acid groups using sodium hydroxide (NaOH) solution. In a typical hydrolysis, 1 mL of ethyl 10-undecenoate capped silicon nanocrystal solution (at a concentration of 10 mg/mL) was mixed with 2 mL of DI water with pH adjusted to 8.5 for 7.4 nm nanocrystals, or 9.5 for 10.6 nm nanocrystals, forming a turbid and phase separated solution. Ethanol was added drop-wise to the mixture while stirring until it became transparent and homogenous, and then stirred for another 10 min. The transparent

mixture was transferred to a 100 KDa cutoff centrifugal filter and centrifuged at 1100 G for 5 min to remove excess solvent. Ethanol was added to the concentrated nanocrystal dispersion, which was then centrifuged again at 1100 G for 5 min. The centrifugal filtration process was repeated 5 times to completely remove toluene and water and yield silicon nanocrystal dispersed in ethanol, which can then be transferred to water following the procedure described in the previous paragraph.

4.2.7 Materials Characterization

UV-Vis absorption spectroscopy was performed on a Varian Cary 50 Bio ultraviolet-visible (UV-vis) spectrophotometer using a 10 mm path length quartz cuvette. PL spectra were acquired on a Varian Cary Eclipse fluorescence spectrophotometer. PL quantum yields were estimated relative to Rhodamine B in ethanol.[27] Time-resolved PL derived from Time-Correlated Single Photon Counting (TCSPC) measurement was performed on a Fluorolog-3 spectrophotometer (Horiba Jobin Yvon) with InGaAs photomultiplier tube for visible detection and 371 nm NanoLED laser (1 ns plus duration) for excitation.

Attenuated total reflectance Fourier transform infrared (ATR-FTIR) spectroscopy was performed on a Thermo Mattson Infinity Gold FTIR spectrometer equipped with a Spectra-Tech Thermal ARK attenuated total reflectance module. The sample chamber was purged with N_2 gas for 30 min to remove the CO_2 signal from the spectra. Nanocrystals were drop cast onto the ATR module crystal plate and measurements were acquired over 512 scans at a resolution of 4 cm^{-1}. The ATR module background was

acquired under the same conditions without sample. The average transmittance is reported with background subtraction.

Transmission electron microscopy (TEM) images were acquired using a FEI Tecnai Biotwin TEM operated at 80 kV accelerating voltage. Nanocrystals were drop cast onto 200 mesh carbon-coated copper grids (Electron Microscopy Science) for imaging.

X-ray diffraction (XRD) was performed on a Rigaku R-Axis Spider Diffractometer with an image plate detector and a graphite monochromator using Cu Kα radiation (λ=0.15418 nm). Nanocrystals were drop cast onto a glass slide, collected with a needle, and placed onto a nylon loop. Mineral oil was applied to secure the sample as necessary. Two-dimensional diffraction data were collected for 60 min while rotating the sample stage at 10^{o} per minute, and radially integrated with 2DP Spider software (version 1.0, Rigaku Americas Corp.)

X-ray photoelectron spectroscopy (XPS) was performed using a Kratos Axis Ultra X-ray photoelectron spectrometer, utilizing a monochromatic Al Kα X-ray source (hν=1486.5 eV at 150 W (10 mA and 15 kV), hybrid optics (employing a magnetic and electrostatic lens simultaneously), and a multi-channel plate coupled to a hemispherical photoelectron kinetic analyzer. The instrument work function was calibrated to give a binding energy (BE) of 368.3 eV for the Ag $3d_{5/2}$ line for metallic silver. Spectra were charge-corrected by shifting the BE of the carbon 1s (graphite-like carbon) to 284.5 eV. Samples were prepared by drop casting nanocrystals onto indium tin oxide coated glass slides, which were secured to the experimental tray using double-sided Cu tape. High-

resolution spectra were collected with 20 eV pass energy at 0.1 eV intervals and 1500 ms integration time. Casa XPS analysis software (Version 2.3.16 PR 1.6) was used for peak deconvolution.

Thermal Gravimetric analysis (TGA) was performed using a Mettler Toledo TGA-1. In a typical measurement, 2 mg of nanocrystals was drop cast into a 70 μL alumina crucible (Mettler Toledo). The sample was then heated from 25oC to 800oC in 50 mL/min air flow at a heating rate of 10oC/min, and held at 800oC in 50 mL/min air flow for 90 minutes to completely remove organic components and oxidize silicon to silicon dioxide.

4.3 RESULTS AND DISCUSSION

4.3.1 Carboxylic Acid Passivation of Silicon Nanocrystals

Silicon nanocrystals with diameters from 2 to 3 nm can be efficiently passivated with 10-undecenoic acid through room temperature hydrosilylation, while larger nanocrystals must be passivated with ethyl 10-undecenoate and then hydrolyzed to yield carboxylic acid terminated surface (Figure 4.1). Carboxylic acid functionalized silicon nanocrystals are dispersed in ethanol and can be easily transferred to water through centrifugal filtration.

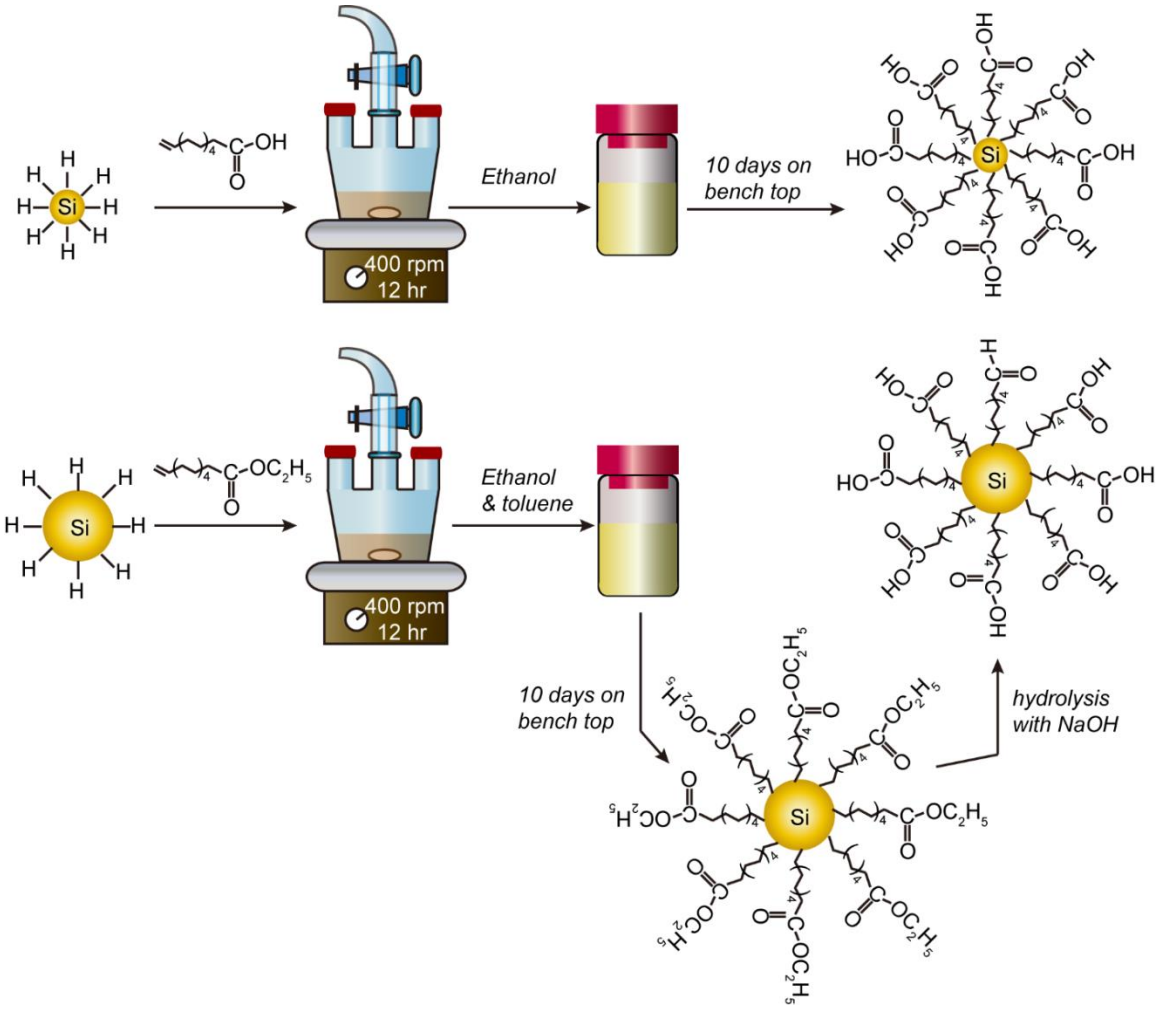

Figure 4.1: Schematic description for passivating silicon nanocrystals of various diameters with carboxylic acid.

4.3.2 Comparison Between Silicon Nanocrystals Dispersed in Water versus in Ethanol

2.7 nm silicon nanocrystals passivated with 10-undecenoic acid through room temperature hydrosilylation can disperse in water at a very high concentration. Figure 1a shows a solution of silicon nanocrystal in pH 7.4 water at a concentration of 10 mg/mL, which is 200 times higher than that of silicon nanocrystal passivated with the same ligand

through UV irradiation-initiated hydrosilylation.[24] The high water dispersibility of silicon nanocrystals is likely due to the high packing density of 10-undecenoic acid on nanocrystal surface. These silicon nanocrystals are brightly fluorescent. Figure 4.2b show UV-vis (dotted curves) and PL (solid curves) spectra of silicon nanocrystal dispersed in ethanol (blue curves) and water (black curves). The dispersion concentrations were adjusted for two samples to show the same absorbance at 322 nm, the excitation wavelength for PL spectra. Nanocrystals have an emission peak at ~700 nm in both ethanol and water dispersions, indicating that there is no immediate change in nanocrystal core size after transfer from ethanol to water. The emission intensity drops by ~30% after transfer to water, suggesting a lower PL quantum yield for nanocrystal dispersed in water than that in ethanol. The PL quantum yield can be estimated using rhodamine B dissolved in ethanol as a standard, following the equation:

$$QY_{SiNC} = \frac{I_{SiNC}/ABS_{SiNC}}{I_{rb}/ABS_{rb}} \times QY_{SiNC} \times \left(\frac{n_{solvent\ for\ SiNC}}{n_{solvent\ for\ rb}}\right)^2 \quad (1)$$

Where I is the integrated PL intensity, ABS is absorbance at the excitation wavelength, n is refractive index of the solvent, and SiNC and rb stand for silicon nanocrystals and rhodamine B, respectively. Silicon nanocrystal had a PL quantum yield of 11.8% in ethanol, and 7.9% in water. Figure 1c shows time-resolved PL spectra for silicon nanocrystals dispersed in ethanol and in water, with a 620nm detection wavelength and 371nm excitation wavelength. Both spectra can be fit to a triple exponential decay:

$$\mathrm{I} = A_1 \times e^{\frac{t}{\tau_1}} + A_2 \times e^{\frac{t}{\tau_2}} + A_3 \times e^{\frac{t}{\tau_3}} \quad (2)$$

with $A_1 + A_2 + A_3 = 1$. For silicon nanocrystal dispersed in ethanol, the fitting parameters are: A_1=0.3, A_2=0.3, A_3=0.4, τ_1=0.4 μs, τ_2=3 μs, τ_3=30 μs; while those for nanocrystal dispersed in water are A_1=0.6, A_2=0.2, A_3=0.2, τ_1=0.4 μs, τ_2=3 μs, τ_3=20 μs. The faster PL decay rate of silicon nanocrystals dispersed in water compared to those in ethanol suggests there is more PL quenching for nanocrystals in water, consistent with their lower quantum yield.

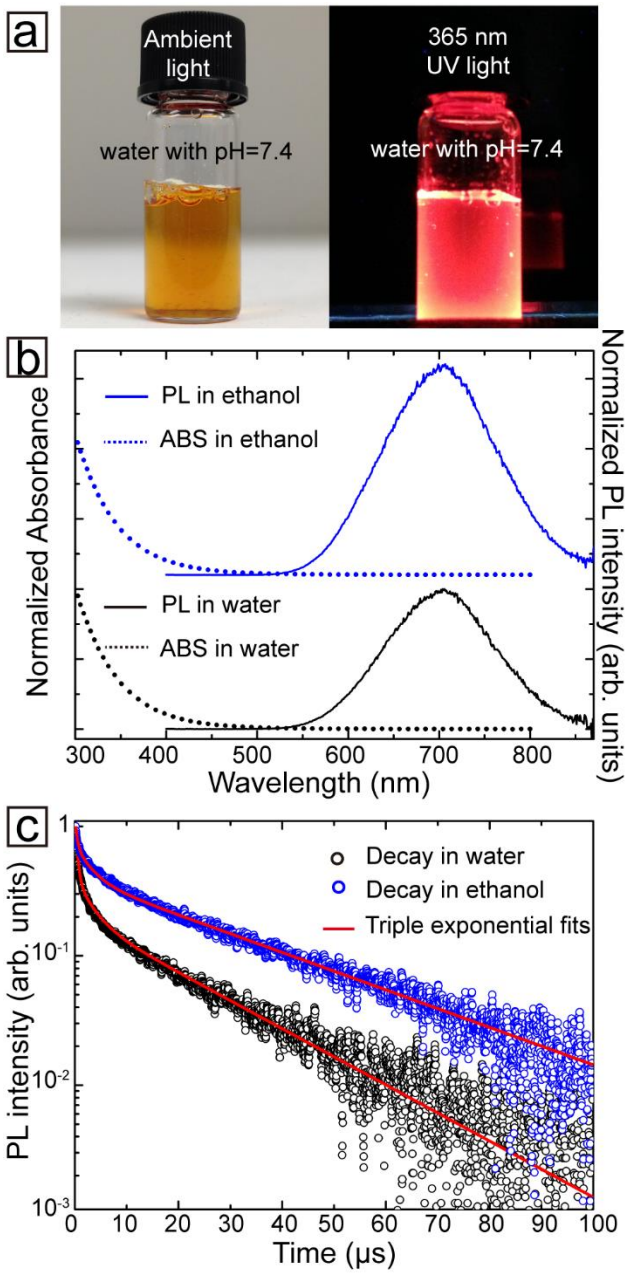

Figure 4.2: (a) Pictures of silicon nanocrystals dispersed in pH 7.4 water at a concentration of 10 mg/mL under ambient light (left) and 365 nm UV light (right). (b) Absorbance (dotted curves) and PL spectra (solid curves) for silicon nanocrystals dispersed in ethanol (blue curves) and water (black curves), excited at 322 nm. (c) Time-resolved PL spectra of silicon nanocrystals dispersed in ethanol (blue circles) and water (black circles) and excited at 371nm, fit to triple exponential decay functions (red curves).

The FTIR spectrum of silicon nanocrystal dispersed in ethanol shows absorption peaks at 2925, 2850, and 1720cm^{-1} for CH_2 asymmetric, symmetric, and C=O stretching, respectively.[25] Si-H stretching at ~2200 cm^{-1}, and Si-O stretching at ~1100 cm^{-1} are also present in the FTIR because 10-undecenoic acid cannot passivated all the surface silicon atoms due to steric repulsion. The FTIR spectrum for silicon nanocrystals dispersed in water shows the same peaks observed for nanocrystals dispersed in ethanol, with the addition of absorption peaks from COO^- asymmetric and symmetric stretching at 1600 and 1400 cm^{-1}, indicating a portion of carboxylic acid groups are deprotonated. [28]

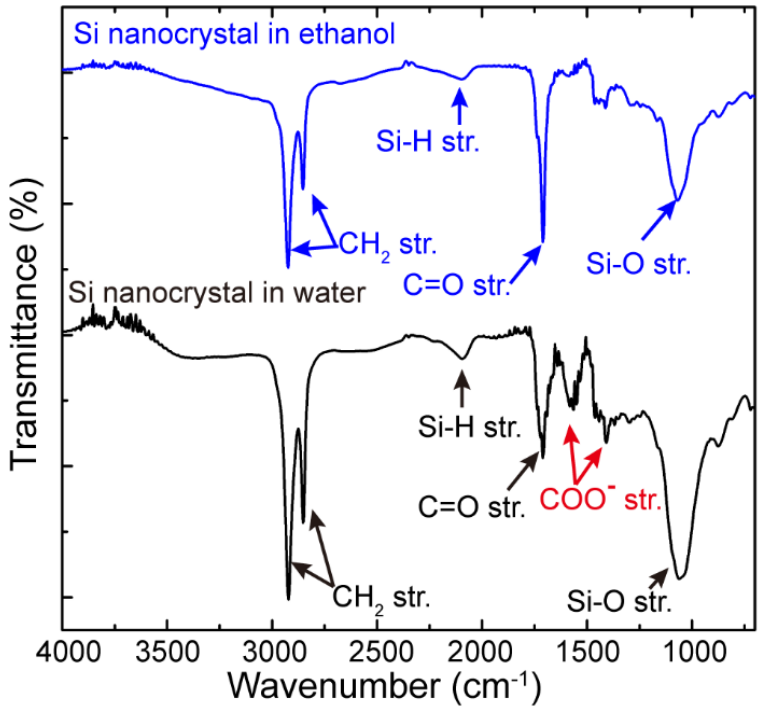

Figure 4.3: FTIR spectra of silicon nanocrystals dispersed in ethanol (black curve) and water (blue curve), showing carboxylic acid groups on water-dispersed nanocrystal surfaces are partially deprotonated.

XPS of silicon nanocrystals dispersed in ethanol (Figure 4.4a) and water (Figure 4.4b) clearly show Si^0 contributions at 99.8 (Si^0 $2p_{1/2}$) and 99.3 eV (Si^0 $2P_{3/2}$), as well as

Si-C bonding at 101.9 eV. Oxidized states, such as Si^{4+} (103.7 eV), Si^{3+} (102.6 eV), Si^{2+} (101.5 eV), and Si^{1+} (100.4 eV) are also present in the spectra, confirming the surface oxidization on silicon nanocrystals.[25] Silicon nanocrystals dispersed in ethanol and in water exhibit similar relative intensities of Si^{0}, Si-C, and Si^{n+}, indicating no immediate change to the silicon surface after dispersion in water.

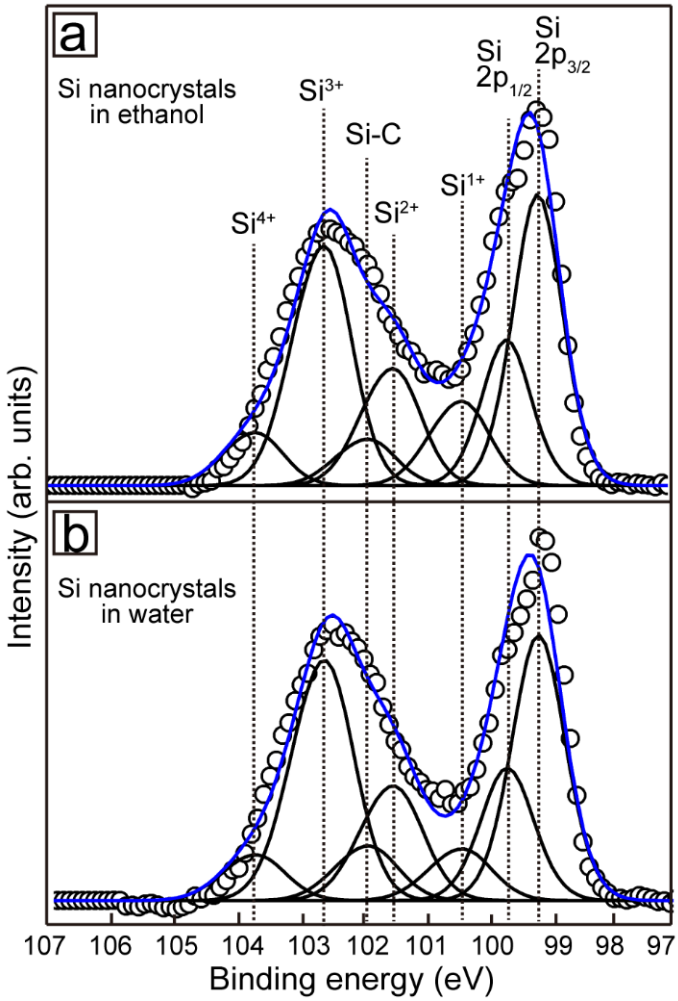

Figure 4.4: Silicon 2p XPS of silicon nanocrystals dispersed in (a) ethanol and (b) water. The black circles represent the measured intensity, black curves are the contributions from different silicon states (labeled with dotted lines), and blue curve is a summary of all the contributions.

TEM images show silicon nanocrystals with an average diameter of 2.7 nm, and the nanocrystal size does not change during transfer from ethanol to water. (Figure 4.5)

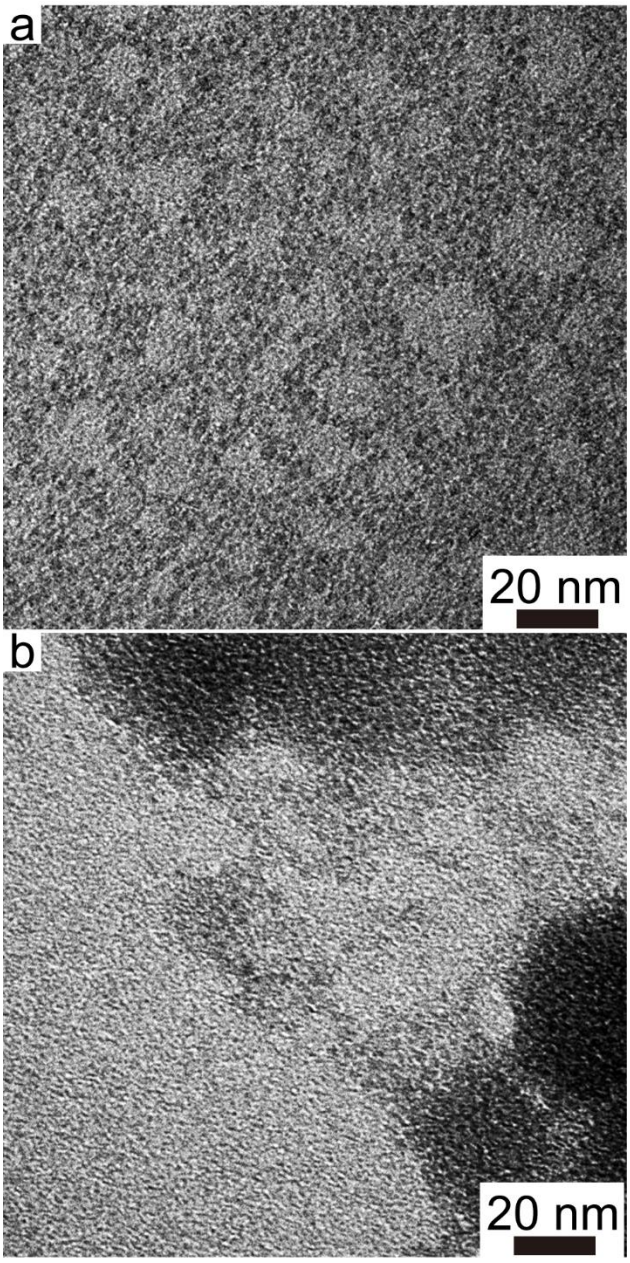

Figure 4.5: TEM images of 2.7 nm 10-undecenoic acid passivated silicon nanocrystal dispersed in (a) ethanol and (b) water.

XRD data for silicon nanocrystals dispersed in ethanol and water (Figure 4.6) are both indexed to diamond cubic silicon (PDF # 027–1402, a=b=c=5.43088 Å), indicating that the silicon crystal structure did not change during the transfer from ethanol to water.

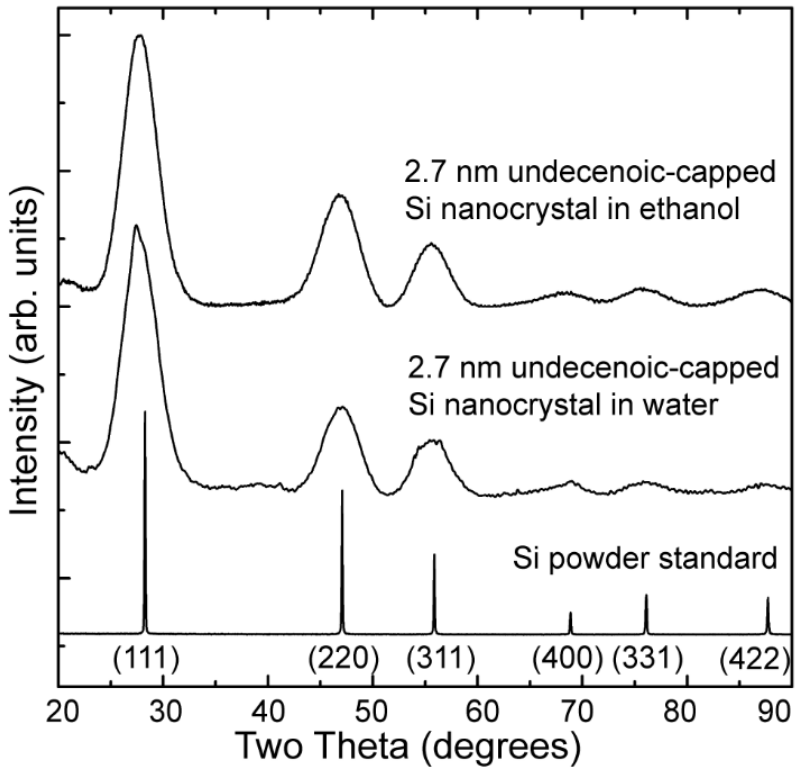

Figure 4.6: XRD of silicon nanocrystals dispersed in ethanol and water, showing diamond cubic silicon crystalline structure. A reference pattern is provided for diamond cubic Si (PDF # 027–1402, a=b=c=5.43088 Å).

4.3.3 Stability of Silicon Nanocrystals Dispersed in Water

To measure the spectral stability of silicon nanocrystals, the absorbance spectra of 2.7 nm silicon nanocrystals dispersed in water was acquired every 5 hours for a month. The absorbance at the PL excitation wavelength (322nm), is plotted against time in figure 4.7a. The absorbance drops by approximately 38% in a month, which is likely due to the

decrease of the crystalline silicon core size by oxidization at the surface of the nanocrystals.

Figure 4.7b shows integrated PL intensity and average PL emission wavelength of 2.7 nm silicon nanocrystals dispersed in water against time. The emission intensity increased in the first 3 days, likely due to the passivation of surface defects, i.e. residual dangling bonds, by oxidation.[29] After that time the PL intensity starts to decrease, correlating with the drop in absorbance at the excitation wavelength (322nm). Compared to the initial values, PL intensity dropped by less than 10% in a month, while the absorbance dropped by 38%, indicating an increase in PL quantum yield to 10.8% after a month. The average PL emission wavelength exhibited a ~32 nm blue shift over a month, which could be a result of silicon core shrinking due to surface oxidization.

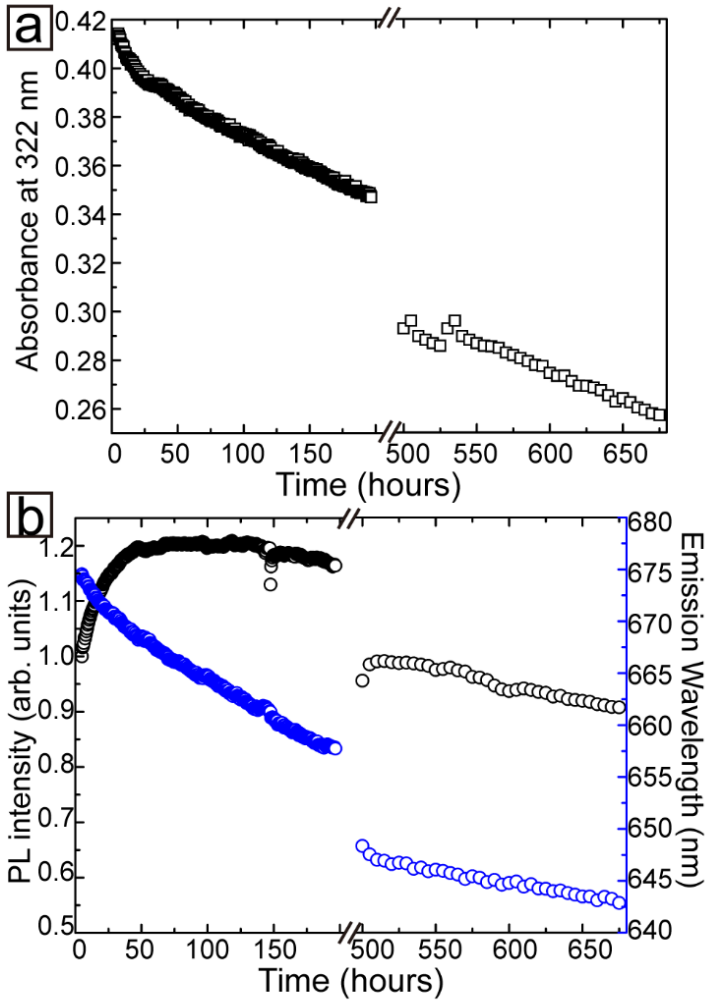

Figure 4.7: (a) Plot of absorbance at 322 nm against time. (b) Plots of integrated PL emission intensity (black) and average PL emission wavelength (blue) against time.

Surface oxidization of silicon nanocrystals dispersed in water over extend period of time was confirmed with FTIR and XPS. Figure 4.8 shows FTIR spectra for 2.7 nm silicon nanocrystals dispersed in water for 1 hour, 1 week, and 3 weeks, which are normalized to exhibit same value for CH_2 asymmetric stretching (2925 cm^{-1}) absorption. The spectra show absorption peaks corresponding to CH_2 stretching, Si-H stretching,

C=O stretching, COO^- stretching, and Si-O stretching. The nanocrystals dispersed in water for longer periods of time exhibit stronger absorption peak for Si-O stretching in FTIR, indicating the silicon nanocrystals are gradually oxidized in water.

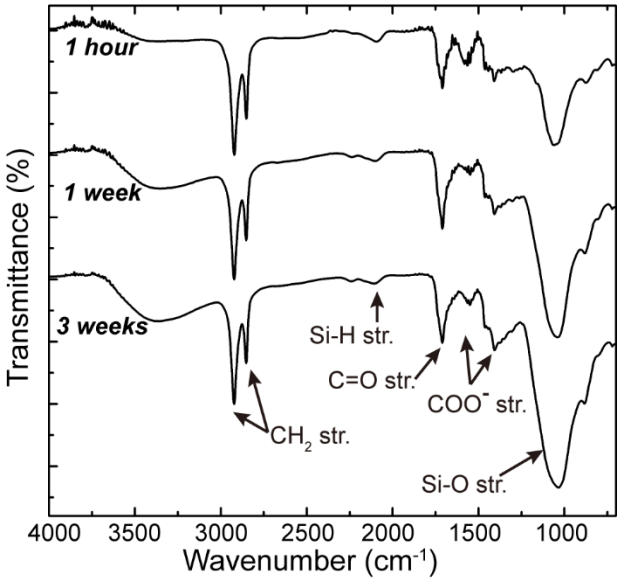

Figure 4.8: FTIR spectra of 2.7 nm 10-undecenoic acid capped silicon nanocrystals that were dispersed in pH 7.4 water for 1 hour, 1 week, and 3 weeks. Data was normalized to exhibit the same value for CH_2 asymmetric stretching (2925 cm^{-1}) absorption.

Figure 4.9 shows XPS data for 2.7 nm 10-undecenoic acid capped silicon nanocrystals that were dispersed in water for 1 hour, 1 day, 6 days, and 18 days. Si^0, Si-C bonding, and Si^{n+} oxidized states are clearly present in all the spectra. The silicon nanocrystals dispersed in water for longer periods of time exhibited smaller Si^0 contribution and larger Si^{n+} contribution (see Si^{4+}, for example), which again confirms the gradual oxidization of silicon nanocrystal surfaces in water. Surface oxidization causes a decrease in the silicon core diameter, leading to the observed drop in absorbance and PL blue shift.

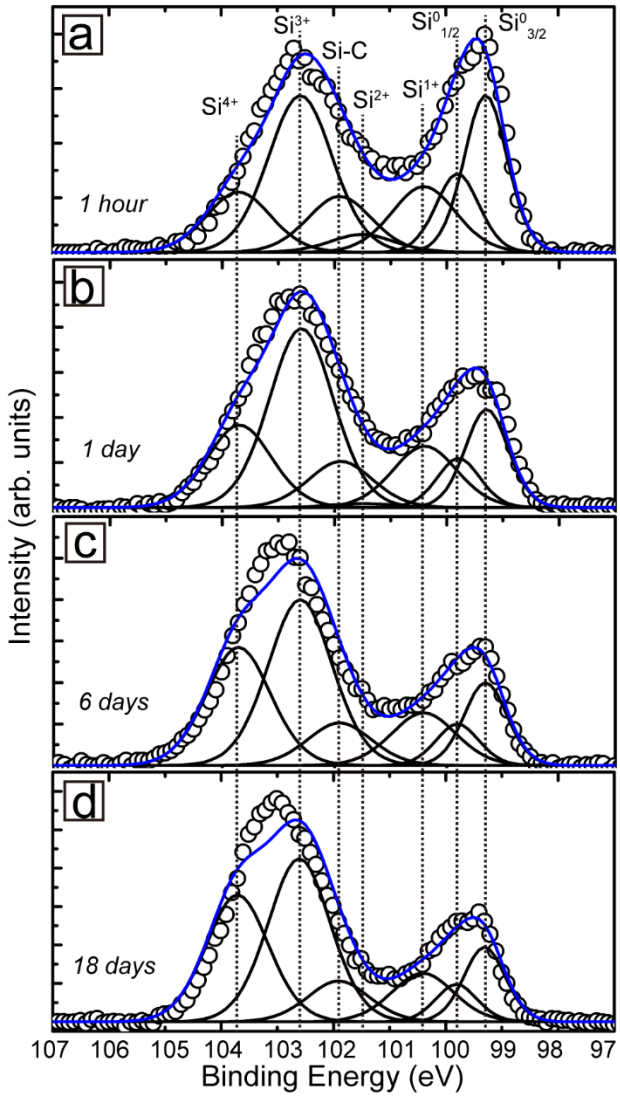

Figure 4.9: XPS of 2.7 nm silicon nanocrystals that were dispersed in water for (a) 1 hour, (b) 1day, (c) 6 days, and (d) 18 days. The black circles represent the measured intensity, black curves are the contributions from different silicon states (labeled with dotted lines), and blue curve is a summary of all the contributions.

4.3.4 Ligand Packing Density on Silicon Nanocrystal Surface

The high dispersibility and PL stability for silicon nanocrystals in aqueous solutions may be due to the high ligand packing density on their surfaces. TGA was used to determine the mass of the nanocrystal inorganic silicon core using the final mass of the sample after the TGA measurement was complete, assuming that all of the silicon had become SiO_2. The mass of the organic capping ligands can be calculated as the difference between the overall mass of the silicon nanocrystals and the mass of the inorganic silicon core. The ligand packing density can be calculated through Equation 3;

$$\rho_{packing\ density} = {M_L * N_A * \rho_{Si} * r}/{3MW_L * M_{Si}} \quad (3)$$

where M_L is ligand mass, M_{Si} is silicon mass, MW_L is the molecular weight of ligand, ρ_{Si} is silicon density at room temperature (2.329 g/cm^3), and r is nanocrystal radius. The ligand packing density on the surface of 2.7nm silicon nanocrystals passivated with 10-undecenoic acid through room temperature hydrosilylation is 5.2 nm^{-2}, corresponding to 119 ligands per nanocrystal, while that of 2.7nm nanocrystals passivated with 1-dodecene through thermal hydrosilylation at 190^{o}C is 6.3 nm^{-2}, corresponding to 142 ligands per nanocrystal. Theoretical simulations suggest that a 2.68 nm diameter silicon nanocrystal would have 143 silicon atoms on the surface.[30] Thus, it appears that 1-dodecene passivation through thermal hydrosilylation at 190^{o}C yields an almost "perfectly" dense ligand packing of one ligand per surface silicon atom, while 10-undecenoic acid passivation at room temperature is slightly less dense. This may be due to the stronger steric repulsion between bulky carboxylic acid groups. It is worthwhile to mention that

even a "perfectly" passivated silicon nanocrystal shows Si-O and Si-H absorption peaks in FTIR and silicon oxidization states in XPS[8] because a portion of surface silicon atoms have multiple available binding sites, such as those on (100) planes.

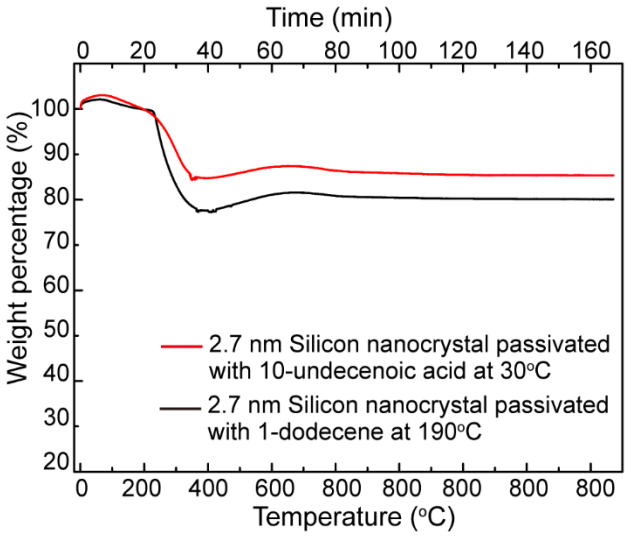

Figure 4.10: TGA data of 2.7 nm silicon nanocrystal passivated with 10-undecenoic acid through room temperature hydrosilylation (red curve), and 2.7 nm silicon nanocrystal passivated with 1-dodecene through thermal hydrosilylation at 190°C (black curve).

4.3.5 Large Silicon Nanocrystals Dispersed in Water

Large silicon nanocrystals (>5 nm) cannot be directly passivated with 10-undecenoic acid, and are instead passivated with ethyl 10-undecenoate through room temperature hydrosilylation and then the ester is hydrolyzed to carboxylic acid. Figure 11 shows FTIR spectra for 7.4 nm (Figure 4.11a) and 10.6 nm (Figure 4.11b) ethyl 10-undecenoate passivated silicon nanocrystals before and after hydrolysis. CH_3 and C=O stretching are clearly present in spectra before hydrolysis, corresponding to an ester group, while CH_3 disappears in the spectra after hydrolysis, indicating that ester groups

are hydrolyzed to carboxylic acid groups. Si-O stretching absorptions at ~1100 cm^{-1} are greatly enhanced, due to surface oxidization by the basic water used in hydrolysis (pH 8.5-9.5).

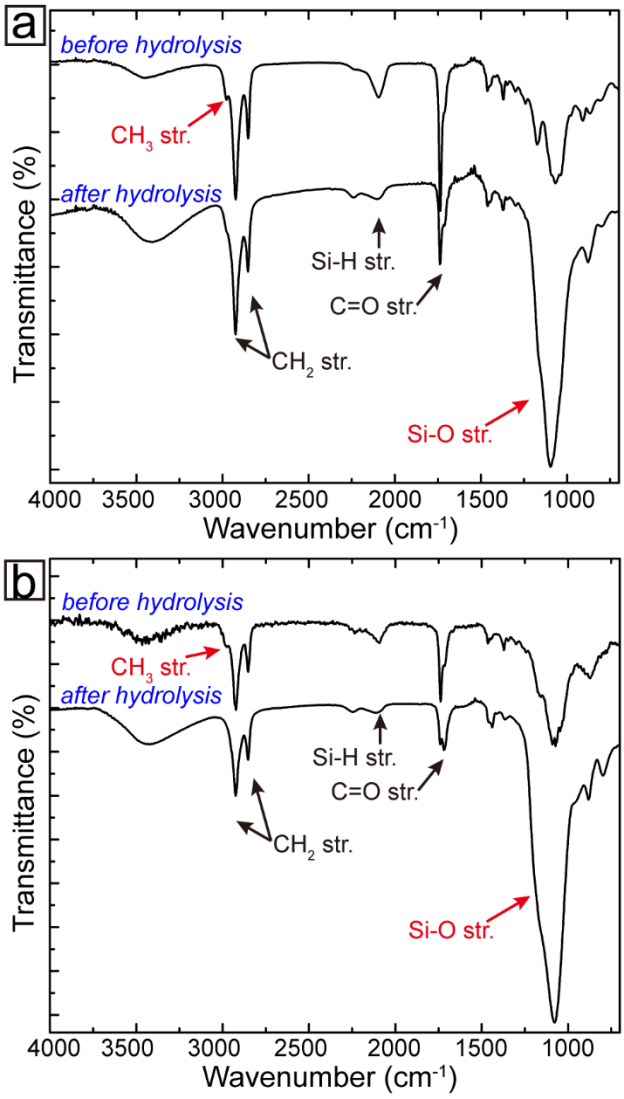

Figure 4.11: FTIR spectra of (a) 7.4 nm and (b) 10.6 nm ethyl 10-undecenoate capped silicon nanocrystals before and after hydrolysis.

After hydrolysis silicon nanocrystals are terminated with carboxylic acid groups and can be dispersed in water by filtering. Figure 4.12 show TEM images for 7.4 nm

(Figure 4.12a) silicon nanocrystals dispersed in water with pH adjusted to 8.0, and 10.6 nm (Figure 4.12b) silicon nanocrystals dispersed in water with pH adjusted to 9.0. The minimum pH for dispersing silicon nanocrystal in water is size dependent: larger nanocrystals require higher pH to disperse.

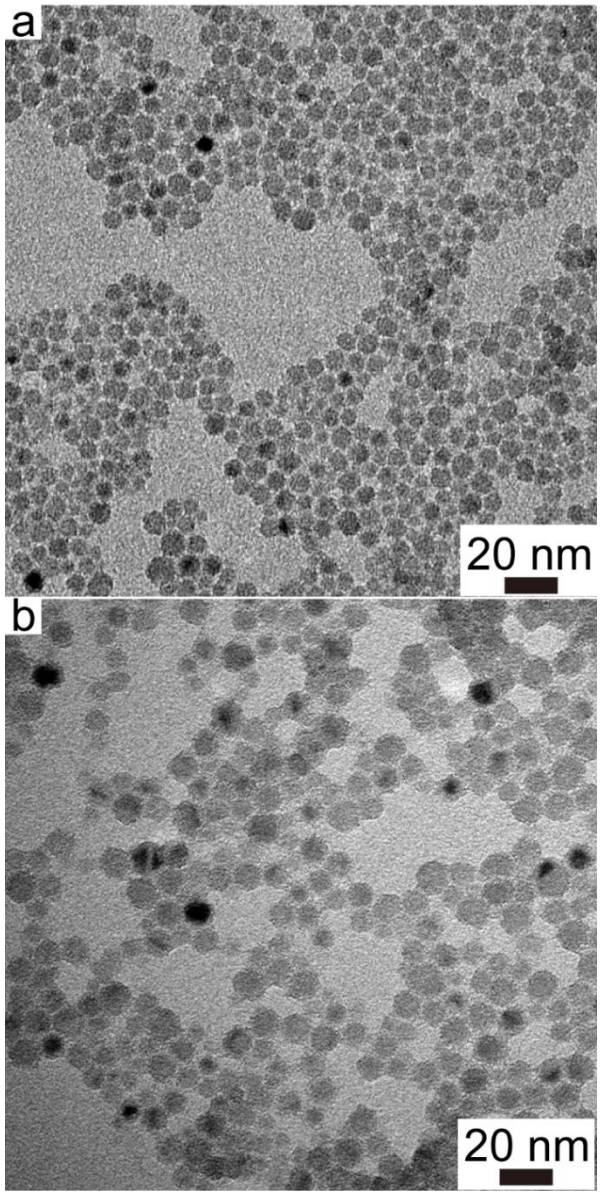

Figure 4.12: TEM images of (a) 7.4 nm silicon nanocrystals dispersed in pH 8.0 water, and (b) 10.6 nm silicon nanocrystals dispersed in pH 9.0 water.

The potential between charged particles dispersed in aqueous solution follows Derjaguin-Landau-Verwey-Overbeek (DLVO) theory, in which electrostatic repulsion between the electric double layers at the surface of particles balances van der Waals attraction to prevent aggregation. The electric double layer thickness is usually considered to be approximately 1.5 times[31] the Debye screening length k^{-1}, which can be calculated using Equation 4:[31]

$$k^{-1} = \left(\varepsilon_{water}\varepsilon_0 k_B T \Big/ \sum_i \rho_i e^2 z_i^2\right)^{1/2} \quad (4)$$

Where ε_{water} is the dielectric constant of water at 25°C, ε_0 is vacuum permittivity, k_B is Boltzmann constant, T is absolution temperature, ρ_i is the number density of ion i in solution, e is elementary charge, and z_i is the valency of ion i. In the case of nanocrystals dispersed in low ionic strength solutions, for example DI water with pH adjusted to 8.0 by sodium hydroxide, the Debye screening length is k^{-1}=308 nm, which is much larger than the radius of silicon nanocrystals in this study. Hence, the electric double layer interaction falls into the thick double layer situation, where a nanocrystal can be positioned within the electric double layer of another nanocrystal and influenced by the field of double layer. The interaction potential can be written as:[32]

$$V_{DL} = \left(4\pi^2 r\sigma^2 \Big/ \varepsilon k^2\right) \times \left[-In(1 - e^{-2kL}) + In\left(1 + e^{-kL} \Big/ 1 - e^{-kL}\right)\right] \propto r \quad (5)$$

under the assumption that the sample is composed of monodisperse nanocrystals with radius r and constant surface charge density σ. In Eqn. 5, L is the separation distance between nanocrystals, and k is the Debye-Hückel parameter. The van der Waals

attraction potential energy between spherical particles with radius of r_1 and r_2 is given by:[33]

$$V_{van\ der\ Waals} = -A/6 \times \left[\frac{2r_1r_2}{L^2-(r_1+r_2)^2} + \frac{2r_1r_2}{L^2-(r_1-r_2)^2} + In\frac{L^2-(r_1+r_2)^2}{L^2-(r_1-r_2)^2}\right] \quad (6)$$

in which A is the Hamaker constant. Considering the case of nanocrystals with very small radii (< 5 nm) in a dilute solution, we can assume that $r_1 = r_2 \ll L$, Eqn. 6 is simplified to:

$$V_{van\ de\ Waals} = -2Ar^2/3L^2 \propto r^2 \quad (7)$$

The strength of electric double layer repulsion between nanocrystals is proportional to their radius r, while van der Waals attraction is proportional to r^2. In order to reach a balance, larger nanocrystals need to have higher surface charge density σ. For silicon nanocrystals terminated with carboxylic acid, a higher surface charge density occurs at higher pHs when a larger portion of carboxylic acid groups that are deprotonated. In a solution of 2.7 nm silicon nanocrystals at a concentration of 10 mg/mL, the Wigner–Seitz radius[34] of nanocrystals is ~11 nm, hence the average inter-nanocrystal separation is 22 nm. This is less than the Debye screening length but much larger than the nanocrystal radius, which verifies the assumptions made for simplifying the expression for electric double layer interactions and van der Waals attraction.

4.4 CONCLUSION

In conclusion, silicon nanocrystals are passivated with 10-undecenoic acid (2.7 nm) or ethyl 10-undecenoate (7.4 and 10.6 nm) through room temperature

hydrosilylation. 2.7 nm silicon nanocrystal can be easily transferred to water at a concentration of 10 mg/mL with high emission stability. 7.4 and 10.6 nm silicon nanocrystals must be hydrolyzed before they can be dispersed in water. Surface oxidization has been found to be the main contributor to silicon nanocrystal degradation in water over extended periods of time. The high aqueous dispersibility and emission stability of silicon nanocrystal passivated through room temperature hydrosilylation is attributed to the densely packed capping ligands which protect the silicon core from oxidization.

4.5 REFERENCES

(1) Hessel, C. M.; Reid, D.; Panthani, M. G.; Rasch, M. R.; Goodfellow, B.W.; Wei, J.; Fujii, H.; Akhavan, V.; Korgel, B. A. Synthesis of Ligand-Stabilized Silicon Nanocrystals with Size-Dependent Photoluminescence Spanning Visible to Near-Infrared Wavelengths. *Chem. Mater.* **2012**, *24*, 393-401.

(2) Mastronardi, M. L.; Maier-Flaig, F.; Faulkner, D.; Henderson, E. J.; Kübel, C.; Lemmer, U.; Ozin, G. A. Size-Dependent Absolute Quantum Yields for Size-Separated Colloidally-Stable Silicon Nanocrystals. *Nano Lett.* **2012**, *12*, 337-342.

(3) Miller, J. B.; Van Sickle, A. R.; Anthony, R. J.; Kroll, D. M.; Kortshagen, U. R.; Hobbie, E. K. Ensemble Brightening and Enhanced Quantum Yield in Size-Purified Silicon Nanocrystals. *ACS Nano* **2012**, *6*, 7389-7396.

(4) Sykora, M.; Mangolini, L.; Schaller, R. D.; Kortshagen, U.; Jurbergs, D.; Klimov, V. I. Size-Dependent Intrinsic Radiative Decay Rates of Silicon Nanocrystals at Large Confinement Energies, *Phy. Rev. Lett*. **2008**, *100*, 067401.

(5) Wilson, W. L.; Szajowski, P. F.; Brus, L. E. Quantum Confinement in Size-Selected, Surface-Oxidized Silicon Nanocrystals. *Science* **1993**, *262*, 1242-1244.

(6) Singh, V.; Yu, Y.; Sun, Q.-C.; Korgel, B. A.; Nagpal, P. Pseudo-Direct Bandgap Transitions in Silicon Nanocrystals: Effect on Optoelectronics and Thermoelectrics. *Nanoscale* **2014**, *6*, 14643-14647.

(7) Gu, L.; Hall, D. J.; Qin, Z.; Anglin, E.; Joo, J.; Mooney, D. J.; Howell, S. B.; Sailor, M. J. In vivo Time-Gated Fluorescence Imaging with Biodegradable Luminescent Porous Silicon Nanoparticles. *Nat. Commun.* **2012**, *4*, 2326.

(8) Hessel, C. M.; Rasch, M. R.; Hueso, J. L.; Goodfellow, B. W.; Akhavan, V. A.; Puvanakrishnan, P.; Tunnel, J. W.; Korgel, B. A. Alkyl Passivation and Amphiphilic Polymer Coating of Silicon Nanocrystals for Diagnostic Imaging. *Small* **2010**, *6*, 2026-2034.

(9) Erogbogbo, F.; Yong, K.-T.; Roy, I.; Xu, G.; Prasad, P. N.; Swihart, M. T. Biocompatible Luminescent Silicon Quantum Dots for Imaging of Cancer Cells. *ACS Nano* **2008**, *2*, 873-878.
(10) Kovalev, D.; Fujii, M. Silicon Nanocrystals: Photosensitizers for Oxygen Molecules. *Adv. Mater.* **2005**, *17*, 2531-2544.
(11) Xiao, L.; Gu, L.; Howell, S. B.; Sailor, M. J. Porous Silicon Nanoparticle Photosensitizers for Singlet Oxygen and Their Phototoxicity against Cancer Cells. *ACS Nano* **2011**, *5*, 3651-3659.
(12) Goller, B.; Polisski, S.; Wiggers, H.; Kovalev, D. Silicon Nanocrystals Dispersed in Water: Photosensitizers for Molecular Oxygen. *Appl. Phys. Lett.* **2010**, *96*, 211901.
(13) Kelly, J. A.; Veinot, J. G. C. An Investigation into Near-UV Hydrosilylation of Freestanding Silicon Nanocrystals. *ACS Nano* **2010**, *8*, 4645-4656.
(14) Hua, F.; Swihart, M. T.; Ruckenstein, E.; Efficient Surface Grafting of Luminescent Silicon Quantum Dots by Photoinitiated Hydrosilylation. *Langmuir* **2005**, *21*, 6054-6062.
(15) Zhang, S.; Li, J.; Lykotrafitis, G.; Bao, G.; Suresh S. Size-Dependent Endocytosis of Nanoparticles. *Adv. Mater.* **2009**, *21*, 419-424.
(16) Osaki, F.; Kanamori, T.; Sando, S.; Sera, T.; Aoyama, Y. A Quantum Dot Conjugated Sugar Ball and Its Cellular Uptake. On the Size Effects of Endocytosis in the Subviral Region. *J. Am. Chem. Soc.* **2004**, *126*, 6520-6521.
(17) Choi, H. S.; Liu, W.; Misra, P.; Tanaka, E.; Zimmer, J. P.; Ipe, B. I.; Bawendi, M. G.; Frangioni, J. V. Renal Clearance of Quantum Dots. *Nat. Biotech.* **2007**, *25*, 1165-1170.
(18) Erogbogbo, F.; Tien, C.-A.; Chang, C.-W.; Yong, K.-T.; Law, W.-C.; Ding, H.; Roy, I.; Swihart, M. T.; Prasad, P. N. Bioconjugation of Luminescent Silicon Quantum Dots for Selective Uptake by Cancer Cells. *Bioconjugate Chem.* **2011**, *22*, 1081-1088.
(19) Medintz, I. L.; Tetsuouyeda, H.; Goldman, E. R.; Mattoussi, H. Quantum Dot Bioconjugates for Imaging, Labelling and sensing. *Nat. Mater.* **2005**, *4*, 435-446.
(20) Moan, J. On the Diffusion Length of Singlet Oxygen in Cells and Tissues. *J. Photochem. Photobiol. B: Biol* **1990**, *6*, 343-347.
(21) Juzenas, P.; Chen, W.; Sun, Y.-P.; Coelho, M. A. N.; Generalov, R.; Generalov, N.; Christensen, I. L. Quantum Dots and Nanoparticles for Photodynamic and Radiation Therapies for Cancer. *Adv. Drug Deliv Rev.* **2008**, *60*, 1600-1614.
(22) Li, Z. F.; Ruchenstein, E. Water-Soluble Poly(acrylic acid) Grafted Luminescent Silicon Nanoparticles and Their Use as Fluorescent Biological Staining Labels. *Nano Lett.* **2004**, *4*, 1463-1467.
(23) Sato, S.; Swihart, M. T. Propionic-Acid-Terminated Silicon Nanocrystals: Synthesis and Optical Characterization. *Chem. Mater.* **2006**, *18*, 4083-4088.
(24) Clark, R. J.; Dang, M. K. M.; Veinot, J. G. C. Exploration of Organic Acid Chain Length on Water-Soluble Silicon Quantum Dot Surfaces. *Langmuir* **2010**, *26*, 15657-15664.

(25) Yu, Y.; Hessel, C. M.; Bogart, T. D.; Panthani, M. G.; Rasch, M. R.; Korgel, B. A. Room Temperature Hydrosilylation of Silicon Nanocrystals with Bifunctional Terminal Alkenes. *Langmuir* **2013**, *29*, 1533-1540.
(26) Hessel, Colin M.; Henderson Eric J.; Veinot, Jonathan G.C. Hydrogen Silsesquioxane: A Molecular Precursor for Nanocrystalline Si-SiO2 Composites and Freestanding Hydride-Surface-Terminated Silicon Nanoparticles. *Chem. Mater.* **2006**, *18*, 6139-6146.
(27) Casey, K. G.; Quitevis, E. L. Effect of Solvent Polarity on Nonradiative Processes in Xanthene Dyes: Rhodamine B in Normal Alcohols. *J. Phys. Chem.* **1988**, *92*, 6590-6594.
(28) Socrates, G. Infrared Characteristic Group Frequencies, *John Wiley & Sons* UK, 2nd edition, **1994**.
(29) Zhelev, Z.; Jose, R.; Nagase, T.; Ohba, H.; Bakalova, R.; Ishikawa, M.; Baba, Y. Enhancement of the Photoluminescence of CdSe Quantum Dots during Long-Term UV-Irradiation: Privilege or Fault in Life Science Research? *J. Photochem. Photobiol. B: Biol.* **2004**, *75*, 99-105.
(30) Yilmaz, D. On the Strain in Silicon Nanocrystals. Ph.D. Thesis, Bilkent University, Ankara, *Turkey*, **2009**.
(31) Scholz, F. Electroanalytical Methods Guide to Experiments and Applications. *Springer: New York*, **2002**.
(32) Ohshima, H. Diffuse double layer interaction between two spherical particles with constant surface charge density in an electrolyte solution. *Colloid & Polymer Sci.* **1975**, *253*, 158-163.
(33) Hamaker, H. C. The London-van der Waals Attraction between Spherical Particles. *Physica IV* **1937**, *10*, 1058-1072.
(34) Girifalco, L. A. Statistical Mechanics of Solids. *Oxford University Press: Oxford,* **2003**.

Chapter 5: Magnetofluorescent Chemically-Coupled Nanocrystals of Iron Oxide and Silicon

5.1 INTRODUCTION

Multifunctional nanocrystals with fluorescent and magnetic response could be used as multimodal imaging contrast agents for medical diagnostics (i.e., fluorescence and magnetic resonance imaging (MRI)), provide targeted cell labelling and magnetic separation,[1-5] or combined diagnosis and therapy—so-called theranostics—with fluorescence imaging with magnetic heating response. Bifunctional heterostructures have been made by coupling fluorescent agents, such as organic dyes,[5,7,8] quantum dots,[4,9-15] and rare earth element-doped nanocrystals,[3,16,17] with magnetic nanocrystals like γ-Fe_2O_3,[1,10,11] Fe_3O_4,[16,18] or PtFe[9]. Among the available fluorescent agents, Si nanocrystals, or quantum dots, are fairly unique in that they are biocompatible and biodegradable,[19,20] they fluoresce in the red-to-near infrared (NIR) wavelength range, with size-tunable emission wavelengths,,[21,22] with long radiative lifetimes suitable for time-gated imaging. Multifunctional nanocrystals have been created using a few different approaches, such as heterostructure synthesis, molecular linking of different types of nanocrystals, or mixing in a host matrix such as a surfactant micelle or polymer/silica capsule. For instance, CdS and iron oxide have been coupled by forming CdS/γ-Fe_2O_3 heterojunctions,[15] dimercapto-succinimide acid coupling of γ-Fe_2O_3 and core-shell CdSe/ZnS nanocrystals,[4] and encapsulation of CdS and iron oxide nanocrystals in polyethylene glycol (PEG)-modified phospholipid micelles.[12] Fluorescent Si

nanocrystals with magnetic response have been made in a few instances. Si nanocrystals have been encapsulated with γ-Fe_2O_3 nanocrystals in PEGylated phospholipid micelles,[23] hybrid Si/iron oxide nanocrystals have been made by a co-sputtering process,[23b] and Si nanocrystals have been doped with magnetic impurity atoms of Mn.[23c,23d] Chemically-coupled fluorescent Si and magnetic nanocrystals, however, have not yet been made.

Here we report the synthesis of colloidal, water-dispersible complexes of molecularly-linked Si and γ-Fe_2O_3 nanocrystals with hydrodynamic diameter between 20 to 40 nm. The optimum hydrodynamic size for particles crossing through the cell membrane via receptor-mediated endocytosis is between 25 and 50 nm.[20,24,25] These structures are made by derivatizing Si nanocrystals with the bifunctional ligand, 10-undecenoic acid. The molecule bonds to the Si nanocrystals via the alkene by hydrosilylation and the carboxylate group is free to bond to the Fe_2O_3 nanocrystals. The Fe_2O_3nanocrystals are capped with hydrophobic ligands, but the Si nanocrystals are passivated with polar functional groups, and as the Fe_2O_3 nanocrystals become surrounded by hydrophilic Si nanocrystals, the entire complex becomes water dispersible. The difference in solvent dispersibility is one feature that distinguishes the nanocrystal complexes from nanocrystal mixtures.

5.2 EXPERIMENTAL DETAILS

5.2.1 Materials

FOx-16 was purchased from Dow Corning, 10-undecenoic acid (>98%), iron (0) pentacarbonyl, diphenyl ether (98%), and 1-octene (>90%) was purchased from Sigma-Aldrich. Ethanol, chloroform, toluene and hydrochloric acid (HCl, 37.5%) were from Fisher Scientific. Hydrofluoric acid (HF, 48%) was obtained from EMD chemicals. Deionized (DI) water was obtained using a Barnstead Nanopure Filtration System (17 MΩ resistance).

5.2.2 Iron Oxide Nanocrystal Synthesis

Fe_2O_3 nanocrystals were synthesized by thermal decomposition of iron (0) pentacarbonyl[28] in diphenyl ether at 260^{o}C with 10-undecenoic acid capping ligands. 20 mL of dipenyl ether was mixed with 2.4 mL of 10-undecenoic acid in a 50 mL three-neck round bottom flask and purged with nitrogen gas at 100^{o}C for 1 hour. 0.4 mL of $FeCO_5$ was injected into the flask, which was then quickly heated to 265^{o}C (10-undecenoic acid starts to decompose at 275^{o}C). The reaction was kept at 265^{o}C for 6 hr, and allowed to cool to 180^{o}C, at which temperature the reaction was exposed to air to oxidize the Fe nanocrystals to iron oxide. The nanocrystal product was precipitated and redispersed three times with toluene/ethanol as the solvent/antisolvent combination, and dispersed in toluene for further use.

5.2.3 Silicon Nanocrystals Synthesis

Si nanocrystals were synthesized by thermal decomposition of hydrogen silsesquioxane (HSQ) at 1100^{o}C, followed by HF wet etching and passivation by hydrosilylation with 10-undecenoic acid.[22] In a typical synthesis, 20 mL of flowable oxide (commerical name: FOx-16, purchased from Dow Corning) was evaporated in vacuum for 6 hours to form dry hyrogen silsesquioxane (HSQ), which was annealed at 1100^{o}C for 1 hour under forming gas (93% nitrogen gas and 7% hydrogen gas) flow, leading to a brown glassy material. This brown material contained SiO_2 ambedded Si nanocrystals, which was ground with an agate mortar and pestle and shaken with 3 mm diameter borosilicate glass beads to form a fine powder. Hydride-terminated Si nanocrystals were obtained by etching 300 mg of this powder with 10 mL of 48% hydroflouric acid and 1 mL of 37% hydrocloric acid in dark (cover the light) for 4 hours. Hydride-terminated Si nanocrystals were rinsed once with DI water, twice with ethanol, and once with chloroform, and dispersed with ethanol until further use.

5.2.4 Nanocrystal Coupling Reactions

2 mL ethanol dispersion of hydride-terminated Si nanocrystal was mixed with 3 mL of toluene dispersion of Fe_2O_3 nanocrystals, 2 mL of 10-undecenoic acid, 2 mL of 1-octene in a 20 mL vial, which was then sealed with a septum. Nitrogen gas was bubbling through the solution for 30 min to remove the dissolved oxygen. The mixture was sealed in the vial and allowed to react without stirring at room temperature for 7 days. Figure

5.1 illustrates the experimental setup. The initially turbid mixture becomes transparent in 5 days, indicating the formation of the colloidal heterostructures.

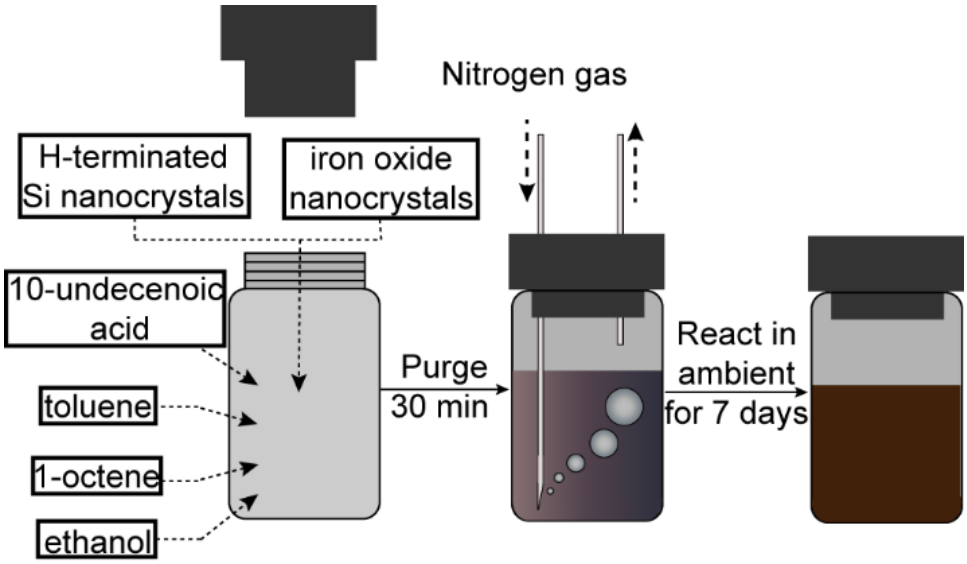

Figure 5.1: Experimental approach for coupling Si and Fe_2O_3 nanocrystals.

The coupled Si and Fe_2O_3 nanocrystals were cleaned by a centrifugal filtration process that was repeated 7 times. In each filtration, 10 mL of ethanol was used to dilute 2 mL of the 2 mg/mL heterostructure dispersion, and the volume of the diluted dispersion was reduced to 2 mL with a 100 KDa cuttoff centrifugal filter (millipore, ultra-15), centrifuging at 1200 G (centrifugal force) for 5 min. The Si- Fe_2O_3 conjugates were finally dispersed in ethanol.

5.2.5 Materials Characterization

Photoluminescence (PL) spectra were acquired on a Varian Cary Eclipse fluorescence spectrophotometer with a 10 mm path-length quartz cuvette. Ultraviolet-visible (UV-vis) absorbance spectroscopy was performed on a Varian Cary 50 Bio UV-

vis spectrophotometer. PL quantum yields were estimated in comparison to Rhodamine 101 dissolved in anhydrous ethanol, which is assumed to have 100% QY.

Transmission Electron Microscopy (TEM) was performed on a FEI Tecnai Biotwin TEM with 80 kV accelerating voltage. Samples were drop cast in ethanol onto 200 mesh carbon-coated copper grids for imaging (Electron Microsopy Science).

X-ray diffraction (XRD) was performed using a Rigaku R-Axis Spider Diffractometer with Cu K_α radiation (λ=0.15418 nm). Nanocrystals were drop cast onto a glass slide and placed onto a nylon loop with a needle. Mineral oil was applied to secure the sample if necessary. Two-dimensional diffraction data were collected for 15 min while rotating the sample stage at 10^o per minute and radially integrated using 2DP Spider software (version 1.0, Rigaku Americas Corp.)

Dynamic light scattering (DLS) data were collected at 25°C using a Zetasizer Nano ZS instrument (Malvern) with a laser wavelength of 630 nm and scattering angle θ of 173°. Disposable, polystyrene low-volume microcuvettes (Malvern) were used for DLS. The cuvettes were rinsed 3 times with DI water passed through an alumina based Anotop 10 syringe filter (20 nm pore-size, Whatman cat. no. 6809-1002). The cuvettes were filled with 50 μL of 0.1 mg/mL heterostructure dispersions for a typical DLS measurement.

5.3 RESULTS AND DISCUSSION

5.3.1 Dispersibility and Magnetic Response of Si-Fe_2O_3 Nanocrystals Conjugates

Figure 5.2a shows dispersions of the fluorescent 10-undecenoic acid-capped (2.3 nm diameter) Si nanocrystals and the magnetic 10-undecenoic acid-capped (7.0 nm diameter) Fe_2O_3 nanocrystals shown in the TEM images in Figures 5.2d and 5.2e.combined in various ratios in the raw solution (the mixture of toluene, ethanol, 10-undecenoic acid, and 1-octene) . The dispersions become darker in color with increasing amounts of Fe_2O_3 and the fluorescence changes color slightly, yet the fluorescence is still relatively bright. The Si- Fe_2O_3 nanocrystal conjugates disperse in ethanol or water (Figure 5.2b), whereas the 10-undecenoic acid-capped Fe_2O_3 nanocrystals are hydrophobic and do not disperse in polar solvents, indicating that in the nanocrystal conjugates the hydrophobic Fe_2O_3 nanocrystals are surrounded by hydrophilic Si nanocrystals. Correspondingly, the nanocrystal conjugates aggregate in hexane (Figure 5.2c) and no freely dispersed Fe_2O_3 nanocrystals are found in the supernatant, indicating that all of the Fe_2O_3 nanocrystals are coupled to the Si nanocrystals. The precipitated fluorescent nanocrystal conjugates also respond to a permanent magnet as shown in Figure 5.2c.

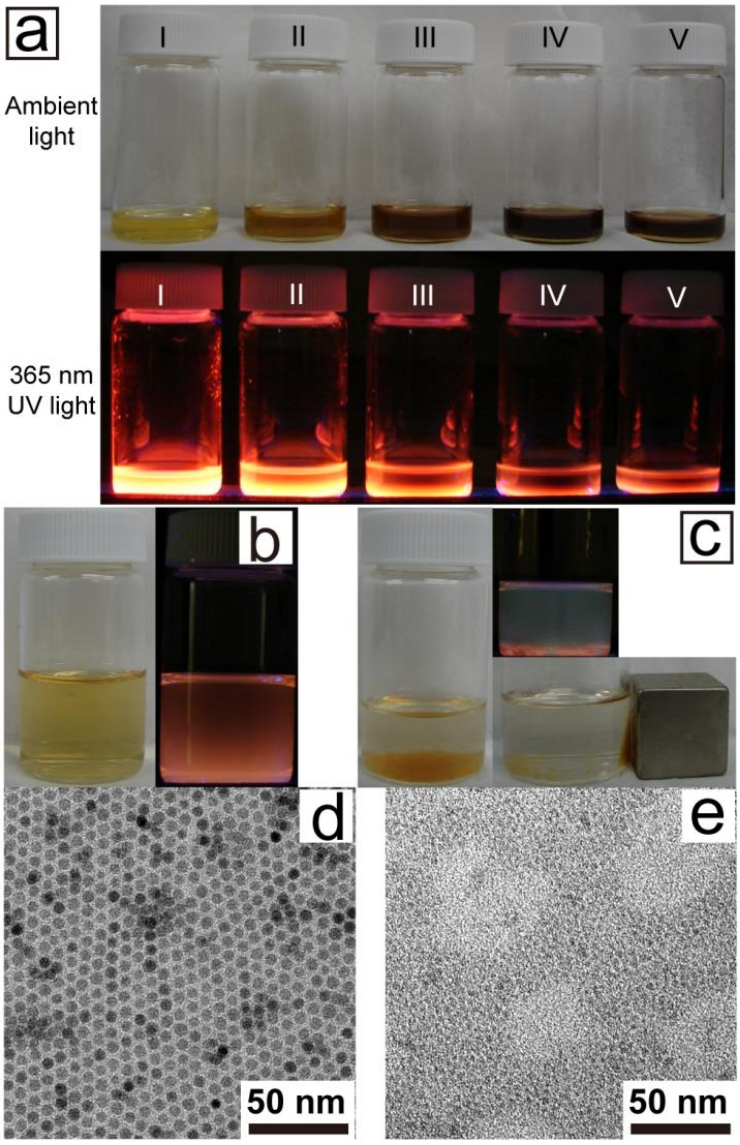

Figure 5.2: (a) Photographs of dispersions of Si- Fe_2O_3 nanocrystal assemblies dispersed in raw solutions under ambient light (top), and 365 nm UV light (bottom). The vials labelled with I to V correspond to Si nanocrystal to Fe_2O_3 ratios (by particle number) of ∞(no Fe_2O_3), 66:1, 33:1, 24:1, and 20:1, respectively. (b) Photographs of Si- Fe_2O_3 nanocrystal assemblies dispersed in ethanol, under ambient light (left), and 365 nm UV light (right). (c) Photographs of Si- Fe_2O_3 assemblies aggregated in hexane, under ambient light (left), 365 nm UV light (top right), and next to a permanent magnet bar (bottom right). TEM images of 10-undecenoic acid-capped (d) Fe_2O_3 and. (e) Si nanocrystals. The average diameters of the Si and Fe_2O_3 nanocrystals are 2.3 nm and 7.0 nm, respectively.

5.3.2 Structure of the Si-Fe_2O_3 Nanocrystal Conjugates

Figure 5.3 shows TEM images of Si- Fe_2O_3 nanocrystal conjugates made with a Si ratio to Fe_2O_3 ratio of 20:1. A mixture of Si- Fe_2O_3 nanocrystal conjugates along with free, uncoupled Si nanocrystals are observed in the field of view. There are no free Fe_2O_3 nanocrystals. The excess of Si nanocrystals used to make the conjugates ensures that all of the Fe_2O_3 nanocrystals are complexed with Si nanocrystals. Figures 3b-3i show higher magnification TEM images of various Si- Fe_2O_3 nanocrystal conjugates. The Fe_2O_3 nanocrystals are present at the core of the conjugate, surrounded by a multilayer shell of Si nanocrystals.

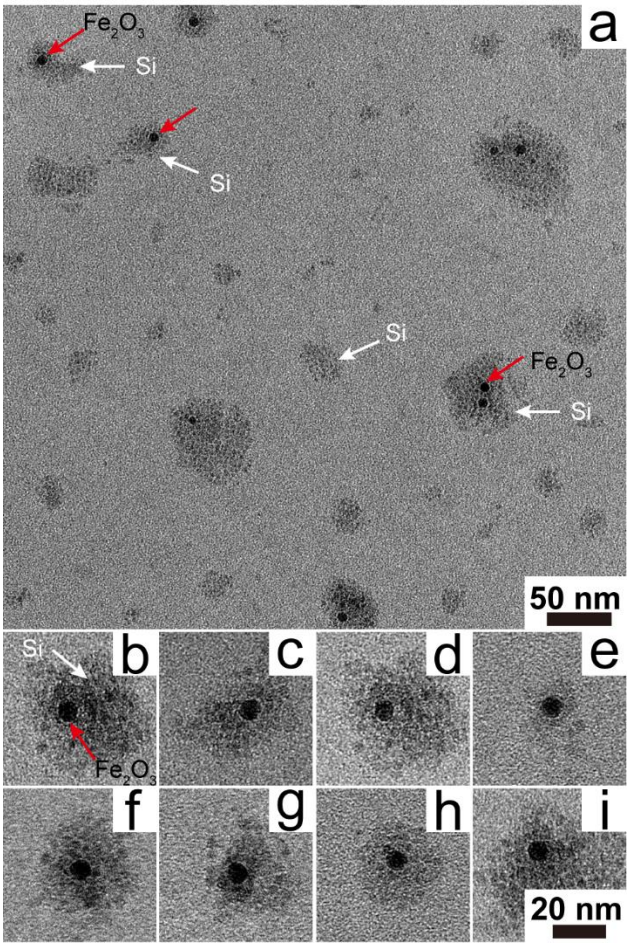

Figure 5.3: TEM images of (a) a field of Si- Fe_2O_3 nanocrystal conjugates made with an Si to Fe_2O_3 ratio of 20:1 and(b)-(i) individual nanocrystal conjugates. The larger diameter particles with darker contrast are the Fe_2O_3 nanocrystals and the smaller, lighter contrast particles are Si.

Figure 5.4 shows XRD data for the Fe_2O_3 and Si nanocrystals. The Fe_2O_3 nanocrystals are maghemite (γ-Fe_2O_3, JCPDS no. 39-1346, S.G. $P4_132$, a = 8.3515 Å) and the Si nanocrystals have diamond cubic Si crystal structure (JCPDS no. 27-1402, S. G. $Fd\bar{3}m$, a= 5.430710 Å). XRD of the conjugated Fe_2O_3 and Si nanocrystals show diffraction patterns from both γ-Fe_2O_3 and diamond cubic Si, indicating that the chemical

linking does not change the crystal structure of either nanocrystal material. The XRD peak widths are consistent with the nanocrystal size measured by TEM.

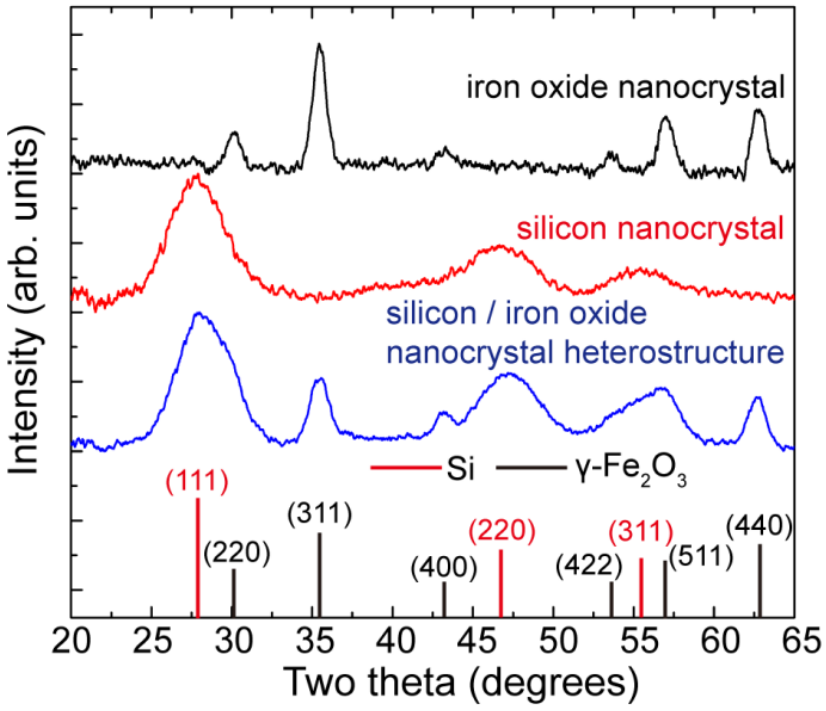

Figure 5.4: XRD data for the nanocrystals of Fe_2O_3 (black), Si (red), and the Si- Fe_2O_3 complexes with Si to Fe_2O_3 ratio of 66:1(blue).

5.3.3 Hydrodynamic Size Analysis of Conjugates

The Si- Fe_2O_3 nanocrystal conjugates were also examined by dynamic light scattering (DLS) to determine their hydrodynamic diameter when dispersed in ethanol. TEM provides direct imaging of the conjugates, but there is always the possibility that sample drying onto the TEM grid leads to aggregation that does not actually exist in the dispersion. DLS provides confirmation that the size of the conjugates observed by TEM represents the true conjugate size in the dispersions.

Figure 5.5 shows DLS data for four different Si- Fe_2O_3 nanocrystal conjugate samples made by combining different ratios of Si and Fe_2O_3 nanocrystals. The data are provided as plots of the normalized intensity correlation function $C(\tau)$ versus delay time τ. The data were fit to Equations (1)-(4):[29]

$$C(\tau) = \beta e^{-2\Gamma\tau} \quad (1)$$

$$\Gamma = Dq^2 \quad (2)$$

$$D = {}^{kT}/_{3\pi\mu d} \quad (3)$$

$$q = {}^{4\pi n}/_{\lambda} \sin({}^{\theta}/_{2}) \quad (4)$$

in which τ is delay time, D is diffusion constant, μ is viscosity of dispersant, k is Boltzmann's constant, T is temperature, n is refractive index of dispersant, λ is the wavelength of laser, q is the wave vector of the laser, θ is scattering angle, and β is an arbitrary factor between 0 and 1, to determine the hydrodynamic diameter, *d*. The best fits of Eqns (1)-(4) to the data in Figure 5.5 give diameters of 21 nm, 22 nm, 27 nm, and 22 nm, for the conjugates made with Si:Fe_2O_3 nanocrystal ratios of 66:1, 44:1, 24:1, and 20:1. The free, or uncoupled, Si nanocrystals do not affect the DLS data as these relatively small, 4.4 nm hydrodynamic diameter, nanocrystals are dispersed and the scattering intensity is proportional to d^6, such that the scattering signal is overwhelmed by the conjugates. (scattering from individual Si nanocrystals contributes less than 0.01% of the signal compared to the conjugates). The hydrodynamic diameter of the conjugates was also found to increase slightly to 40 nm.

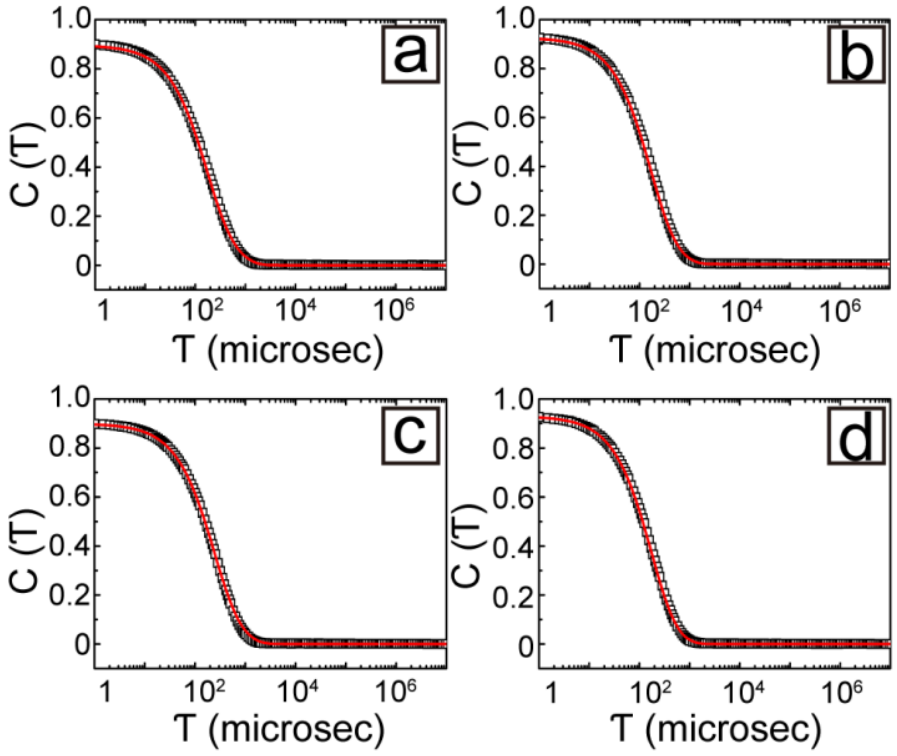

Figure 5.5: Plots of normalized intensity correlation function against delay time for Si-Fe_2O_3 nanocrystal conjugates dispersed in ethanol made with Si to Fe_2O_3 nanocrystal ratios of (a) 66:1, (b) 44:1, (c) 24:1, and (d) 20:1. The black circles represent correlation data, and red lines represent the best fits of Eqns (1)-(4) to the data with hydrodynamic diameters of (a) 21 nm, (b) 22 nm, (c) 27 nm, and (d) 22 nm.

5.3.4 Si/Fe_2O_3 Nanocrystal Conjugate Photoluminescence

Figure 5.6 shows UV-vis absorbance and PL spectra for Si/Fe_2O_3 nanocrystal conjugates compared to simple mixtures of Si and Fe_2O_3 nanocrystals. When photoexcited with 350 nm light, the conjugates exhibit two PL emission bands centered at 440-450 nm and 610 nm; whereas the nanocrystal mixture emits only a single peak at 610 nm. As the Fe_2O_3 to Si ratio was increased in the formation of the conjugates, the 450 nm emission became more intense, probably due to a decrease in the amount of free Si

nanocrystals. The PL quantum yields of the conjugates made with Si to Fe_2O_3 nanocrystal ratios of 66:1, 44:1, 24:1, and 20:1 were 4%, 6%, 10%, and 12%, respectively. The PL quantum yield of the unconjugated (free) Si nanocrystals was 16%. The decreased PL quantum yield of the conjugates indicates that the Fe_2O_3 nanocrystals are quenching to PL from the Si nanocrystals to some extent. The 450 nm PL from the conjugates matches the emission of the Fe_2O_3 nanocrystals, which is between 400 and 550 nm and probably results from ligand-to-metal charge-transfer.[30,31] The PL emission of Fe_2O_3 nanocrystals is greatly enhanced by coupling to Si nanocrystals in the heterostructure. The reason of this enhancement is being investigated.

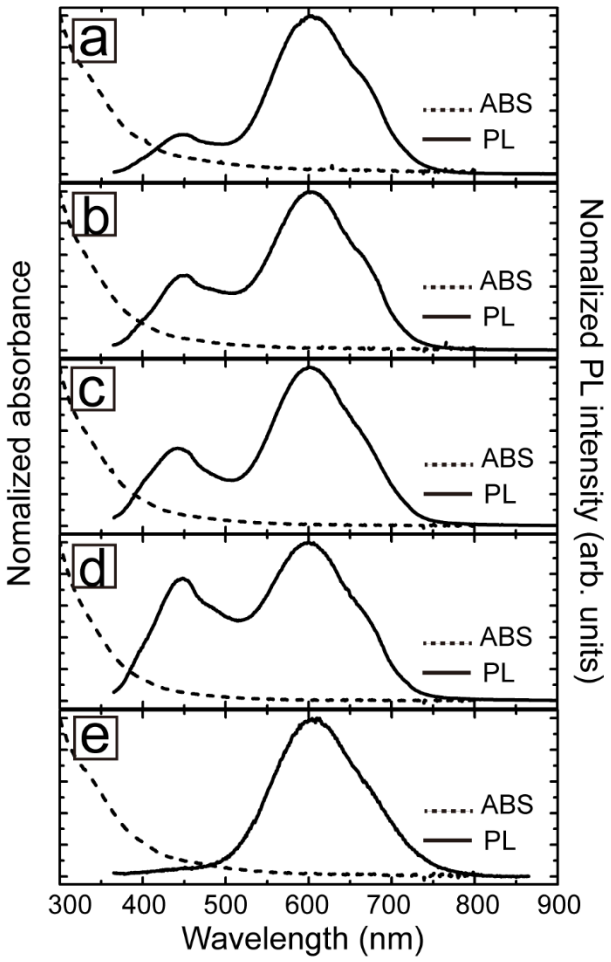

Figure 5.6: Optical absorbance and PL (λ_{exc}=350 nm) spectra of Si/Fe_2O_3 nanocrystal conjugates formed with Si to Fe_2O_3 ratios of (a) 66:1, (b) 33:1, (c) 24:1, (d) 20:1, and (e) a 26:1 mixture of Si and Fe_2O_3 nanocrystals dispersed in ethanol and toluene mixture with 1:1 volume ratio.

5.3.5 Si and Iron Oxide Nanocrystal Coupling Mechanism

Si-Fe_2O_3 nanocrystal conjugation occurs via the bifunctional undecenoic acid ligand. As illustrated in Figure 5.7, 10-undecenoic acid can attach to Fe_2O_3 via the carboxylic acid group,[32] and bond to Si via hydrosilylation at the alkene group.[22] Two mechanisms are possible for coupling between the Si and Fe_2O_3 nanocrystals. As shown in Figure 5.7, Si nanocrystals is coupled to the Fe_2O_3 nanocrystals by an acid-promoted

room temperature hydrosilylation[22] with the hydride-terminated Si nanocrystal and the exposed alkenes surrounding the undecenoic acid-capped Fe_2O_3 nanocrystals. In mechanism II, 10-undecenoic acid first passivate the hydride-terminated surface of Si nanocrystals to form 10-undecenoic acid-capped Si nanocrystals, which then undergo ligand exchange with the ligand on Fe_2O_3 nanocrystal. As control experiments, no heterostructure could be found if no 10-undecenoic acid was added into the synthesis, and mixing 10-undecenoic acid capped Si and Fe_2O_3 nanocrystal did not yield any heterostructures neither, indicating mechanism I and II can only lead to efficient nanocrystal coupling if they act simultaneously. In this coupling process, 10-undecenoic acid is the coupling ligand for Si and Fe_2O_3 nanocrystals; toluene and ethanol serve as solvent and stabilizer for the resonance form of carboxylic acid which promotes room temperature hydrosilylation;[22] 1-octene can passivate the sites on Si nanocrystal surface where 10-undecenoic acid cannot reach because of steric repulsion, leading to a higher synthesis yield than that without 1-octene.

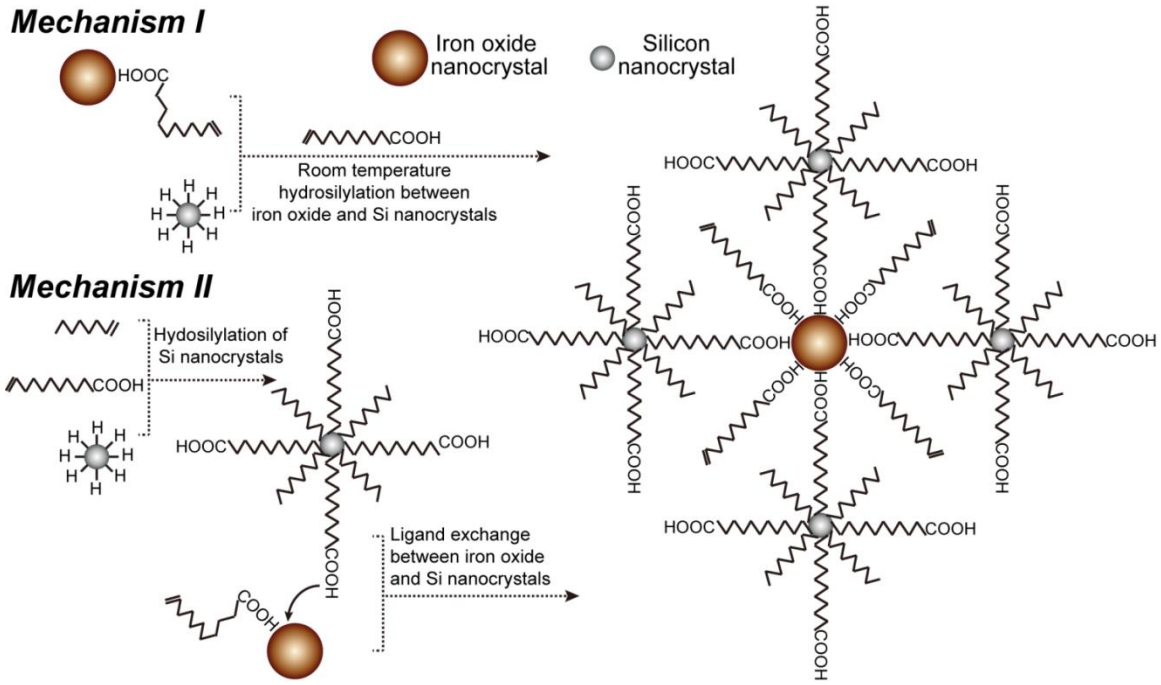

Figure 5.7: Proposed mechanisms for room temperature coupling between Si and Fe_2O_3 nanocrystals.

5.4 CONCLUSION

Fluorescent-magnetic heterostructures of Si quantum dots coupled to Fe_2O_3 nanocrystals were synthesized through room temperature coupling between Si and Fe_2O_3 nanocrystals by 10-undecenoic acid. The hydrophobic Fe_2O_3 nanocrystal appears in the center of heterostructure with hydrophilic Si nanocrystals exposed to the environment, providing dispersibilty in polar solvents like ethanol or water. The heterostructure show intense PL and magnetic response, and has hydrodynamic diameter within the optimum range for cell labeling. We propose two possible mechanisms for the heterostructure formation: I) direct hydrosilylation between 10-undecanoic acid on Fe_2O_3 nanocrystal

and hydride-terminated Si nanocrystal; and II) ligand exchange of 10-undecenoic acid-capped Si nanocrystal and10-undecenoic acid on Fe_2O_3 nanocrystal.

5.5 REFERENCES

(1) Vollath, D. Bifunctional Nanocomposites with Magnetic and Luminescence Properties. *Adv. Mater.* **2010**, *22*, 4410-4415.

(2) Corr, S. A.; Rakovich, Y. P.; Gun'ko, Y. K. Multifunctional Magnetic-fluorescent Nanocomposites for Biomedical Applications. *Nanoscale Rev. Lett.* **2008**, *3*, 87-104.

(3) Wang, L.; Yang, Z.; Zhang, Y.; Wang, L. Bifunctional Nanoparticles with Magnetization and Luminescence. *J. Phys. Chem. C* **2009**, *113*, 3955-3959.

(4) Wang, D.; He, J.; Rosenzweig, N.; Rosenzweig, Z. Superparamagnetic Fe2O3 Beads−CdSe ZnS Quantum Dots Core-Shell Nanocomposite Particlesfor Cell Separation. *Nano Lett.* **2004**, *4*, 409-413.

(5) Howes, P.; Green, M.; Bowers, A.; Parker, D.; Varma, G.; Kallumadil, M.; Hughes, M.; Warley, A.; Brain, A.; Botnar, R. Magnetic Conjugated Polymer Nanoparticles as Bimodal Imaging Agents. *J. Am. Chem. Soc.* **2010**, *132*, 9833-9842.

(6) Sailor, M. J.; Park, J.-H. Adv. Mater., Hybrid Nanoparticles for Detection and Treatment. *2012*, **24**, 3779-3802.

(7) Lu, C.-W.; Hung, Y.; Hsiao, J.-K.; Yao, M.; Chung, T.-H.; Yang, Y.-S.; Huang, D.-M.; Chen, Y.-C. BifunctionalMagnetic Silica Nanoparticles for Highly Efficient Human Stem Cell Labelling. *Nano Lett.* **2007**, *7*, 149-154.

(8) Liu, J.; Zhang, Y.; Yan, C.; Wang, C.; Xu, R.; Gu, N. Synthesis of MagneticLuminescent Alginate-Templated Composite Microparticles with Temperature-Dependent Photoluminescence under High-Frequency Magnetic Field. *Langmuir* **2010**, *26*, 19066-19072.

(9) Hu, H.; Zheng, R.; Zhang, X.; Xu, B. Facile One-Pot Synthesis of Bifunctional Heterodimers of Nanoparticles A Conjugate of Quantum Dot and Magnetic Nanoparticles. *J. Am. Chem. Soc.* **2004**, *126*, 5664-5665.

(10) Ang, C. Y.; Giam, L.; Chan, Z. M.; Lin, A. W. H.; Devlin, H. Gu, E.; Papaefthymiou, G. C.; Selvan, S. T.; Ying, J. Y. Facile Synthesis of Fe2O3 Nanocrystals without Fe(CO)5 Precursor and One-Pot Synthesis of Highly Fluorescent Fe2O3–CdSe Nanocomposites. *Adv. Mater.* **2009**, *21*, 869-873.

(11) Insin, N.; Tracy, J. B.; Lee, H.; Zimmer, J. P.; Weatervelt, R. M.; Bawendi, M. G. Incorporation of Iron Oxide Nanoparticles and Quantum Dots into Silica Microspheres. *ACS Nano* **2008**, *2*, 197-202.

(12) Park, J.-H.; von Maltzahn, G.; Ruoslahti, E.; Bhatia, S. N.; Sailor, M. J. Micellar Hybrid Nanoparticles for Simultaneous Magnetofluorescent Imaging and Drug Delivery. *Angew. Chem. Int. Ed.* **2008**, *47*, 7284-7288.

(13) Thakur, D.; Deng, S.; Baldet, T.; O Winter, pH Sensitive CdS-Iron Oxide Fluorescent-Magnetic Nanocomposites. *Nanotechnol.* **2009**, *20*, 485601.
(14) Selvan, S. T.; Patra, P. K.; Ang, C. Y.; Ying, J. Y. Synthesis of Silica-Coated Semiconductor and Magnetic Quantum Dots and Their Use in the Imaging of Live Cells. *Angew. Chem. Int. Ed.* **2007**, *46*, 2448-2452.
(15) Kwon, K.-W.; Shim, M. γ -Fe2O3II-VI Sulfide Nanocrystal Heterojunctions. *J. Am. Chem. Soc.* **2005**, *127*, 10269-10275.
(16) Wang, B.; Hai, J.; Wang, Q.; Li, T.; Yang, Z. Coupling of Luminescent Terbium Complexes to Fe3O4 Nanoparticles for Imaging Applications. *Angew. Chem. Int. Ed.* **2011**, *50*, 3063-3066.
(17) Xu, H.; Cheng, L.; Wang, C.; Ma, X.; Li, Y.; Liu, Z. Polymer encapsulated upconversion nanoparticleiron oxide nanocomposites for multimodal imaging and magnetic targeted drug delivery. *Biomater*. **2011**, *32*, 9364-9373.
(18) Guo, L.; Park, J.-H.; Duong, K. H.; Ruoslahti, E.; Sailor, M. J. Magnetic Luminescent Porous Silicon Microparticles for Localized Delivery of Molecular Drug Payloads. *Small* **2010**, *6*, 2546-2552.
(19) Park, J.-H.; Gu, L.; von Maltzahn, G.; Ruoslahti, E.; Bhatia, S. N.; Sailor, M. J. Biodegradable luminescent porous silicon nanoparticles for in vivo applications *Nat. Mater.* **2009**, *8*, 331-336.
(20) Hessel, C. M.; Rasch, M. R.; Hueso, J. L.; Goodfellow, B. W.; Akhavan, V. A.; Puvanakrishnan, P.; Tunnel, J. W.; Korgel, B. A. Alkyl Passivation and Amphiphilic Polymer Coating of Silicon Nanocrystals for Diagnostic Imaging. *Small* **2010**, *6*, 2026-2034.
(21) Hessel, C. M.; Reid, D.; Panthani, M. G.; Rasch, M. R.; Goodfellow, B. W.; Wei, J.; Fujii, H.; Akhavan, V.; Korgel, B. A. Synthesis of Ligand-Stabilized Silicon Nanocrystals with Size-Dependent Photoluminescence Spanning Visible to Near-Infrared Wavelengths. *Chem. Mater.* **2012**, *24*, 393-401.
(22) Yu, Y.; Hessel, C. M.; Bogart, T. D.; Panthani, M. G.; Rasch, M. R.; Korgel, B. A. Room Temperature Hydrosilylation of Silicon Nanocrystals with Bifucntional Terminal Alkenes. *Langmuir* **2013**, *29*, 1533-1540.
(23) (a) Erogbogbo, F.; Yong, K.-T.; Hu, R.; Law, W.-C.; Ding, H.; Chang, C.-W.; Prasad, P. N.; Swihart, M. T. Biocompatible Magnetofluorescent Probes Luminescent Silicon Quantum Dots Couple with Superparamagnetic Iron III Oxide. *ACS Nano* **2010**, *4*, 5131-5138. (b) Sato, K.; Yokosuka, S.; Takigami, Y.; Hirakuri, K.; Fujioka, K.; Manome, Y.; Sukegawa, H.; Iwai, H.; Fukata, N. Size-Tunable Silicon/Iron Oxide Hybrid Nanoparticles with Fluorescence, Superparamagnetism, and Biocompatibility. *J. Am. Chem. Soc.* **2011**, *133*, 18626-18633. (c) Tu, C.; Ma, X.; Pantazis, P.; Kauzlarich, S. M.; Louie, A. Y. Paramagnetic, Silicon Quantum Dots for Magnetic Resonance and Two-Photon Imaging of Macrophages. *J. Am. Chem. Soc.* **2010**, *132*, 2016-2023. (d) Zhang, X.; Brynda, M.; Britt, R. D.; Carroll, E. C.; Larsen, D. S.; Louie, A. Y.; Kauzlarich, S. M. Synthesis and Characterization of Manganese-Doped Silicon

Nanoparticles: Bifunctional Paramagnetic-Optical Nanomaterial. *J. Am. Chem. Soc.* **2007**, *129*, 10668-10669.
(24) Buriak, J. M. Organometallic Chemistry on Silicon and Germanium Surfaces. *Chem. Rev.* **2002**, *102*, 1271-1308.
(25) Jiang, W.; Kim, B. Y. S.; Rutka, J. T.; Chan, W. C. W. Nanoparticles-Mediated Cellular Response is Size-Dependent. *Nat. Nanotechnol.* **2008**, *3*, 145-150.
(26) Choi, H. S.; Liu, W.; Misra, P.; Tanaka, E.; Zimmer, J. P.; Ipe, B. I.; Bawendi, M. G. J. V Frangioni, Renal Clearance of Quantum Dots. *Nat. Biotechnol.* **2007**, *25*, 1165-1170.
(27) Hessel, C. M.; Henderson; E. J.; Veinot, J. G.C. Hydrogen Silsesquioxane: A Molecular Precursor for Nanocrystalline Si-SiO2 Composites and Freestanding Hydride-Surface-Terminated Silicon Nanoparticles. *Chem. Mater.* **2006**, *18*, 6139-6146.
(28) Smith, D. K.; Goodfellow, B. W.; Smilgies, D.-M.; Korgel B. A. Self-Assembled Simple Hexagonal AB_2 Binary Nanocrystal Superlattices: SEM, GISAXS, and Defects. *J. Am. Chem. Soc.* **2009**, *131*, 3281-3290.
(29) Rasch, M. R.; Yu, Y.; Bosocy, C.; Goodfellow, B. W.; Korgel, B. A. Chloroform-Enhanced Incorporation of Hydrophobic Gold Nanocrystals into Dioleoylphosphatidylcholine (DOPC) Vesicle Membranes. *Langmuir* **2012**, *28*, 12971-12981.
(30) Cherepy, N. J.; Liston, D. B.; Lovejoy, J. A.; Mei, H.; Zhang, J. Z. Ultrafast Studies of Photoexcited Electron Dynamics in γ- and α-Fe_2O_3 semiconductor Nanoparticles. *J. Phys. Chem. B* **1998**, *102*, 770-776.
(31) Sherman, D. M.; Waite, T. D. Electroic Spectra of Fe^{3+} Oxides and Oxide Hydroxides in the Near IR to Near UV. *Am. Mineral*, **1985**, *70*, 1262-1269.
(32) Polito, L.; Colombo, M.; Monti, D.; Melato, S.; Caneva, E.; Prosperi, D. Resolving the Structure of Ligands Bound to the Surface of Superparamagnetic Iron Oxide Nanoparticles by High-Resolution Magic-Angle Spinning NMR Spectroscopy. *J. Am. Chem. Soc.* **2008**, *130*, 12712-12724.

Chapter 6: Synthesis and Ligand Exchange of Thiol-Capped Silicon Nanocrystals

6.1 INTRODUCTION

Silicon (Si) is an extraordinarily useful semiconductor, employed in a wide variety of commercial applications, including transistors, optical detectors and solar cells; yet, it is a very poor light-emitter.[1] By creating *quantum dots*, Si can be made to emit light efficiently with color that can be tuned with size from near infrared to visible wavelengths.[2-5] These optical properties make Si quantum dots an earth-abundant alternative to toxic cadmium (Cd) and lead (Pb)-containing nanocrystal light emitters.[6,7] Si is also biodegradable,[7] and offers other unique electronic and thermoelectric properties,[8] that are potentially useful for a range of applications such as imaging contrast agents,[6,7,9,10] sensors,[7] light-emitting diodes,[11,12] photovoltaic devices,[13-15] thin film transistors,[16,17] and optical displays[18] to name a few.[2,19]

Colloidal quantum dots are stabilized using molecular (typically organic) capping ligands to prevent oxidation and corrosion, provide dispersibility in solvents, and prevent aggregation.[20,21] So far, the most common and effective approach to capping Si nanocrystals involves the addition of alkenes by hydrosilylation.[3,10,22-30] This provides good stabilization of the luminescence, even in the presence of air, but the hydrocarbon ligands are covalently and irreversibly bonded to the Si surface, which makes synthesis by arrested precipitation from Si reactants impossible in the presence of alkenes and prevents further manipulations, as in the deposition of an inorganic shell or an exchange of capping ligands. In this context, amines have shown some promise as a labile ligand

for Si; for example, dodecylamine has been applied as a capping ligand for Si nanorod synthesis aided with tin and gold seed particles.[30-33] However, amines have been shown to significantly influence the optical properties of Si nanocrystals.[34-36]

Here, we show that alkanethiols can be used as capping ligands for Si nanocrystals and allow for ligand exchange with alkenes. Alkanethiols have been used extensively as capping ligands on many other types of nanocrystals, but not Si.[37-46] We find that thiol-capped Si nanocrystals exhibit size, crystallinity and PL properties similar to those of the alkene-passivated Si nanocrystals, but are very susceptible to hydrolysis and degradation in the presence of moisture. Dodecanethiol could also be exchanged with alkenes by a subsequent thermally-promoted hydrosilylation reaction.

6.2 EXPERIMENTAL DETAILS

6.2.1 Materials

FOx-16 was purchased from Dow Corning. 1-Dodecanethiol ($CH_3(CH_2)_{11}SH$>98%), anhydrous toluene (C_7H_8), anhydrous ethanol (C_2H_5OH), and anhydrous methanol (CH_3OH) were purchased from Sigma-Aldrich. Ethanol, chloroform, and hydrochloric acid (HCl, 37.5%) were obtained from Fisher Scientific. Hydrofluoric acid (HF, 48%) was obtained from EMD Chemical. Deionized (DI) water was obtained using a Barnstead Nanopure Filtration System (17 MΩ resistance).

6.2.2 Si Nanocrystal Synthesis

Hydride-terminated Si nanocrystals were synthesized using published procedures.[3,47] In a typical synthesis, 30 mL of FOx-16 is evaporated under vacuum in a Schlenk line to form a white residue of hydrogen silsesquioxane (HSQ). This is heated under forming gas (93% N_2 gas and 7% H_2 gas) flow at 1100-1250^{o}C for 1 hour. Diameters of about 2.5 nm, 5 nm, and 8 nm, are obtained by heating at 1100^{o}C, 1200^{o}C, and 1250^{o}C, respectively. The reaction product is ground with agate mortar and pestle for 30 min and then shaken in a wrist-action shaker for 9 hours with 3 mm borosilicate glass beads to create a fine, brown powder. This powder is etched with 48% HF and 37.5% HCl (10:1 v/v) in the dark for 4-6 hours. Hydride-terminated Si nanocrystals are isolated from the HF etching solution by centrifugation at 8000 rpm for 5 min, followed by rinses with ethanol (twice) and chloroform. The nanocrystals are dispersed in 1-dodecanethiol (~1 mL per 1 mg nanocrystals). Then, in a three-neck flask on a Schlenk line, the dispersion is put through three freeze-pump-thaw cycles and heated to 190^{o}C with N_2 gas flow for 12 hr. The initially turbid dispersion gradually becomes optically clear. The reaction is cooled, the flask is sealed and moved into a nitrogen-filled glove box. The nanocrystal dispersion is centrifuged at 8000 rpm for 5 min and the supernatant is collected. The nanocrystals are then precipitated with anhydrous ethanol and centrifugation. The precipitate is collected and redispersed with anhydrous toluene. This washing procedure is carried out two more times. The yield of thiol-passivated Si nanocrystals depends on the nanocrystal size, with yields of nearly 100%, 80%, and 20% for nanocrystals with diameters of 2.5 nm, 5.0 nm and 8.0 nm, respectively.

6.2.3 Materials Characterization

Photoluminescence (PL) spectra were acquired on a Fluorolog-3 spectrophotometer (Horiba Jobin Yvon) with an InGaAs photomultiplier tube for visible detection and a Hamamatsu H10330-45 detector for near infrared (NIR) detection. PL spectra were obtained from Si nanocrystals dispersed in anhydrous toluene in 10 mm path length quartz cuvettes. Time-resolved PL derived from time correlated single photon counting (TCSPC) were collected by exciting the sample in a 1 mm cuvette using a 35-ps pulse-width, 405 nm diode laser operated between 1 kHz and 40 MHz. PL was focused into a fiber optic running to a 300 mm grating spectrograph using a quartz lens. Time-resolved dynamics were obtained using single-photon sensitive avalanche photodiode and time-to-amplitude converter. The TCSPC data were fit to a bi-exponential decay:

$$\mathrm{I} = A_1 e^{-\frac{t}{\Gamma_1}} + A_2 e^{-\frac{t}{\Gamma_2}} \quad . \tag{1}$$

In Eqn (1), $A_1 + A_2 = 1$, and the average PL lifetime was calculated as

$$\Gamma = A_1\Gamma_1 + A_2\Gamma_2 \quad . \tag{2}$$

Transmission electron microscopy (TEM) images were acquired digitally using a FEI Tecnai Biotwin TEM operated at 80 kV accelerating voltage or a JEOL 2010F TEM operated at 200 kV. Nanocrystal samples were prepared by drop casting toluene dispersions onto a 200 mesh carbon-coated copper grids (Electron Microscopy Science). Some TEM images were obtained on graphene supports using previously described methods.[48]

X-ray diffraction (XRD) data were obtained on a Rigaku R-Axis Spider Diffractometer with a two-dimensional (2D) image plate detector, a graphite monochromator, and Cu Kα radiation (λ=0.15418 nm). XRD samples were prepared by drying the nanocrystals on a glass slide and transferring them to a nylon loop with a needle. Mineral oil was applied to secure the sample as needed. Diffraction data were collected for 60 min while rotating the sample stage at 10^{o} min^{-1}. The 2D diffraction data were radially integrated with 2DP Spider software (version 1.0, Rigaku Americas Corp.)

Attenuated total reflectance Fourier transform infrared (ATR-FTIR) spectra were obtained on a Thermo Mattson Infinity Gold FTIR spectrometer with a Spectra-Tech Thermal ARK attenuated total reflectance module. The sample and detector chambers were purged with N_2 for 30 minutes to eliminate CO_2 background signal. Nanocrystals dispersed in anhydrous toluene with concentration of ~5 mg/ml were drop cast onto the crystal plate of the ARK module and dried in N_2 gas flow. Both measurements and background scans were made by acquiring 512 scans at a resolution of 4 cm^{-1}. The average transmittance is reported with background subtracted.

X-ray photoelectron spectroscopy (XPS) was measured with a Kratos Axis Ultra XPS, utilizing monochromatic Al K_α X-rays ($h\nu$ = 1486.5 eV) at 150 W (10 mA and 15 kV), hybrid optics (employing a magnetic and electrostatic lens simultaneously), and a multi-channel plate coupled to a hemispherical photoelectron kinetic analyzer. The instrument work function is calibrated to give a binding energy (BE) of 368.3 eV for the Ag $3d_{5/2}$ line for metallic silver. Spectra were charge-corrected to the main line of the

carbon 1s spectrum of Super P carbon (graphite-like carbon) set to 284.5 eV. High resolution XPS spectra were collected with a pass energy of 20 eV, at a 0.1 eV step. The base pressure in the analysis chamber was initially ~$2x10^{-9}$ Torr, but increased to ~$4x10^{-8}$ Torr due to outgassing of the samples. Casa XPS analysis software (Version 2.3.16 PR 1.6) was used for peak deconvolution, by applying a Shirley background and line-shapes with a Gaussian (70%) and Lorentzian (30%) combination.[22] Samples were removed from an N_2-filled glove box (~ 5 ppm of molecular oxygen) and immediately transferred to the ultra-high vacuum XPS chamber using an interface/capsule set-up. This set-up was designed and built at the Surface Analysis Laboratory of the Texas Materials Institute at UT Austin to directly couple to the XPS chamber, allowing samples to only expose to environment free of O_2 and moisture.

6.3 RESULTS AND DISCUSSION

6.3.1 Size, Crytsallinity and Optical Properties

The HSQ decomposition route used here to produce Si nanocrystals yields relatively uniform hydride-capped quantum dots with diamond cubic Si crystal structure and controlled size.[3,29] The hydride-terminated surfaces provide an effective model system to study Si capping ligand chemistry—in this case, the thermally-promoted thiolation illustrated in Figure 1a. Since the size of the nanocrystals can affect Si surface reactivity,[22,49] three different average diameters were studied: 2.5, 5.0 and 8.0 nm. As the photographs in Figure 1b show, dispersions of hydride-terminated Si nanocrystals in dodecanethiol are very turbid and then become optically clear as the alkanethiol capping

ligand layer forms on the nanocrystals. Figure 6.2 shows TEM images of the nanocrystals after thiol capping, which are well-dispersed and not aggregated. The dodecanethiol-capped nanocrystals are brightly luminescent when kept in an inert environment, with size-dependent PL emission peak maxima. Figure 1c shows the PL emission spectra: the 2.5 nm nanocrystals emit at 720 nm (1.72 eV) and the 8.0 nm nanocrystals emit at 1010 nm (1.22 eV). These values are shifted to higher energy from the bulk band gap of Si of 1.1 eV as a result of quantum confinement. The PL lifetimes determined from TCSPC measurements (see Figure 1d) were also size-dependent—26.4 μs, 81.8 μs, and 282.6 μs, for diameters of 2.5, 5.0 and 8.0 nm, respectively—and similar to those of alkene-capped Si nanocrystals,[5,26] porous silicon,[50] and theoretical calculations.[51]

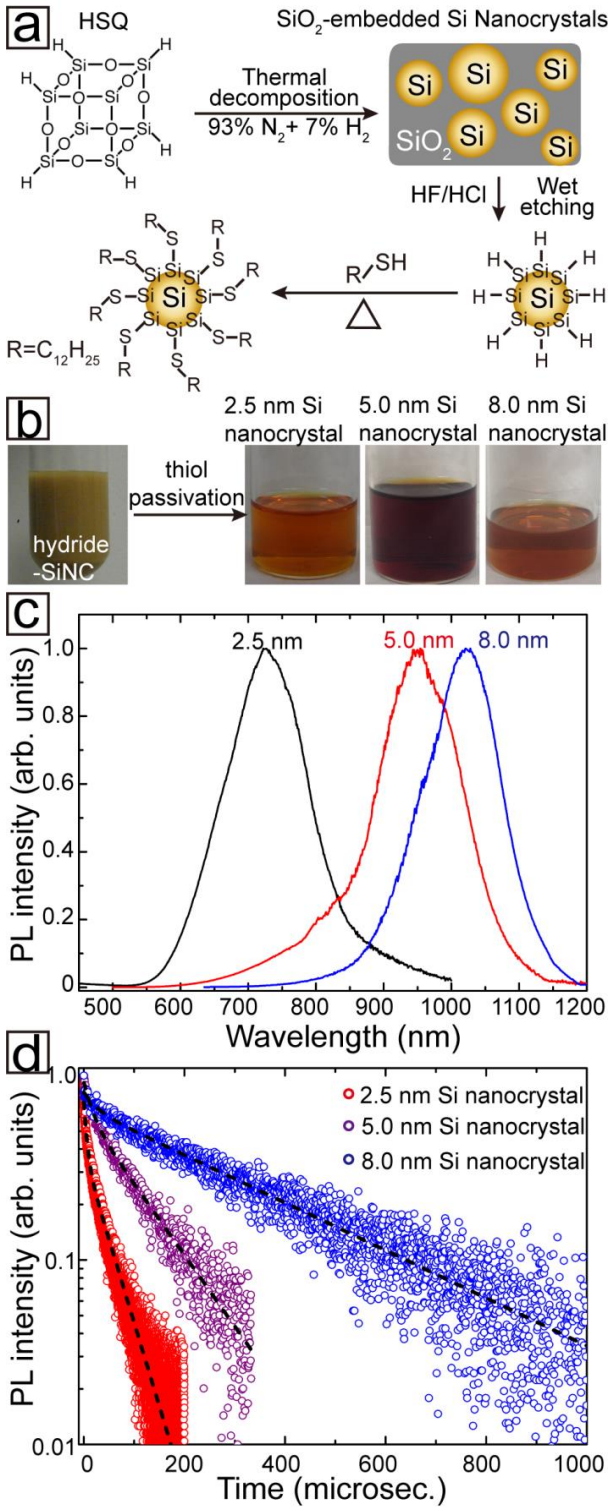
a
HSQ
SiO2-embedded Si Nanocrystals
Thermal decomposition
93% N2+ 7% H2
Si
SiO2
HF/HCl
Wet etching
R/SH
R=C12H25
b
2.5 nm Si nanocrystal
5.0 nm Si nanocrystal
8.0 nm Si nanocrystal
thiol passivation
hydride -SiNC
c
2.5 nm
5.0 nm
8.0 nm
PL intensity (arb. units)
Wavelength (nm)
d
2.5 nm Si nanocrystal
5.0 nm Si nanocrystal
8.0 nm Si nanocrystal
PL intensity (arb. units)
Time (microsec.)

Figure 6.1

Figure 6.1: (a) Schematic description of the synthesis of dodecanethiol-capped Si nanocrystals. (b) Photographs of Si nanocrystal dispersions. The hydride-terminated Si nanocrystals from a turbid dispersion when initially added to 1-dodecanethiol and then form optically clear dispersions after thiolation has occurred. The dodecanethiol-capped Si nanocrystals have been isolated and redispersed in anhydrous toluene. (c) PL emission spectra of 2.5 nm, 5.0 nm, and 8.0 nm diameter dodecanethiol-capped Si nanocrystals photoexcited at 350, 400, and 420 nm, respectively. The PL intensities of the three samples are normalized in the plot. The PL quantum yield of the 2.5 nm nanocrystals was 12%. (d) Time correlated single photon counting (TCSPC) spectra of 2.5 nm, 5.0 nm, and 8.0 nm diameter dodecanethiol-capped Si nanocrystals dispersed in anhydrous toluene, which can be fitted with bi-exponential decay using Eqn (1), showing average PL life time of 26.4, 81.8, and 282.6 μs for of 2.5 nm, 5.0 nm, and 8.0 nm diameter dodecanethiol-capped Si nanocrystals, respectively.

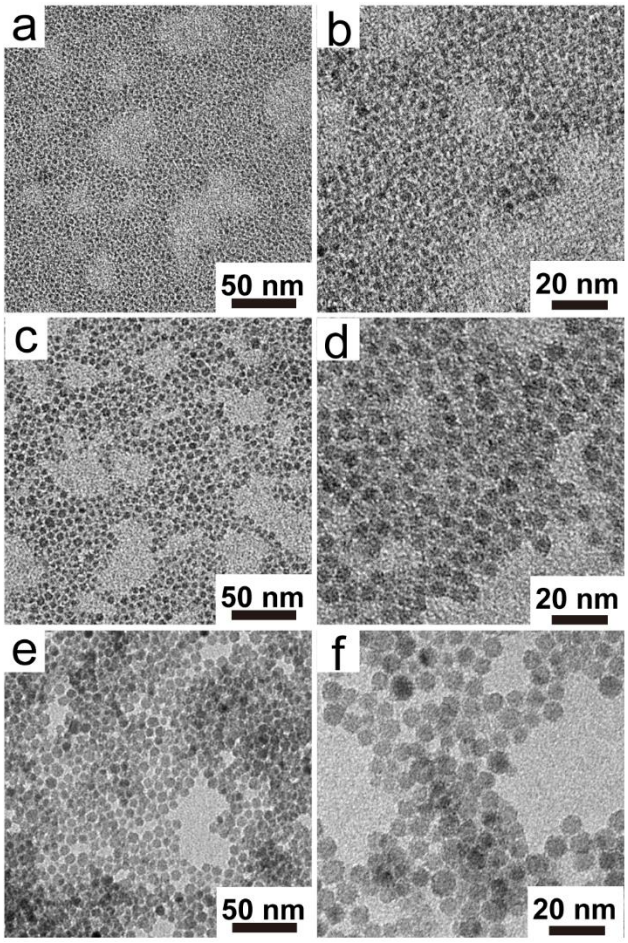

Figure 6.2: TEM images of dodecanethiol-capped Si nanocrystals with average diameters of (a), (b) 2.5 nm; (c), (d) 5.0 nm; (e), (f) 8.0 nm.

The dodecanethiol-capped nanocrystals retain the diamond cubic crystal structure of the starting material, confirmed by XRD (Figure 6.3) and TEM (Figure 6.4). Each diffraction pattern in Figure 6.3 indexes to the diamond cubic crystal structure of Si. The observed crystalline lattice spacings in the TEM images in Figure 6.4 are also consistent with diamond cubic Si. Furthermore, the XRD peak widths in Figure 6.3 are consistent with the average particle diameters determined from the TEM images.

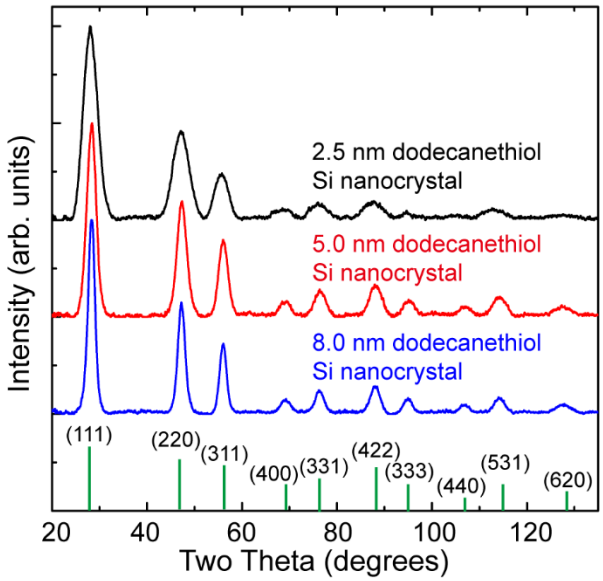

Figure 6.3: XRD data for dodecanethiol-capped Si nanocrystals. The average diameter of each sample is indicated and a reference pattern is provided for diamond cubic Si (PDF # 027–1402, a=b=c=5.43088 Å). All diffraction peaks are accounted for by indexing the pattern to diamond cubic Si. The average nanocrystal diameters determined from the XRD peaks by Debye-Scherrer analysis are 2.3, 4.6, and 7.5 nm, which are close to those determined by TEM (2.5, 5.0, and 8.0 nm).

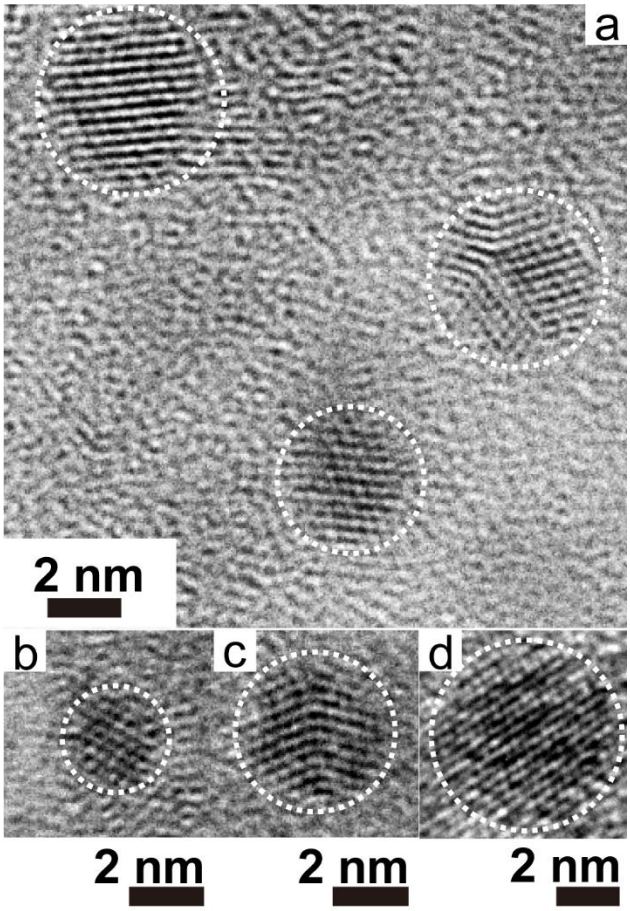

Figure 6.4: TEM images of dodecanethiol-capped Si nanocrystals from the samples with average diameters of (a) 5.0 nm, (b) 2.5 nm, (c) 5.0 nm, and (d) 8.0 nm.

6.3.2 Capping Ligand Characterization and Stability

ATR-FTIR spectra and XPS were used to verify the bonding of dodecanethiol to the Si nanocrystals. Figure 6.5 shows a comparison of ATR-FTIR spectra for 1-dodecanethiol and dodecanethiol-capped Si nanocrystals. The 1-dodecanethiol spectrum exhibits CH_3 stretching vibrations (asymmetric stretch at 2955 cm^{-1} and symmetric stretch at2946-2879 cm^{-1}), CH_2 stretching vibrations (symmetric stretch at2946-2879 cm^{-1} and symmetric stretch at 2850 cm^{-1}), C-H deformation vibrations

between 1450 and 1250 cm^{-1}, C-S stretching vibration at 715 cm^{-1}, and a weak but detectable (See Figure 6.5b) S-H stretching vibration at 2575 cm^{-1}.[52] The dodecanethiol-capped Si nanocrystals exhibit C-H (both CH_3 and CH_2) and C-S vibrations similar to the 1-dodecanethiol spectra, with additional Si-H stretching vibrations between 2290 and 2240 cm^{-1}, Si-O stretching vibration at ~1100 cm^{-1}, and Si-H deformation vibration at 875 cm^{-1}.[52,53] The observation of Si-H in the spectra indicates that not all Si surface atoms can be passivated by the capping ligands as a result of steric hindrance in the ligand layer, which is also typical of Si nanocrystals after alkene passivation.[10,22] The absence of the S-H stretch in the nanocrystal spectra is consistent with attachment of dodecanethiol to the Si nanocrystal surface by S-H bond cleavage.[54]

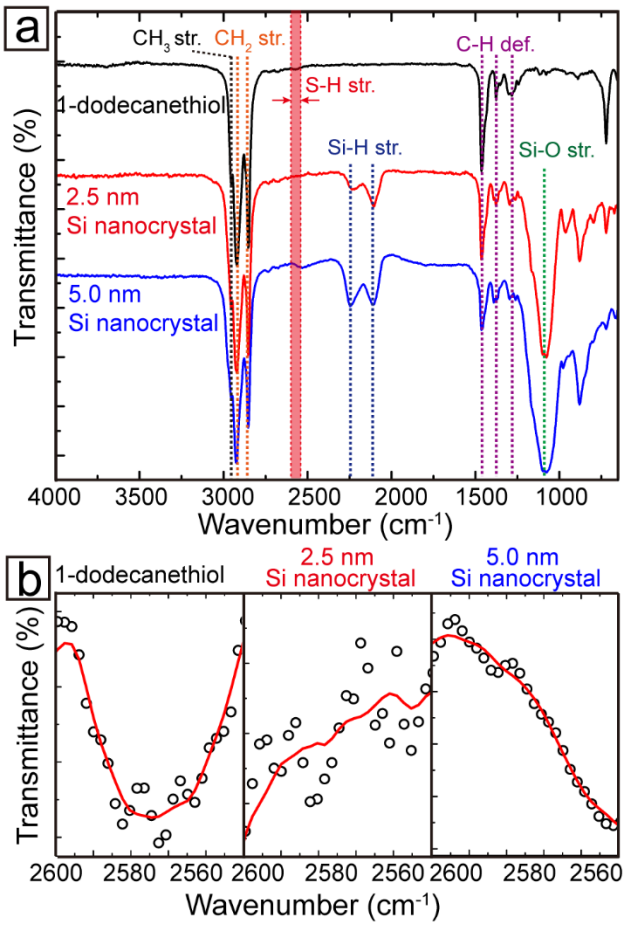

Figure 6.5: (a) ATR-FTIR spectra of 1-dodecanthiol compared to dodecanethiol-capped Si nanocrystals with average diameters of 2.5 nm and 5.0 nm; (b) shows the ATR-FTIR spectral region between 2600 and 2550 cm^{-1} characteristic of the S-H stretch.

XPS data also indicate that Si-S bonding occurs between the dodecanethiol capping ligands and the Si surface through the formation of an Si-S bond. Figure 6.6 shows the XPS signal from the sulfur (S) 2p spectral region for the dodecanethiol-capped Si nanocrystals. The S $2p_{1/2}$ and S $2p_{3/2}$ doublet is present, yet shifted from the free thiol value of 165 eV[55,56] for the S $2p_{1/2}$ peak to 163.8 eV for the 2.5 nm nanocrystals and 163.3 eV for the 5.0 nm nanocrystals. This size-dependent peak shift is also seen in

thiolate-protected gold nanocrystals and has been attributed to the negative charge-bearing sulfur atoms attached to the nanocrystal surface.[57,58]

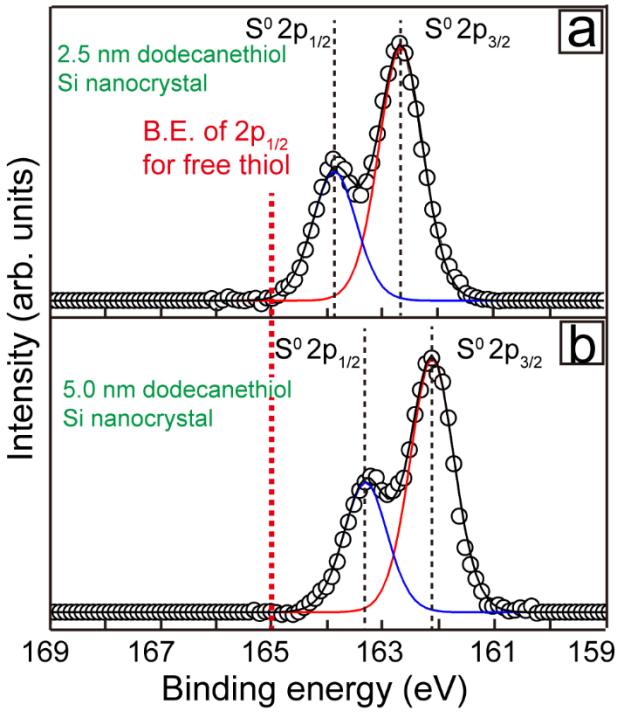

Figure 6.6: XPS S 2p spectra for 2.5 and 5 nm diameter dodecanethiol-capped Si nanocrystals. The S $2p_{1/2}$ and S $2p_{3/2}$ doublet is fitted using a 1:2 peak area ratio with same full width at half maximum (FWHM) and 1.2 eV splitting.[56]

Figure 6.7 shows the Si 2p XPS signal from the nanocrystals. The doublet expected from zero valent Si at (Si^0 $2p_{1/2}$) 99.3 eV and (Si^0 $2p_{3/2}$) 99.8 eV is present, which further confirms that the thiolated nanocrystals are composed of zero-valent Si and have not been significantly oxidized or degraded during the thiolation procedure. We assign the significant peak at 101.9 eV to the Si-S bond between the capping ligands and the Si surface, following reports of the Si 2p binding energy of Si(100) with S adatoms.[59] As with alkene-treated Si nanocrystals, there is also some evidence of residual surface oxidation, with small yet measurable contributions from various Si^{1+} (100.4 eV), Si^{2+}

(101.5 eV), Si^{3+} (102.6 eV), and Si^{4+} (103.7 eV) species.[22] Figures 6.7b and 6.7c show XPS data acquired after exposing the nanocrystals to air. The Si-S feature in the Si 2p region drops in intensity and completely disappears after drying in air. The signal in the S 2p region is also lost and Si^{3+} and Si^{4+} signals increase significantly as a result of surface oxidation in the absence of capping ligand protection. The instability of the thiolate capping ligand layer in the presence of air is similar to that of SiS_x compounds.[60,61]

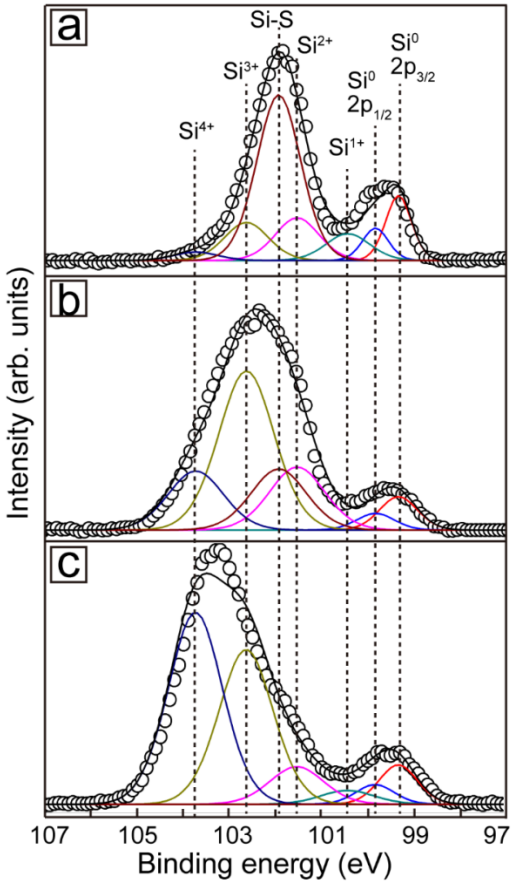

Figure 6.7: XPS Si 2p spectra for dodecanethiol-capped Si nanocrystals with 2.5 nm diameter (a) immediately after preparation, (b) after exposure to air for 4 days, and (c) after being dried in air for 5 hr, showing various amounts of surface oxidation.

Exposing the dodecanethiol-capped Si nanocrystals to air also decreased the luminescence of the material. Figure 6.8 shows PL spectra of 2.5 nm diameter dodecanethiol-capped Si nanocrystals after exposure to air for 5 days and after exposure to trace water by the addition of a single drop of ethanol containing <0.2% (wt%) of water to a toluene dispersion. Five days of air exposure decreased the quantum yield by more than 50% and shifted the peak emission to slightly shorter wavelength—both indicative of surface oxidation.[62] The addition of trace water to the nanocrystals had an even more dramatic effect on the nanocrystals as it immediately quenched the PL of the sample. A video of this observation along with a comparison to alkene-passivated Si nanocrystals has also been recorded. The Si-S bonded capping ligands are highly susceptible to hydrolysis. Thiol capping of Si is quite different than germanium, whereas dodecanethiol-passivated Ge nanowires are very stable, even when submerged in boiling water.[63]

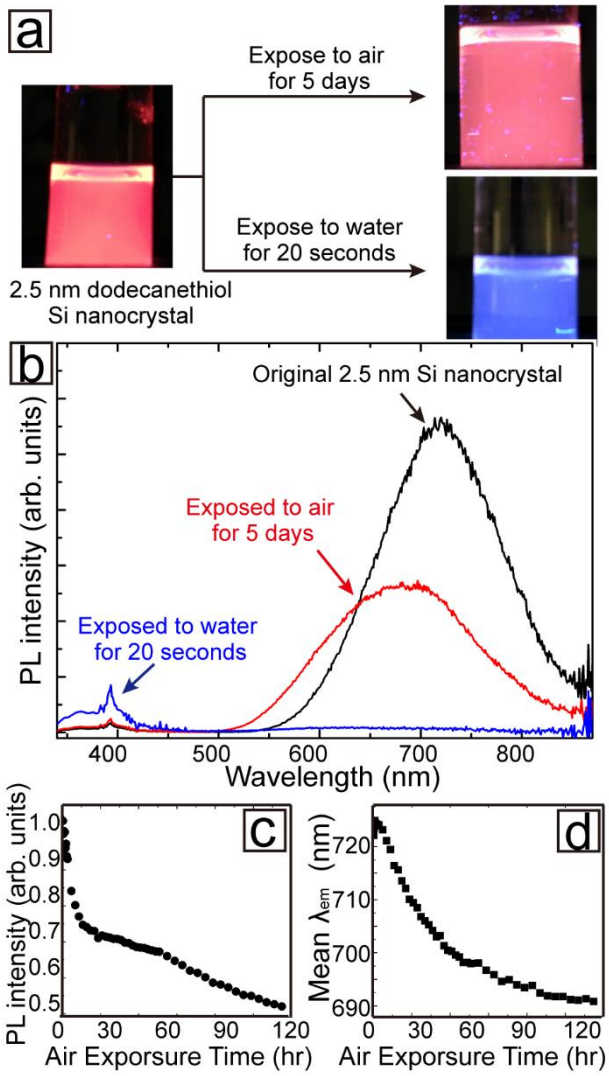

Figure 6.8: (a) Photographs of 2.5 nm dodecanethiol-capped Si nanocrystals dispersed in anhydrous toluene under 365 nm UV light before and after exposure to air for 5 days, and after exposure to trace amount of water for 20 s. (b) PL emission spectra (λ_{exc}=320 nm) of 2.5 nm dodecanethiol-capped Si nanocrystals dispersed in anhydrous toluene before (black curve) and after exposure to air for 5 days (red curve), and water for 20 s (blue curve). (c) The integrated PL intensity measured for 2.5 nm dodecanethiol-capped Si nanocrystals exposed to air. The PL quantum yield drops by 50% drop in 5 days. (d) Plot of average PL emission wavelength of 2.5 nm dodecanethiol-capped Si nanocrystal against the time that sample expose to air, showing 35 nm blue shift in 5 days.

Dodecanethiol capping ligands could also be exchanged with alkenes by heating 1-dodecene at 190°C under nitrogen. The ligand-exchanged nanocrystals remain luminescent when exposed to water and do not undergo hydrolysis. The S 2p XPS signal is also lost after alkene repassivation (See Figures 6.9a and 6.9b). The reverse capping ligand exchange reaction of replacing alkenes with thiols does not occur. For instance, heating dodecene-capped Si nanocrystal in 1-dodecanethiol does not lead to a reappearance of the S 2p XPS signal (Figures 6.9c and 6.9d).

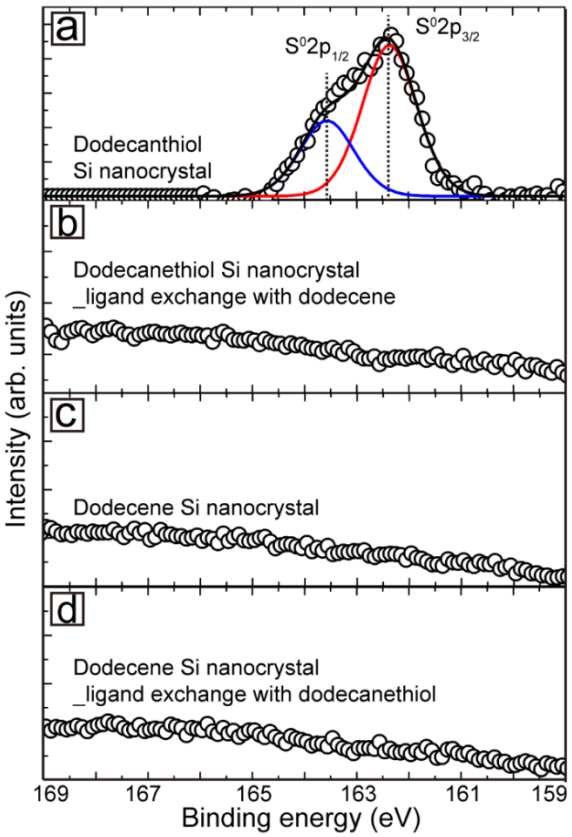

Figure 6.9: XPS S 2p signal of (a) dodecanethiol-capped Si nanocrystal, (b) and same sample heated in 1-dodecene, showing successful ligand exchange from dodecanethiol to dodecene. XPS S 2p signal of (c) dodecene-capped Si nanocrystal, and (d) same sample heated in 1-dodecanethiol, showing no evidence of ligand exchange from dodecene to dodecanethiol.

6.3.3 Mechanism of Thermally-Induced Thiolation of Si Nanocrystals

Two alternative mechanisms, illustrated in Figure 6.10, are proposed two explain the passivation of Si nanocrystal surfaces by thermally-promoted thiolation. One pathway is similar to the thermally-initiated radical reaction for hydrosilylation, in which the Si-H bond on the Si nanocrystal surface is cleaved at elevated temperature to yield silyl radicals and H atoms that react with the thiol to evolve H_2 gas and thiol radicals,[64,65] which finally react with silyl radicals to generate Si-S bonds. An alternative mechanism involves the oxidation of thiols (RSH) by residual O_2 to create disulfides (RS-SR), which are reduced and cleaved by silicon hydride (Si-H) on the surface of Si nanocrystal through the reaction: $\mathrm{RS-SR + Si-H \rightarrow RS-Si + RSH}$, similar to the reaction between disulfide and sodium borohydride[55] and sodium hydride.[66,67]

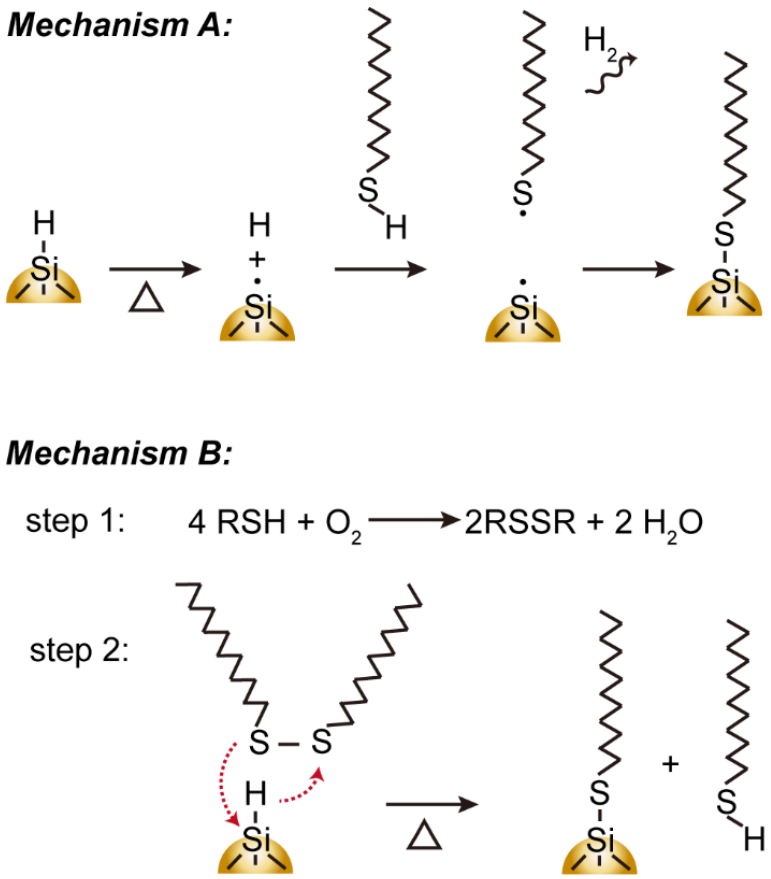

Figure 6.10: Proposed mechanisms for thermal-induced thiolation of hydride-terminated Si nanocrystals.

6.4 CONCLUSION

Dodecanethiol provides effective capping ligand passivation of Si nanocrystals, provided that water exposure is avoided. The Si-S bond is relatively stable to oxidation in the presence of dry air, and under inert conditions, the thiol-capped nanocrystals exhibit photoluminescence similar to alkene-passivated Si nanocrystals. FTIR and XPS confirmed that the alkanethiol ligands are covalently bonded to the Si nanocrystals. Although thiols do not provide the stability against oxidation that alkenes can provide, they offer a route to ligand exchange for Si nanocrystals.

6.5 REFERENCE

(1) Streetman, B.; Banerjee, S. Solid State Electronic Devices, 7th Edition, *Prentice Hall, USA,* **2015**.

(2) Mastronardi, M. L.; Henderson, E. J.; Puzzo, D. P.; Ozin, G. A. Small Silicon, Big Opportunities: The Development and Future of Colloidally-Stable Monodisperse Silicon nanocrystals. *Adv. Mater.* **2012**, *24*, 5890-5898.

(3) Hessel, C. M.; Reid, D.; Panthani, M .G.; Rasch, M. R.; Goodfellow, B. W.; Wei, J.; Fujii, H.; Akhavan, V.; Korgel, B. A. Synthesis of Ligand-Stabilized Silicon Nanocrystals with Size-Dependent Photoluminescence Spanning Visible to Near-Infrared Wavelengths. *Chem. Mater.* **2012**, *24*, 393-401.

(4) Brus, L. Luminescence of Silicon Materials: Chains, Sheets, Nanocrystals, Nanowires, Microcrystals, and Porous Silicon. *J. Phys. Chem.* **1994**, *98*, 3575-3581.

(5) Wilson, W. L.; Szajowski, P. F.; Brus, L. E. Quantum Confinement in Size-Selected, Surface-Oxidized Silicon Nanocrystals. *Science* **1993**, *262*, 1242-1244.

(6) Erogbogbo, F.; Yong, K.-T.; Roy, I.; Xu, G.; Prasad, P. N.; Swihart, M. T. Biocompatible Luminescent Silicon Quantum Dots for Imaging of Cancer Cells. *ACS Nano* **2008**, *2*, 873-878.

(7) Park, J.-H.; Gu, L.; Von Maltzahn, G.; Ruoslahti, E.; Bhatia, S. N.; Sailor, M. J. Biodegradable Luminescent Porous Silicon Nanoparticles for in vivo Applications. *Nature Mater.* **2009**, *8*, 331-336.

(8) Singh, V.; Yu, Y.; Sun, Q.-C.; Korgel, B. A.; Nagpal, P. Pseudo-Direct Bandgap Transitions in Silicon Nanocrystals: Effect on Optoelectronics and Thermoelectrics. *Nanoscale* **2014**, *6*, 14643-14647.

(9) Erogbogbo, F.; Yong, K.-T.; Hu, R.; Law, W.-C.; Ding, H.; Chang, C.-W.; Prasad, P. N.; Swihart, M. T. Biocompatible Magnetofluorescent Probes: Luminescent Silicon Quantum Dots Coupled with Superparamagnetic Iron (III) Oxide. *ACS Nano* **2010**, *4*, 5131-5138.

(10) Hessel, C. M.; Rasch, M. R.; Hueso, J. L.; Goodfellow, B. W.; Akhavan, V. A.; Puvanakrishnan, P.; Tunnel, J. W.; Korgel, B. A. Alkyl Passivation and Amphiphilic Polymer Coating of Silicon Nanocrystals for Diagnostic Imaging. *Small* **2010**, *6*, 2026-2034.

(11) Cheng, K.-Y.; Anthony, R.; Kortshagen, U. R.; Holmes, R. J. Hybrid Silicon Nanocrystal-Organic Light-Emitting Devices for Infrared Electroluminescence. *Nano Lett.* **2010**, *10*, 1154-1157.

(12) Puzzo, D. P.; Henderson, E. J.; Helander, M. G.; Wang, Z.; Ozin, G. A.; Lu, Z. Visible Colloidal Nanocrystal Silicon Light-Emitting Diode. *Nano Lett.* **2011**, *11*, 1585-1590.

(13) Jiang, C.-W.; Green, M. A. Silicon Quantum Dot Superlattices: Modeling of Energy Bands, Densities of States, and Mobilities for Silicon Tandem Solar Cell Applications. *J. Appl. Phys.* **2006**, *99*, 114902.

(14) Priolo, F.; Gregorkiewicz, T.; Galli, M.; Krauss, T. F. Silicon Nanostructure for Photonics and Photovoltaics. *Nature Nanotech.* **2014**, *9*, 19-32.

(15) Beard, M. C.; Knutsen, K. P.; Yu, P.; Luther, J. M.; Song, Q.; Metzger, W. K.; Ellingson, R. J.; Nozik, A. J. Multiple Exciton General in Colloidal Silicon Nanocrystals. *Nano Lett.* **2007**, *7*, 2506-2512.
(16) Guo, L.; Leobandung, E.; Chou, S. Y. A Silicon Single-Electron Transistor Memory Operating at Room Temperature. *Science* **1997**, *275*, 649-651.
(17) Pereira, R. N.; Niesar, S.; You, W. B.; da Cunha, a. F.; Erhard, N.; Stegner, A. R.; Wiggers, H.; Willinger, M.-G.; Stutzmann, M.; Brandt, M. S. Solution-Processed Networks of Silicon Nanocrystals: The Role of Internanocrystal Medium on Semiconducting Behavior. *J. Phys. Chem. C* **2011**, *115*, 20120-20127.
(18) Tu, C.-C.; Zhang, Q.; Lin, L. Y.; Cao, G. Brightly Photoluminescence Phosphor Materials Based on Silicon Quantum Dots with Oxide Shell Passivation. *Optics Express* **2012**, *20*, A69-A74.
(19) Pavesi, L; Turan, R., Eds. Silicon Nanocrystals: Fundamentals, Synthesis and Applications*, Wiley-VCH, Germany*, **2010**.
(20) Steigerwald, M. L.; Alivisatos, A. P.; Gibson, J. M.; Harris, T. D.; Kortan, R.; Muller, A. J.; Thayer, A. M.; Duncan, T. M.; Douglass, D. C.; Brus, L. E. Surface Derivatization and Isolation of Semiconductor Cluster Molecules. *J. Am. Chem. Soc.* **1988**, *110*, 3046-3050.
(21) Alivisatos, A. P. Semiconductor Clusters, Nanocrystals, and Quantum Dots. *Science* **1996**, *271*, 933-937.
(22) Yu, Y.; Hessel, C. M.; Bogart, T. D.; Panthani, M. G.; Rasch, M. R.; Korgel, B. A. Room Temperature Hydrosilylation of Silicon Nanocrystals with Bifunctional Terminal Alkenes. *Langmuir* **2013**, *29*, 1533-1540.
(23) Yang, Z.; Iabal, M.; Dobbie, A. R.; Veinot, J. G. C. Surface-Induced Alkene Oligomerization: Does Thermal Hydrosilylation Really Lead to Monolayer Protected Silicon Nanocrystals? *J. Am. Chem. Soc.* **2013**, *135*, 17595-17601.
(24) Kelly, J. A.; Henderson, E. J.; Clark, R. J.; Hessel, C. M.; Cavell, R. G.; Veinot, J. G. C. X-ray Absorption Spectroscopy of Functionalized Silicon Nanocrystals. *J. Phys. Chem. C* **2010**, *114*, 22519-22525.
(25) Miller, J. B.; Van Sickle, A. R.; Anthony, R. J.; Kroll, D. M., Kortshagen, U. R.; Hobbie E. K. Ensemble Brightening and Enhanced Quantum Yield in Size-Purified Silicon Nanocrystals. *ACS Nano* **2012**, *6*, 7389-7396.
(26) Mastronardi, M .L.; Maier-Flaig, F.; Faulkner, D.; Henderson, E. J.; Kübel, C.; Lemmer, U.; Ozin, G. A. Size-Dependent Absolute Quantum Yields for Size-Separated Colloidally-Stable Silicon Nanocrystals. *Nano Lett.* **2012**, *12*, 337-342.
(27) Li, X.; He, Y.; Swihart, M. T. Surface Functionalization of Silicon Nanoparticles Produced by Laser-Driven Pyrolysis of Silane Followed by HF-HNO3 Etching. *Langmuir* **2004**, *20*, 4720-4727.
(28) Lu, X.; Hessel, C. M.; Yu, Y.; Bogart, T. D.; Korgel, B. A. Colloidal Luminescent Silicon Nanorods. *Nano Lett.* **2013**, *13*, 3101-3105.
(29) Yu, Y.; Bosoy, C. A.; Hessel, C. M.; Smilgies, D.-M.; Korgel, B. A. Silicon Nanocrystal Superlattices *ChemPhysChem* **2013**, *14*, 84-87.

(30) Locritani, M.; Yu, Y.; Bergamini, G.; Baroncini, M.; Molloy, J. K.; Korgel, B. A.; Ceroni, P. Silicon Nanocrystals Functionalized with Pyrene Units: Efficient-Harvesting Antennae with Bright Near-Infrared Emission. *J. Phys. Chem. Lett.* **2014**, *5*, 3325-3329.
(31) Heitsch, A. T.; Hessel, C. M.; Akhavan, V. A.; Korgel, B. A. Colloidal Silicon Nanorod Synthesis. *Nano Lett.* **2009**, *9*, 3042-3047.
(32) Heitsch, A. T.; Akhavan, V. A.; Korgel, B. A. Rapid SFLS Synthesis of Si Nanowires Using Trisilane with in situ Alkyl-Amine Passivation. *Chem. Mater.* **2011**, *23*, 2697-2699.
(33) Lu, X.; Korgel, B. A. A Single-Step Reaction for Silicon and Germanium Nanorods. *Chem. Euro. J.* **2014**, *20*, 5874-5879.
(34) Dasog, M.; Veinot, J. G. C. Size Independent Blue Luminescence in Nitrogen Passivated Silicon Nanocrystals. *Phys. Stat. Sol. A* **2012**, *209*, 1844-1846.
(35) Dasog, M.; De los Reyes, G. B.; Titova, L. V.; Hegmann, F. A.; Veinot, J. G. C. Size vs Surface: Tuning the Photoluminescence of Freestanding Silicon Nanocrystals across the Visible Spectrum via Surface Groups. *ACS Nano* **2014**, *8*, 9636-9648.
(36) Dasog, M.; Yang, Z.; Regli, S.; Atkins, T. M.; Faramus, A.; Singh, M. P.; Muthuswamy, E.; Kauzlarich, S. M.; Tilley, R. D.; Veinot, J. G. C. Chemical Insight into the Origin of Red and Blue Photoluminescence Arising from Freestanding Silicon Nanocrystals. *ACS Nano* **2013**, *7*, 2676-2685.
(37) Brust, M.; Walker, M.; Bethell, D.; Schiffrin, D. J.; Whyman, R. Synthesis of Thiol-Derivatised Gold Nanoparticles in a Two-Phase Liquid-Liquid System. *Chem. Commun.* **1994**, 801-802.
(38) Korgel, B. A.; Fullam, S.; Connolly, S.; Fitzmaurice, D. Assembly and Self-Organization of Silver Nanocrystal Superlattices: Ordered "Soft Spheres" *J. Phys. Chem. B* **1998**, *102*, 8379-8388.
(39) Lee, D. C.; Smith, D. K.; Heitsch, A. T.; Korgel, B. A. Colloidal Magnetic Nanocrystals: Synthesis, Properties and Applications. *Annu. Rep. Prog. Chem., Sect. C: Phys. Chem.* **2007**, *103*, 351-402.
(40) Sardar, R.; Funston, A. M.; Mulvaney, P.; Murray, R. W. Gold Nanoparticles: Past, Present, and Future. *Langmuir* **2009**, *25*, 13840-13851.
(41) Desireddy, A.; Conn, B. E.; Guo, J.; Yoon, B.; Barnett, R. N.; Monahan, B. M.; Kirschbaum,K. Griffith, W. P.; Whetten, R. L.; Landman, U.; Bigioni, T. P. Ultrastable Silver Nanoparticles. *Nature* **2013**, *501*, 399-402.
(42) Quiros, I.; Yamada, M.; Kubo, K.; Mizutani, J.; Kurihara, M.; Nishihara, H. Preparation of Alkanethiolate-Protected Palladium Nanoparticles and Their Size Dependence on Synthetic Conditions. *Langmuir* **2002**, *18*, 1413-1418.
(43) Castro, E. G.; Salvatierra, R. V.; Schreiner W. H.; Oliveira, M. M.; Zarbin, A. J. G. Dodecanethiol-Stabilized Platinum Nanoparticles Obtained by a Two-Phase Method: Synthesis, Characterization, Mechanism of Formation, and Electrocatalytic Properties. *Chem. Mater*. **2010**, *22*, 360-370.
(44) Aldana, J.; Wang, Y. A.; Peng, X. Photochemical Instability of CdSe Nanocrystals Coated by Hydrophilic Thiols. *J. Am. Chem. Soc.* **2001**, *123*, 8844-8850.

(45) Nosaka, Y.; Yamaguchi, K.; Miyama, H.; Hayashi, H. Preparation of Size-Controlled CdS Colloids in Water and Their Optical Properties. *Chem. Lett.* **1988**, *17*, 605-608.
(46) Liang, L.; Pandey, A.; Werder, D. J.; Khanal, B. P.; Pietryga, J. M.; Klimov, V. I. Efficient Synthesis of Highly Luminescent Copper Indium Sulfide-Based Core/Shell Nanocrystals with Surprisingly Long-Lived Emission. *J. Am. Chem. Soc.* **2011**, *133*, 1176-1179.
(47) Hessel, C. M.; Henderson E. J.; Veinot, J. G.C. Hydrogen Silsesquioxane: A Molecular Precursor for Nanocrystalline Si-SiO2 Composites and Freestanding Hydride-Surface-Terminated Silicon Nanoparticles. *Chem. Mater.* **2006**, *18*, 6139-6146.
(48) Panthani, M. G.; Hessel, C. M.; Reid, D.; Casillas, G.; José-Yacamán, M.; Korgel, B. A. Graphene-supported high-resolution TEM and STEM imaging of silicon nanocrystals and their capping ligands. *J. Phys. Chem. Lett.* **2012**, *116*, 22463-22468.
(49) Kelly, J. A.; Shukaliak, A. M.; Fleischauer, M. D.; Veinot, J. G. C. Size-Dependent Reactivity in Hydrosilylation of Silicon Nanocrystals *J. Am. Chem. Soc.* **2011**, *133*, 9564-9571.
(50) Vial, J. C.; Bsiesy, A.; Gaspard, F.; Hérino, R.; Ligeon, M.; Muller, F.; Romestain, R. Mechanisms of Visible-Light Emission from Electro-Oxidized Porous Silicon. *Phys. Rev. B* **1992**, *45*, 14171-14176.
(51) Proot, J. P.; Delerue, C.; Allan, G. Electronic Structure and Optical Properties of Silicon Crystallites: Application to Porous Silicon. *App. Phys. Lett.* **1992**, *61*, 1948-1950.
(52) Socrates, G. Infrared Characteristic Group Frequencies, second edition, *John Wiley & Sons UK*, **1994**.
(53) Lucovsky, G.; Nemanich, R. J.; Knights, J. C. Structural interpretation of the vibrational spectra of a-Si:H alloys. *Phys. Rev. B* **1979**, *19*, 2064-2073.
(54) Although the vibration observed for 1-dodecanethiol between 2600 and 2550 cm-1 is relatively weak, it is recognized fairly easily when present because this spectral region is relatively free of other absorption bands.[52]
(55) Joseph, Y.; Besnard, I.; Rosenberger, M.; Guse, B.; Nothofer, H.-G.; Wessels, J. M.; Wild, U.; Knop-Gericke, A.; Su, D.; Schlögl, R.; Yasuda, A.; Vossmeyer, T. Self-Assembled Gold Nanoparticle/Alkanethiol Films: Preparation, Electron Microscopy, XPS-Analysis, Charge Transport, and Vapor-Sensing Properties. *J. Phys. Chem. B* **2003**, *107*, 7406-7413.
(56) Castner, D. G. X-ray Photoelectron Spectroscopy Sulfur 2p Study of Organic Thiol and Disulfide Binding Interactions with Gold Surfaces. *Langmuir* **1996**, *12*, 5083-5086.
(57) Bourg, M.-C.; Badia, A.; Lennox, R. B. Gold-Sulfur Bonding in 2D and 3D Self-Assembled Monolayers: XPS Characterization. *J. Phys. Chem. B* **2000**, *104*, 6552-6567.

(58) Hostetler, M. J.; Wingate, J. E.; Zhong, C.-J.; Harris, J. E.; Vachet, R. W.; Clark, M. R. Londono, J. D.; Green, S. J.; Stokes, J. J.; Wignall, G. D.; Glish, G. L.; Porter, M. D.; Evans, N. D.; Murray, R. W. Alkanethiolate Gold Cluster Molecules with Core Diameters from 1.5 to 5.2 nm: Core and Monolayer Properties as a Function of Core Size. *Langmuir* **1998**, *14*, 17-30.
(59) Lai, Y.-H.; Yeh, C.-T.; Lin, Y.-H.; Hung, W.-H. Adsorption and thermal decomposition of H2S on Si(100). *Surf. Sci.* **2002**, *519*, 150-156.
(60) Haas, A. The Chemistry of Silicon-Sulfur Compounds. *Angew. Chem. Int. Ed.* **1965**, *4*, 1014-1023.
(61) Sommer, L. H.; McLick, J. Stereochemistry of Asymmetric Silicon. IX. The Silicon-Sulfur Bond. *J. Am. Chem. Soc.* **1967**, *89*, 5806-5812.
(62) Őğüt, S.; Chelikowsky, J. R.; Louie, S. G. Quantum Confinement and Optical Gaps in Si Nanocrystals. *Phys. Rev. Lett.* **1997**, *79*, 1770-1773.
(63) Holmberg, V. C.; Korgel, B. A. Corrosion resistance of thiol- and alkene-passivated germanium nanowires. *Chem. Mater.* **2010**, *22*, 3698-3703.
(64) Armstrong, D. A.; Wilkening, V. G. Effects of pH in the γ-Radiolysis of Aqueous Solutions of Cysteine and Methyl Mercaptan. *Can. J. Chem.* **1964**, *42*, 2631-2635.
(65) Patai, S. The Chemistry of the Thiol Group. *John Wiley & Sons London,* **1974**.
(66) Krull, L.H.; Friedman, M. Reduction of Protein Disulfide Bonds by Sodium Hydride in Dimethyl Sulfoxide. *Biochem. Biophys. Res. Commun.* **1967**, *29*, 373-377.
(67) Wall, J. S. Disulfide Bonds: Determination, Location, and Influences on Molecular Properties of Proteins. *Agricultural and Food Chem.* **1971**, *19*, 619-625.

Chapter 7: Silicon Nanocrystal Superlattice[§]

7.1 INTRODUCTION

Colloidal nanocrystals with precisely controlled size and shape can be assembled into ordered superlattices.[1] Superlattices have been made of Au[10], Ag[11,12], Pd[13], Fe[14], PbSe[15], PbS[17], PbTe[18], Fe_2O_3 [10, 17, 19], $CoPt_3$ [20], Ag_2Te[18], FePt[17], CdTe[21] and CdSe [21,22] nanocrystals and explored for various applications, including sensors, [2-4] transistors,[5,6] data storage,[7] solar cells, [8] and thermoelectrics. [9] Here, we report the first superlattices of colloidal silicon (Si) nanocrystals. Compared to other types of colloidal nanocrystal superlattices, the superlattices of organic ligand-capped Si nanocrystals have much higher thermal stability.[2]

Si is one of the most commercially important semiconductors, but Si nanocrystal superlattices have not yet been reported partly because of the inability to obtain sufficiently monodisperse colloidal Si nanocrystals. Si nanocrystals are especially interesting for optoelectronic applications requiring light emission since bulk Si is a poor light emitter due to its indirect band gap. Si nanocrystals—or quantum dots—can exhibit bright, size-tunable, visible photoluminescence and electroluminescence,[28-31] making Si nanocrystals suitable as a down-converting phosphor or the active emitting material in light-emitting diodes.[32] Si quantum dots are also being explored as a laser source.[23] Photovoltaic devices utilizing Si quantum dots have also been proposed[25] because of

---

[§] Portion of this Charpter appears in Yu, Y.; Bosoy, C. A.; Hessel, C. M.; Smilgies, D.-M.; Korgel, B. A. *ChemPhysChem* 14, 84-87, (**2013**). Y. Yu performed the experiemnts. All authors contributed to writing the text. B. A. Korgel provided the funding through research grants.

their size-tunable optical absorption edge, much higher absorption coefficient and the potential for multiexciton generation (MEG).[36] Most of these applications require arrays of nanocrystals and there have been efforts to fabricate them. Most collections of Si nanocrystals studied to date have been disordered with a significant size distribution. However, some success has been achieved by thermal annealing of alternating layers of amorphous Si and SiO_2 to yield periodically arranged monolayers of relatively monodisperse Si nanocrystals in SiO_2.[24-27] Here we report the assembly of Si nanocrystal superlattices with extended face centered cubic (fcc) periodic order.

7.2 EXPERIMENT DETAILS

7.2.1 Materials

FOx-16 was purchased from Dow Corning, 1-dodecene (96%), 1-octadecene (95%) were purchased from Sigma-Aldrich. Ethanol, toluene, hexanes, chloroform, and Hydrochloric acid (HCl, 37.5%) were from Fisher Scientific. Hydrofluoric acid (HF, 48%) was obtained from EMD chemicals. Deionized (DI) water was obtained using a Barnstead Nanopure Filtration System (17 MΩ resistance).

7.2.2 Si Nanocrystal Synthesis

3 g of HSQ is heated in a flow of forming gas (93% N2, 7% H2) at 1100 ^{o}C or 1250 ^{o}C for 1 hour to yield brown glassy product, which is ground with an agate mortar and pestle to a brown powder. The grain size of the powder is reduced further in a wrist-action shaker for 9 hours with 30 g of 3 mm diameter borosilicate glass beads.

300 mg of powder, composed of SiO_2-embedded Si nanocrystals [24], is suspended in 10 ml of 40% HF and 1.5 ml of 25% HCl and stirred in dark for 16 hours. Hydride-terminated Si nanocrystals are isolated by centrifugation at 8000 rpm for 5 minutes, and then rinsed twice with 8 ml of ethanol and once with 8 ml of chloroform. The final light brown material is dispersed in 8 ml of 1-dodecene by sonication to form a brown turbid dispersion, which is transferred to a three neck flask and degassed with 3 freeze-pump-thaw cycles. The turbid dispersion is heated at 190^{o}C in a N_2 flow for 18 hours and cooled down to room temperature. The resulting clear solution is centrifuged at 8000rpm for 5 minutes and the precipitate (unpassivated nanocrystals) is discarded. 20 ml of acetone is added to the supernatant to crash out the passivated nanocrystals, which are then collected by centrifugation and dispersed in 2ml of hexanes. The passviated nanocrystals dispersed in hexane are then washed three times by precipitation with ethanol as antisolvent (20 ml) and dispersed in 2 ml of hexanes.

7.2.3 Size-Selective Precipitation

Add ethanol drop by drop to the hexanes dispersion of Si nanocrystal until the transparent dispersion turn to translucent with the addition of one drop. The dispersion was then centrifuged at 8000 rpm for 5 minutes and the precipitate (extra large or poorly passivated nanocrystals) was discarded. Add one more drop of ethanol to the supernatant, centrifuge the dispersion at 8000 rpm for 5 minutes, and discard the precipitate. Repeat adding one drop of ethanol, centrifugation, discarding the precipitate for 5 times, then add

15 ml of ethanol to the dispersion, centrifuge at 10000 rpm for 10 minutes, discard the supernatant (extra small nanocrystals), and dispersed the precipitate with 2 ml of hexanes.

After repeat the process mentioned in the last paragraph twice, 5 ml of ethanol was added to the hexane dispersion, then the dispersion was centrifuged at 10000 rpm for 10 minute, and the supernatant was discarded, while the precipitate was dispersed in 1 ml of hexanes. 1 ml of ethanol was added to the dispersion, and the dispersion was centrifuged at 8000rpm for 5 minutes. Precipitate was dispersed in 1 ml of hexanes and marked as sample 1. Add 4 ml of ethanol to the supernatant, and centrifuged at 10000 rpm for 10 minutes, the precipitate was dispersed in 1 ml of hexanes and marked as sample 2.

7.3 RESULTS AND DISCUSSION

Figure 7.1 shows a grazing incidence small angle X-ray scattering (GISAXS) pattern and transmission electron microscopy (TEM) images of colloidal Si nanocrystal superlattices formed by drop-casting from chloroform. The Si nanocrystals were obtained by thermal decomposition of hydrogen silsesquioxane (HSQ) followed with HF etching, thermal hydrosilyation with 1-dodecene and finally a size-selective precipitation. The GISAXS pattern exhibits rings and spots that index to an fcc superlattice with lattice constant a_{SL}=15.5 nm. The presence of the diffraction spots indicate that some of the superlattice domains have specific $(111)_{SL}$ or $(100)_{SL}$ orientation with respect to the substrate. Based on the diffraction spot size, these ordered superlattice grains are about 120 nm in size. The rings indicate that some of the superlattice also occurs with

random orientations with respect to the substrate. In the TEM images in Figure 7.1, regions of fcc superlattice oriented with (111) and $(11\bar{2})$ planes parallel to the substrate were observed.

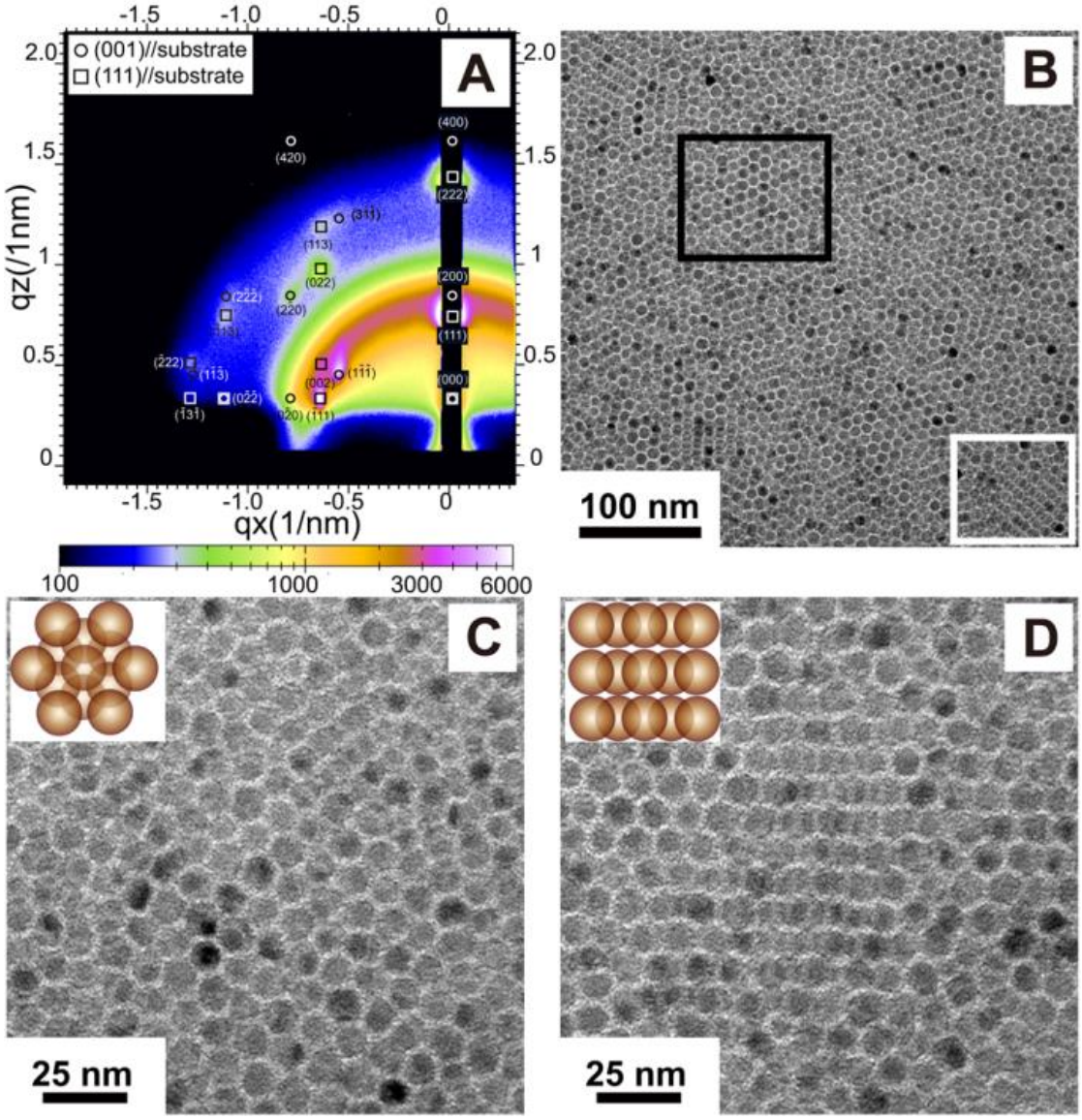

Figure 7.1

Figure 7.1: A) GISAXS of a Si nanocrystal superlattice. Circles and squares highlight spots associated with (001)- and (111)-oriented FCC superlattice, respectively. B) TEM image of superlattice of Si nanocrystal, the area highlighted with black rectangle corresponds to (111)-oriented FCC superlattice, the area highlighted with white rectangle corresponds to $(11\bar{2})$-oriented FCC superlattice; C) TEM image of a (111)-oriented domain, inset: depiction of [111] projection; D) TEM image for $(11\bar{2})$-oriented FCC superlattice, inset: depiction of a $[11\bar{2}]$ projection.

Based on the lattice constant of a=15.5 nm, the center-to-center separation between neighbouring Si nanocrystals is 11.0 nm, and with an average Si core diameter of 8.0±1.2 nm measured by SAXS, the edge-to-edge separation in the superlattice is 1.5 nm. The length of a fully-extended C_{12} alkyl capping ligand is 1.7 nm.

The thermal stability of the Si nanocrystal superlattices was also tested. Figure 7.2 shows GISAXS of a FCC superlattice of Si nanocrystals as it was heated from 35°C to 375°C. The $(1\bar{1}\bar{1})$ and $(2\bar{2}0)$ diffraction spots are still present in the GISAXS pattern up to 280°C, although the higher order diffraction spots have disappeared indicating that some disorder occurs but the superlattice retains its FCC structure. Even up to 375°C—the highest temperature possible in the experimental setup—the Si nanocrystal superlattice still showed $(1\bar{1}\bar{1})$ and $(2\bar{2}0)$ diffraction spots, indicating that the nanocrystals remain unsintered. The Si nanocrystal superlattices are much more stable than superlattices of other kinds of nanocrystals. For example, superlattices of dodecanethiol-capped Ag nanocrystal disorder at 180°C.[11] Superlattices of oleic acid-capped PbSe nanocrystals,[15] oleic acid-capped PbS nanocrystals,[34] and dodecanethiol-capped Au nanocrystals [35] sinter at much lower temperatures of 168°C, 230°C, and 200°C, respectively. The high thermal stability is attributed to the strong covalent Si-C bonded alkane ligand layer on the Si nanocrystals. Thermal gravimetric analysis (TGA) of Si nanocrystals (Figure 7.2F) showed three stages of ligand desorption: (1) evaporation of free ligand at around 190°C; (2) desorption and evaporation of bound ligand between 270°C and 520°C; and (3) oxidation of the Si core between 520°C and 800°C.

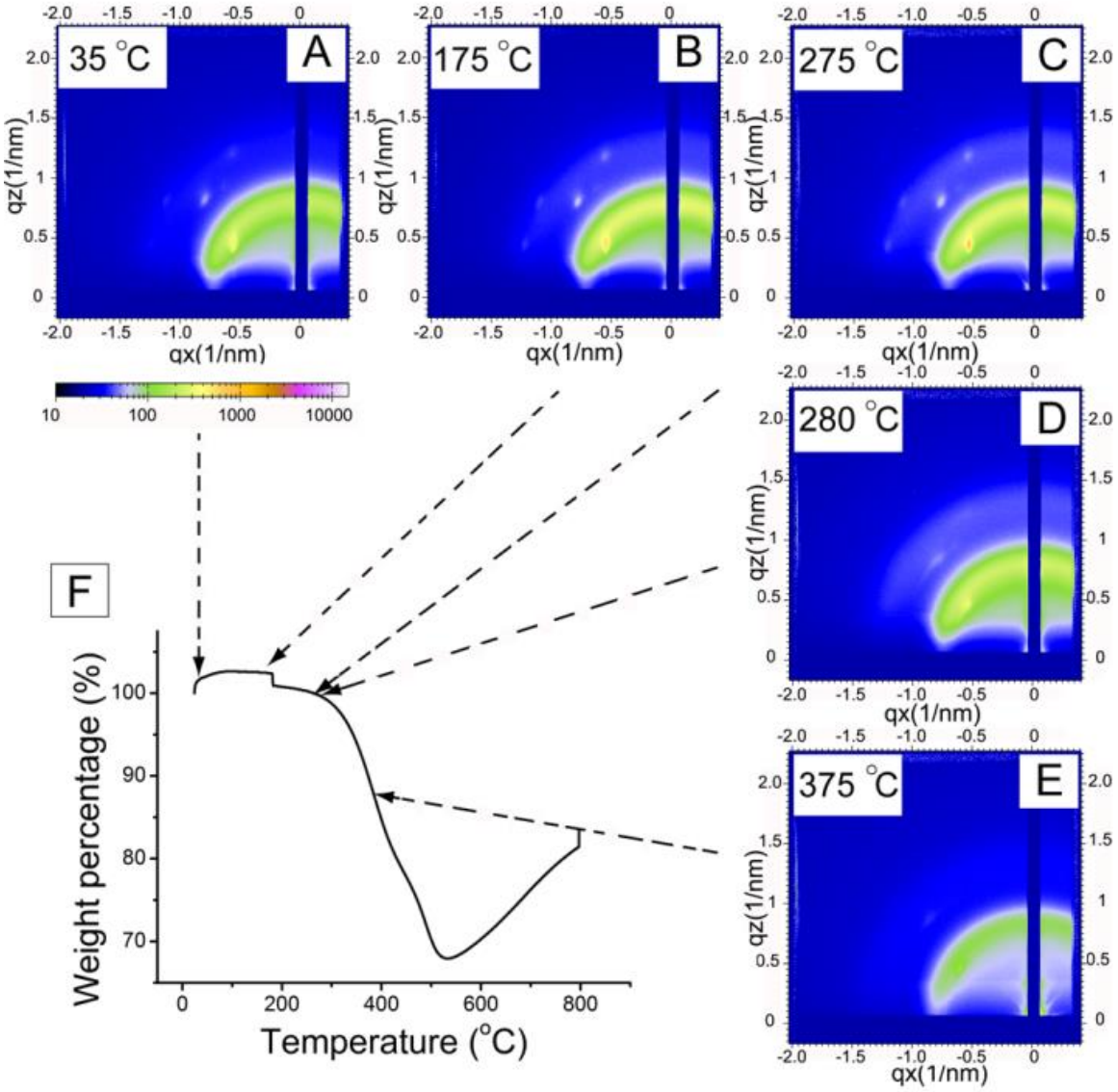

Figure 7.2: A-E) GISXAS of a (100)-oriented FCC superlattice of Si nanocrystals as it was heated to the indicated temperature. F) TGA of Si nanocrystals.

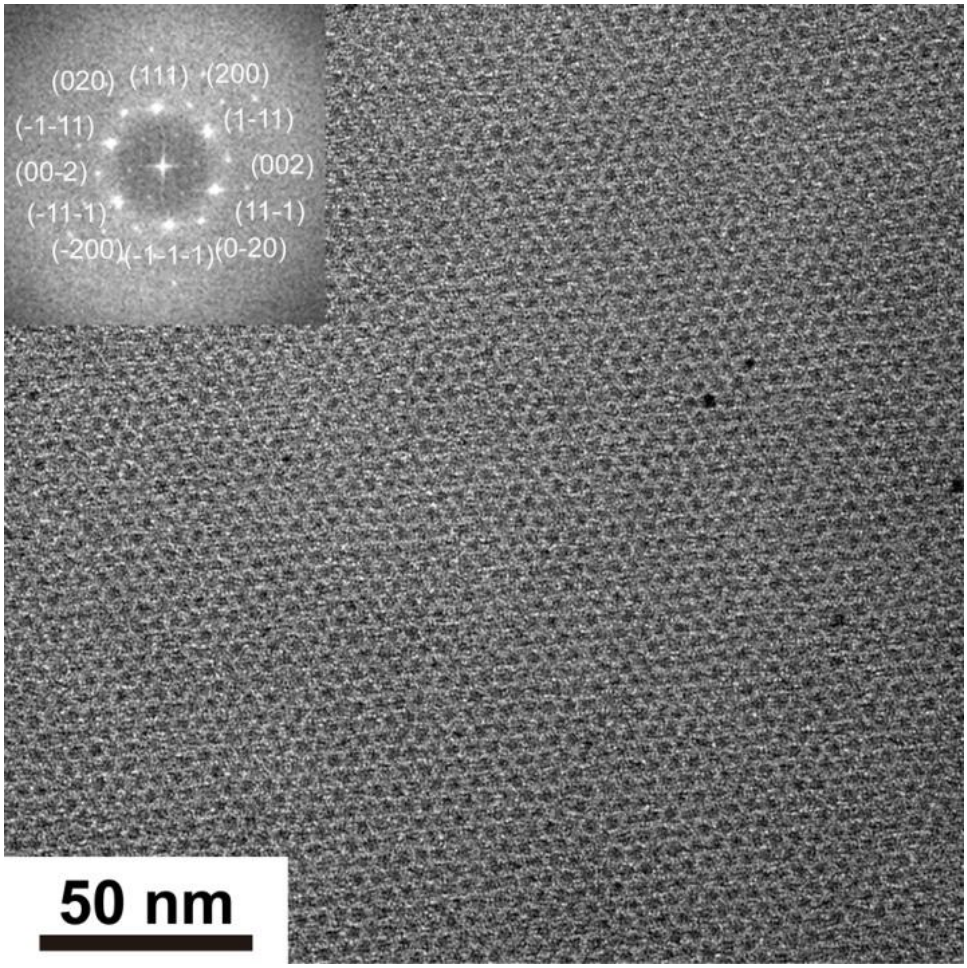

Figure 7.3: TEM image of a superlattice of 2.4 nm diameter Si nanocrystals capped with a mixture of dodecene/octadene. Inset: Fast Fourier transform (FFT) of the TEM image. Indexed to an FCC superlattice. The superlattice is oriented with its (111) planes on the substrate and has a lattice constant of a_{SL}=8.3 nm.

Figure 7.3 shows a TEM image of an FCC superlattice of smaller 2.4 nm diameter Si nanocrystals capped with a mixture of 1-dodecene and 1-octadecene. The $(110)_{SL}$ d-spacing is 4.8 nm, corresponding to the lattice constant a_{SL}=8.3 nm. From solution SAXS, the Si core diameter is 2.4±0.52 nm. It is somewhat surprising that nanocrystals with a polydispersity of just over 20% can form a superlattice. Based on the superlattice

dimensions and the nanocrystal diameter it appears that there is excess ligand in the superlattice. Unlike the larger nanocrystals, the smaller nanocrystals could not be completely dried into a film, even when stored under vacuum at 150^{o}C for 12 hours, which indicates a significant excess of ligand in the sample. The excess ligand in the superlattice appears to be important for enabling superlattice assembly from these relatively polydisperse nanocrystals.

7.4 CONCLUSION

Superlattices of colloidal organic ligand-stabilized Si nanocrystals are reported here for the first time. Superlattices with FCC structure were observed for both large (8.0 nm diameter) and small (2.4 nm diameter) nanocrystals. GISAXS showed that a significant amount of superlattice grains had specific orientations with respect to the substrate with $(111)_{SL}$ and $(100)_{SL}$ planes parallel to the underlying substrate. Superlattices with $(11\bar{2})_{SL}$ planes oriented parallel to the substrate were also observed by TEM. The Si nanocrystal superlattices were found to be very thermally stable, much more than other types of nanocrystal superlattices. Their thermal stability appears to relate to the robust covalent Si-C bonding of the capping ligand layer.

7.5 REFERENCE

(1) Murray, C. B.; Kagan, C. R.; Bawendi, M. G. Synthesis and Characterization of Monodisperse Nanocrystals and Close-Packed Nanocrystal Assemblies. *Annu. Rev. Mater. Sci.* **2000**, *30*, 545-610.
(2) Katz, E.; Willner, I. Integrated Nanoparticle-Biomolecule Hybrid Systems: Synthesis, Properties, and Applications. *Angew. Chem. Int. Ed.* **2004**, *43*, 6042-6108.
(3) Shipway, A. N.; Katz, E.; Willner, I. Nanoparticle Arrays on Surface for Electronic, Optical, and Sensors Applications. *ChemPhysChem* **2000**, *1*, 18-52.

(4) Rosi, N. L.; Mirkin, C. A. Nanostructure in Biodiagnostics. *Chem. Rev.* **2005**, *105*, 1547-1562.
(5) Talapin, D. V.; Murray, C. B. PbSe Nanocrystal Solids for n- and p-Channel Thin Film Field-Effect Transistors. *Science* **2005**, *310*, 86-89.
(6) Urban, J. J.; Talapin, D. V.; Shevchenko, E. V.; Kagan, C. R.; Murray, C. B. Synergism in Binary Nanocrystal Superlattices Leads to Enhanced p-Type Conductivity in Self-Assembled PbTe/Ag_2Te Thin Films. *Nat. Mater.* **2007**, *6*, 115-121.
(7) Suganuma, Y.; Trudeau, P.-E.; Dhirani, A.-A. Multi-Valued Analogue Information Storage Using Self-Assembled Nanoparticle Films. *Nanotechnology* **2005**, *16*, 1196-1203.
(8) Gur, I.; Fromer, N. A.; Geier, M. L.; Alivisatos, A. P. Air-Stable All-Inorganic Nanocrystal Solar Cells Processed From Solution. *Science* **2005**, *310*, 462-465.
(9) Kovalenko, M. V.; Spokoyny, B.; Lee, J.-S.; Scheele, M.; Weber, A.; Perera, S.; Landry, D.; Talapin, D. V. Semiconductor Nanocrystals Functionalized with Antimony Telluride Zintl Ions for Nanostructure Thermoelectrics. *J. Am. Chem. Soc.* **2010**, *132*, 6686-6695.
(10) Smith, D. K.; Goodfellow, B.; Smilgies, D.-M.; Korgel, B. A. Self-Assembled Simple Hexagonal AB2 Binary Nanorystal Superlattices: SEM, GISAXS, and Defects. J. Am. Soc. Chem. 2009, 131, 3281-3290.
(11) Korgel, B. A.; Zaccheroni, N.; Fitzmaurice, D. "Melting transition" of a quantum dots solid: collective interactions influence the thermally-induced order-disorder transition of a silver nanocrystal superlattice. J. Am. Chem. Soc. 1999, 121, 3533-3534.
(12) Korgel, B. A.; Fitzmaurice, D. Small-angle X-ray-Scattering Study of Silver-Nanocrystal Disorder-Order Phase Transitions. *Phys. Rev. B* **1999**, *59*, 14191-14201.
(13) Shevchenko, E. V.; Talapin, D. V.; Kotov, N. A.; O'Brien, S.; Murray, C. B.; Structural Diversity in Binary Nanoparticles Superlattice. *Nature* **2006**, *439*, 55-59.
(14) Saunders, A. E.; Korgel, B. A. Observation of an AB phase in bidisperse nanocrystal superlattices. *ChemPhysChem* **2005**, *6*, 61-65.
(15) Goodfellow, B. W.; Patel, R. N.; Panthani, M. G.; Smilgies, D.-M.; Korgel, B. A. Melting and sintering of a body-centered cubic superlattice of PbSe nanocrystals followed by small angle X-ray scattering. J. Phys. Chem. C 2011, 115, 6397-6404.
(16) Redl, F. X.; Cho, K.-S.; Murray, C. B.; O'Brien, S. Three-Dimensional Binary Superlattices of Magnetic Nanocrystals and Semiconductor Quantum Dots. *Nature* **2003**, *423*, 968-971.
(17) Talapin, D. V.; Shevchenko, E. V.; Murray, C. B.; Titov, A. V.; Král, P. Dipole-Dipole Interactions in Nanocrystal Superlattices. *Nano Lett.* **2007**, *7*, 1213-1219.
(18) Urban, J. J.; Talapin, D. V.; Shevchenko, E. V.; Kagan, C. R.; Murray, C. B. Synergism in Binary Nanocrystal Superlattices Leads to Enhanced p-Type

Conductivity in Self-Assembled PbTe/Ag_2Te Thin Films. *Nat. Mater.* **2007**, *6*, 115-121.
(19) Shevchenko, E. V.; Kortright, J. B.; Talapin, D. V.; Aloni, S.; Alivisatos, A. P. Quasi-Ternary Nanoparticle Superlattice Through Nanoparticle Design. *Adv. Mater.* **2007**, *19*, 4183-4188.
(20) Shevchenko, E. V.; Talapin, D. V.; Murray, C. B.; O'Brien, S. Structural Characterization of Self-Assembled Multifunctional Binary Nanoparticle Superlattices. *J. Am. Chem. Soc.* **2006**, *128*, 3620-3637.
(21) Chen, Z.; Moore, J.; Radtke, G.; Sirringhaus, H.; O'Brien, S. Binary Nanoparticle Superaltticesin the Semiconductor-Semiconductor System: CdTe and CdSe. *J. Am. Chem. Soc.* **2007**, *129*, 15702-15709.
(22) Overgaag, K.; Evers, W.; Nijs, B.; Koole, R.; Meeldijk, J.; Vanmaekelbergh, D. Binary Superlattice of PbSe and CdSe Nanocrystals. *J. Am. Chem. Soc.* **2008**, *130*, 7833-7835.
(23) Pavesi, L.; Dal Negro, L.; Mazzoleni, C.; Franzò, G.; Priolo, F. Optical Gain in Silicon Nanocrystals. *Nature* **2000**, *408*, 440-444.
(24) Tsybeskov, L.; Hirschman, K. D.; Duttagupta, S. P.; Zacharias, M.; Fauchet, P. M.; McCaffrey, J. P.; Lockwood, D. J. Nanocrystalline-Silicon Superlattice Produced by controlled Recrystallization. *Appl. Phys. Lett.* **1998**, *72*, 43-45.
(25) Jiang, C.-W.; Green, M. A. Silicon Quantum Dots Superlattice: Modelingof Energy Bands. Densities of States,and Nobilities for Silicon Tandem Solar Cell Applications. *J. Appl. Phys* **2006**, *99*, 114902.
(26) Zacharias, M.; Heitmann, J.; Scholz, R.; Kahler, U.; Schmidt, M.; Bläsing, J. Size-Controlled Highly Luminescent Silicon Nanocrystals: A SiO/SiO_2 superlattice approach. *Appl. Phys. Lett.* **2002**, *80*, 661-663.
(27) Heitmann, J.; Müller, F.; Zacharias, M.; Gösele, U. Silicon Nanocrystal: Size Matters. *Adv. Mater.* **2005**, *17*, 795-803.
(28) Hessel, C.M.; Reid, D.; Panthani, M. G.; Rasch, M. R., Goodfellow, B. G.; Wei, J.; Hiromasa, F.; Akhavan, V.; Korgel, B. A. Synthesis of Ligand-Stabilized Silicon Nanocrystals with Size-Dependent Photoluminescence Spanning Visible to Near-Infrared Wavelengths. *Chem. Mater.* **2012**, *24*, 393-401.
(29) Hessel, C. M.; Rasch, M. R.; Hueso, J. L.; Goodfellow, B. W.; Akhavan, V. A.; Puvanakrishnan, P.; Tunnel, J. W.; Korgel, B. A. Alkyl Passivation and Amphiphilic Polymer Coating of Silicon Nanocrystals for Diagnostic Imaging. *Small*, **2010**, *6*, 2026-2034.
(30) Mastronardi, M. L.; Maier-Flaig, F.; Faulkner, D.; Henderson, E. J.; Kübel, C.; Lemmer, U.; Ozin, G. A. Size-Dependent Absolute Quantum Yield for Size-Separated Colloidally-Stable Silicon Nanocrystals. *Nano Lett.* **2012**, *12*, 337-342.
(31) Miller, J. B.; Van Sickle, A. R.; Anthony, R. J.; Kroll, D. M.; Kortshagen, U. R.; Hobbie, E. K. Ensemble Brightening and Enhanced Quantum Yield in Size-Purified Silicon Nanocrystals. *ACS Nano* **2012**, *6*, 7389-7396.

(32) Lepage, H.; Kaminski-Cachopo, A.; Poncet, A.; le Carval, G. Simulation of Electron Transport in Silicon Nanocrystal Solids. *J. Phys. Chem. C* **2012**, *116*, 10873-10880.
(33) Puzzo, D. P.; Henderson, E. J.; Helander, M. G.; Wang, Z.; Ozin, G. A.; Lu, Z. Visiblle Colloidal Nanocrystal Silicon Light-Emitting Diode. *Nano Lett.* **2011**, *11*, 1585-1590.
(34) Lee, B.; Podsiadlo, P.; Rupich, S.; Talapin, D. V.; Rajh, T.; Shevchenko, E. V. Comparison of Structural Behavior of Nanocrystals in Randomly Packed Films and Long-Range Ordered Superlattices by Time-Resolved Small Angle X0ray Scattering. *J. Am. Chem. Soc.* **2009**, *131*, 16386-16388.
(35) Coutts, M. J.; Cortie, M. B.; Ford, M. J.; McDonagh, A. M. Rapid and Controllable Sintering of Gold Nanoparticles Inka at Room Temperature Using a Chemical Agent. *J. Phys. Chem. C.* **2009**, *113*, 1325-1328.
(36) Beard, M. C.; Knutsen, K. P.; Yu, P.; Luther, J. M.; Song, Q.; Metzger, W. K.; Ellingson, R. J.; Nozik, A. J. Multiple Exciton General in Colloidal Silicon Nanocrystals. *Nano Lett.* **2007**, *7*, 2506-2512.

Chapter 8: Self-Assembly and Thermal Stability of Binary Superlattices of Gold and Silicon Nanocrystals[§]

8.1 INTRODUCTION[3]

Nanocrystal superlattices and their self-assembly have been widely studied as experimental models to gain deeper understanding about ordering processes that occur in nature, and as a route to new materials with unique and synthetically tunable properties.[1-12] Nanocrystals can be made with a tremendous range of composition, size, shape and surface chemistry, enabling wide tunability of material properties and the interparticle interactions involved in the assembly process. Binary nanocrystal superlattices in particular represent an interesting class of these materials. Self-assembly of nanocrystals with two distinct sizes can yield mesoscopic composition profiles that cannot be obtained any other way and BSLs have been made with metals,[13-15] semiconductors,[16-18] and magnets.[3,13,14,19] Recently, ternary nanocrystal superlattices have been made by matching nanocrystals with three distinct sizes.[20-22] Nonetheless, BSLs containing one of the most commercially important semiconductors, silicon (Si), have not yet been made. BSL formation requires nanocrystals with uniform size and shape, and appropriate size matching between two nanocrystal components and only recently have sterically-stabilized Si nanocrystals been made with sufficiently narrow size distributions to form superlattices.[23] Here, we take these highly uniform Si

[§] Portion of this chapter appears in Yu, Y.; Bosoy, C. A.; Smilgies, D.-M.; Korgel, B. A. *Journal of Physical Chemistry Letters* 4, 3677-3682, (**2013**). Y. Yu performed the experiments. All anthors contributed to writing the text. B. A. Korgel provided funding through research grants.

nanocrystals and form BSLs. Si nanocrystals (5.4 nm diameter) were combined with Au nanocrystals (1.9 nm diameter)—both capped with dodecyl ligands—to form BSLs with simple hexagonal AB_2 structure. The structure of these BSLs is typical of sterically-stabilized nanocrystals in this size range and size ratio; however, the thermal decomposition of these BSLs was found to occur by a new and unique pathway. When the BSL is heated above 190^{o}C, Au nanocrystals coalesce and migrate to the surface of the superlattice while the Si nanocrystals retain a metastable simple hexagonal superlattice structure.

8.2 EXPERIMENTAL DETAILS

8.2.1 Materials

FOx-16 was purchased from Dow Corning, 1-dodecene (96%), 1-octadecene (95%), Gold (III) chloride trihydrate ($HAuCl_4 \cdot 3H_2O$, >99.9%), tetraoctylammonium bromide (TOAB, 98%), 1-dodecanthiol (>98%), 1-octadecanethiol (98%), sodium borohydride ($NaBH_4$,>98%) were purchased from Sigma-Aldrich. Ethanol, toluene, hexanes, chloroform, and Hydrochloric acid (HCl, 37.5%) were from Fisher Scientific. Hydrofluoric acid (HF, 48%) was obtained from EMD chemicals. Deionized (DI) water was obtained using a Barnstead Nanopure Filtration System (17 MΩ resistance).

8.2.2 Si nanocrystals Synthesis

In a typical synthesis, 20 ml flowable oxide (FOx-16, purchased from Dow Corning Corporation) was evporated in vacuum to form dry white hydrogen

silsesquioxane (HSQ), which was then annealed in forming gas (93% nitrogen, 7% hydrogen) at 1250 ^{o}C for 1 hour to yield a brown glassy product (SiO_2-embedded Si nanocrystals). The brown material was ground with an agate mortar and pestle to a powder, and the grain size of the powder was further reduced to around 200 nm in a wrist-action shaker for 9 hours with 30 g of 3 mm diameter borosilicate glass beads.

600 mg of brown powder (contains SiO_2-embedded Si nanocrystal) was suspended in 20 ml of 48% HF and 3 ml of HCl, and stirred in dark for 20 hours to yield hydride-terminated Si nanocrystals, which was isolated by centrifugation at 8000 rpm for 5 mintues. The hydride-terminated Si nanocrystals were rinsed twice with 10 ml of ethanol, once with 10 ml of chloroform, and dispersed in 16 ml of 1-dodecene, forming a brown turbid dispersion. The dispersion was tranferred to a three-neck flask, degassed with 3 freeze-pump-thaw cycless, and heated to 190 ^{o}C in nitrogen for 20 hours. The turbid dispersion slowly turned clear during heating. The optically clear dispersion was centrifuged at 8000 rpm for 5 minutes and the precipitate (unpassivated and poorly passivated nanocrystals) was discarded. The supernatant was splited into two 30 ml glass centrifuge tubes, and 20 ml acetone was added to each tube to precipitate the passivated nanocrystals, which was collected by centrifugation. The passivated Si nanocrystals was dispersed with 4 ml of hexanes, and further washed three times by precipiation with solvent combination of hexanes (solvent) and ethanol (antisolvent).

8.2.3 Au Nanocrystals Synthesis

328 mg of gold (III) chloride trihydrate ($HAuCl_4 \cdot 3H_2O$) was dissolved in 20 ml of deionized water (DI water), then poured into a solution of 6.562 g of tetraoctylammonium (TOAB) in 80 ml of toluene. The mixture was stirred at 600 rpm for 1 hour to complete the phase transfer of Au ions. Extract the organic phase and discard the aqueous phase. 600 μl of 1-dodecanethiol was added to the organic phase, which was stirred at 600 rpm. 378 mg of sodium borohydride ($NaBH_4$) was dissolved in 20 ml of DI water in an ice bath to form a colorless solution, which was quickly poured into the organic phase while stirring. The two phase mixture was stirred at 600 rpm for 12 hours before the organic phase (contains 1-dodecanethiol-capped Au nanocrystals) was extracted. Ethanol was added to the organic phase at a ratio of 4 ml ethanol / 1 ml of organic phase to precipitate the capped nanocrystals, which were collected by centrifugation at 8500 rpm for 5 minutes. Nanocrystals was dispersed in around 3 ml of toluene and centrifuged at 10000 rpm for 5 minutes, precipitate (poorly capped nanocrystals) was discarded. The Au nanocrystals were wash again by using methanol was antisolvent, and stored in toluene at a concentration of 25 mg/ml.

8.2.4 Size-Selective Precipitation

Ethanol was added dropwise to a hexanes dispersion of Si nanocrystals until it became slightly opalescent. The dispersion was centrifuged at 8000 rpm for 5 minutes, the precipitate, containing extra-large or poorly passivated nanocrystals, was discarded. One more drop of ethanol was added into the supernatant to make it opalescent, then the

dispersion was centrifuged again to get rid of precipitate. 20 ml of ethanol was added to the supernatant, which was centrifuged at 10000 rpm for 10 minutes. The supernatant, containing extra-small nanocrystals, was discarded, and the precipitate was dispersed in 4 ml of hexanes. After this size distribution narrowing process was repeated three times, the Si nanocrystals were dispersed in 6 ml of hexanes.

8.2.5 Superlattice Assembly

500 μl of Au nanocrystal toluene dispersion (2.5 mg/ml) was mixed with 350 μl of Si nanocrystal hexanes dispersion (4 mg/ml) in a vial. The number ratio of Au nanocrysals to Si nanocrystls in the mixture is approximately 2.3:1. As illustrated in Figure S1, the vial was tilted (~30^{o}) and a 7 mm × 7 mm Si wafer was carefully slid into the vial. The vial was left uncapped, and the solvent in the vial was allowed to evaporate at room temperature

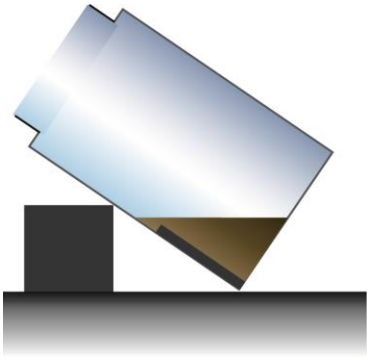

Figure 8.1: Illustration of the slow-drying process used to form BSLs.

8.2.6 Grazing incidence small-angle X-ray scattering (GISAXS)

GISAXS was performed on D1 beam line of the Cornell High Energy Synchrotron Source (CHESS), using monochromatic X-ray radiation of wavelength of

1.154 Å with a bandwidth of ~0.017 Å. A fiber coupled CCD camera with a pixel size of 46.9 μm × 46.9 μm and a total of 1024 × 1024 pixels was used to acquire the GISAXS pattern images, which were dark current corrected, distortion corrected, and flat field corrected by the acquisition software. The sample-to-detector distance was 959 mm, determined by using a silver behenate powder standard. The typical incident angle of the X-ray beam was 0.25^{o}, and the exposure time was around 0.1 to 1 s. The GISAXS patterns were calibrated and integrated using the Fit2D software (version: 12_077_i686_WXP). 3D index of GISAXS diffraction spots were performed with our own software.

8.3 RESULTS AND DISCUSSION

Si nanocrystals were synthesized by thermal decomposition of hydrogen silsesquioxane, followed by HF etching, thermal hydrosilylation with 1-dodecene, and a final narrowing of the size distribution by solvent/antisolvent size-selective precipitation.[23,24] These nanocrystals have been shown to have a uniform spherical shape and capping ligand coverage.[25] Au nanocrystals were synthesized by gold (III) chloride trihydrate ($HAuCl_4$ $3H_2O$) reduction with sodium borohydride ($NaBH_4$) in the presence of 1-dodecanthiol.[26,27] The nanocrystal size was determined from small angle X-ray scattering (SAXS) measurements of nanocrystals dispersed in toluene by considering the X-ray scattering intensity expected for a collection of non-interacting nanocrystals of radius *R*,[2]

$$I(q) \propto \int_0^\infty N(R)P(qR)R^6 dR \qquad (1)$$

assuming a Gaussian size distribution $N(R)$, with average radius $\bar{R}$, and standard deviation σ,

$$N(R) = \frac{1}{\sigma 2\pi} \exp\left[\frac{-(R-\bar{R})^2}{2\sigma^2}\right] \quad (2)$$

and using the shape factor for solid homogeneous spheres

$$P(qR) = \left[3\frac{\sin(qR) - qR\cos(qR)}{(qR)^3}\right]^2 \quad (3)$$

The scattering vector is $q = (4\pi/\lambda)\sin(\theta/2)$ where λ is the X-ray wavelength and θ is the scattering angle. Fitting Eqns (1)-(3) to the SAXS data in Figures 8.2c and 8.2d gave average diameters of $d_{core,Si}$=5.40±0.53 nm and $d_{core,Au}$=1.88±0.19 nm for the Si and Au nanocrystals, respectively. Figures 2a and 2b show GISAXS data for superlattices formed with Si or Au nanocrystals. The Si nanocrystal superlattice is FCC with a lattice constant of $a_{sl,Si}$ = 9.8 nm and the Au nanocrystal superlattice is BCC with a lattice constant $a_{sl,Au}$ = 3.9 nm.

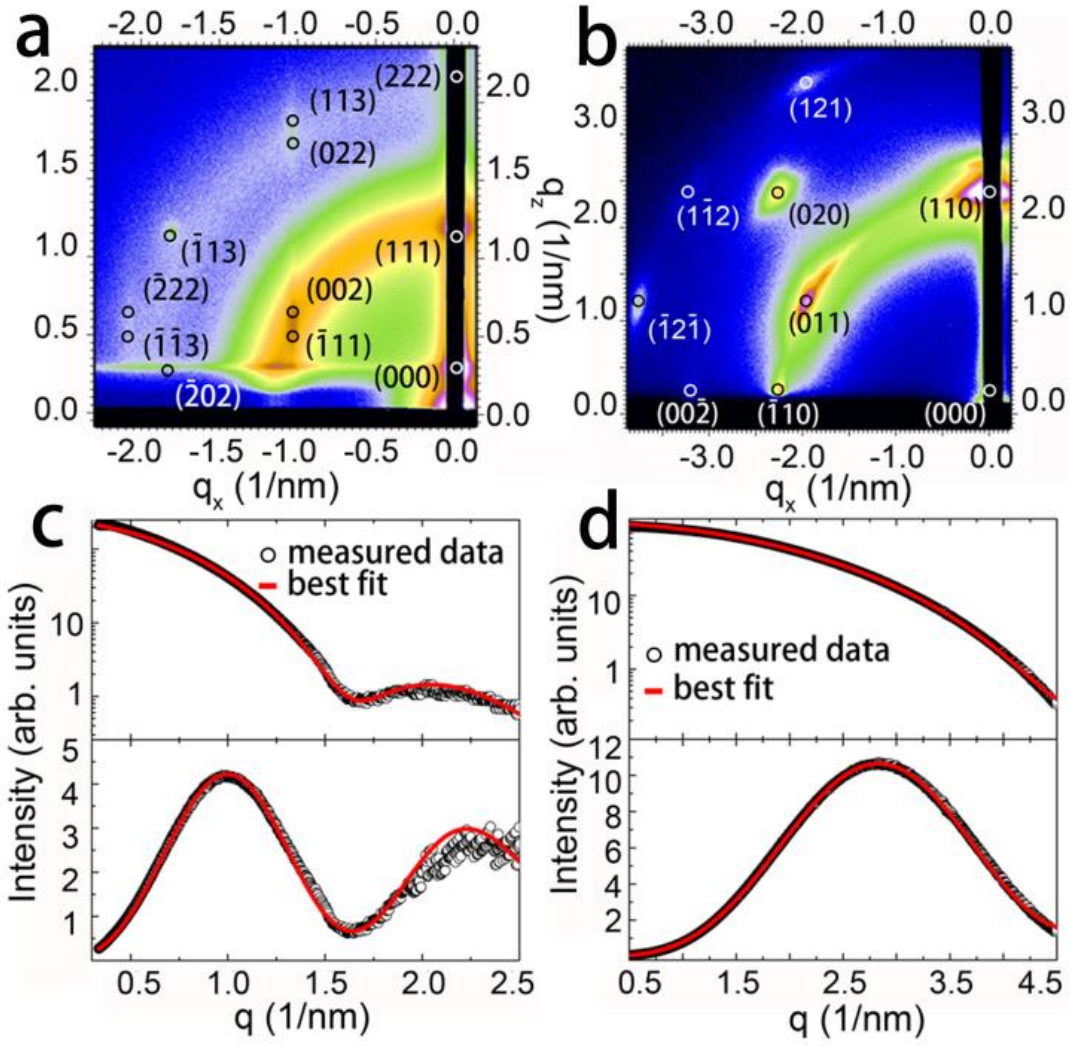

Figure 8.2: GISAXS patterns obtained for superlattices of (a) dodecene-capped Si and (b) dodecanethiol-capped Au nanocrystals used to form BSLs. The diffraction spots index to an (c) FCC superlattice with lattice constant of $a_{sl,Si}$ = 9.8 nm and a (b) BCC superlattice with lattice constant $a_{sl,Au}$ = 3.9 nm. (c,d) SAXS data (black circles) for (c) Si and (d) Au nanocrystals dispersed in toluene The best fits of Eqns (1)-(3) (red lines) to the data gave $\bar{R} = 2.70$ nm ($\sigma = 0.26$ nm) and $\bar{R} = 0.94$ nm ($\sigma = 0.10$ nm) for the Si and Au nanocrystals, respectively.

Figure 8.3 shows TEM images of BSLs formed with the 5.4 nm diameter dodecene-passivated Si nanocrystals and 1.9 nm diameter dodecanethiol-capped Au nanocrystals. The BSL structure is simple hexagonal (sh) AB_2 (A=Si; B=Au) similar to

the intermetallic compound AlB_2 with the larger Si nanocrystals creating a simple hexagonal lattice with smaller Au nanocrystals filling triangular prism interstitial positions. The three different crystallographic projections of the BSLs of $(001)_{bsl}$, $(110)_{bsl}$, and $(100)_{bsl}$ planes viewed down along the lattice directions of $[001]_{bsl}$, $[110]_{bsl}$, and $[210]_{bsl}$, respectively, shown in Figure 8.3, along with indexing of the Fast Fourier transforms (FFTs) of the images are consistent with sh-AB_2 superlattice structure. Figure 8.4 shows a GISAXS pattern for a BSL of the Si and Au nanocrystals. The pattern exhibits distinct diffraction spots indicating that BSL order is of relatively long-range. It indexes to a sh-AB_2 structure with lattice constants of $a_{bsl} = b_{bsl} = 6.70$ nm, $c_{bsl} = 6.45$ nm, $\gamma_{bsl} = 120^o$. These dimensions are similar to those determined by TEM, except that the lattice parameter c_{bsl}, is slightly contracted, by 3.7%. The GISAXS pattern indicates that the superlattice is oriented with $(001)_{bsl}$ planes on the substrate, and therefore, the lattice contraction in the $[001]_{bsl}$ direction occurs *towards the substrate*, most likely as a result of evaporation of solvent retained by the capping ligands after the BSL deposits on the substrate, similar to other evaporated films of BSLs,[13] ordered block copolymers,[28] and mesoporous metal oxides,[29] as illustrated in Figure 8.4c.

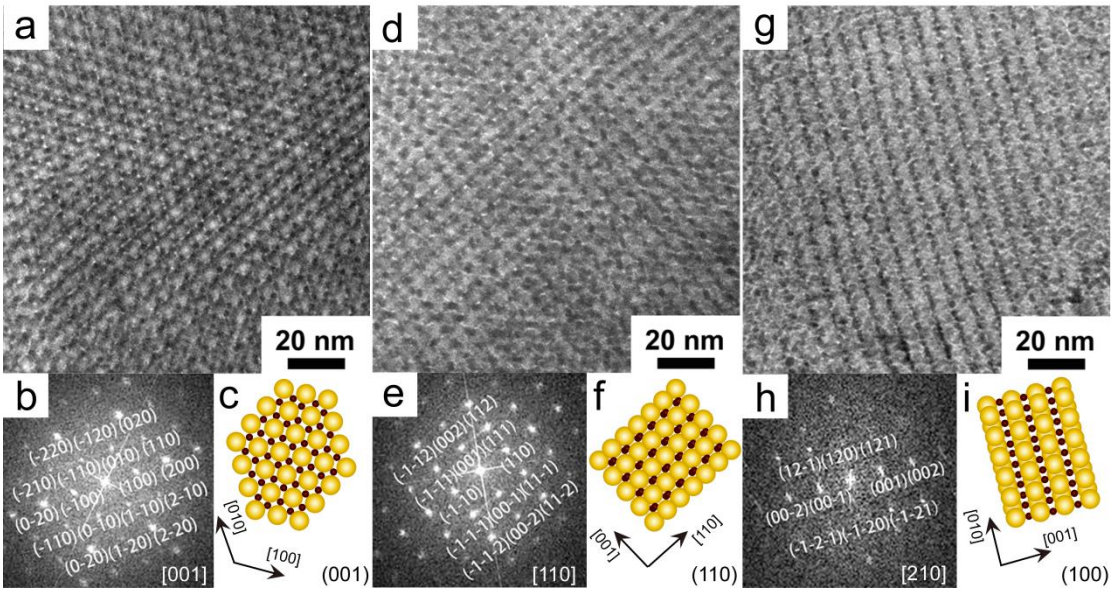

Figure 8.3: TEM images and FFTs of Si/Au BSLs oriented on the grid with different planes: (a,b) $(001)_{bsl}$; (d,e) $(110)_{bsl}$; (g,i) $(100)_{bsl}$. FFTs are indexed to sh-AB_2 structure projections, with zone axes in the bottom left corner of each image. (c) depiction of $(001)_{bsl}$,(f) depiction of $(110)_{bsl}$, and (i) depictions $(100)_{bsl}$ planes of sh-AB_2 BSLs. The d-spacings of $(100)_{bsl}$ and $(001)_{bsl}$ superlattice planes are 5.82 nm and 6.74 nm, corresponding to lattice constants of a_{bsl} = 6.72 nm and c_{bsl} = 6.74 nm.

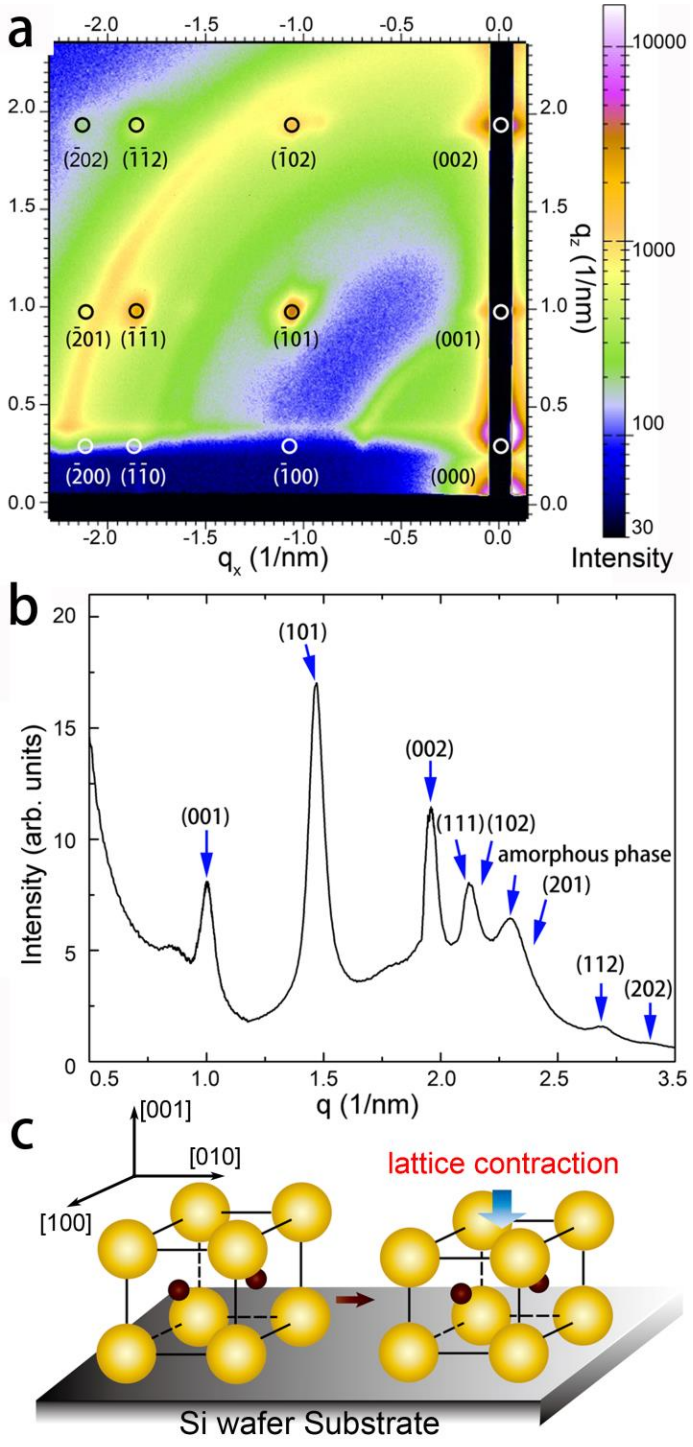
a
(2̄02)
(1̄1̄2)
(1̄02)
(002)
(2̄01)
(1̄1̄1)
(1̄01)
(001)
(2̄00)
(1̄1̄0)
(1̄00)
(000)
q_x (1/nm)
q_z (1/nm)
Intensity
10000
1000
100
30
b
(101)
(002)
(001)
(111)
(102)
amorphous phase
(201)
(112)
(202)
Intensity (arb. units)
q (1/nm)
c
[001]
[010]
[100]
lattice contraction
Si wafer Substrate

Figure 8.4

Figure 8.4: (a) GISAXS pattern of a Si/Au BSL. The pattern indexing corresponds to a simple hexagonal AB_2 structure with lattice constants of $a_{bsl} = b_{bsl} = 6.70$ nm, $c_{bsl} = 6.45$ nm, $\gamma_{bsl} = 120^o$, oriented with the $(001)_{bsl}$ plane on the substrate, which also correspond to a centered orthorhombic (SG 65, *Cmmm*) lattice, with dimensions $a_{bsl} = 6.70$ nm, $b_{bsl} = 11.60$nm, $c_{bsl} = 6.45$ nm, oriented with its $(001)_{bsl}$ plane on the substrate. (b) Radial integration of the GISAXS pattern, clearly showing diffraction peaks corresponding to the lattice planes in BSLs. (c) Depiction of Si/Au sh-AB_2 BSL unit cell oriented on the substrate with its $(001)_{bsl}$ plane. The BSL was contracted a long its $[001]_{bsl}$ direction toward the substrate.

BSL formation was also attempted with larger 6.10 nm diameter Si nanocrystals (9.8% polydispersity) and the 1.9 nm diameter Au nanocrystals, but BSL formation was not observed. The radius ratio for the 5.4 nm diameter Si nanocrystals and the 1.9 nm diameter Au nanocrystals is nearly ideal for sh-AB_2 BSL formation.[13,30] One of the primary driving forces for superlattice formation is space-filling, and entropy encourages the nanocrystals to create the densest structure possible—this is the reason that sterically-stabilized nanocrystals tend to form fcc superlattices.[2] The appropriate value to use to check the efficiency of space-filling by the nanocrystals in the structure is the soft sphere radius, which includes some of the capping ligand layer.[2] For instance, in the pure Si and Au nanocrystal superlattices, the center-to-center nearest neighbor spacing was 6.93 nm and 3.38 nm, respectively. This includes the diameter of the non-deformable inorganic cores of the nanocrystals and part of the organic ligand shell and represents the soft sphere diameters of the nanocrystals. The effective thickness of the ligand shell is therefore 0.76 nm and 0.74 nm for the Si and Au nanocrystals, respectively. Their similar shell thickness is consistent with their similar C_{12} alkyl ligand capping. It should be appreciated that not all of the ligand volume resides in this soft sphere shell, and the remainder of the ligands fill the rest of the interstitial space in the superlattice.[2] The soft sphere diameters of the Si and Au nanocrystals in the BSL were determined by first calculating the Si nanocrystal soft sphere diameter, which is equal to the Si-Si center-to-center nearest neighbor spacing (i.e., the $(001)_{bsl}$ d-spacing of 6.70 nm) and then the Au nanocrystal soft sphere diameter could be calculated by subtracting this value from the Si-Au center-to-center nearest neighbor distance of 5.12 nm. The soft sphere diameter

of the Au nanocrystals in the BSL is then 3.53 nm. The (soft sphere) radius ratio of the Au and Si nanocrystal soft is 0.527, which nearly matches the ideal radius ratio for an sh-AB_2 superlattice of 0.528. The ligand shell thicknesses of the Si and Au nanocrystal soft spheres in the BSL of 0.65 nm and 0.83 nm are also quite close to those in the pure nanocrystal superlattices. It appears that the ligand shell is slightly more compressed for the Si nanocrystals and slightly more expanded for the Au nanocrystals in the BSL.

The thermal stability of the Si-Au BSLs was also studied. Si nanocrystal superlattices are much more stable than Au nanocrystal superlattices at elevated temperature.[23] For instance, superlattices of the Au nanocrystals degrade when heated to 190^{o}C, whereas the Si nanocrystal superlattices retain their structure when heated to at least 200^{o}C. Interestingly, when a BSL was heated in air from 20^{o}C to 200^{o}C, the GISAXS pattern (Figure 8.5a) showed little change, apart from a slight loss in peak intensity. At 200^{o}C, the pattern indexes to a simple hexagonal structure with $a_{bsl} = b_{bsl} =$ 6.69 nm, c_{bsl} = 6.45 nm, $\gamma_{bsl} = 120^o$, with $(001)_{bsl}$ orientation on the substrate. TEM, however, revealed that the Au nanocrystals coalesce when heated above 190^{o}C; for instance, the Au nanocrystals in the TEM image in Figure 8.5b of a BSL heated to 200^{o}C have grown significantly to 8-10 nm diameter. Still, the underlying Si nanocrystal superlattice is intact and the Si nanocrystals have not changed size. An FFT of the TEM image in Figure 8.5b still indexes to a simple hexagonal lattice with similar dimensions as the initial sh-AB_2 BSL. XRD (Figure 8.5c) also showed that Au nanocrystals in the BSL grow significantly when heated to 200^{o}C—i.e, the Au diffraction peaks sharpen significantly—whereas, the Si diffraction peaks remain relatively broad.

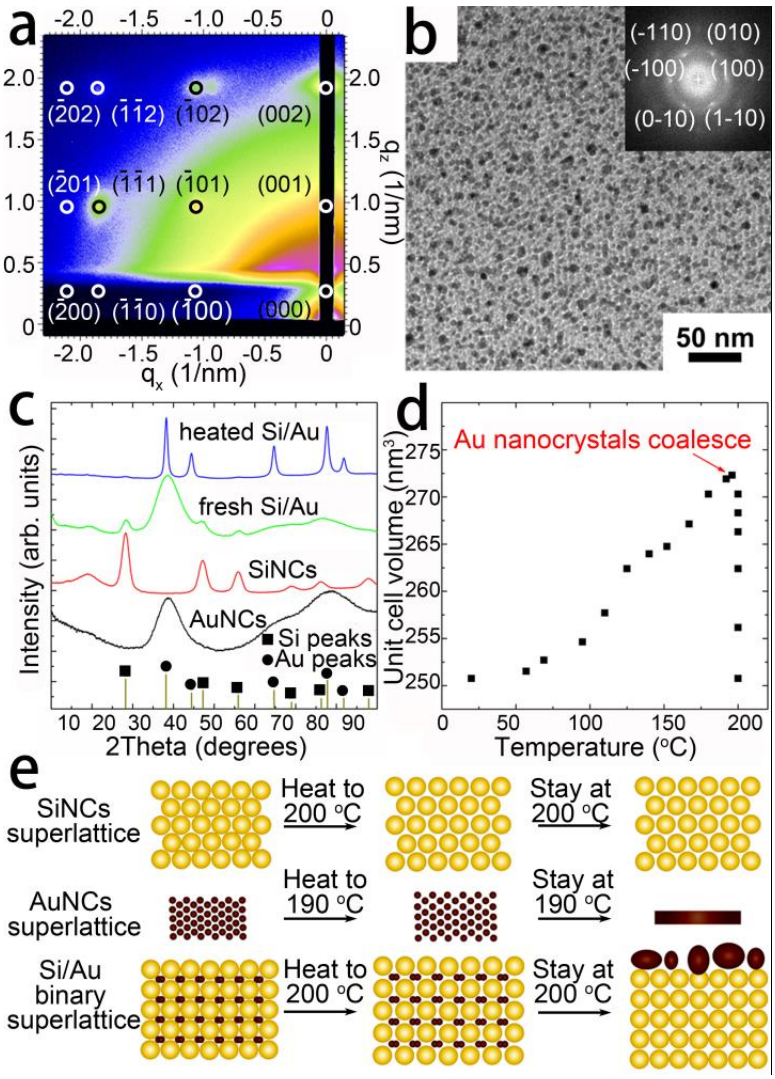

Figure 8.5: (a) GISAXS pattern of Si/Au BSL which was heated at 200°C for 10 minutes. The circles correspond to the simulated spots of simple hexagonal superlattice with lattice constants $a_{bsl} = b_{bsl} = 6.69$ nm, $c_{bsl} = 6.45$ nm, $\gamma_{bsl} = 120^{o}$, oriented on the substrate with its $(001)_{bsl}$ plane. (b) TEM image and FFT of a heated Si/Au BSL oriented on the grid with its $(001)_{bsl}$ plane. (c) XRD of Au nanocrystals, Si nanocrystals, fresh Si/Au BSLs, and heated Si/Au BSLs, showing the coalescence of Au nanocrystals. (d) Plot of unit cell volume of Si/Au BSLs against temperature, which shows slow lattice expansion due to thermal expansion of capping ligands and fast lattice shrinkage due to the Au nanocrystal coalescence. (e) Depiction of thermal behaviors of Si nanocrystal superlattice, Au nanocrystal superlattice, and Si/Au BSLs.

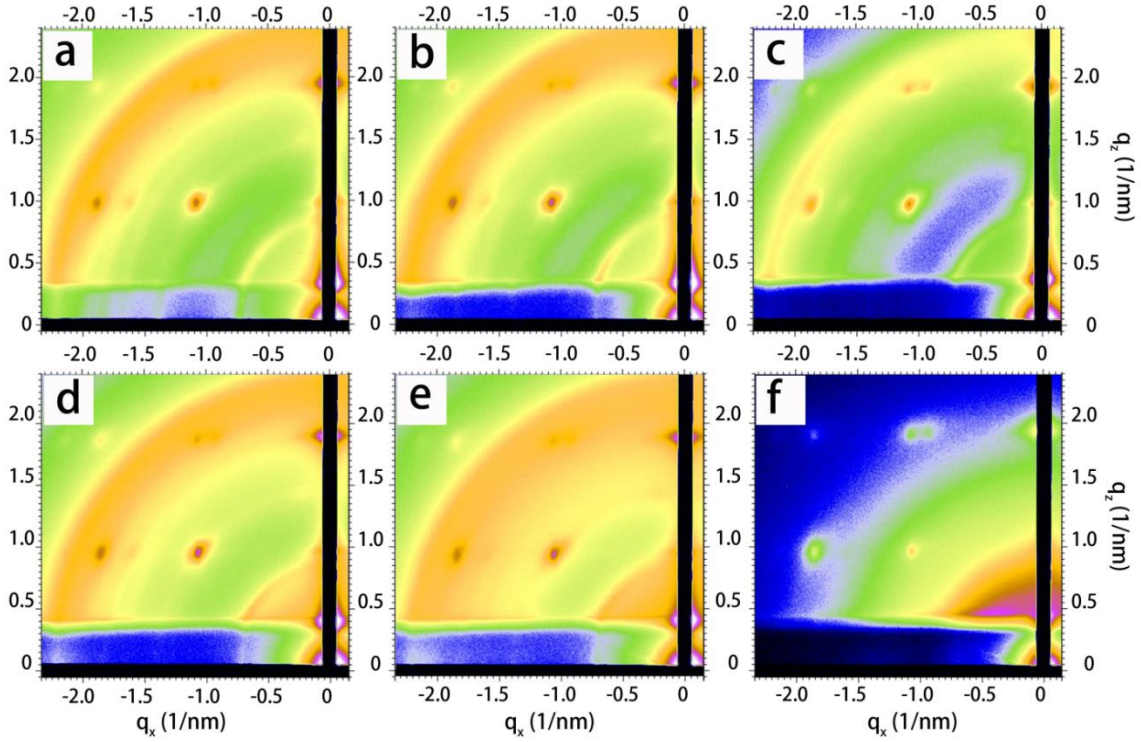

Figure 8.6: GISAXS patterns of a sh-AB_2 BSL of Si and Au nanocrystals heated to various temperatures: (a) 20 ^{o}C, (b) 50^{o} C, (c) 95 ^{o}C, (d) 152 ^{o}C, (e) 199 ^{o}C, and (f) after heating at 200 ^{o}C for 10min.

When the BSL structure was followed by GISAXS during heating from 20^{o}C to 200^{o}C (Figure 8.5), an expansion of the lattice was observed (Figure 8.5d) up to 190^{o}C. Then abruptly at 200^{o}C, the superlattice structure contracted significantly. The lattice expansion results from the thermal expansion of the organic ligands.[31,32] The sharp lattice contraction at 200^{o}C is probably related to migration of the Au nanocrystals from their interstitial positions to the surface of the superlattice, as illustrated in Figure 8.4e. The surprising result is that despite the loss of Au nanocrystals from the BSL, the simple hexagonal Si nanocrystal structure remains intact, despite its very low packing density. The reason for the retention of sh structure is probably related to two factors. First, the

Si nanocrystals do not coalesce. Unlike the Au nanocrystals, the Si nanocrystals are stable at 200^{o}C and retain their primary particle size. This might be related to the Si cores, but the ligands are also covalently bonded (Si-C) to the Si surface and do not desorb at this low temperature. The second reason is probably that the energy barrier to transform the simple hexagonal superlattice into the thermodynamically preferred fcc structure is substantial. Such a superlattice rearrangement requires shifting entire lattice planes by nearly a particle radius (i.e., $R\sqrt{3}/2$). The van der Waals attraction between neighboring nanocrystals is too high to overcome in the timeframe of the experiment.

Figures 8.7-8.9 show low magnification TEM images of ordered domains of Si/Au binary superlattices covering areas of about 10 μm^2.

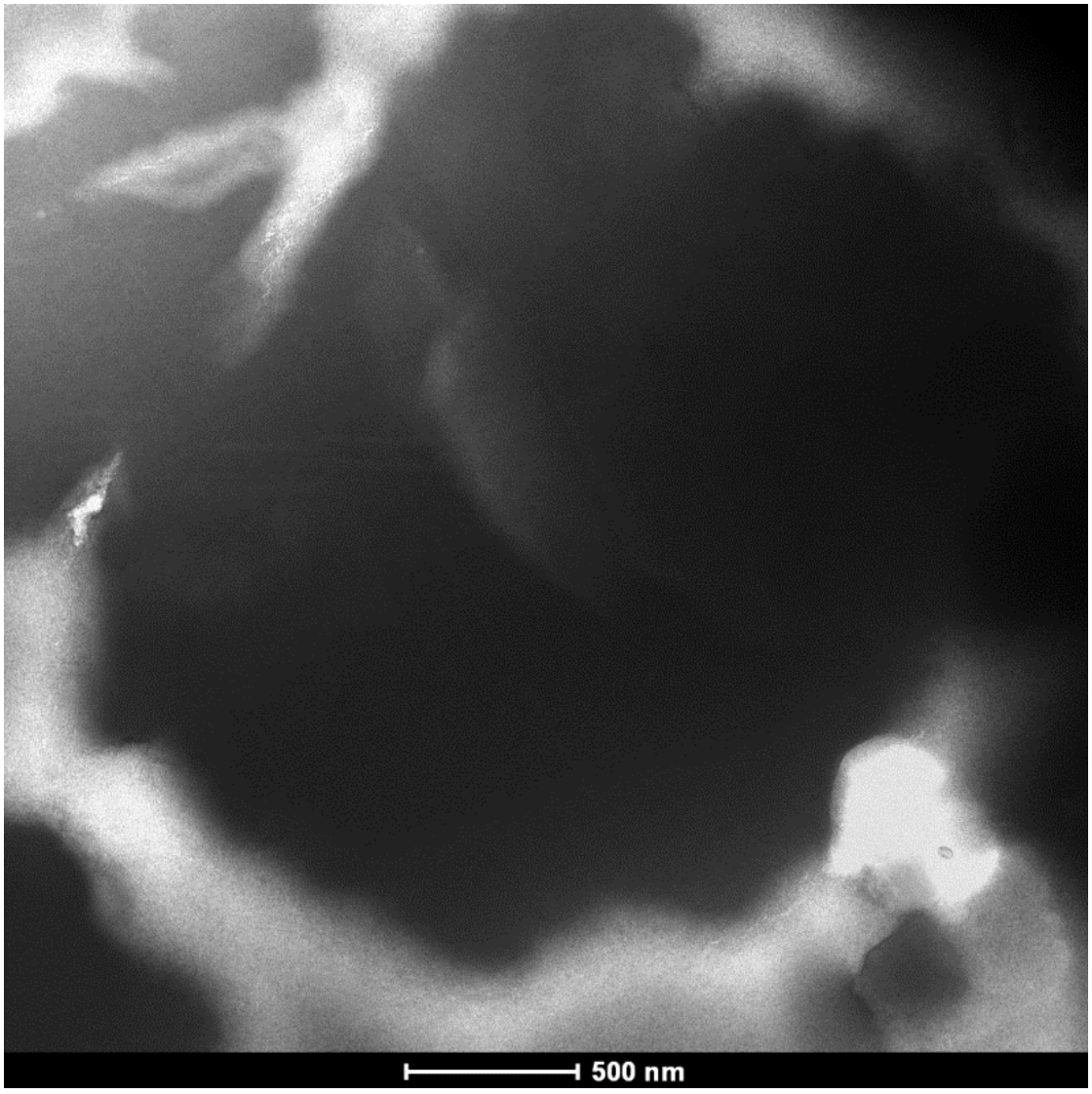

Figure 8.7: Low magnification TEM image of a BSL domain covering ~10 μm^2.

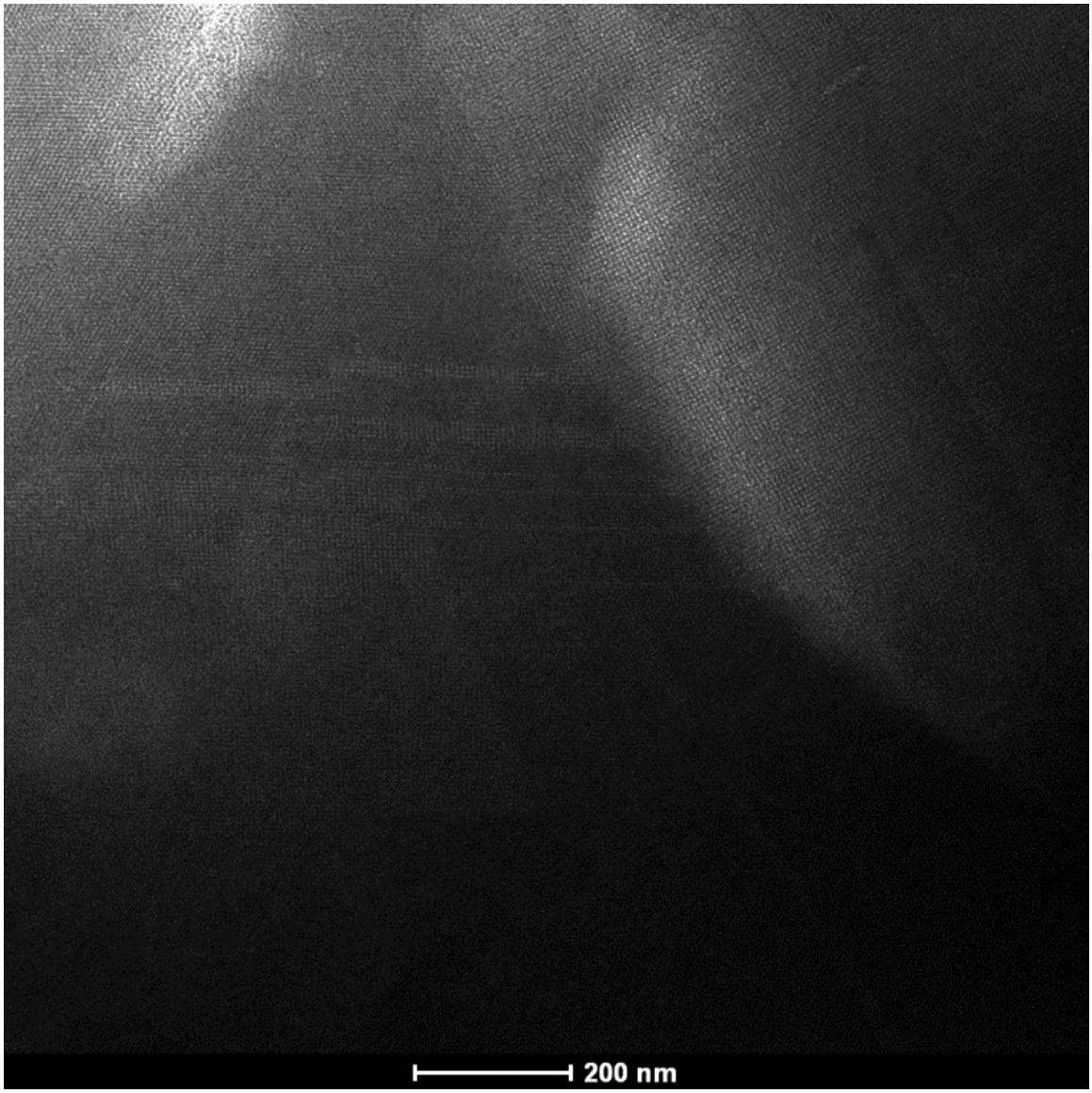

Figure 8.8: TEM image of the BSL in Figure 8.7 with slightly higher magnification.

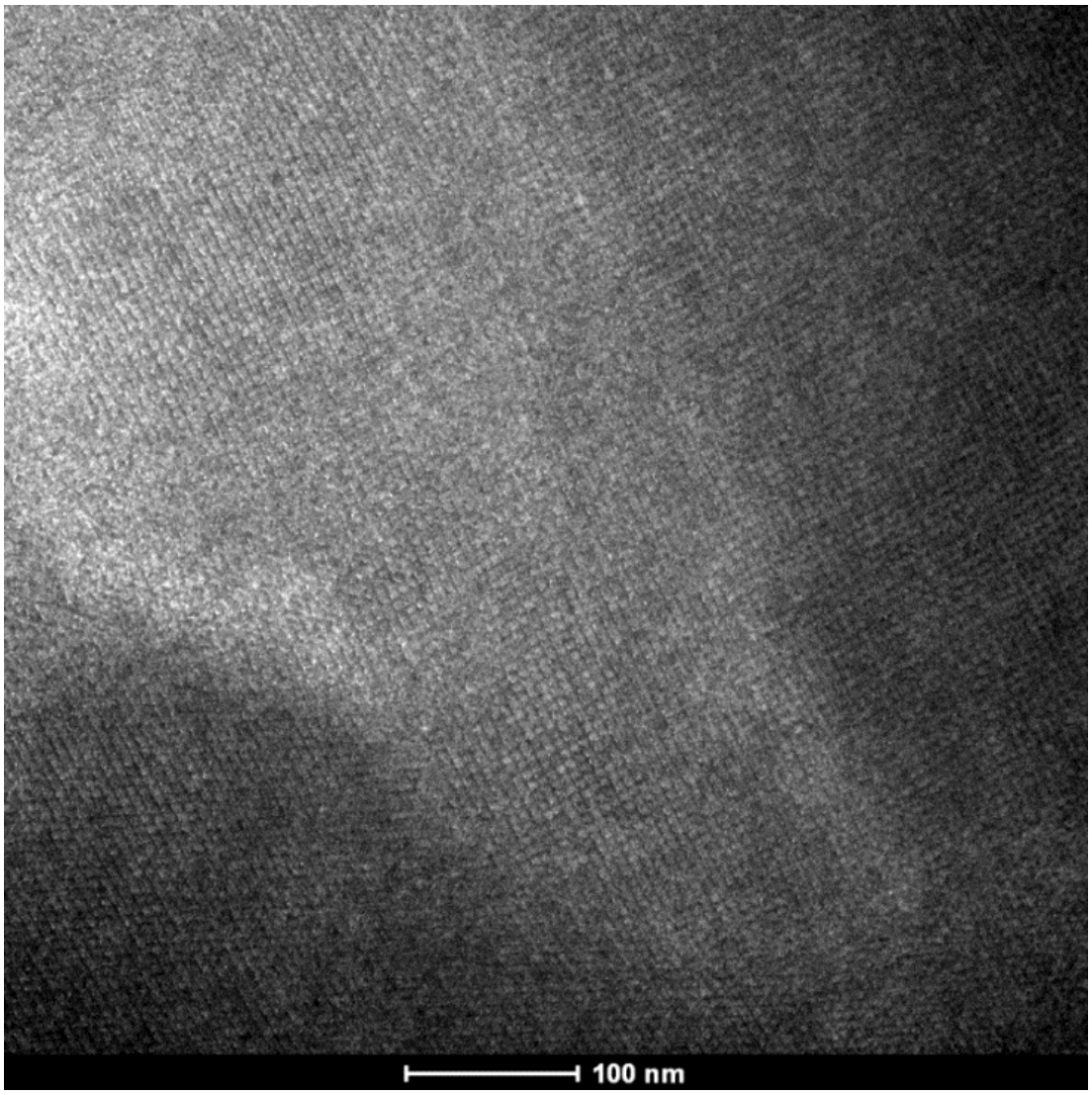

Figure 8.9: TEM image of the BSL shown in Figures 8.7 and 8.8 with slightly higher magnification than Figure 8.8.

Figure 8.10 shows a monolayer of Si and Au nanocrystals, confirming that both Si and Au nanocrystals deposit on the substrate. However, BSL formation was not observed from nanocrystals with this size ratio. A superlattice is shown in Figure 8.11 in which only Si nanocrystals was observed. A GISAXS pattern (Figure 8.12) of a superlattice of

6.10 nm diameter Si nanocrystals indexed to an FCC structure with lattice constant a_{sl} = 10.6 nm, oriented on the substrate with $(111)_{sl}$ plane.

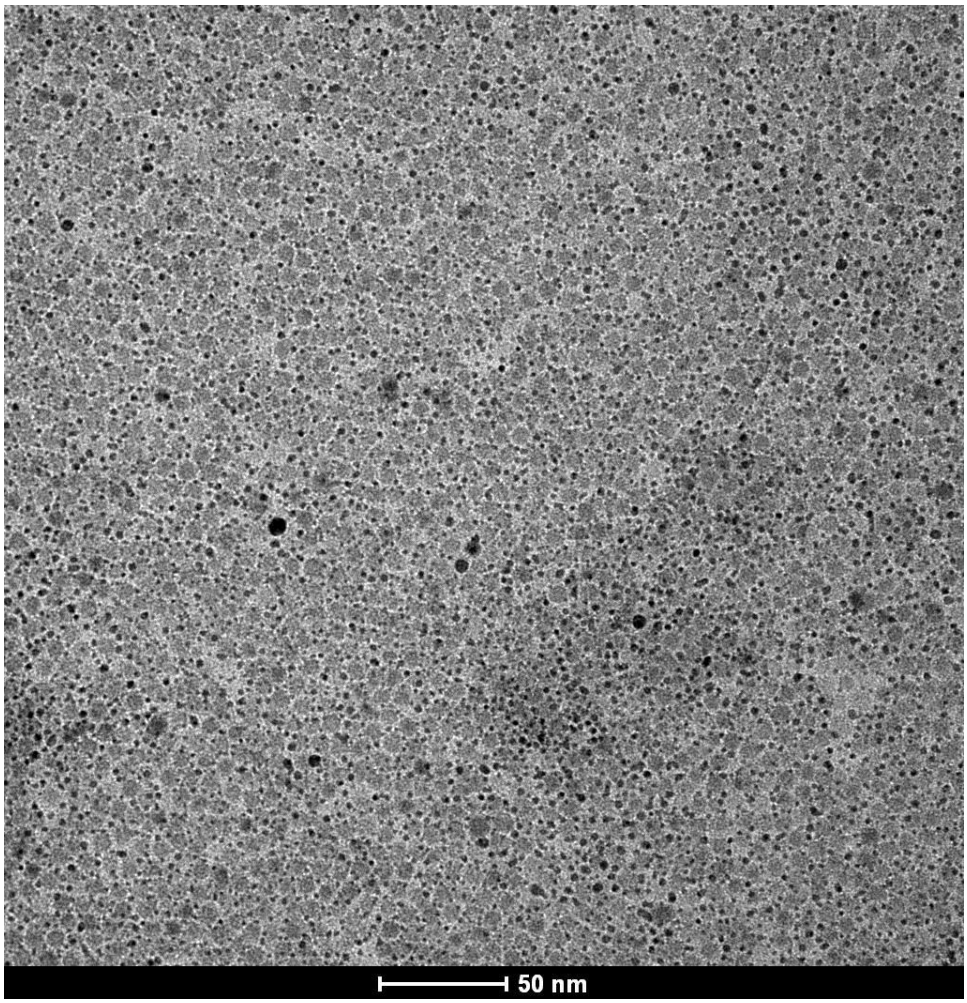

Figure 8.10: TEM image of a monolayer of 6.10 nm Si and 1.88 nm Au nanocrystals.

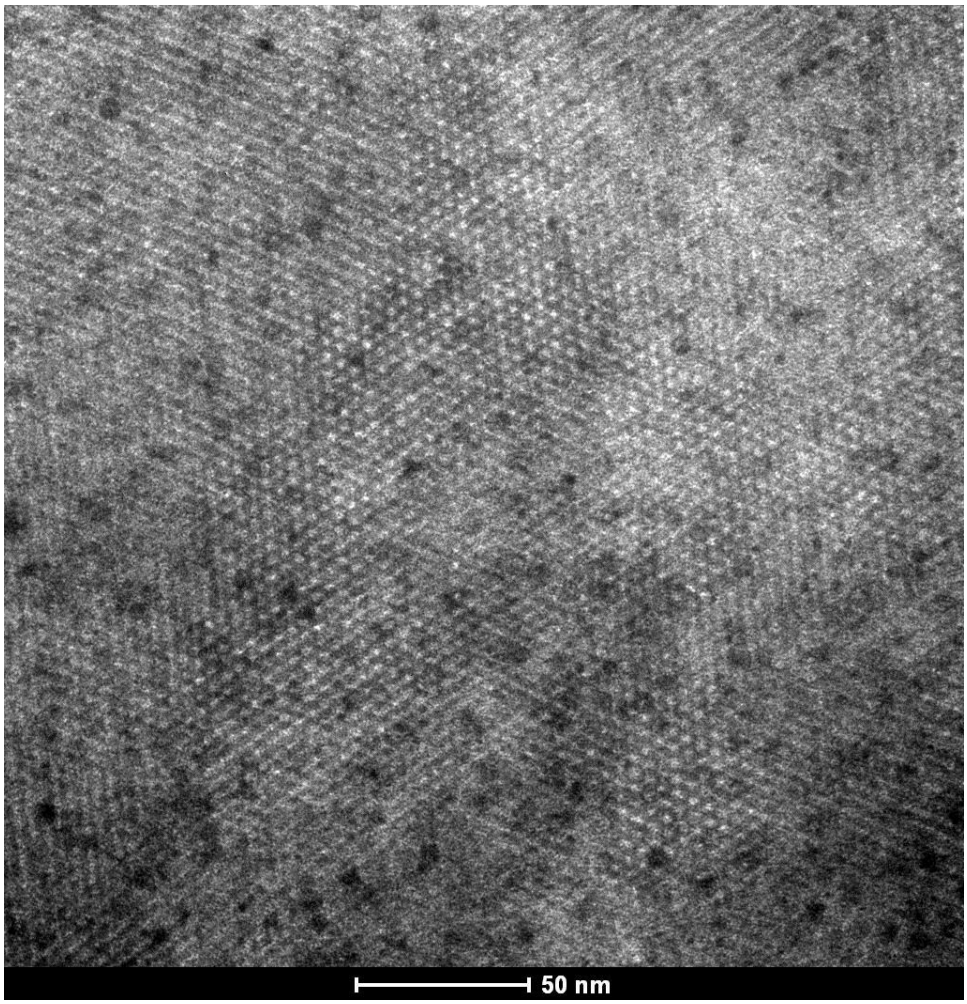

Figure 8.11: TEM image of an ordered superlattice of Si nanocrystals of 6.1 nm Si nanocrystals.

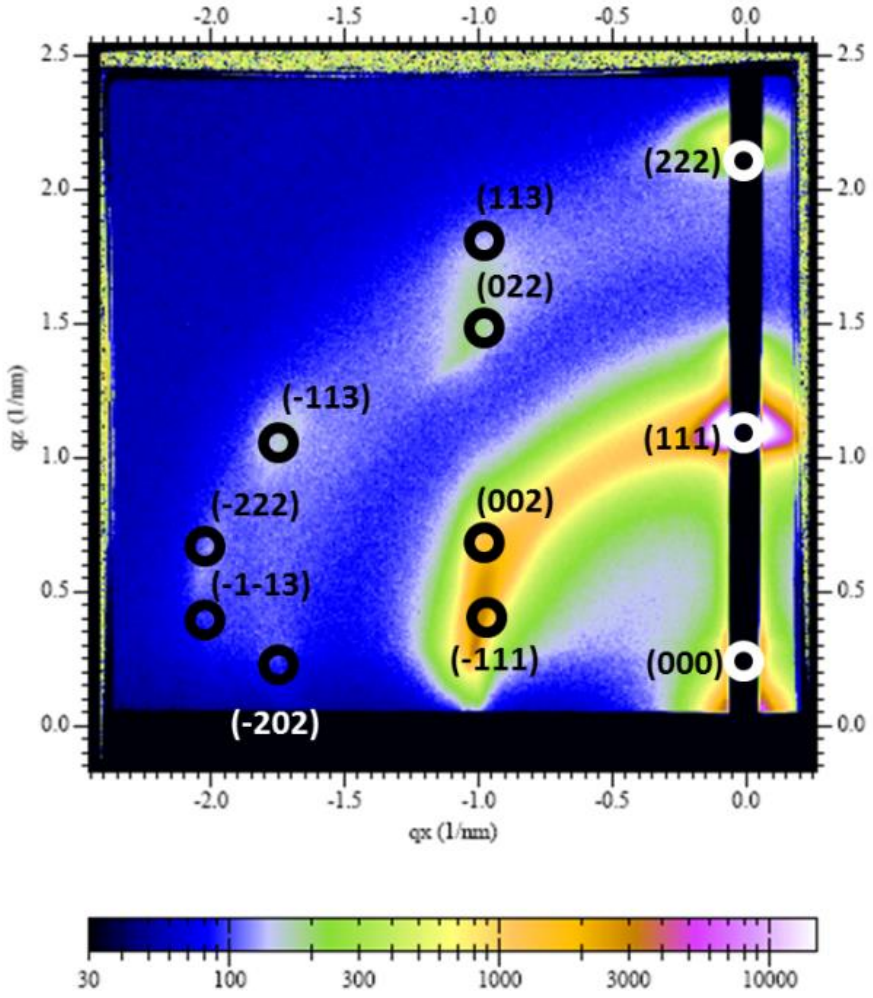

Figure 8.12: GISAXS pattern of 6.10 diameter Si nanocrystal superlattice.

Si and Au nanocrystal superlattices were heated while acquiring GISAXS data. Figure 8.13 shows GISAXS patterns for 1.88 nm Au nanocrystal superlattice during heating. The similar diffraction spots were present before the sample was heated to 190^{o}C indicating that the superlattice structure was stable below 190^{o}C. The diffraction spots disappeared when the temperature reached 190^{o}C, indicating that the superlattice sintered after reaching 190^{o}C. Figure 8.14 shows a GISAXS patterns for 5.40 nm Si

nanocrystal superlattice during heating, showing that the superlattice structure was stable at these temperatures up to at least 200^{o}C.

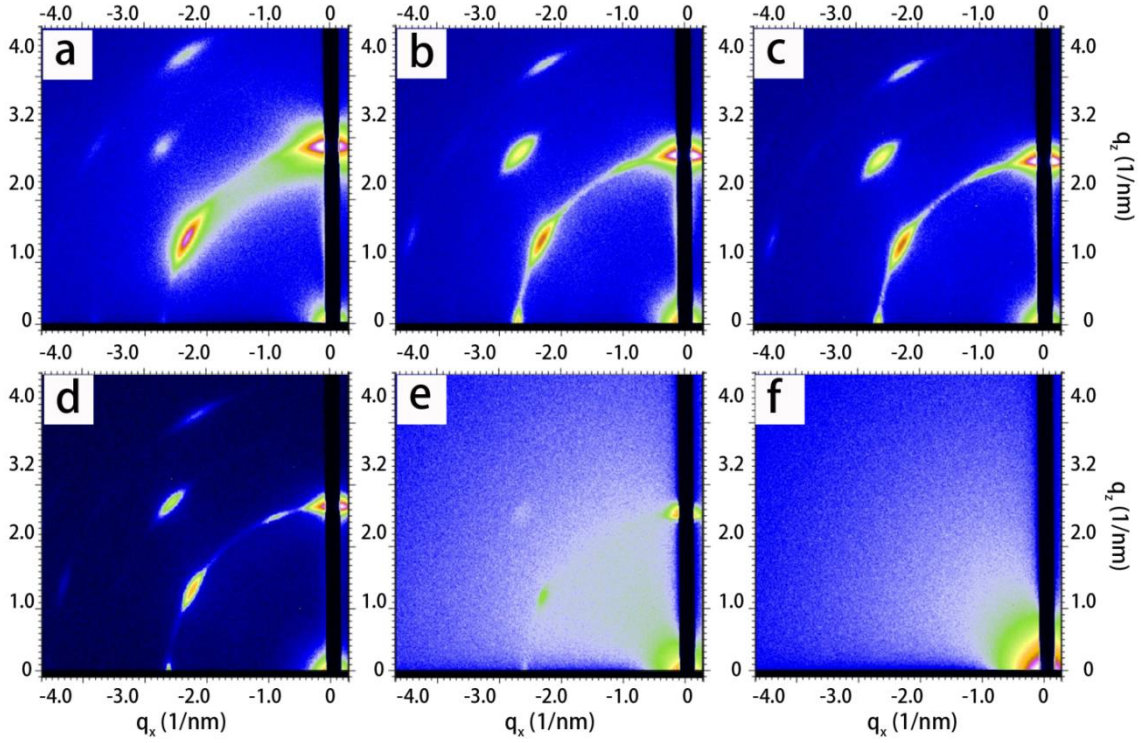

Figure 8.13: GISAXS patterns of 1.88 nm diameter 1-dodecanethiol-capped Au nanocrystal superlattice at various temperatures: (a) 50 ^{o}C; (b) 100 ^{o}C; (c) 140 ^{o}C; (d) 180 ^{o}C; (e) 190 ^{o}C; (f) 200 ^{o}C.

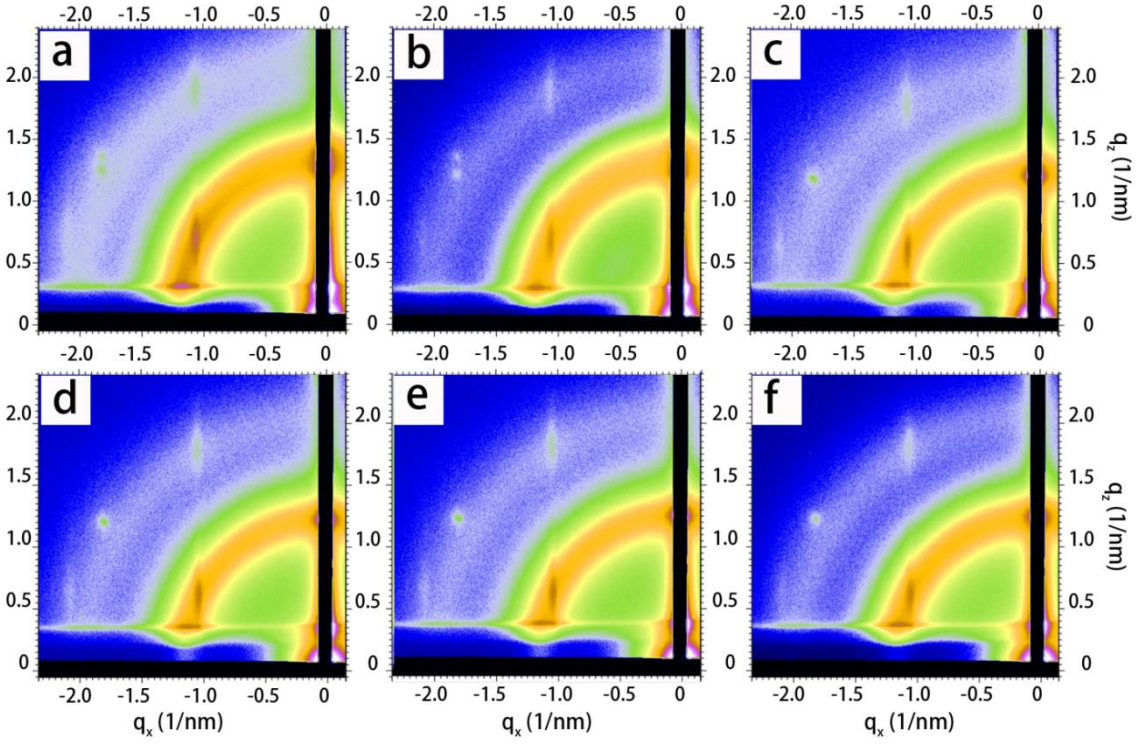

Figure 8.14: GISAXS patterns of 5.40 nm diameter 1-dodecene-capped Si nanocrystal superlattice at various temperatures: (a) 50 ^{o}C; (b) 110 ^{o}C; (c) 170 ^{o}C; (d) 190 ^{o}C; (e) 195 ^{o}C; (f) 200 ^{o}C.

8.4 CONCLUSION

In conclusion, Si nanocrystals have been used to form BSLs for the first time. It will be interesting to measure the optical and optoelectronic properties of these Au/Si BSLs. Si nanocrystals, or quantum dots, exhibit bright luminescence that can be tuned by size from visible to near-infrared wavelengths,[24,33,34] but the radiative rate for electron-hole recombination and light emission is typically very slow due to the indirect band gap of Si—usually 10-100 μs.[35,36] since One strategy to enhance the optical properties of Si nanocrystals, or quantum dots, is to position them near a material with a plasmonic

optical response, such as Au.[16,-37-40] BSLs can provide a unique experimental testbed for examining optical interactions between Si and Au. The Au/Si BSLs also reveal a new approach to creating superlattices with open structures. In this case, a simple hexagonal superlattice of Si nanocrystals is created by heating the Si/Au BSL to drive the Au out of the lattice. Instead of tuning interparicle interactions and the self-assembly process,[9,11] one of the nanocrystals in the BSL, such as Au nanocrystals in this case, serve as a sacrificial or removable "skeleton" that enables the formation of a metastable open network of nanocrystals, such as the simple hexagonal superlattice of Si nanocrystals shown here. The Si nanocrystals are rather unique in terms of their thermal stability relative to other sterically stabilized nanocrystals, but this result shows it might be possible to create a variety of metastable superlattice structures by converting BSLs to kinetically trapped structures.

8.5 REFERENCE

(1) Murray, C. B.; Kagan, C. R.; Bawendi, M. G. Self-Organization of CdSe Nanocrystallites into Three-Dimensional Quantum Dot Superlattices. *Science* **1995**, *270*, 1335-1338.

(2) Korgel, B. A.; Fullam, S.; Connolly, S.; Fitzmaurice, D. Assembly and Self-Organization of Silver Nanocrystal Superlattice: Ordered "Soft Spheres" *J. Phys. Chem. B* **1998**, *102*, 8379-8388.

(3) Redl, F. X.; Cho, K.-S.; Murray, C. B.; O'Brien, S. Three-Dimensional Binary Superlattice of Magnetic nanocrystals and semiconductor quantum dots. *Nature* **2003**, *423*, 968-971.

(4) Shevchenko, E. V.; Talapin, D. V.; Kotov, N. A.; O'Brien, S.; Murray, C. B. Structural Diversity in Binary Nanoparticle Superlattices. *Nature* **2006**, *439*, 55-59.

(5) Doty, R. C.; Bonnecaze, R. T.; Korgel, B. A. Kinetic Bottleneck to the Self-Organization of Bidisperse Hard Disk Monolayers Formed by Random Sequential Adsorption. *Phys. Rev. E* **2002**, *65*, 061503.

(6) Miszta, K.; de Graaf, J.; Bertoni, G.; Dorfs, D.; Brescia, R.; Marras, S.; Ceseracciu, L.; Cingolani, R.; van Roij, R.; Dijkstra, M.; Manna, L. Hierarchical Self-

Assembly of Suspended Branched Colloidal Nanocrystals into Superlattice Structures. *Nature Mater.* **2011**, *10*, 872-876.
(7) Goubet, N.; Richardi, J.; Albouy, P. A.; Pileni, M. P. How to Predict the Growth Mechanism of Supracrystals from Gold Nanocrystals. *J. Phys. Chem. Lett.* **2011**, *2*, 417-422.
(8) Dylla, R. J.; Korgel, B. A. Temporal Organization of Nanocrystal Self-Assembly Directed by a Chemical Oscillator. *ChemPhysChem* **2001**, *1*, 61-64.
(9) Bishop, K. J. M.; Chevalier, N. R.; Grzybowski, B. A. When and Why Like-Sized, Oppositely Charged Particles Assemble into Diamond-like Crystals. *J. Phys. Chem. Lett.* **2013**, *4*, 1507-1511.
(10) Son, J. S.; Lee, J.-S.; Shevchenko, E. V.; Talapin, D. V. Magnet-in-the-Semiconductor Nanomaterials: High Electron Mobility in All-Inorganic Arrays of FePt/CdSe and FePt/CdS Core-Shell Heterostructures. *J. Phys. Chem. Lett.* **2013**, *4*, 1918-1923.
(11) Macfarlane, R. J.; Jones, M. R.; Lee, B.; Auyeung, E.; Mirkin, C. A. Topotactic Interconversion of Nanoparticle Superlattices. *Science* **2013**, *341*, 1222-1225.
(12) Ben-Simon, A.; Eshet, H.; Rabani, E. On the Phase Behavior of Binary Mixtures of Nanoparticles. *ACS Nano* **2013**, *7*, 978-986.
(13) Smith, D. K.; Goodfellow, B.; Smilgies, D.-M.; Korgel, B. A. Self-Assembled Simple Hexagonal AB_2 Binary Nanorystal Superlattices: SEM, GISAXS, and Defects. *J. Am. Soc. Chem.* **2009**, *131*, 3281-3290.
(14) Shevchenko, E. V.; Talapin, D. V.; Murray, C. B.; O'Brien, S. Structural Characteriztion of Self-Assembled Multifunctional Binary Nanoparticle Superlattices. *J. Am. Soc. Chem.* **2006**, *128*, 3620-3637.
(15) Saunders, A. E.; Korgel, B. A. Observation of an AB Phase in Bidisperse Nanocrystal Superlattice. *ChemPhysChem* **2005**, *6*, 61-65.
(16) Shevchenko, E. V.;Ringler, M.; Schwemer, A.; Talapin, D. V.; Klar, T. A.; Rogach, A. L.; Feldmann, J.; Alivisatos, A. P. Self-Assembled Binary Superlattices of CdSe and Au nanocrystals and Their Fluorescence Properties. *J. Am. Soc. Chem.* **2008**, *130*, 3274-3275.
(17) Lu, C.; Chen, Z.; O'Brien, S. Optimized Conditions for the Self-Organization of CdSe-Au and CdSe-CdSe Binary Nanoparticle Superlattices. *Chem. Mater.* **2008**, *20*, 3594-3600.
(18) Evers, W. H.; De Nijs, B.; Filion, L.; Castillo, S.; Dijkstra, M.; Vanmaekelbergh, D. Entropy-Driven Formation of Binary Semiconductor-Nanocrystal Superlattices. *Nano Lett.* **2010**, *10*, 4235-4241.
(19) Lee, D. C.; Smith, D. K.; Heitsch, A. T.; Korgel, B. A. *Annu. Rep. Prog. Chem., Sect. C: Phys. Chem.* **2007**, *103*, 351-402.
(20) Shevchenko, E. V.; Kortright, J.; Talapin, D. V.; Aloni, S.; Alivisatos, A. P. Quasi-Ternary Nanoparticle Superlattices Through Nanoparticle Design. *Adv. Mater.* **2007**, *19*, 4183-4188.
(21) Evers, W. H.; Friedrich, H.; Filion, L.; Dijkstra, M.; Vanmaekelbergh, D. Observation of a Ternary Nanocrystal Superlattice and Its Structural

Characterization by Electron Tomography. *Angew. Chem. Intl. Ed.* **2009**, *48*, 9655-9657.
(22) Dong, A.; Ye, X.; Chen, J.; Murray, C. B. Two-Dimensional Binary and Ternary Nanocrystal Superlattices: The Case of Monolayers and Bilayers. *J. Am. Chem. Soc.* **2011**, *11*, 1804-1809.
(23) Yu, Y.; Bosoy, C. A.; Hessel, C. M.; Smilgies, D.-M.; Korgel, B. A. Silicon Nanocrystal Superlattices. *ChemPhyChem* **2013**, *14*, 84-87.
(24) Hessel, C.M.; Reid, D.; Panthani, M. G.; Rasch, M. R., Goodfellow, B. G.; Wei, J.; Hiromasa, F.; Akhavan, V.; Korgel, B. A. Synthesis of Ligand-Stabilized Silicon Nanocrystals with Size-Dependent Photoluminescence Spanning Visible to Near-Infrared Wavelengths. *Chem. Mater.* **2012**, *24*, 393-401.
(25) Panthani, M. G.; Hessel, C. M.; Reid, D.; Casillas, G.; Jose-Yacaman, M.; Korgel, B. A. Graphene-Supported High-Resolution TEM and STEM Imaging of Silicon Nanocrystals and their Capping Ligands. *J. Phys. Chem. C* **2012**, *116*, 22463-22468.
(26) Brust, M.; Walker, M.; Bethell, D.; Schiffrin, D. J.; Whyman, R. Synthesis of Thiol-Derivatised Gold Nanoparticles in a Two-Phase Liquid-Liquid System. *J. Chem. Soc., Chem. Commun.* **1994**, 801-802.
(27) Rasch, M. R.; Rossinyol, E.; Hueso, J. L.; Goodfellow, B. W.; Arbiol, J.; Korgel, B. A. Hydrophobic Gold Nanoparticle Self-Assembly with Phosphatidylcholine Lipid: Membrane-Loaded and Janus Vesicles. *Nano Lett.* **2010**, *10*, 3733-3739.
(28) Bosworth, J. K.; Paik, M. Y.; Ruiz, R.; Schwartz, E. L.; Huang, J. Q.; Ko, A. W.; Smilgies, D. M., Black, C. T.; Ober C. K. Control of Self-Assembly of Lithographically Patterned Block Copolymer Films. *ASC Nano* **2008**, *2*, 1396-1402.
(29) Ruland, W.; Smarsly, B. M. Two-Dimensional Small-Angle X-Ray Scattering of Self-Assembled Nanocomposite Films with Oriented Arrays of Spheres: Determination of Lattice Type, Preferred Orientation, Deformation and Imperfection. *J. Appl. Cryst.* **2007**, *40*, 409-417.
(30) Bodnarchuk, M. I.; Kovalenko, M. V.; Heiss, W.; Talapin, D. V. Energetic and Entropic Contributions to Self-Assembly of Binary Nanocrystal Superlattices: Temperature as the Structure-Directing Factor. *J. Am. Chem. Soc.* **2010**, *132*, 11967-11977.
(31) Korgel, B. A.; Zaccheroni, N.; Fitzmaurice, D. "Melting Transition" of a Quantum Dot Solid: Collective Interactions Influence the Thermally-Induced Order-Disorder Transition of a Silver Nanocrystal Superlattice. *J. Am. Chem. Soc.* **1999**, *121*, 3533-3534.
(32) Korgel, B. A. Correlated Membrane Fluctuations in Nanocrystal Superlattices. *Phys. Rev. Lett.*, **2001**, *86*, 127-130.
(33) Hessel, C. M.; Rasch, M. R.; Hueso, J. L.; Goodfellow, B. W.; Akhavan, V. A.; Puvanakrishnan, P.; Tunnel, J. W.; Korgel, B. A. Alkyl Passivation and Amphiphilic Polymer Coating of Silicon Nanocrystals for Diagnostic Imaging. *Small*, **2010**, *6*, 2026-2034.

(34) Puzzo, D. P.; Henderson, E. J.; Helander, M. G.; Wang, Z.; Ozin, G. A.; Lu, Z. Visible Colloidal Nanocrystal Silicon Light-Emitting Diode. *Nano Lett.* **2011**, *11*, 1585-1590.
(35) Vial, J. C.; Bsiesy, A.; Gaspard, F.; Hérino, R.; Ligeon, M.; Muller, F.; Romestain, R. Mechanisms of Visible-Light Emission from Electro-Oxidized Porous Silicon. *Phys. Rev. B* **1992**, *45*, 14171-14176.
(36) Mastronardi, M. L.; Maier-Flaig, F.; Faulkner, D.; Henderson, E. J.; Kübel, C.; Lemmer, U.; Ozin, G. A. Size-Dependent Absolute Quantum Yield for Size-Separated Colloidally-Stable Silicon Nanocrystals. *Nano Lett.* **2012**, *12*, 337-342.
(37) Huh, C.; Choi, C.-J.; Kim, W.; Kim, B. K.; Park, B.-J.; Jang, E.-H.; Kim, S.-H.; Sung, G. Y. Enhancement in Light Emission Efficiency of Si Nanocrystal Light-Emitting Diodes by Surface Plasmon Coupling. *Appl. Phys. Lett.* **2012**, *100*, 181108.
(38) Takeda, E.; Nakamura, T.; Fujii, M.; Miura, S.; Hayashi, S. Surface Plasmon Polarity Mediated Photoluminescence from Excitons in Silicon Nanocrystals. *Appl. Phys. Lett.* **2006**, *89*, 101907.
(39) Biteen, J. S.; Pacifici, D.; Lewis, N. S.; Atwater, H. A. Enhanced Radiative Emission Rate and Quantum Efficiency in Coupled Silicon nanocrystal-Nanostructured Gold Emitters. *Nano Lett.* **2005**, *5*, 1768-1773.
(40) Ratchford, D.; Shafiei, F.; Kim, S.; Gray, S. K.; Li X. Manipulating Coupling between a Single Semiconductor Quantum Dot and Single Gold Nanoparticle. *Nano Lett.* **2011**, *11*, 1049-1054.

Chapter 9: The Underlying Role of Halide Surfactants in Ordered Structure Transitions of Heated Gold Nanocrystal Superlattices

9.1 INTRODUCTION

Ligand-stabilized nanocrystals in the quantum regime exhibit physical properties that are fundamentally different from their bulk counterparts and can be tuned synthetically by manipulating their size.[1-3] Owing to the collective electronic coupling between the neighboring nanocrystals,[4] ordered assembly of uniform nanocrystals, or superlattice, exhibit interesting new properties, which depend on their superlattice structure.[5] In this case, nanocrystal serves as building blocks to form "artificial solids" or "metamaterials",[6,7] which is an analog to real solids. Most of the solids exhibit structure polymorphism, for example, diamond and graphite for carbon, α-Fe (body-centered cubic, BCC) and γ-Fe (face-centered cubic, FCC) for iron, α-Al_2O_3 (rhombohedral) and γ-Al_2O_3 (cubic spinel) for alumina. These structures can transform between each other in response to environment conditions, like temperature or pressure. Superlattices can also show structural polymorphism. PbSe and PbS nanocrystal superlattice have been shown to have BCC to FCC and body-centered tetragonal (BCT) phase transition via solvent annealing.[8, 9] Binary superlattice consisting of same nanocrystals can self-assembled to different structures, depending on the deposition conditions.[10-13] Our group have shown heating can cause sub-2 nm diameter dodecanthiol-capped Au nanocrystal supperlattice to rearrange from BCC to hexagonal closed-packed structure (HCP), to simple cubic AB_{13}, to hexagonal AB_5, and finally to coalesced phase.[14]

Temperature and solvents have already found to be important in polymorphism of both solids [37,38] and nanocrystal superlattices.[8,10] Generation of polymorphs and transitions between polymorphs in solids are significantly influenced by additives or impurities. For instance, introducing sulfur additive to calcium carbide would lead to two polymorphs when cooling from 600 to -200^{o}C: high temperature cubic phase IV and middle temperature tetragonal phase II, while pure calcium carbide show 4 polymorphs under the same condition;[39] adding a small amount of carbon (<0.02%) to iron will result in a much lower phase transition temperature from α-Fe to γ-Fe.[22] The role of additives in transitions between nanocrystal superlattice polymorphs has not been studied.

Ligand stabilized nanocrystal consists of rigid inorganic nanocrystal core and flexible yet incompressible organic ligands.[15,16] The ligand shell occupies a significant amount of volume of superlattice, up to around 90% in the case of sub-2 nm diameter Au nanocrystal, which make nanocrystal quite different from hard-sphere particles. Hard spheres, i.e. opals[17,18] tend to form close-packed lattice like FCC to achieve the highest packing density (74%), while dodecanethiol-capped sub-2 nm diameter Au nanocrystals tend to assemble to a BCC (packing density: 68%) superlattice. The flexible ligand shell is also responsible for structural transitions in PbSe and PbS nanocrystals superlattice during solvent annealing.

Here, we report the necessity of halide ion additives in heating-induced structural transitions of dodecanethiol-capped sub-2 nm Au nanocrystal superlattice, and discuss the role of halide ion additives based on halide additive-capping ligand interactions.

9.2 EXPERIMENTAL DETAILS

9.2.1 Materials

Gold (III) chloride trihydrate ($HAuCl_4 \cdot 3H_2O$, >99.9%), tetraoctylammonium bromide (TOAB, 98%), tetraoctylphosphonium bromide (TOPB, 97%), tetraoctylammonium hydrogen sulfate (TOAHS, 97%) 1-dodecanthiol (>98%), sodium borohydride ($NaBH_4$,>98%), hexadecanol (>99%), dodecylamine (98%), hexadecane (99%), dodecanoic acid (98%), dibenzyl ether (99%), tetrabutylammonium bromide (>98%), tetraheptylammonium bromide (>99%), tetraoctadecylammonium bromide (98%), and tetraoctylammonium chloride (>97%) were purchased from Sigma-Aldrich. Toluene (99.9%) was purchased from Fisher. Tetraoctylammonium iodide (THAI, >99%), cetyltrimethylammonium bromide (CTAB, >96%), cetyltrimethylammonium chloride (CTAC, >96%) was purchased from Fluka. All chemicals were used as received and water was doubly-distilled and deionized.

9.2.2 Au Nanocrystal Synthesis

Au nanocrystals were synthesized using a modified Brust-Schiffrin method.[23,24] In a typical synthesis, 20 mL of an aqueous solution of 328 mg of gold (III) chloride trihydrate ($HAuCl_4 \cdot 3H_2O$, 0.83 mmol) is mixed with 80 mL of toluene with 6.562 g of tetraoctylammonium bromide (TOAB, 12.0 mmol). This two-phase mixture is stirred at 600 rpm for 1 hour to complete the phase transfer of $AuCl_4^-$ ions into the organic phase. The organic phase is extracted and the colorless aqueous phase is discarded. 600 µl of 1-dodecanethiol (2.5 mmol) is added to the organic phase, which is stirred at 600 rpm for

10 min. 20 mL of an aqueous solution of 378 mg of sodium borohydride ($NaBH_4$, 10.0 mmol) prepared in an ice bath is quickly poured into the organic phase while stirring. The two phase mixture is stirred at 600 rpm for 12 hours before the organic phase containing the dodecanethiol-capped Au nanocrystals is extracted.

The nanocrystals are purified by adding 4 mL of ethanol to every 1 mL of crude organic reaction product and then centrifuging at 8500 rpm for 5 min. The supernatant is discarded and the nanocrystals are redispersed in 3 mL of toluene. This dispersion is centrifuged at 10,000 rpm for 5 min to precipitate poorly capped nanocrystals. The supernatant is collected and 500 μL of additional 1-dodecanthiol is added to the nanocrystal dispersion. 20 mL of ethanol is added to the nanocrystal dispersion which is then centrifuged at 8000 rpm for 5 min. The supernatant is discarded and the nanocrystals are redispersed in 3 mL of toluene. 20 mL of ethanol is added to the nanocrystal dispersion again, and followed with centrifuging at 8000 rpm for 5 min, discarding supernatant, and redispersing nanocrystals with 3 mL of toluene. 20 mL of methanol is added to the nanocrystal dispersion, which was centrifuged at 8500 rpm for 5 min. The supernatant is discarded and the nanocrystals are redispersed in 3 mL of toluene. This dispersion is centrifuged at 10,000 rpm for 5 min to precipitate poorly capped nanocrystals. The supernatant is retained and dried to determine the mass of the nanocrystals. The nanocrystals are redispersed in toluene at a concentration of approximately 25 mg/mL until further use.

9.2.3 Grazing incidence small-angle X-ray scattering (GISAXS)

Grazing-incidence small-angle X-ray scattering (GISAXS) is performed on D1 beam line of the Cornell High Energy Synchrotron Source (CHESS), using monochromatic X-ray radiation of wavelength of 1.154 Å with a bandwidth of ~0.017 Å. A fiber coupled CCD camera (MedOptics) of 1024 × 1024 pixels with pixel size of 46.9 μm × 46.9 μm and 14-bit dynamic range per pixel is used to acquire the GISAXS pattern images, which are dark current corrected, distortion corrected, and flat field corrected by the acquisition software. The sample-to-detector distance is 569.0 mm, determined by using silver behenate powder as a calibration standard. The typical incident angle of the X-ray beam is 0.25^{o}, and the exposure time is around 0.1 to 1 sec. GISAXS patterns are background-subtracted, calibrated and integrated using Fit2D software (version: 12_077_i686_WXP). The GISAXS diffraction spots were indexed using our own software as described in Ref 25. GISAXS samples were prepared by drop-casting 20 μL of toluene with Au nanocrystals dispersed at a concentration of 20 mg/mL onto a hand-cut 7 mm × 7 mm silicon wafer placed under a 20 mL vial during drying. *In situ* heating of the superlattice is carried out using a copper heating block, as shown in Figure 1, equipped with a heating rod connected to a variac and a thermal couple connected to a temperature controller. GISAXS patterns were acquired every 5 sec. Contour plots are generated by radial integration of the 2D scattering intensity. The *d*-spacing related to the scattering features are determined from the 2D scattering vector $q = \sqrt{{q_x}^2 + {q_z}^2}$ where $q = (4\pi/\lambda) * \sin(\theta/2)$ (λ is the X-ray wavelength and θ is the scattering angle):

$$d = \frac{\lambda}{2\sin(\theta/2)} = \frac{2\pi}{q} = \frac{2\pi}{\sqrt{(q_x)^2+(q_z)^2}} \quad (1)$$

Some SAXS data were obtained using a Molecular Metrology system with a rotating copper anode X-ray source (Bruker Nonius FR591, λ = 0.154 nm) operating at 3.0 kW and 2D multiwire gas-filled detector (Molecular Metrology, Inc.). The nanocrystal films used for these measurements were prepared on a 1 cm × 1 cm glass cover slide. To make a SAXS sample with additive, 2 mg Au nanocrystals were dispersed in 0.1 mL toluene with additives (i. e. TOAB) dissolved in it, forming toluene dispersion with additive at a concentration of 5 mM and Au nanocrystals at a concentration of 20 mg/mL. 20μL of this dispersion was drop-cast onto a 1 cm × 1 cm glass cover slide and dried in air. This sample was then heated to 190°C in air for 5 min and allowed to cool back to room temperature prior to the SAXS measurement.

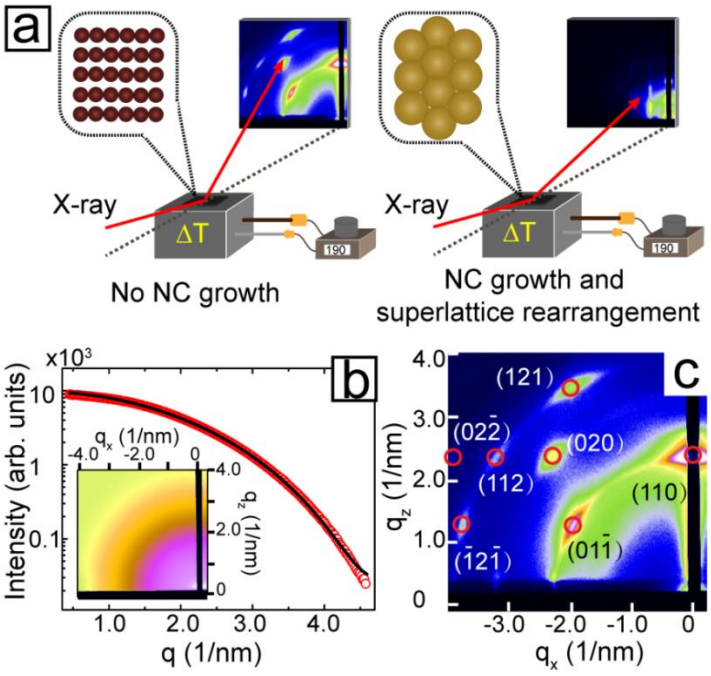

Figure 9.1

Figure 9.1: (a) Illustration of the GISAXS system with *in situ* heating capability. (b) SAXS data obtained from the dodecanethiol-capped Au nanocrystals disepersed in toluene. The data (red) are fit (black) to Eqns (2)-(4) to determine the nanocrystal size (average diameter of 1.9±0.19 nm). The inset shows the 2D scattering pattern. (c) GISAXS of a superlattice formed with the same nanocrystals measured in (b). The GISAXS pattern indexes to a BCC superlattice with a lattice constant of 3.90 nm, oriented with $(110)_{SL}$ planes parallel to the substrate.

The diameter of the Au cores of the nanocrystals was determined from SAXS measurements of nanocrystals dispersed in toluene (5 mg/mL). Solution scattering data were obtained using the same beam setup with the sample in a glass capillary tube and background-subtracted and calibrated. The X-ray scattering intensity I(q), was fit to a model for a collection of non-interacting spherical nanocrystals:[15]

$$I(q) \propto \int_0^\infty N(R)P(qR)R^6 dR \quad (2)$$

In Eqn (2), P(qR) is the shape factor for nanocrystals of radius *R*. N(R) is the size distribution, which is taken to be Gaussian with average radius $\overline{R}$, and standard deviation σ:

$$N(R) = \frac{1}{\sigma 2\pi} exp\left[\frac{-(R-\bar{R})^2}{2\sigma^2}\right] \quad (3)$$

$P(qR)$ is the shape factor for a solid homogeneous sphere:

$$P(qR) = \left[3\frac{sin(qR)-qR\,cos(qR)}{(qR)^3}\right]^2 \quad (4)$$

9.2.4 Transmission Electron Microscopy (TEM)

Transmission electron microscopy (TEM) images were obtained using a Tecnai Biotwin TEM operated at 80 kV accelerating voltage. Samples were prepared by dropping 5 μL of toluene with gold nanocrystals dispersed at a concentration of 2.5 mg/mL onto a carbon-coaed copper grid (Electron Microscopy Science, CF200-Cu) held with anticapillary reverse tweezers (Dumont, Biology Grade) in a 20 mL vial above 2 mL of toluene. After depositing the nanocrystals, the TEM grids were heated in air on a copper heating block, with a heating rod connected to a variac and a thermal couple

connected to a temperature controller, and then allowed to cool in air back to room temperature prior to imaging. TEM images were analyzed using Image-Pro Plus software (Media Cybernetics, Inc. version: 6.0.0.260).

9.3 RESULTS AND DISCUSSION

9.3.1 Dodecanethiol-Capped Au Nanocrystal Superlattices

Figure 9.1b shows SAXS profiles of the dodecanethiol-capped Au nanocrystals dispersed in toluene that were used throughout the study. The average diameter of nanocrystals is 1.9±0.19 nm, as determined by fitting Eqns (2)-(4) to the solution scattering data. Figure 9.1c show a GISAXS pattern from a superlattice formed from these nancorystals. The diffraction pattern indexes to a BCC superlattice preferentially oriented with $(110)_{SL}$ superlattice planes on the substrate. The lattice constant of the superlattice a_{SL}, is 3.90 nm. Based on the superlattice unit cell volume and the Au nanocrystal core diameter, the Au cores occupy 12% of the total available volume with the remainder being occupied by capping ligand.

Figure 9.2a shows GISAXS data (contour plot) acquired *in situ* from the BCC Au nanocrystal superlattice heated to 190^{o}C. The superlattice is essentially stable for almost 395 sec after reaching 190^{o}C, at which point the superlattice degrades and the Au nanocrystals sinter. During the first 30 sec after reaching 190^{o}C (Figs. 9.2b and 9.2g), the BCC superlattice expands slightly (a_{BCC} (25^{o}C)=3.90 nm; a_{BCC} (190^{o}C after 30 sec)= 3.96 nm), consistent with the thermal expansion of the capping ligands as observed in previous studies.[19] After 155 sec, the superlattice begins to contract; the superlattice

constant determined from Figures 9.2c and 9.2h is a_{BCC} (190°C after 155 sec)=3.90 nm. This shrinkage might be occurring because of residual solvent or perhaps capping ligand chain reorganization that leads to more efficient space-filling. After 340 sec (Figs. 9.2d and 9.2i), a weak scattering feature begins to emerge at low *q* indicating the onset of sintering. The main diffraction pattern still indexes to a BCC superlattice, but with a significant expansion (a_{BCC} (190°C after 340 sec)= 4.16 nm). This expansion is probably the consequence of the ligand desorption from the sintered regions, which add to the volume of the superlattice. If this is the case, it means that diffusion of free ligand within the superlattice readily occurs at elevated temperature. The inset in Figure 9.2a summarizes the change in BCC lattice constant over time. Between 340 and 370 sec, the superlattice continues to sinter and the residual superlattice continues to expand. The increasing ligand volume that results from the movement of ligands from the sintered regions into the superlattice eventually triggers a transition[9] from BCC to FCC (Figs. 9.2e and 9.2j). The new FCC superlattice structure is oriented preferentially with $(111)_{SL}$ planes parallel to the substrate with a lattice constant of a_{FCC} (190°C after 370 sec)=5.20 nm. BCC to FCC superlattice transitions have also been observed from PbSe and PbS superlattices swollen with solvent vapor.[8] After 395 sec, the Au nanocrystals sinter and the superlattice structure is destroyed (Figs. 9.2f and 9.2k).

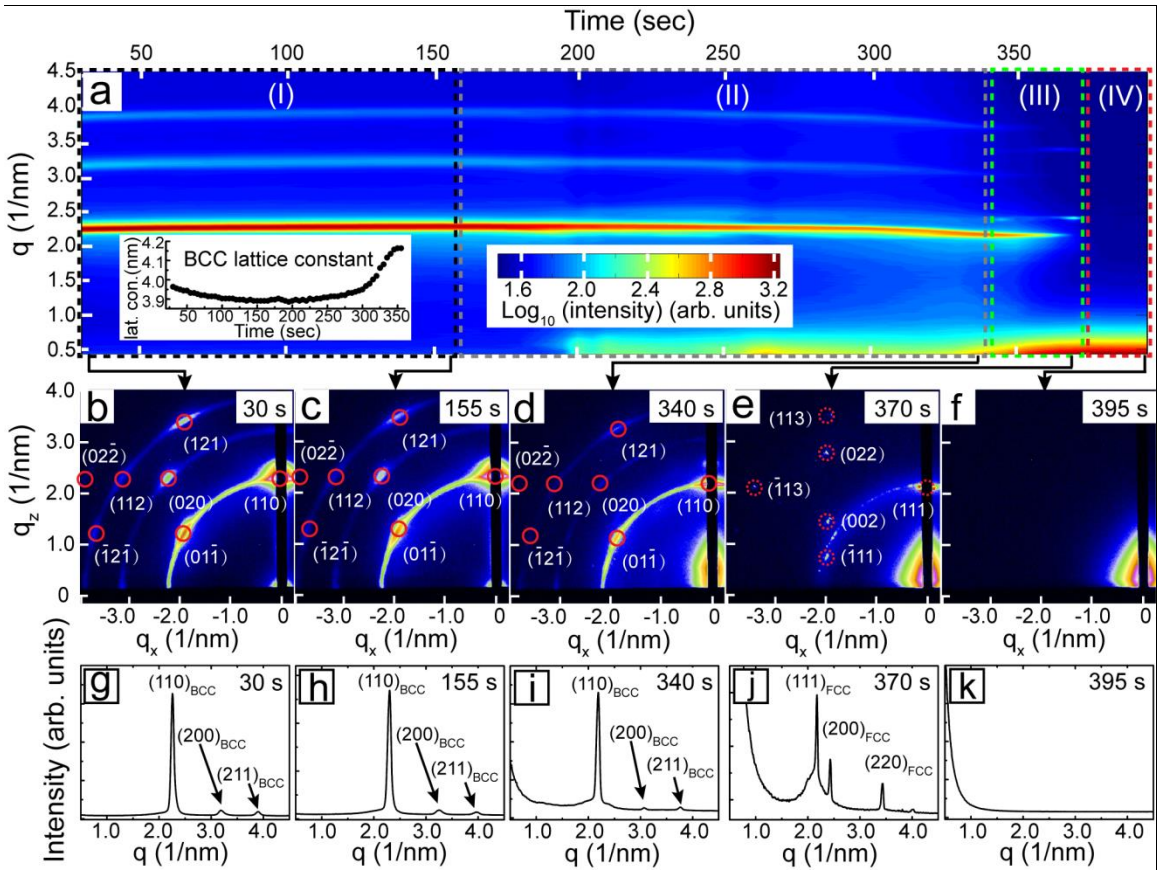

Figure 9.2: GISAXS data acquired *in situ* after heating a superlattice of 1.9 nm diameter dodecanthiol-capped Au nanocrystals to 190°C. The inset shows plot of BCC lattice constant against time. (a) Contour plot of the radially integrated scattering intensity versus q as a function of time after reaching 190°C. (b-f) show the full 2D GISAXS patterns of the Au nanocrystal superlattice held at 190°C for (b) 30 sec (BCC structure with a_{SL}=3.96 nm, oriented with $(110)_{SL}$ on the substrate), (c) 155 sec (BCC structure superlattice with a_{SL}=3.90 nm, oriented with $(110)_{SL}$ on the substrate), (d) 340 sec (BCC structure with a_{SL}=4.16 nm, oriented with $(110)_{SL}$ on the substrate, (e) 370 sec (FCC structure with a_{SL}=5.20 nm, with $(111)_{SL}$ on the substrate), and (f) 395 sec (the superlattice has collapsed). (g-k) Radial integrations of the GISAXS data in (b-f).

The BCC superlattice of 1.9 nm diameter dodecanethiol-capped Au nanocrystals heated to 190°C, exhibits a series of structural changes: (I) expansion due to ligand thermal expansion, (II) shrinkage due to loss of residual solvent or ligand reorganization,

(III) sintering of regions that provide excess free ligand that expands the superlattice, eventually inducing (IV) a structural transition from BCC to FCC, followed by (V) complete sintering. There is no significant change in Au core size accompanying these structure changes prior to sintering. For example, Figure 9.3 shows TEM images of dodecanetihol-capped Au nanocrystal superlattices heated in air to 190^{o}C and held there for 1, 2 or 20 min. The superlattice retains its BCC structure (Figs. 9.3b and 9.3c) until sintering (Fig. 9.3d), without any change in nanocrystal size.

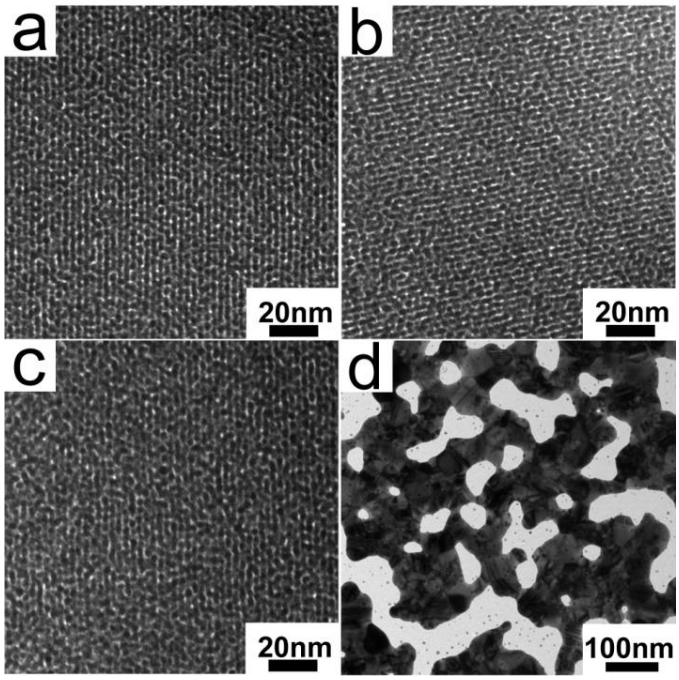

Figure 9.3: TEM images of 1.9 nm diameter dodecanethiol-capped Au nanocrystal superlattices (a) prior to heating and after heating at 190^{o}C for (b) 1 min, (c) 2 min and (d) 20 min. The superlattices in (a-c) have BCC structure with $(110)_{SL}$ planes oriented on the substrate. The as-deposited superlattice in (a) has $(1\bar{1}0)_{SL}$ *d*-spacing of 2.77 nm, which corresponds to a lattice constant of 3.92 nm that is close to the value of lattice constant determined from GISAXS. After 20 min of heating, the Au nanocrystals have sintered into a bicontinuous network.

9.3.2 Dodecanethiol-Capped Au Nanocrystal Superlattices with Various Added Surfactants Heated to 190°C

The dodecanethiol-capped Au nanocrystals do not change size when heated until they sinter at very high temperature. The size-stability of the dodecanethiol-capped Au nanocrystals initially puzzled us because we had observed an astonishing range of superlattice structural transitions when some dodecanethiol-capped Au nanocrystal superlattices were heated, turning from BCC superlattices into a range of new binary superlattice (BSL) structures in which the Au core sizes changed significantly in a controlled manner.[14] We found that some Au nanocrystal superlattices exhibited these structural changes and some did not and proposed that some residual phase transfer catalyst (TOAB) might have been responsible for the difference. We then tested a variety of different additives.

Figure 9.4 shows SAXS data for superlattices of 1.9 nm diameter dodecanethiol-capped Au nanocrystal superlattices with various additives after being heated to 190°C and then cooled back to room temperature. The superlattice without any additive (Fig. 9.4a) exhibited the expected BCC structure. The measured superlattice constant of 3.95 nm is almost identical to the unheated superlattice, indicating no nanocrystal growth or superlattice rearrangement occurred. Similarly, no change in nanocrystal size was observed when the superlattices were infiltrated with excess 1-dodecanthiol (Fig. 9.4b), hexadecanol (Fig. 9.4c), dodecylamine (Fig. 9.4d), hexadecane (Fig. 9.4e), dodecanoic acid (Fig. 9.4f), dibenzyl ether (Fig. 9.4g), or TOAHS (Fig. 9.4m). In contrast, superlattices infiltrated with TBAB (Fig. 9.4h), THAB (Fig. 9.4i), TOAB (Fig. 9.4j),

TOAC (Fig. 9.4k), THAI (Fig. 9.4l), CTAC (Fig. 9.4n), and CTAB (Fig. 9.4o) all showed significant changes. Thiols, alcohols, amines, hydrocarbons, carboxylic acids, ethers, and alkyl sulfate salts did not affect the thermal stability of the dodecanethiol-capped Au nanocrystals; whereas, halide ions, i.e. Cl^-, Br^-, and I^-, significantly destabilized the nanocrystals and made them prone to thermally-induced ripening. *In situ* GISAXS of heated superlattices also showed that halide ions significantly lowered the sintering temperature. Figure 9.5 shows *in situ* GISAXS data of Au nanocrystal superlattices with added TOAB, TOPB and TOAHS heated from room temperature to 205^{o}C. Superlattices without any additives (Fig. 9.5a) and with TOAHS (Fig. 9.5d) showed no significant change in structure until sintering at 204-205^{o}C. In contrast, the addition of TOAB (Fig. 9.5b) and TOPB (Fig. 9.5c) induced structural rearrangements at much reduced temperatures of 170^{o}C and 165^{o}C, respectively. TOAHS—an alkyl salt with the same TOA^+ cation as TOAB—had no impact on the thermal stability of the superlattices, whereas, the presence of Br^- in both TOAB and TOPB significantly depressed the sintering temperature.

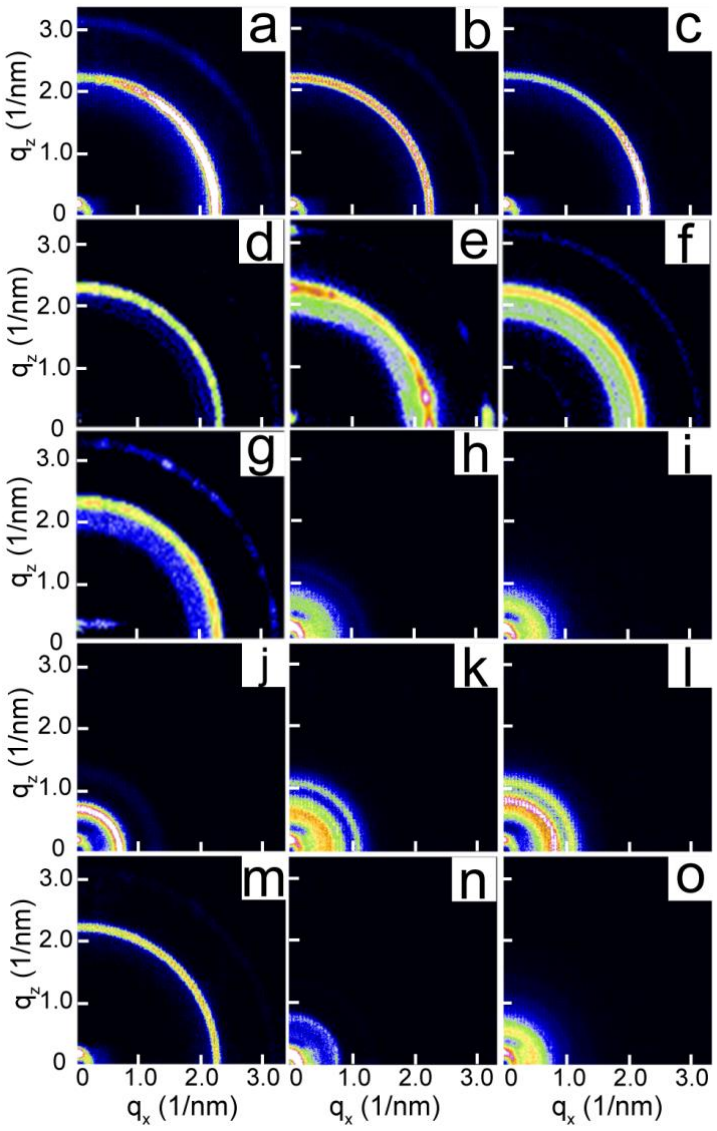

Figure 9.4: Transmission SAXS of superlattices of 1.9 nm diameter dodecanthiol-capped Au nanocrystals infiltrated with various additives after being heated at 190°C: (a) no additive, showing BCC superlattice with $(110)_{SL}$ diffraction ring at 2.25 nm^{-1} and $(200)_{SL}$ ring at 3.1 nm^{-1}, (b) 1-dodecanthiol, (c) hexadecanol, (d) dodecylamine, (e) hexadecane, (f) dodecanoic acid, (g) dibenzyl ether, (h) tetrabutylammonium bromide, (i) tetraheptylammonium bromide, (j) tetraoctadecylammonium bromide, (k) tetraoctylammonium chloride, (l) tetraheptylammonium iodide, (m) tetraoctylammonium hydrogen sulfate, (n) cetyltrimethylammonium chloride, (o) cetyltrimethylammonium bromide.

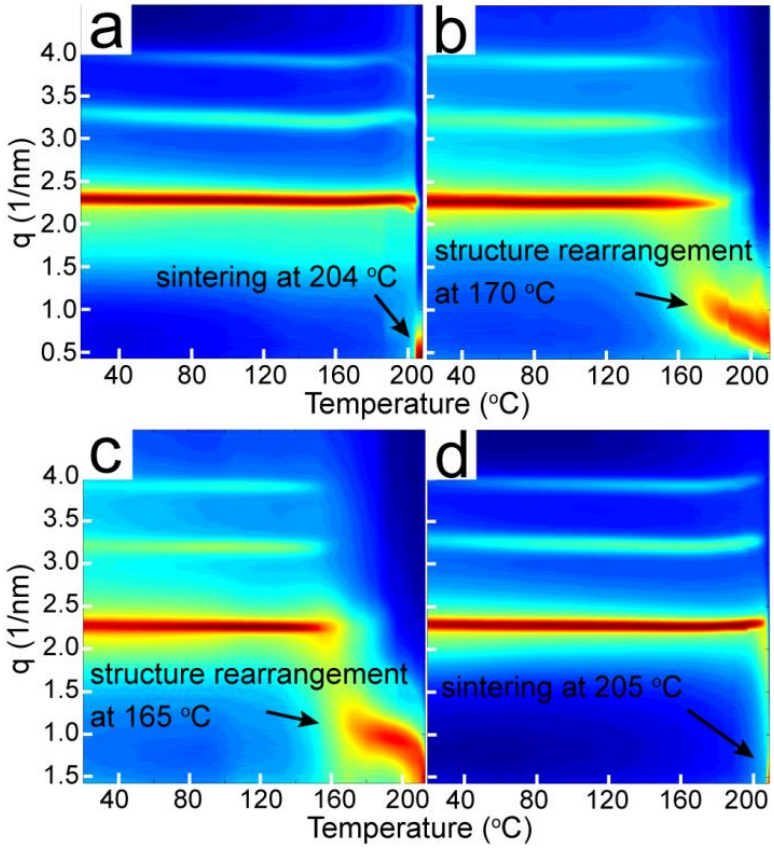

Figure 9.5: Contour plots of the radially integrated scattering intensity as a function of scattering vector *q* and temperature during heating the nanocrystal superlattice of (a) 1.9 nm diameter dodecanthiol-capped Au nanocrystals without additives, showing sintering at 204°C, and1.9 nm diameter dodecanthiol-capped Au nanocrystals with various added surfactants: (b) TOAB, showing structural rearrangement at 170°C, (c) TOPB, showing structural rearrangement at 165°C, and (d) TOAHS, showing sintering at 205°C. The ratio of added surfactant to thiol was 1:6 in all cases.

9.3.3 Superlattices of Dodecanethiol-Capped Au Nanocrystals Infiltrated with TOPB

The change in structure of superlattices infiltrated with TOPB was examined in finer detail. TOPB was included in superlattices of 1.9 nm diameter dodecanethiol-capped Au nanocrystals with a [TOPB]:[thiol] mole ratio of 1:6 and heated to 190°C.

Figure 9.6 shows *in situ* GISAXS patterns obtained from the superlattice heated to 190°C. Before heating, GISAXS showed that the BCC superlattice is oriented predominantly with $(110)_{SL}$ planes on the substrate with a slightly larger lattice constant (3.92 nm) than superlattices without added TOPB (3.90 nm). Figure 9.7a also shows a TEM image of the superlattice, which is clearly BCC. Once heated to 190°C (Figs. 9.6b and 9.6c), the BCC structure expands slightly (a_{BCC} (190°C after 40 sec)=3.96 nm), similar to the superlattice without added TOPB. But after 65 sec at 190°C (Figs. 9.6d and 9.6e), the diffraction pattern changes completely from its BCC spot pattern to a series of diffraction rings. This new diffraction pattern indexes to an icosahedral AB_{13} binary superlattice (ico-AB_{13} BSL) with lattice a constant of 15.6 nm. One of the distinguishing features of an ico-AB_{13} BSL is the prominent $(531)_{BSL}$ diffraction peak (labeled as d_8 at q=2.39 nm^{-1} in Fig. 9.6e).[26,27] TEM was also used to confirm the ico-AB_{13} BSL structure (Fig. 9.7c). The ico-AB_{13} BSL structure is similar to $NaZn_{13}$ (PDF #01-071-9884, space group 226) with simple cubic symmetry and has been widely observed for various nanocrystal assemblies.[11,13,16] The appearance of rings in the GISAXS pattern indicates a loss of preferential superlattice orientation on the substrate.

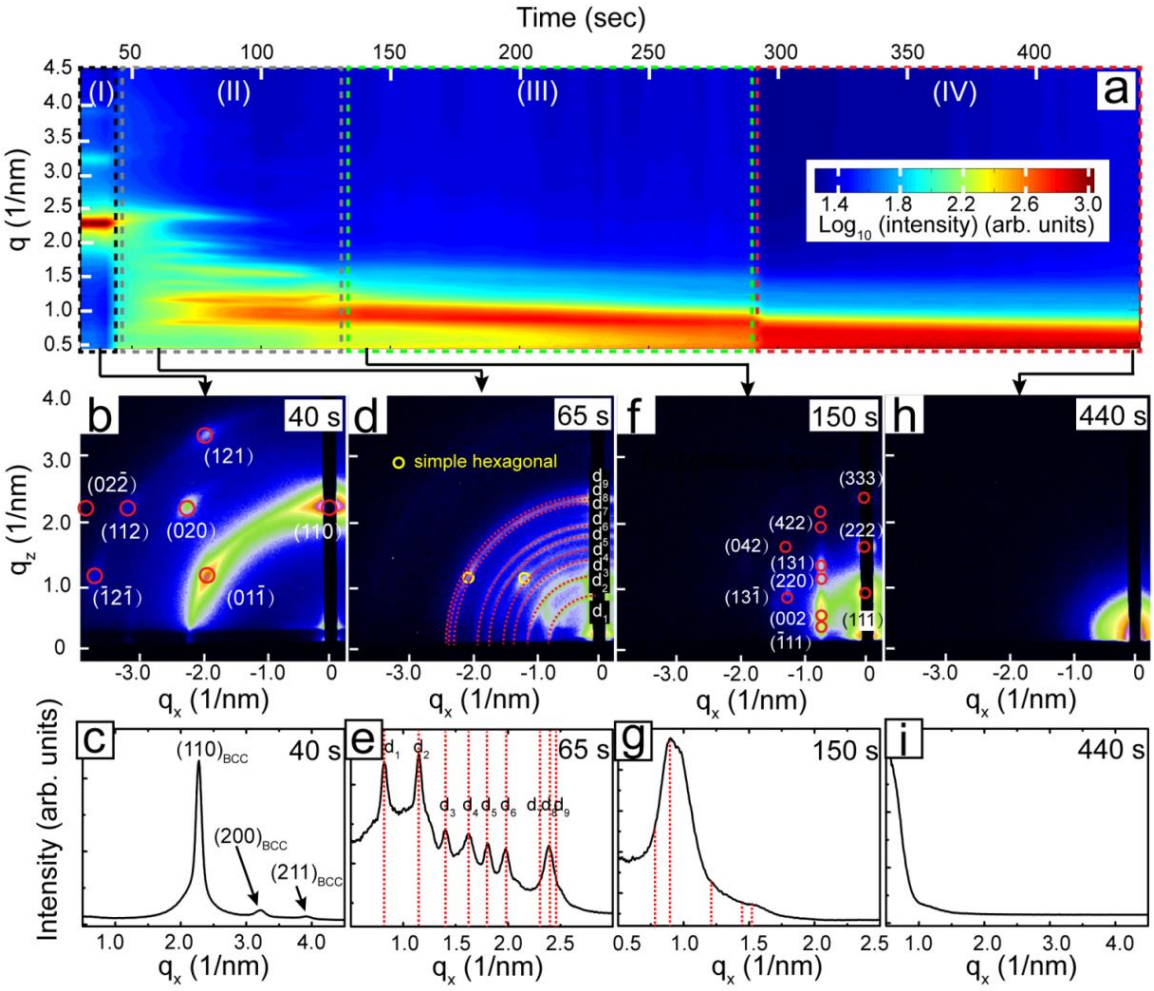
Time (sec)
50
100
150
200
250
300
350
400
(I)
(II)
(III)
(IV)
a
q (1/nm)
1.4 1.8 2.2 2.6 3.0
Log10 (intensity) (arb. units)
b
40 s
(121)
(02$\bar{2}$)
(112)
(020)
(110)
($\bar{1}$2$\bar{1}$)
(01$\bar{1}$)
d
65 s
simple hexagonal
f
150 s
(333)
(422)
(222)
(042)
(131)
(220)
(13$\bar{1}$)
(002)
(111)
($\bar{1}$11)
h
440 s
q_z (1/nm)
q_x (1/nm)
c
40 s
$(110)_{BCC}$
$(200)_{BCC}$
$(211)_{BCC}$
e
65 s
g
150 s
i
440 s
Intensity (arb. units)

Figure 9.6

Figure 9.6: *In situ* GISAXS data obtained from a superlattice of 1.9 nm diameter dodecanthiol-capped Au nanocrystals formed with the addition of TOPB (TOPB : thiol=1:6) heated to 190^{o}C. (a) Contour plot of the radially integrated scattering intensity as a function of scattering vector *q* and time (30–450 sec) during *in situ* GISAXS measurement of the nanocrystal superlattice at 190^{o}C. (b) GISAXS pattern of the nanocrystal superlattice being heated at 190^{o}C for 40 sec, indexed to a BCC superlattice with a lattice constant of 3.96 nm, oriented with its $(110)_{SL}$ plane parallel to the substrate. (c) Radial integration of the GISAXS pattern in (b), showing $(110)_{SL}$, $(200)_{SL}$, and $(211)_{SL}$ diffraction peaks for BCC superlattice. (d) GISAXS pattern of the nanocrystal superlattice being heated at 190^{o}C for 65 sec, indexed to an ico-AB_{13} BSL, with a lattice constant of 15.6 nm. The yellow circles highlights the diffraction spots indexed to a simple hexagonal structure. (e) Radial integration of the GISAXS pattern in (d), in which red dash lines labeled d_1 to d_9 are indexed to $(200)_{BSL}$, $(220)_{BSL}$, $(222)_{BSL}$, $(400)_{BSL}$, $(420)_{BSL}$, $(422)_{BSL}$, $(440)_{BSL}$, $(531)_{BSL}$, and $(600)_{BSL}$ diffraction peaks of an ico-AB_{13} BSL ($a_{ico\text{-}AB13}$ (190^{o}C after 65 sec) = 15.6 nm). (f) GISAXS pattern of the nanocrystal superlattice being heated at 190^{o}C for 150 sec, indexed to a FCC superlattice with a lattice constant of 14.2 nm, oriented with its $(111)_{SL}$ plane parallel to the substrate. (g) Radial integration of the GISAXS pattern in (f), in which red dash lines highlight the expected diffraction peaks of a FCC superlattice. (h) GISAXS pattern of the nanocrystal superlattice being heated at 190^{o}C for 440 sec, showing no diffraction features. (i) Radial integration of the GISAXS pattern in (h), showing no diffraction features.

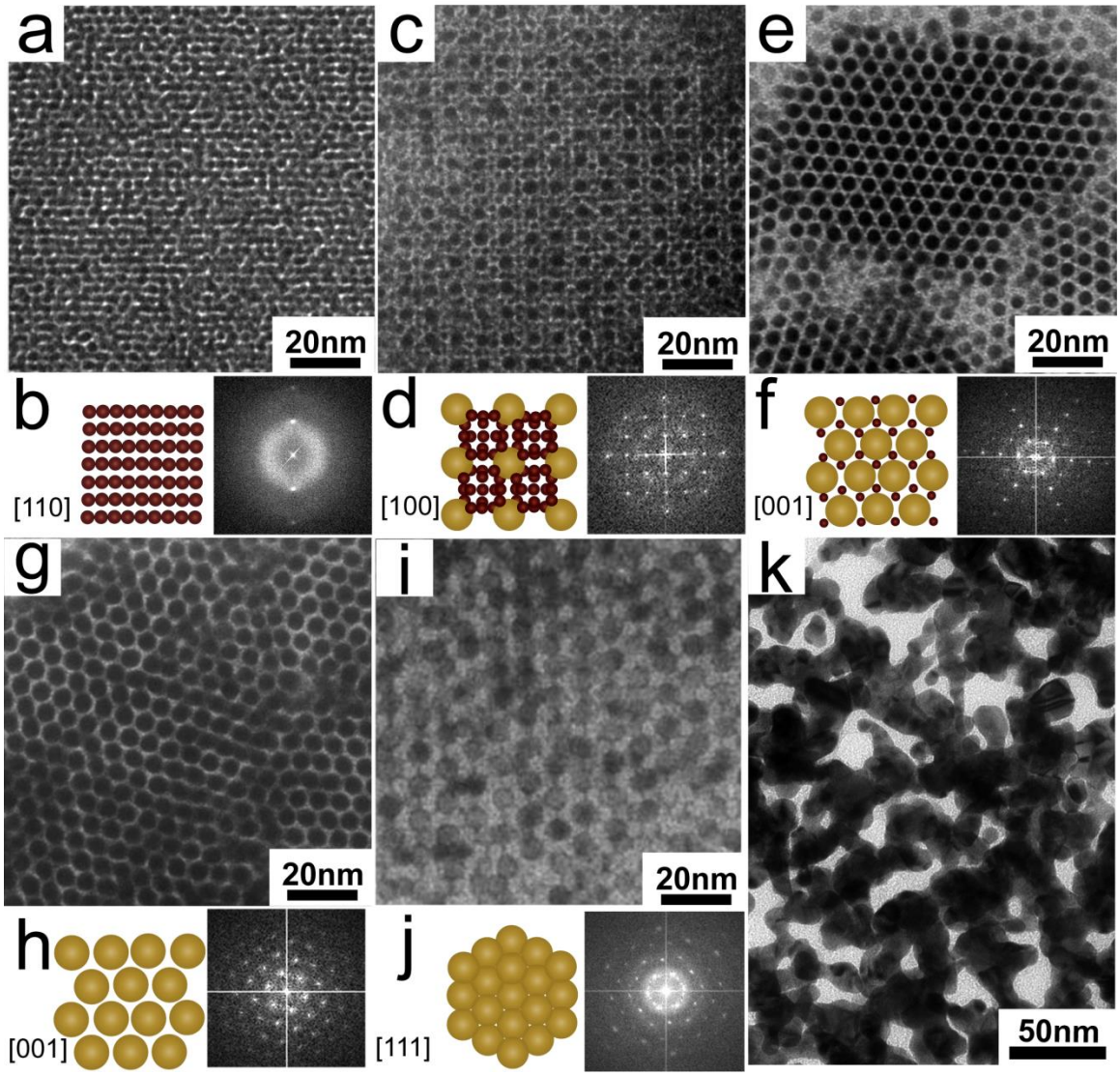
a
20nm
c
20nm
e
20nm
b
[110]
d
[100]
f
[001]
g
20nm
i
20nm
k
50nm
h
[001]
j
[111]

Figure 9.7

Figure 9.7: TEM images of nanocrystal superlattices of 1.9 nm diameter dodecanthiol-capped Au nanocrystals infiltrated with TOPB ([TOPB]:[thiol] mole ratio of 1:6) heated at 190°C for various times. (a) 0 sec, Au nanocrystals formed BCC superlattice, with lattice constant of 3.95 nm, oriented with its $(110)_{SL}$ plane parallel to the substrate, and $[110]_{SL}$ direction perpendicular to the substrate. (b) Scheme of $(110)_{SL}$ planes of BCC superlattice and the Fast Fourier Transform (FFT) of the image in (a). (c) 20 sec, Au nanocrystal experienced Otswald ripening and the superlattice rearranged to an ico-AB_{13} BSL, oriented with its $(100)_{BSL}$ plane parallel to the substrate, and $[100]_{SL}$ direction perpendicular to the substrate. The $(002)_{BSL}$ *d*-spacing of the BSL is 7.32 nm, corresponding to a lattice constant of 14.6 nm. (d) Scheme of $(100)_{BSL}$ planes of ico-AB_{13} BSL and the FFT of the image in (c). (e) 30 sec, the superlattice rearranged to sh-AB_2 BSL, oriented with its $(001)_{BSL}$ plane parallel to the substrate, and $[001]_{SL}$ direction perpendicular to the substrate. The $(100)_{BSL}$ *d*-spacing of 4.88 nm corresponds to a lattice constant of $a_{sh\text{-}AB2}$ (30 sec)= 5.64 nm. (f) Scheme of $(001)_{BSL}$ planes of sh-AB_2 BSL and the FFT of the image in (e). (g) 50 sec, Au nanocrystals formed a simple hexagonal (SH) superlattice, with lattice constant of 6.36 nm, oriented with its $(001)_{SL}$ plane parallel to the substrate, and $[001]_{SL}$ direction perpendicular to the substrate. (h) Scheme of $(001)_{SL}$ planes of SH superlattice and the FFT of the image in (g). (i) 50 sec, Au nanocrystals also formed a FCC superlattice, with lattice constant of 13.5 nm, oriented with its $(111)_{SL}$ plane parallel to the substrate, and $[111]_{SL}$ direction perpendicular to the substrate. (j) Scheme of $(111)_{SL}$ planes of FCC superlattice and the FFT of the image in (i). (k) 20 min, Au nanocrystals coalesced to bicontinuous domains of Au.

In addition to the strong diffraction rings, there are weak diffraction spots (yellow circles in Fig. 9.6d) in the GISAXS pattern. These spots index to a simple hexagonal superlattice with lattice dimension of a=b=c=6.10 nm, $\alpha=\beta=90^{o}$, $\gamma=120^{o}$, oriented with $(001)_{SL/BSL}$ planes parallel to the substrate. It is not possible to determine uniquely from the GISAXS pattern if this superlattice structure is a binary superlattice with simple hexagonal structure or a simple hexagonal superlattice. TEM (Fig. 9.7e) showed that the superlattice structure is sh-AB_2 BSL. After 20 sec of heating of the TEM sample at 190^{o}C, relatively small regions of simple hexagonal AB_2 BSL (sh-AB_2, isostructure with AlB_2, space group 191) are observed by TEM. After heating for 30 sec, the sh-AB_2 BSL becomes the dominant structure as shown in the TEM image in Figure 9.7e. With further heating, TEM (Fig. 9.7f) showed that the small nanocrystals are ultimately consumed by the larger nanocrystals in the sh-AB2 superlattice and the structure transforms to a simple hexagonal superlattice with a lattice constant of 6.36 nm.

After 150 sec at 190^{o}C, the GISAXS pattern (Figs. 9.6f and 9.6g) continues to evolve and now indexes to an FCC superlattice with a lattice constant of 14.2 nm. The spot pattern indicates preferential orientation of the superlattice on the substrate, with $(111)_{SL}$ planes predominantly on the substrate. The FCC structure was also observed by TEM (Figs. 9.7g and 9.7h) and the Au core diameter is 5.6 nm. After 440 sec at 190^{o}C, the diffraction pattern finally collapses (Figs. 9.6h and 9.6i) as the nanocrystals sinter into the bicontinuous structure shown in the TEM image in Figure 9.7k.

The structural transitions that occur in the superlattices with added TOPB involve changes in the Au nanocrystal size. The nanocrystal diameter in the FCC superlattices

of 4.9 nm is much larger than the initial diameter of 1.9 nm. Each structural transition involves changes in nanocrystal size. For instance, the small and large nanocrystals in the ico-AB_{13} BSL have diameters of 3.8 nm and 1.7 nm, respectively.[35] Large Au nanocrystals are growing at the expense of the smaller nanocrystals. In the next structural transition, the sh-AB_2 BSL is composed of large nanocrystals that are even bigger (4.3 nm) and smaller nanocrystals that are even smaller (1.1 nm).[36]

9.3.4 Superlattice Nucleation and Growth

Phase transitions in solids that occur between two phases typically exhibit a nucleation and growth process that is governed by free energy difference between two phases and phase interface energy.[33] In the case of 1.9 nm diameter dodecanthiol-capped Au nanocrystal superlattices with halide anions at 190^{o}C, because of the surface energy of Au-thiol interface, small Au nanocrystal became unstable and tend to undergo Ostwald ripening to increase the nanocrystal size and minimize the area of Au-thiol interface. On the other hand, the introduction of larger nanocrystals to a superlattice made up of smaller nanocrystals would lead to a significant lattice mismatch for the superlattice, and hence, a surface energy at the boundary between a superlattice of small nanocrystals and a superlattice of large nanocrystals. Superlattice ordered structural rearrangement involves replacing thermodynamically-unfavored phase (superlattice of small nanocrystals) with thermodynamically-favored phase (superlattice of large nanocrystals) and surface energy of two-superlattice boundary. It is similar to the case of solid state phase transitions, which suggest that the ordered structure rearrangements of superlattices

could also exhibit a nucleation and growth of new superlattice domains. Figure 9.8a shows a TEM image of a phase boundary between a simple hexagonal superlattice region that is nucleating from the edge of a BCC superlattice domain.

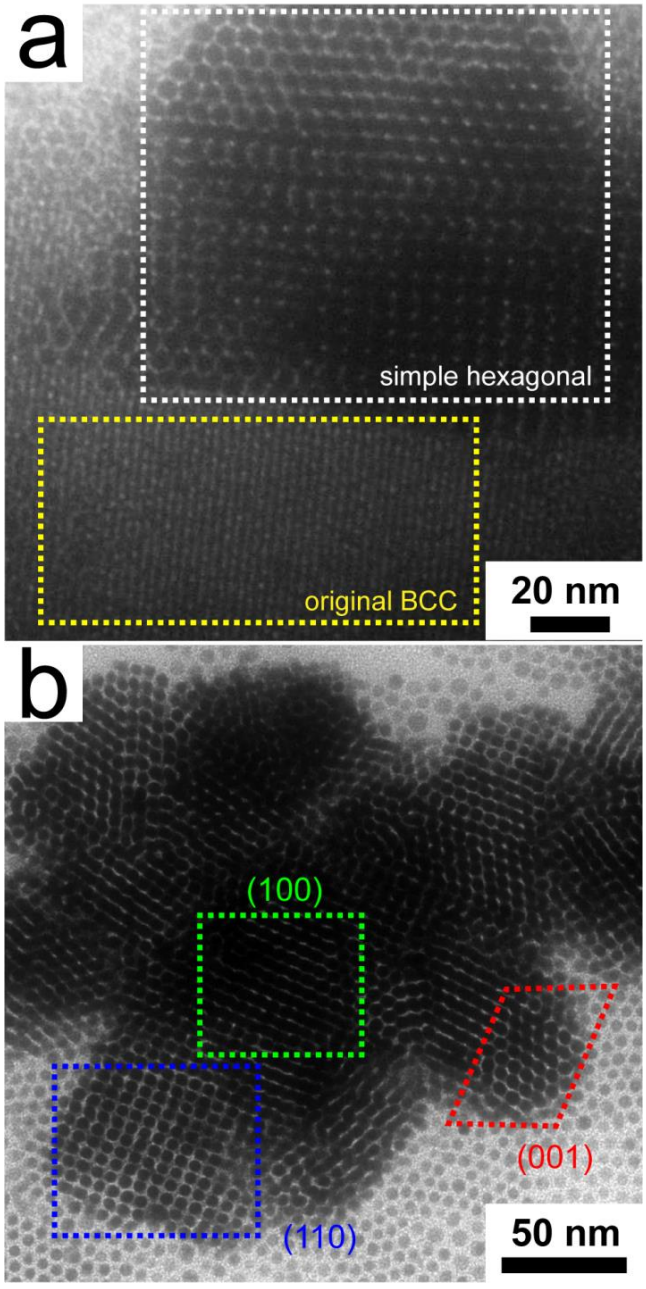

Figure 9.8

Figure 9.8: TEM images of simple hexagonal (SH) superlattice. (a) a domain of SH superlattice (white rectangle) nucleate from BCC superlattice maxtrix (yellow rectangle). (b) BCC superlattice completely rearrange to SH superlattice, in which red parallelogram highlights SH superlattice with $(001)_{SL}$ parallel to the substrate, green rectangle highlights SH superlatttice with $(100)_{SL}$ parallel to the substrate, and blue rectangle highlights SH superlattice with $(110)_{SL}$ parallel to the substrate.

At 190^{o}C, the Au superlattice tends to minimize the Au-thiol interface area and the sintered bicontinuous Au structure is more stable than nanocrystal superlattices. During the Ostwald ripening process towards the sintered film, a series of metastable structures (which are thermodynamically stable for the specific nanocrystal sizes) emerge, like ico-AB_{13} BSL, sh-AB_2 BSL, and FCC superlattice. On the TEM grids, a thermodynamically unstable superlattice, simple hexagonal superlattice emerged during the heating of grid, and kinetically-trapped by quickly cooling the grid. Figure 9.8b shows a TEM image for a domain of completely structural rearranged SH superlattice, in which red parallelogram, green and blue rectangles highlights $(001)_{SL}$, $(100)_{SL}$, and $(110)_{SL}$ planes of a SH superlattice, respectively. The superlattice in the image, especially the $(110)_{SL}$ planes, clearly show that it is a simple hexagonal superlattice, not a binary superlattice. Simple hexagonal superlattice has a packing density of 60%, which is much lower than FCC or HCP (74%), and was previously found to be a kinetically-trapped structure of Si nanocrystal superlattice.[34]

A typical GISAXS pattern of icosahedral AB_{13} binary superlattice (ico-AB_{13} BSL, similar to $NaZn_{13}$, PDF #01-071-9884, space group 226) is shown in Figure 9.9. Diffraction rings indicate that there are no preferential superlattice orientation on the substrate, and can be indexed to ico-AB_{13} BSL. The distinguishing features of an ico-AB_{13} BSL is the prominent $(531)_{BSL}$ diffraction peak, highlighted with green dash line. Other diffraction peaks ((731), (751), and (753)) that are only exhibited by ico-AB_{13} BSL are also visible, and highlighted with green dash lines.

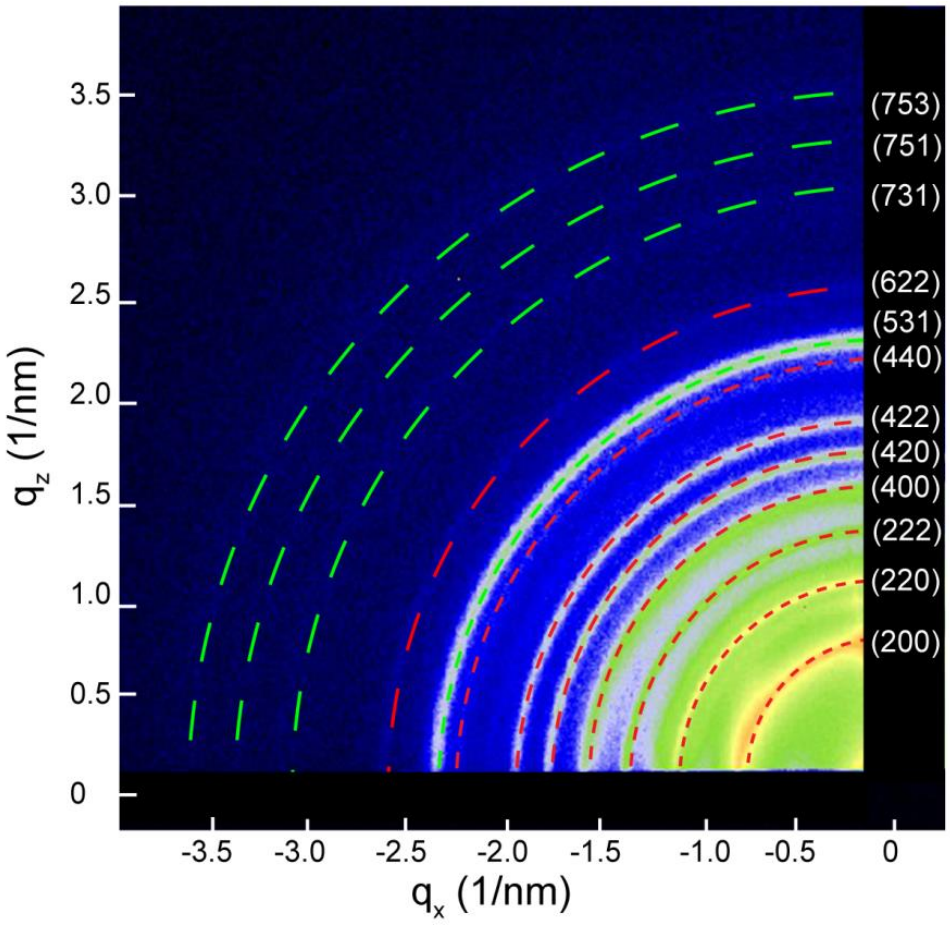

Figure 9.9: GISAXS pattern of ico-AB binary superlattice.

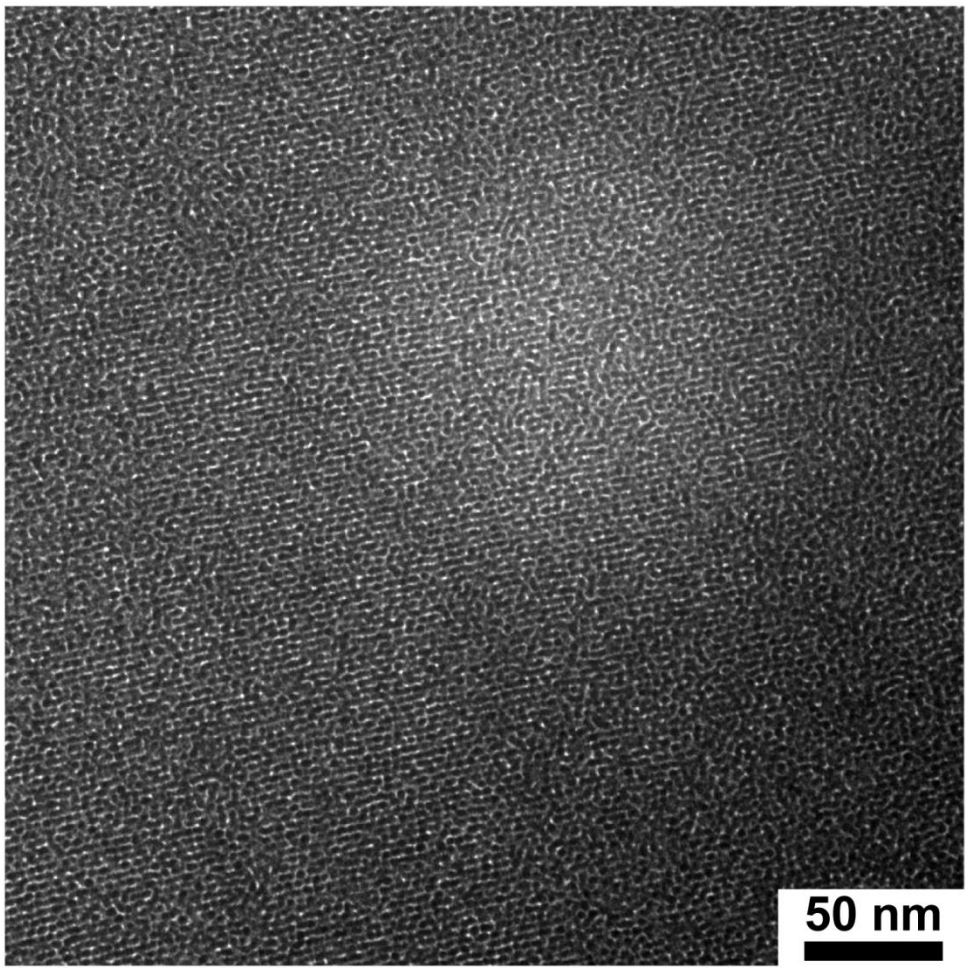

Figure 9.10: TEM image of BCC superlattice of 1.9 nm dodecanthiol-capped Au nanocrystals without any additive, oriented on the substrate with $(110)_{SL}$ planes and $[110]_{SL}$ direction perpendicular to the substrate.

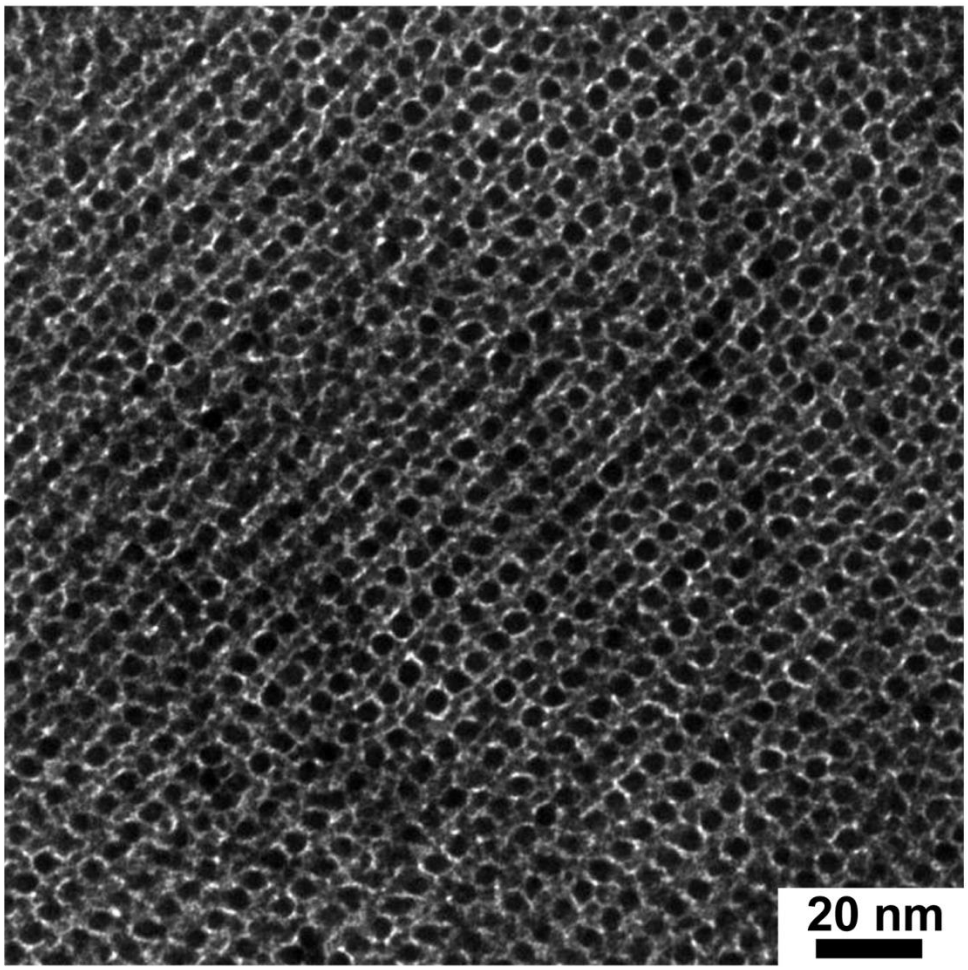

Figure 9.11: TEM image of ico-AB_{13} BSL dodecanthiol-capped Au nanocrystals, oriented on the substrate with $(110)_{BSL}$ planes, and with $[110]_{BSL}$ direction perpendicular to the substrate. This superlattice was obtained by heating BCC superlattice with TOPB ([TOPB]:[thiol]=1:6) in air at 190^{o}C for 30 sec.

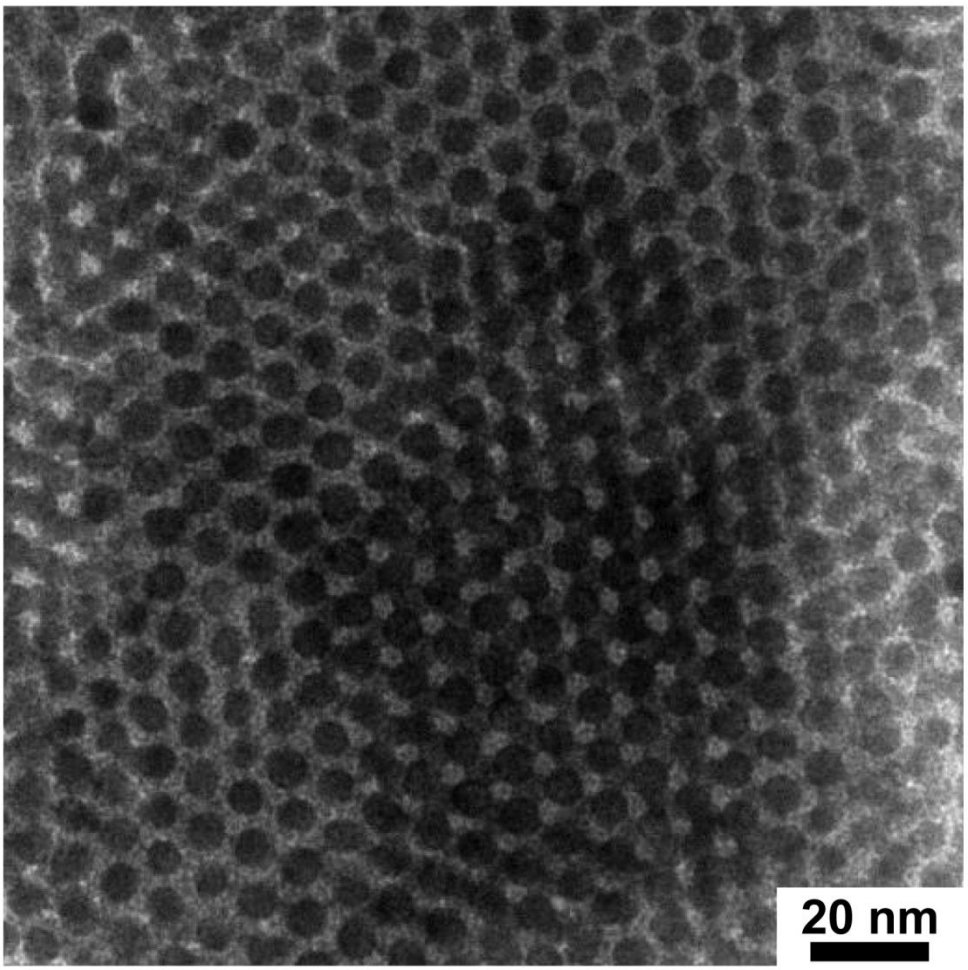

Figure 9.12: TEM image of FCC superlattice of dodecanthiol-capped Au nanocrystals, oriented on the substrate with $(111)_{SL}$ planes, and $(111)_{SL}$ direction perpendicular to the substrate. This superlattice was obtained by heating BCC superlattice with TOPB ([TOPB]:[thiol]=1:6) in air at 190^{o}C for 60 sec.

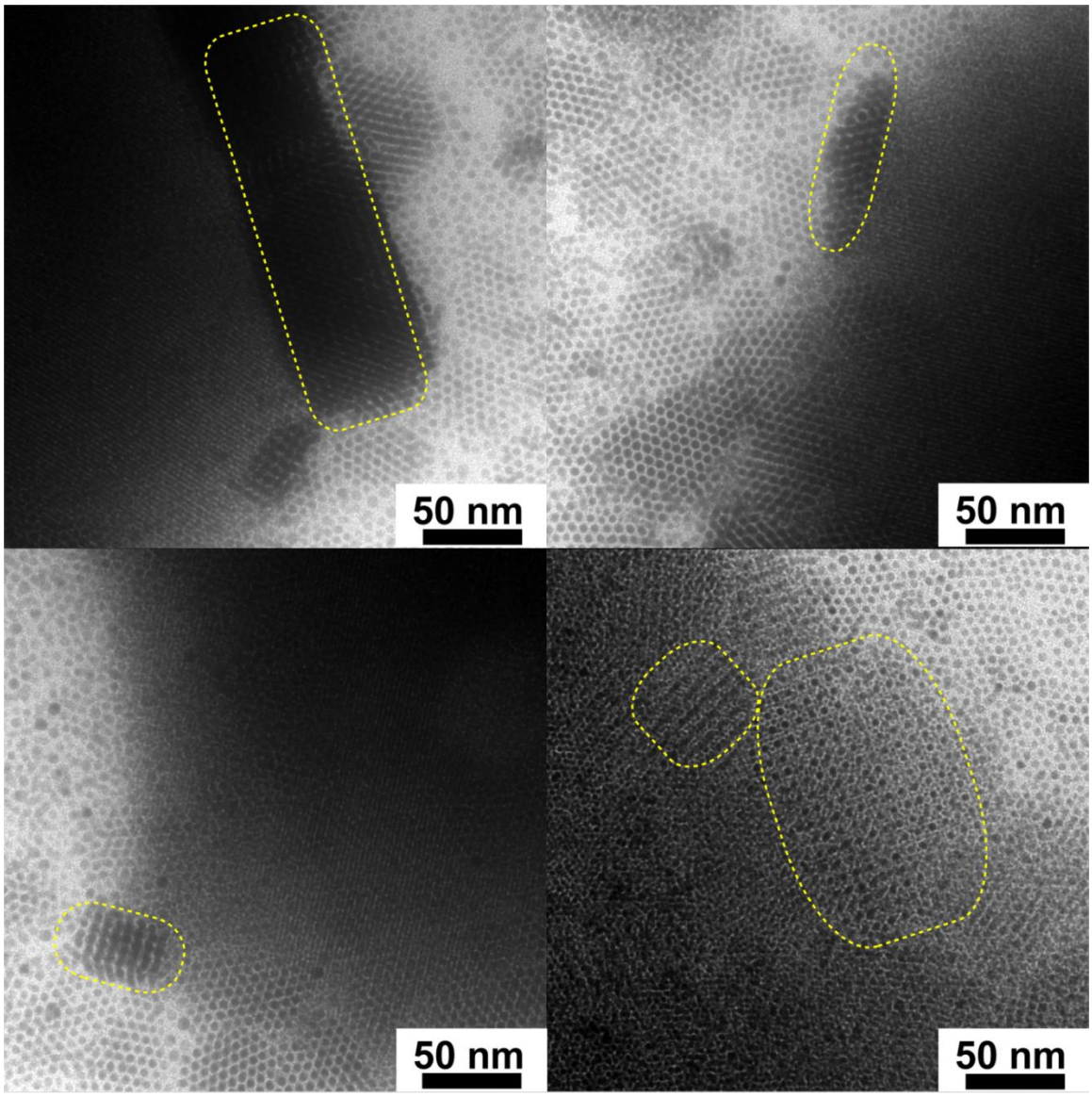

Figure 9.13: TEM images showing "nucleation" process of dodecanthiol-capped Au nanocrystal superlattice (with additional TOPB, [TOPB]:[thiol]=1:6) structural rearrangements. Domains of superlattices (or BSLs) of large nanocrystals "nucleate" on previous superlattices of small nanocrystals, during heating in air at 190^{o}C.

Ostwald ripening of Au nanocrystals in a superlattice occurs in a controlled fashion that leads to superlattice structural rearrangements. However, for Au nanocrystals

that do not form superlattice in the first place, Ostwald ripening takes place in a random manner that leads to Au nanocrystals with faceted shape and random size.

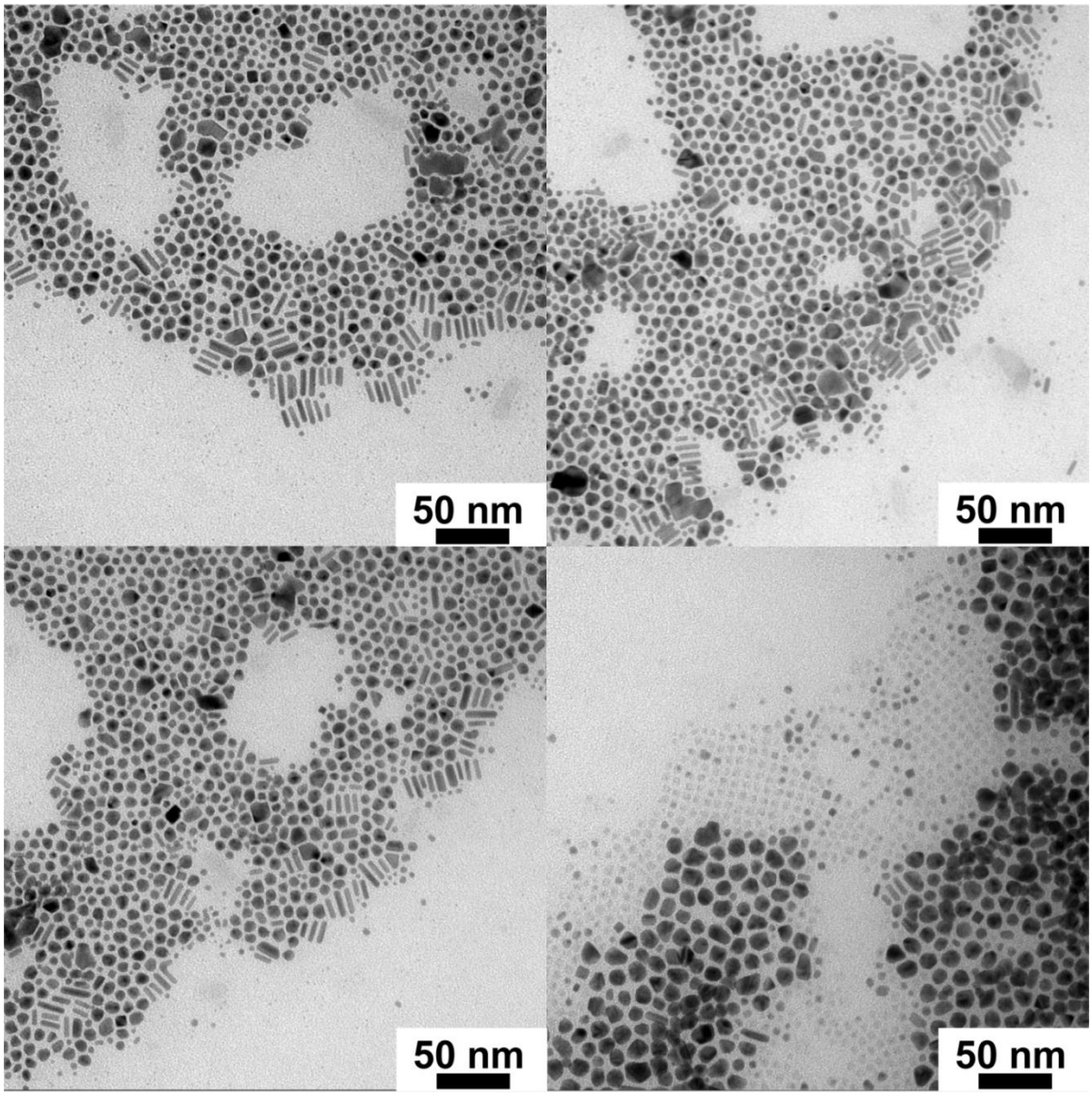

Figure 9.14: TEM images of dodecanethiol-capped Au nanocrystals not forming superlattices (probably due to not enough nanocrystals in these locations) that are heated at 160^{o}C for 9 min (with additional TOPB, [TOPB]:[thiol]=1:6).

9.4 CONCLUSION

The dodecanethiol-capped Au nanocrystals ripen and increase in size during heating when halides are present in the superlattices. This indicates that halides can displace thiolate capping ligands. Oxidation of alkanethiols on the Au nanocrystal surface to alkane sulfonates would lead to ligand desorption from the Au surfaces.[28] Halide anions have been shown to undergo ligand exchange with thiolates on Au surface to promote the Au surface-mediated thiol oxidation and Au nanocrystal ripening in solution.[29,30] TOAB has also been shown to be responsible for the uniform growth of Au nanocrystals in the solid state.[31,32] Residual halides from the synthesis that remain in the superlattice underlie the thermally-promoted ordered structural rearrangements recently observed by Goodfellow, et al.[14] in dodecanethiol-capped Au nanocrystals. The addition of TOPB to Au nanocrystal superlattices exhibited a series of ordered structure rearrangements: from BCC to ico-AB_{13} BSL to sh-AB_2 BSL to simple hexagonal or FCC, and finally to a sintered structure.

The ordered structural rearrangements exhibit a "nucleation-and-growth" process similar to solid state phase transition. Thermodynamically unstable but kinetically-trapped simple hexagonal superlattice is "frozen" on the TEM grid by quickly cooling the grid.

9.5 REFERENCE

(1) Bawendi, M. G.; Steigerwald, M. L.; Brus, L. E. The quantum mechanics of larger semiconductor clusters ("quantum dots") *Auun. Rev. Phys. Chem.* **1990**, *41*, 477-496.

(2) Daniel, M-C; Astruc, D. Gold Nanoparticles: Assembly, Supramolecular Chemistry, Quantum-Size-Related Properties, and Applications toward Biology, Catalysis, and Nanotechnology, *Chem. Rev.* **2004**, *104*, 293-346.
(3) Alivisatos, A. P. Perspectives on the physical chemistry of semiconductor nanocrystals, *J. Phys. Chem.* **1996**, *100*, 13226-13239.
(4) Koole, R.; Liljeroth, P.; Donegá, C. de M.; Vanmaekelbergh, D.; Meijerink, A. Electronic coupling and exciton energy transfer in CdTe quantum-dot molecules, *J. Am. Chem. Soc.* **2006**, *128*, 10436-10441.
(5) Urban, J. J.; Talapin, D. V.; Shevchenko, E. V.; Kagan, C. R.; Murray, C. B. Synergism in binary nanocrystal superlattices leads to enhanced p-type conductivity in self-assembled PbTe/Ag_2Te thin films, *Nat. Mater.* **2007**, *6*, 115-121.
(6) Collier, C. P.; Vossmeyer, T.; Heath, J. R. Nanocrystal superlattices, *Annu. Rev. Phys. Chem.* **1998**, *49*, 371-404.
(7) Murray, C. B.; Kagan C. R.; Bawendi, M. G. Synthesis and characterization of monodisperse nanocrystals and close-packed nanocrystal assemblies, *Annu. Rev. Mater. Sci.* **2000**, *30*, 545-610.
(8) Bian, K.; Choi, J. J.; Kaushik, A.; Clancy, P.; Smilgies, D.-M.; Hanrath, T. Shape-Anisotropy Driven Symmetry Transformations in Nanocrystal Superlattice Polymorphs, *ACS Nano*, **2011**, *5*, 2815-2823.
(9) Goodfellow, B. W.; Korgel, B. A. Reversible Solvent Vapor-Mediated Phase Changes in Nanocrystal Superlattices, *ACS Nano*, **2011**, *5*, 2419-2424.
(10) Bodnarchuk, M. I.; Kovalenko, M. V.; Heiss, W.; Talapin, D. V. Energetic and entropic contributions to self-assembly of binary nanocrystal superlattices: temperatures as the structure-directing factor, *J. Am. Chem. Soc.* **2010**, *132*, 11967-11977.
(11) Shevchenko, E. V.; Talapin, D. V.; O'Brien, S.; Murray, C. B. Polymorphism in AB_{13} nanoparticle superlattices: an example of semiconductor-metal metamaterials, *J. Am. Chem. Soc.* **2005**, *127*, 8741-8747.
(12) Ye, X.; Chen, J.; Murray, C. B. Polymorphism in self-assembled AB_6 binary nanocrystal superlattices, *J. Am. Chem. Soc.* **2011**, *133*, 2613-2620.
(13) Shevchenko, E. V.; Talapin, D. V.; Murray, C. B.; O'Brien, S. Structural Characterization of Self-Assembled Multifunctional Binary Nanoparticle Superlattices, *J. Am. Chem. Soc.* **2006**, *128*, 3620-3637.
(14) Goodfellow, B. W.; Rasch, M. R.; Hessel, C. M.; Patel, R. N.; Smilgies, D.-M.; Korgel, B. A. Ordered structure rearrangements in heated gold nanocrystal superlattices, *Nano Lett.* **2013**, *13*, 5710-5714.
(15) Korgel, B. A.; Fullam, S.; Connolly, S.; Fitzmaurice, D. Assembly and Self-Organization of Silver Nanocrystal Superlattices: Ordered "Soft Spheres" *J. Phys. Chem. B* **1998**, *102*, 8379-8388.
(16) Smith, D. K.; Goodfellow, B. W.; Smilgies D.-M.; Korgel, B. A. Self-assembled simple hexagonal AB_2 binary nanocrystal superlattices: SEM, GISAXS, and defects, *J. Am. Chem. Soc.* **2009**, *131*, 3281-3290.

(17) Murray, M. J.; Sanders, J. V. Close-packed structures of spheres of two different sizes II. The packing densities of likely arrangements. *Philos. Mag. A* **1980**, *42*, 721−740.
(18) Bartlett, P.; Ottewill, R. H.; Pusey, P. N. Superlattice formation in binary mixture of hard-sphere colloids. *Phys. Rev. Lett.* **1992**, *68*, 3801−3804.
(19) Korgel, B. A.; Zaccheroni, N.; Fitzmaurice, D. "Melting Transition" of a Quantum Dot Solid: Collective Interactions Influence the Thermally-Induced Order-Disorder Transition of a Silver Nanocrystal Superlattice. *J. Am. Chem. Soc.* **1999**, *121*, 3533-3534.
(20) Korgel, B. A. Correlated Membrane Fluctuations in Nanocrystal Superlattices. *Phys. Rev. Lett.*, **2001**, *86*, 127-130.
(21) Goodfellow, B. W.; Patel, R. N.; Panthani, M. G.; Smilgies, D.-M.; Korgel, B. A. Melting and sintering of a body-centered cubic superlattice of PbSe Nanocrystals followed by small angle X-ray scattering, *J. Phys. Chem. C* **2011**, *115*,6397-6404.
(22) Okamoto, H. *Desk handbook: Phase diagrams for binary alloys*, 1st ed., *ASM international: Materials Park, OH*, **2000**.
(23) Rasch, M. R.; Rossinyol, E.; Hueso, J. L.; Goodfellow, B. W.; Arbiol, J.; Korgel, B. A. Hydrophobic Gold Nanoparticle Self-Assembly with Phosphatidylcholine Lipid: Membrane-Loaded and Janus Vesicles. *Nano Lett.* **2010**, *10*, 3733-3739.
(24) Brust, M.; Walker, M.; Bethell, D.; Schiffrin, D. J.; Whyman, R. Synthesis of Thiol-Derivatised Gold Nanoparticles in a Two-Phase Liquid-Liquid System. *J. Chem. Soc., Chem. Commun.* **1994**, 801-802.
(25) Smilgies, D.-M.; and Blasini, D. R. Indexation scheme for oriented molecular thin films studied with grazing-incidence reciprocal-space mapping. *J. Appl. Cryst.* **2007**, *40*, 716-718. Israelachvili, J. *Intermolecular & Surface Forces,* 2nd ed.; Academic Press: San Diego, CA, **1992**.
(26) Ketelaar, J. A. A. The crystal structure of alloys of zinc with the alkali and alkaline earth metals and of cadmium with potassium, *J. Chem. Phys.* **1937**, *5*, 668.
(27) Shoemaker, D. P.; Marsh, R. E.; Ewing, F. J.; Pauling, L. Interatomic distances and atomic valences in $NaZn_{13}$, *Acta Cryst.* **1952**, *5*, 637-644.
(28) Li, Y.; Huang, J.; McIver, R. T. Jr.; Hemminger, J. C. Characterization of thiol self-assembled films by laser desorption Fourier transform mass spectrometry, *J. Am. Chem. Soc.* **1992**, *114*, 2428-2432.
(29) Dasog, M.; Scott, R. W. J. Understanding the oxidative stability of gold monolayer-protected clusters in the presence of halide ions under ambient conditions, *Langmuir* **2007**, *23*, 3381-3387.
(30) Hou, W.; Dasog, M.; Scott, R. W. J. Probing the relative stability of thiolate- and dithiolate-protected Au monolayer-protected clusters, *Langmuir* **2009**, *25*, 12954-12961.
(31) Teranishi, T.; Hasegawa, S.; Shimizu, T.; Miyaka, M. Heat-induced size evolution of gold nanoparticles in the solid state, *Adv. Mater.* **2001**, *12*, 1699-1701.

(32) Shimizu, T.; Teranishi, T.; Hasegawa, S.; Miyaka, M. Size evolution of alkanethiol-protected gold nanoparticles by heat treatment in the solid state, *J. Phys. Chem. B* **2003**, *107*, 2719-2724.
(33) Mnyukh, Y. *Fundamentals of solid-state phase transitions, ferromagnetism and ferroelectricity*. DirectScientific Press, 2010.
(34) Yu, Y.; Bosoy, C. A.; Smilgies, D.-M.; Korgel, B. A. Self-assembly and thermal stability of binary superlattices of gold and silicon nanocrystals. *J. Phys. Chem. Lett.* **2013**, *4*, 3677-3682.
(35) Figure 9.7d shows a scheme of the projection of ico-AB_{13} BSL $(100)_{BSL}$ planes and FFT of the TEM image. The center-to-center nearest-neighbor distance between small nanocrystals in the ico-AB_{13} BSL is 3.09 nm ($2*R_{soft\ sphere,small}$), and that between small and large nanocrystals is 4.23 nm ($R_{soft\ sphere,small} + R_{soft\ sphere,large}$), which indicates that the soft sphere diameter of small nanocrystal is 3.09 nm and that of large nanocrystal is 5.37 nm.
(36) The soft sphere diameter for large and nanocrystals are 5.64 nm and 2.97 nm. According to TEM images, (001) projection of sh-AB_2 BSL has a d-spacing of 4.88 nm, corresponding to a lattice constant of a = 5.64 nm. In sh- AB_2 BSL, the soft sphere diameter for large nanocrystal equals to the lattice constant, while the soft sphere diameter for small nanocrystal (2.97 nm) equals to the corner-to-center distance of unit cell (8.61 nm) minus the soft sphere diameter of large nanocrystal (5.64 nm).
(37) Profio, G. D.; Tucci, S.; Curcio, E.; Drioli, E. Controlling Polymorphism with Membrane-Based Crystallizers: Application to Form I and II of Paracetamol *Chem. Mater.* **2007**, *19*, 2386-2388.
(38) Mangin, D.; Puel, F.; Veesler,S. Polymorphism in Processes of Crystallization in Solution: A Practical Review *Org. Process Res. Dev.* **2009**,*13*,1241-1253.
(39) Bredig, M. A. The Polymorphism of Calcium Carbide *J. Phys. Chem.* **1942**, *46*, 801-819.

Chapter 10: Nanocrystal Superlattices that Exhibit Improved Order On Heating[§]

10.1 INTRODUCTION[4]

Beginning with the seminal report of Brust, Schiffrin, and coworkers in 1994,[1] alkanethiol-capped gold (Au) nanocrystals have served as useful models for understanding the synthesis and assembly of organic ligand-stabilized nanocrystals. They are easy to obtain and use: the synthesis is typically carried out at room temperature in air, requiring only a few mixing and separation steps; the nanocrystals are relatively stable and readily dispersible in non-polar solvents; and size distributions can be quite narrow.[2] With uniform particles, superlattices can be formed without difficulty; for example, simple drop-casting on a substrate[3] or liquid interface[4,5] can yield superlattices with relatively long-range order, and their assemblies have been extensively studied.[6] Alkanethiol-capped Au nanocrystals tend to order with either face-centered cubic (fcc) or body-centered cubic (bcc) structures, depending on the nanocrystal size and the ratio of the ligand length to the core diameter.[3] The packing structure (i.e., fcc or bcc) can be relatively insensitive to the assembly approach; however, the morphology of the assembly, the range of order, and nature of the superlattice defects, all depend on details like the nanocrystal concentration,[7] rate of solvent evaporation,[8,9] solvent-substrate interactions,[10] humidity,[11] the presence of excess ligand,[5,12] and even subtle

§ Portion of this chapter appears in .; Jain, A., Guillaussier, A.; Voggu, V. R.; Truskett, T. M.; Smilgies, D.-M.; Korgel,B. A. *faraday discussions* DOI: 10.1039/C5FD00006H (**2015**) Y. Yu performed the experiments. All author contributed to writing the text. B. A. Korgel and T. M. Truskett provided the funding through research grants.

differences in solvent polarity.[13-15] Alkanethiol-capped Au nanocrystals have provided a practical, yet perhaps deceptively simple, model for the study of colloidal particle self-assembly.

Ligand-stabilized nanocrystals are not simple *hard spheres* like the many of the typical sub-micrometer colloidal particles used in the past to mimic the behavior of condensed matter in its various states;[16-21] the soft organic ligand shell provides a buffer between particles even without the presence of solvent, creating a deformable "bond" that is sensitive to changes in temperature.[22,23] The interparticle interactions can be fitted to a Lennard-Jones potential.[24] Luedtke and Landman predicted in 1996 that it might be possible for assemblies of alkanethiol-capped Au nanocrystals to undergo phase transitions, such as superlattice melting.[25] To date, however, there have been no *reversible* structural transformations observed for alkanethiol-capped Au nanocrystal superlattices. The problem is that these nanocrystals are relatively prone to coalescence with only modest increases in temperature. For instance, dodecanethiol-capped Au nanocrystals have been observed to ripen and increase in size in superlattices heated to only 130^{o}C and then sinter at 190~200^{o}C—well below the melting temperature of Au.[26] To date, the only reversible structure transitions in assemblies of any type of ligand-stabilized nanocrystals have been observed at modest temperatures. Hanrath and colleagues for example used room temperature solvent vapor annealing of PbSe nanocrystal superlattices to observe rearrangements between bcc, fcc and amorphous structures.[27-29] Under those conditions, ligand attachment to the nanocrystals remains intact and the interparticle interactions could be reversibly tuned.

Here, we finally show an example of a reversible structure transition in an assembly of alkanethiol-capped Au nanocrystals. A collection of somewhat polydisperse and small (1.66 ± 0.30 nm diameter) octadecanethiol-capped Au nanocrystals were studied by grazing incidence small angle X-ray scattering (GISAXS) with *in situ* heating. At room temperature, the assembly exhibits some body-centered cubic (bcc) superlattice structure, but is predominantly amorphous. Raising the temperature above 45-55^{o}C led to a well-ordered bcc superlattice. The ordering is reversible and the structure again disorders when returned to room temperature. Differential scanning calorimetry (DSC) exhibited an endotherm at the ordering transition during heating and an exotherm upon disordering during cooling. Ordering of the superlattice upon heating is akin to *inverse melting*, which has been observed in ^{3}He,[30] and polymers, poly-4-methyl-pentene-1,[31] and syndiotactic polystyrene,[32] in which crystallization occurs upon heating and melting upon cooling.[33,34] In the case of the octadecanethiol-capped Au nanocrystals, the space-filling of the ligands appears to underlie the structural transition of the nanocrystal superlattice, as the transition temperatures correspond approximately to the melting and solidification temperatures of octadecanethiol.

10.2 EXPERIMENTAL DETAILS

10.2.1 Materials

Gold (III) chloride trihydrate ($HAuCl_4 \cdot 3H_2O$, >99.9%), tetraoctylammonium bromide (TOAB, 98%), 1-dodecanthiol (>98%), 1-octadecanethiol (98%), sodium

borohydride ($NaBH_4$,>98%) were purchased from Sigma-Aldrich. Toluene (99.9%) and absolute ethanol were purchased from Fisher. Deionized (DI) water was obtained using a Barnstead Nanopure Filtration System.

10.2.2 Gold Nanocrystals Synthesis

Au nanocrystals were synthesized with octadecanethiol capping ligands using a modified Brust-Schiffrin method.[1,35] In a typical synthesis, 10 mL of an aqueous solution of 164 mg of $HAuCl_4 \cdot 3H_2O$ (0.415 mmol) is combined with a solution of 3.281 g of TOAB (6.0 mmol) in 40 mL of toluene and stirred for 1 hr. The aqueous phase is then discarded and 1-octadecanethiol (358.2 mg, 1.25 mmol) is added to the toluene solution. An aqueous solution of the reducing agent is made in an ice bath with 189 mg of $NaBH_4$ (5.0 mmol) in 10 mL of DI-H_2O. The $NaBH_4$ solution is then combined with the toluene solution under stirring. After 12 hr, the organic phase is collected.

The nanocrystals were purified by antisolvent precipitation using volumetric ratios of 5:1 ethanol:toluene. Nanocrystals are collected between each precipitation step by centrifugation. After three washes, the nanocrystals were dispersed in 3 mL of toluene and centrifuged to precipitate poorly capped nanocrystals from the sample. The nanocrystal size distribution was further narrowed by size selective precipitation using toluene/ethanol as the solvent/antisolvent pair.[36]

10.2.3 Solution and Grazing Incidence Small Angle X-ray Scattering (SAXS and GISAXS)

SAXS and GISAXS measurements were performed on D1 beam line of the Cornell High Energy Synchrotron Source (CHESS), using monochromatic X-ray radiation with a wavelength of 1.155 Å and bandwidth of ~0.017 Å. GISAXS and SAXS pattern images were acquired with a fiber coupled CCD camera (MedOptics) having 1024 × 1024 pixels with size of 46.9 μm × 46.9 μm and dynamic range of 14-bit for each pixel. All patterns were dark current corrected, distortion corrected, and flat field corrected by the acquisition software with a sample-to-detector distance of 562.0 mm determined using silver behenate powder as a calibration standard.

Solution SAXS measurements were made with the X-ray beam incident angle at 0^{o} using exposure times of 30 sec. Ten patterns were recorded and averaged by the acquisition software. Measurements were made with Au nanocrystals dispersed in toluene at a concentration of 5 mg/mL in glass capillary tubes (1.2 mm diameter) horizontally secured on the top of stage. Background scattering of pure toluene and the capillary tube was subtracted prior to data fitting.

GISAXS data were recorded with an X-ray beam incident angle of 0.25^{o} and an exposure time of around 0.01 to 0.5 sec. Nanocrystal assemblies were prepared by drop-casting 20 μL of toluene dispersion of Au nanocrystals with a concentration of 20 mg/mL onto a hand-cut silicon wafer with a size of approximately 7 mm × 7 mm. GISAXS data were recorded with *in situ* heating of the sample using an aluminum heating stage designed to minimizing the sample height variation due to the thermal expansion of stage.

Fit2D software (version: 12_077_i686_WXP) was used to process and integrate the GISAXS patterns and the GISAXS diffraction spots were indexed using the procedures described in Ref 37.

10.2.4 Differential Scanning Calorimetry (DSC) and Transmission Electron Microscopy (TEM)

DSC was conducted on a Mettler-Toledo DSC1. Samples were scanned in a 75 μL aluminum crucible under N_2 atmosphere from 25°C to 70°C with a heating/cooling rate of 5°C/min. TEM was performed on a FEI Tecnai Biotwin TEM operated at 80 kV accelerating voltage. Nanocrystals were drop cast onto a 200 mesh carbon-coated copper grids for imaging (Electron Microsopy Science).

10.3 RESULTS AND DISCUSSION

The average diameter and size distribution of the octadecanethiol-capped Au nanocrystals were determined by SAXS measurements of nanocrystals dispersed in toluene. Figure 10.1b shows SAXS data fit to calculations of the scattering intensity $I(q)$, expected from a collection of non-interacting spherical particles:[36]

$$I(q) \propto \int_0^\infty N(R)P(qR)R^6 dR \qquad (1)$$

The number distribution $N(R)$, of the nanocrystals of radius R, is assumed to be Gaussian,

$$N(R) = \frac{1}{\sigma 2\pi} \exp\left[\frac{-(R-\bar{R})^2}{2\sigma^2}\right] \qquad (2)$$

with mean radius $\bar{R}$, and standard deviation of σ. The shape factor $P(qR)$, for spherical nanocrystals is

$$P(qR) = \left[3\frac{\sin(qR) - qR\cos(qR)}{(qR)^3} \right]^2 \qquad (3)$$

The scattering wave vector is $q = (4\pi/\lambda)\sin(\theta/2)$, where λ is the X-ray wavelength and θ is the scattering angle. Fitting Eqns (1)-(3) to the data in Fig. 1b yields an average diameter for the nanocrystals of 1.66 ± 0.30 nm (18.3% polydispersity). This size was verified by taking TEM images of the sample.

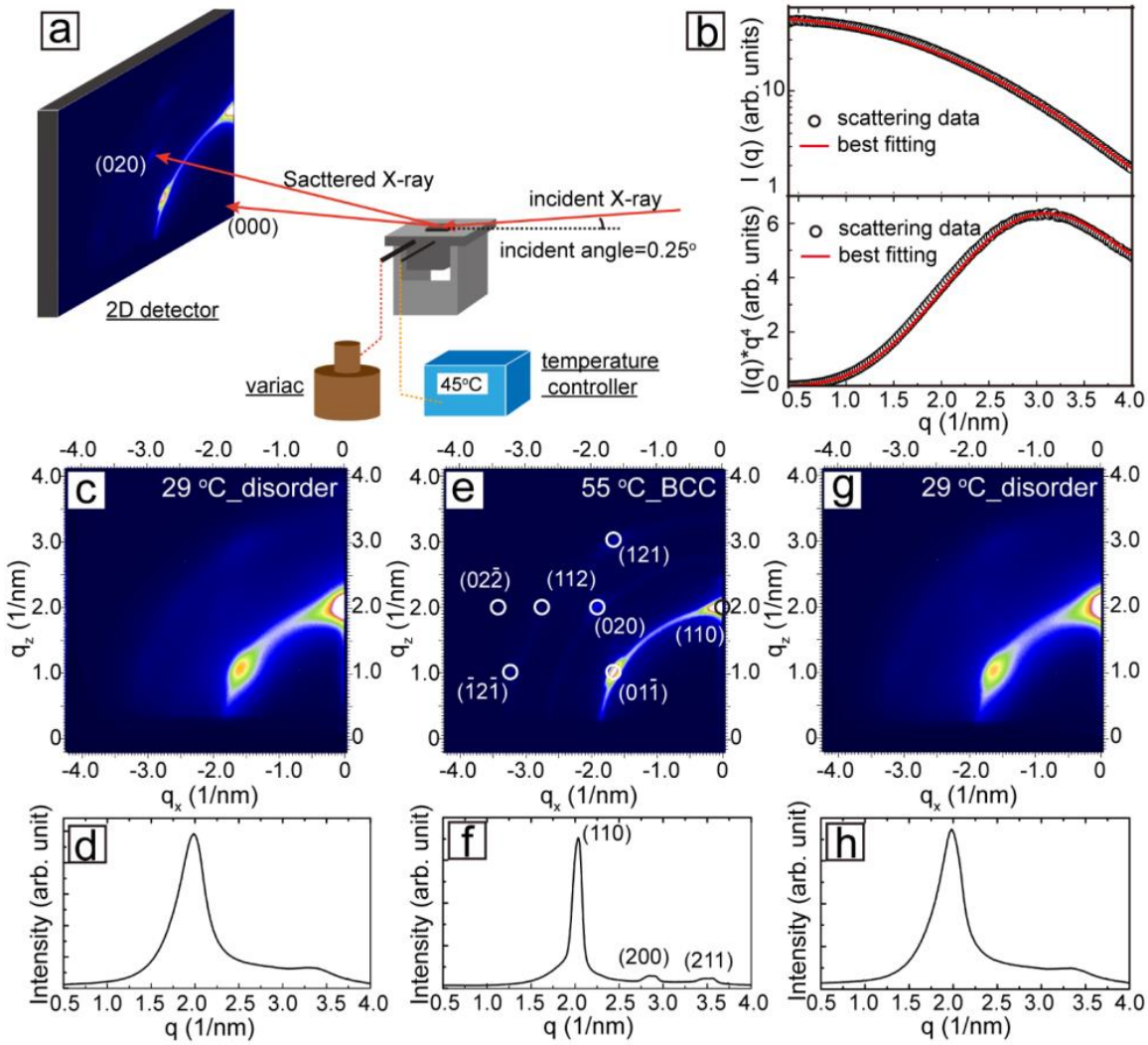

Figure 10.1: (a) Illustration of the GISAXS experiment setup with *in situ* heating capability. (b) SAXS data obtained from octadecanethiol-capped Au nanocrystals dispersed in toluene. A plot of Log($I(q)$) vs. q and a Porod plot are both shown with black circles as the data points and the red curves representing the best fit of Eqns (1)-(3) to the data. GISAXS data are shown for assemblies of these nanocrystals at (c) at 29°C, (e) after heating to 55°C and then (g) cooling back to 29°C. Radial integrations of the patterns in (c), (e) and (g) are shown in (d), (f) and (h), respectively. The GISAXS pattern in (e) and its radial integration in (f) are indexed to a bcc superlattice with a lattice constant of $a_{bcc,SL} = 4.4\,\text{nm}$.

Assemblies of octadecanethiol-capped Au nanocrystals were formed by drop-

casting and were then examined by GISAXS using an experimental setup with *in situ* heating as illustrated in Figure 10.1a. GISAXS provides a powerful tool for determining the structure of nanocrystal films.[38,39] The 2D GISAXS pattern (Fig. 10.1c) of the assembly exhibits a couple of very weak diffraction spots that index to a body-centered cubic (bcc) superlattice.[40] The extent of order, however, is very limited. For instance, the radial integration of the GISAXS pattern shown in Fig. 1d is consistent with an amorphous structure, having a ratio of q values for the first two diffraction peaks of $q_2/q_1 = 1.67$.[41-43] The limited range of order in the assembly reflects the relatively broad size distribution of the particles (>18% polydispersity).

Upon heating however, the superlattice order increased significantly. Figure 10.1e shows a GISAXS pattern obtained from the assembly from Fig. 10.1c heated to 55°C. The diffuse spots observed at room temperature are significantly sharper and more intense, and additional diffraction spots have appeared. As shown in Fig. 1e, the 2D diffraction pattern indexes to a bcc superlattice oriented with its $(110)_{SL}$ planes on the substrate with a lattice constant of $a_{bcc,SL} = 4.4\,\text{nm}$. Diffraction peak indexing is also shown in Fig. 1f for the radial integration of the 2D data. A comparison of the radially-integrated data at 29°C and 55°C reveals quite clearly that the nanocrystal assembly has changed from being largely disordered to an bcc superlattice with relatively long range order.

When the assembly was returned to room temperature, the long-range superlattice order was again lost, as the scattering patterns in Figs 10.1g and 1h show.

The 2D GISAXS pattern and its radial integration in Figs. 10.1g and 1h are similar to those of the initial assembly in Figs. 10.1c and 10.1d.

When the assembly was heated again to 55°C, it reordered. The disorder-to-order and disorder-to-order transitions were reversible for many heating and cooling cycles. Figure 10.2 shows radially integrated GISAXS data obtained from five heating and cooling cycles, showing the reversibility of the transitions.

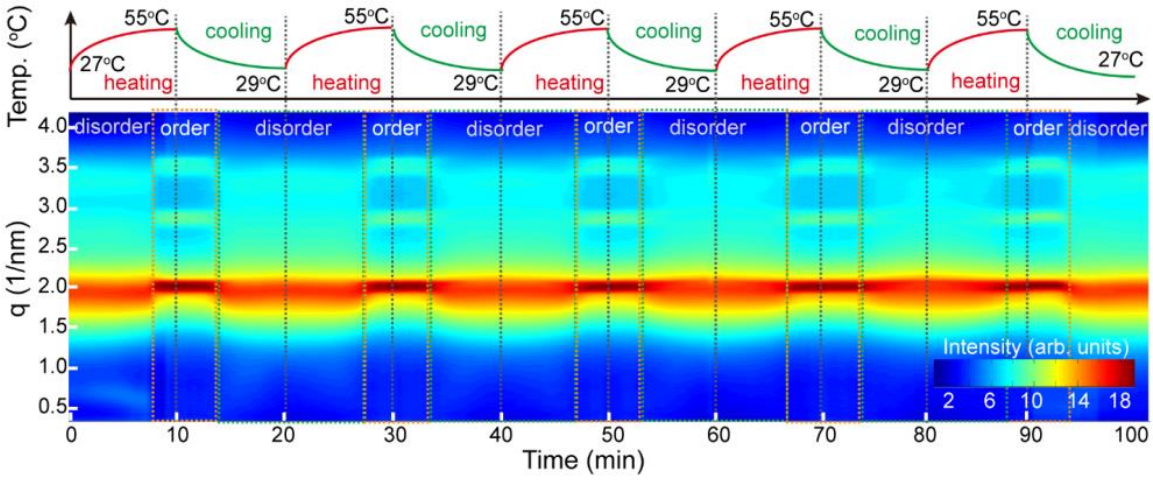

Figure 10.2: Top: A plot of the temperature of the octadecanethiol-capped Au nanocrystal assembly vs. time. Bottom: Contour plot of scattering intensity $I(q)$ vs. time. The GISAXS patterns were recorded with each 1°C increase in temperature. Inset: Intensity scale in which red indicates high scattering intensity with blue indicates low intensity.

The disorder-to-order and order-to-disorder transition temperatures were estimated using the Hansen-Verlet criterion for freezing, which is an empirical rule suggesting that the first peak in the structure factor $S(q)$, is approximately 2.85 when crystallization occurs.[44] Figure 10.3a shows plots of $S(q)$ at various temperatures. The

first peak maxima for $S(q)$ increased from 1.5 to 7 during heating and returned to 1.7 after cooling back near room temperature. Figure 10.3b shows the disorder-to-order (upon heating) and order-to-disorder (upon cooling) transition temperatures determined using the Hansen-Verlet criterion. The heating-induced disorder-to-order transition occurred at temperatures ranging between 45^{o}C and 50^{o}C, shifting slightly in temperature with each heating and cooling cycle. The order-to-disorder transitions occurred at slightly lower temperatures ranging from 35^{o}C to 40^{o}C.

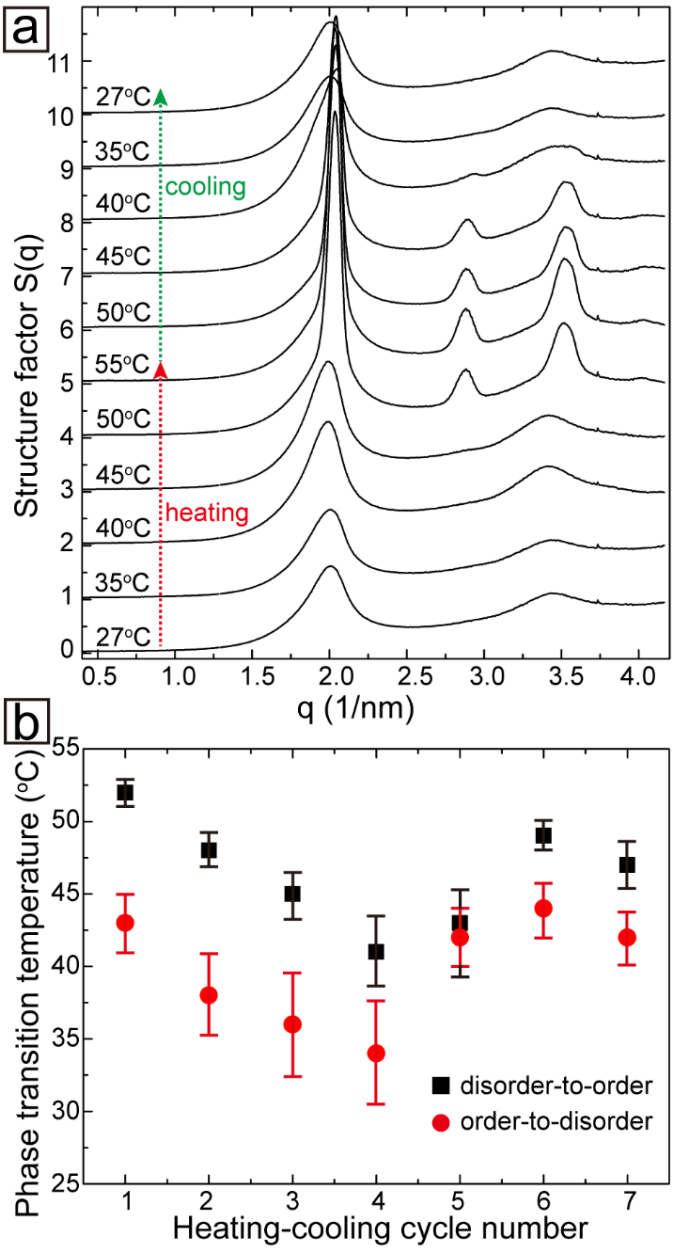

Figure 10.3: (a) $S(q)$ of assemblies of octadecanethiol-capped Au nanocrystals calculated from radially-integrated GISAXS patterns by normalizing the diffraction data with the scattering profiles obtained from the solution SAXS measurements.[45] (b) Disorder-to-order and order-to-disorder transition temperatures determined using the Hansen-Verlet criterion for freezing plotted against heating-cooling cycle number.

The thermal behavior of the nanocrystal assemblies was also examined by DSC. As shown in Fig. 10.4, an endotherm is observed during sample heating at 56°C and an exotherm during sample cooling at 49°C. These temperatures are close to the disorder-order and order-disorder transitions determined from the diffraction data using the Hansen-Verlet criterion (Fig. 10.3b). The transition temperatures and the endotherm and exotherm temperatures measured by DSC are close to the melting and solidification temperatures of octadecanethiol.[46] Therefore, it appears that melting and solidification of the capping ligands is related to the ordering transition observed for the octadecanethiol-capped nanocrystals.

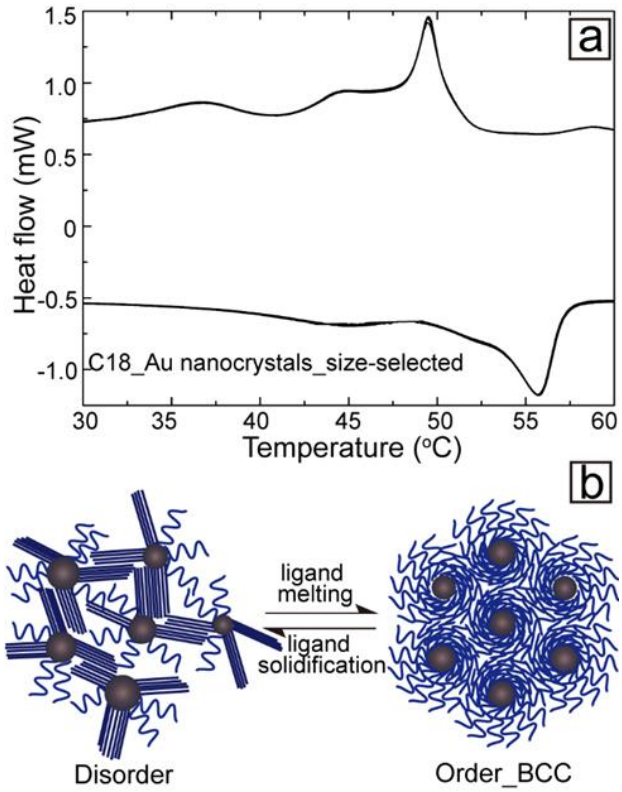

Figure 10.4

Figure 10.4: (a) DSC of size-selected octadecanethiol-capped Au nanocrystals with average diameter of 1.66 ± 0.30 nm (18.3% polydispersity). Multiple overlapping scans confirm that the thermal transitions are reversible. (b) Illustration of how ligand melting and solidification can influence superlattice order.

Geyer, Born and Kraus,[23] reported related phenomena in which aggregates of alkanethiol-capped Au nanocrystals exhibited ordered packing when drop-cast onto TEM grids at temperatures above the ligand melting point, and disordered packing when drop-cast at lower temperatures. They proposed that ligands are solid-like, below their melting point, friction or "stickiness" between assembling particles occurs that inhibits order; whereas, liquid-like ligands provide the necessary mobility to obtain close-packed, ordered structures. Our situation is different, as the nanocrystals are assembled prior to heating (and cooling) and the dynamics of the assembly process are not relevant. In our case, melting or solidification of the ligands appears to influence the uniformity of the interparticle interactions. Below the melting point of octadecanethiol, the ligands pack into ordered bundles, as illustrated in Fig. 10.4b.[25,46] Above the melting temperature of the ligands, the bundles are disrupted and the interparticle interactions become more uniform, again shown in Fig. 10.4b. This melted-ligand layer compensates for the Au core polydispersity and enables the nanocrystals to settle into a structure with ordered packing. An analysis of the effective nanocrystal size distribution that includes the ligand shell shows how this is possible. Polydispersities larger than 10% frustrate ordered packing of hard spheres.[47] And ligand-capped nanocrystals are slightly more tolerant to size non-uniformity because of the deformable capping ligands that can fill space and voids in the superlattice as necessary,[9] but polydispersities above about 12% still typically frustrate ordered packing.[48] In the case of these very small Au nanocrystals (1.66 nm diameter), the relatively long C_{18} capping ligands occupy an extremely large fraction

of the superlattice volume: 94.4%. Considering the excluded volume of the ligands and the Au core diameter of 1.66 nm, the effective diameter of the nanocrystals—considering a ligand shell with uniform thickness and density—is 4.34 nm. The standard deviation in particle diameter due to the Au cores is ±0.30 nm, making the effective polydispersity of the sample only ±6.9%, which is well within the limits required for ordered packing.

We also found that there is a limit to how much the ligands can overcome polydispersity and enable ordering in the superlattice. Assemblies were made with octadecanethiol-capped Au nanocrystals that were not size-selected, having a core size of 1.75 ± 0.35 nm, corresponding to 20% polydispersity. Figures 10.5b and 10.5c show GISAXS patterns obtained from the assemblies at 29^{o}C and 70^{o}C. There is no evidence of superlattice order in either diffraction pattern. Figure 10.5a shows DSC data from these assemblies. The endotherm and exotherm signatures of octadecanethiol melting and solidification are still observed, but the nanocrystals did not order when heated above the octadecanethiol melting point.

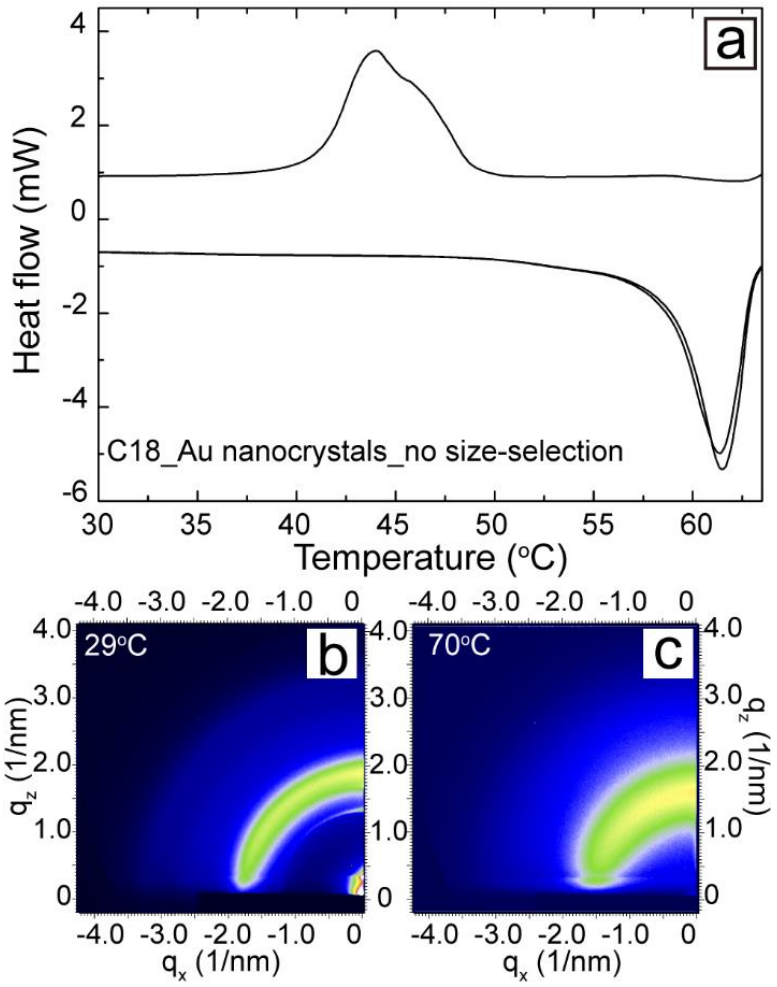

Figure 10.5: (a) DSC of octadecanethiol-capped Au nanocrystals that were not size-selected (average diameter 1.75 ± 0.35 nm (20% polydispersity); and GISAXS patterns of an assembly of these nanocrystals (b) near room temperature, and (c) at 70°C. Neither pattern exhibits any evidence of long range superlattice order.

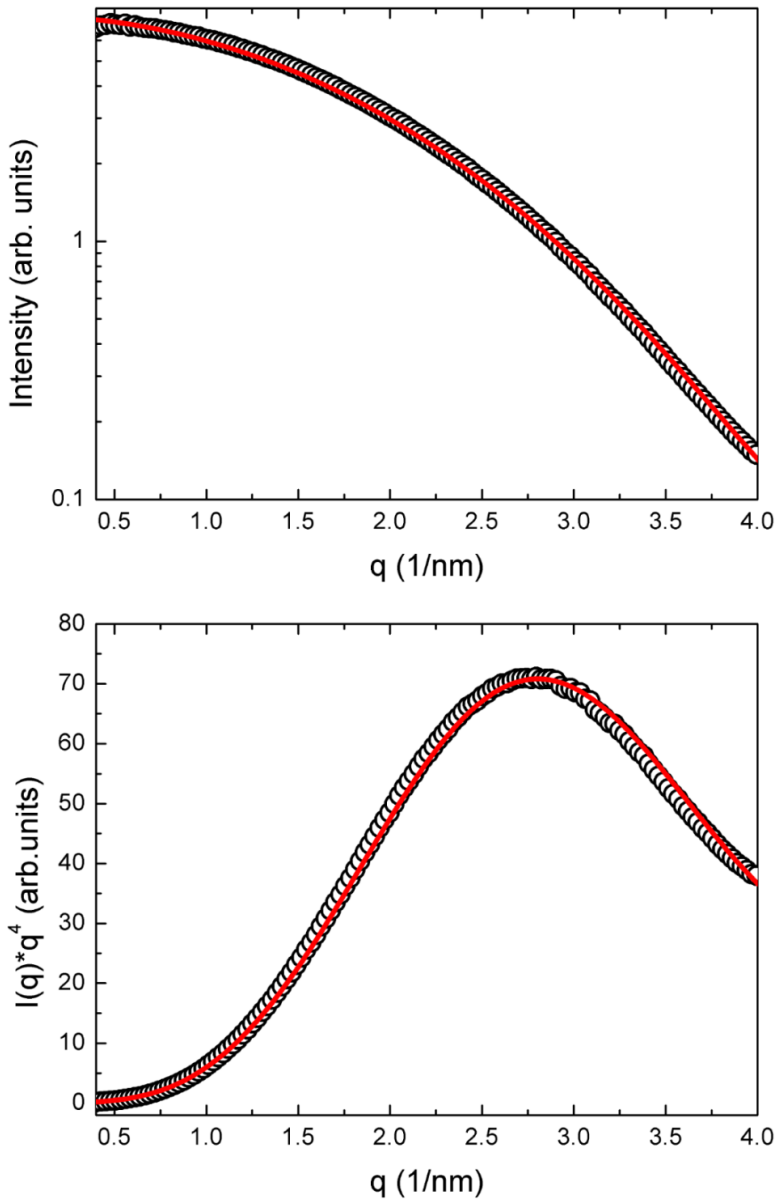

Figure 10.6: Solution SAXS data (black cycles) and the best fitting (red curve) of octadecanethiol-capped Au nanocrystals without size-selective precipitation. Top: Log of intensity vs *q*, Bottom: Porod plot.

Volume fraction occupied by ligand in superlattices of 1.66 nm diameter octadecanethiol-capped Au nanocrystals could be calculated through the BCC lattice parameter *a*, measured by GISAXS and the average Au core diameter measured by

SAXS. V_{core}, the volume fraction occupied by the Au nanocrystal cores is: $V_{core}/V_{total} = 2 * ({}^{4}/_{3} * \pi * R^3)/a^2 = 5.6\%$.

If the remaining volume in the superlattice is occupied by capping ligands (94.4%), the weight fraction of Au in the nanocrystal assemblies is: $W_{core}/W_{total} = (V_{core} * \rho_{Au})/(V_{core} * \rho_{Au} + V_{ligand} * \rho_{ligand}) = 60\%$. This is consistent with thermogravimetric analysis (TGA, Fig. 10.7). TGA was performed on a Mettler Toledo TGA-1, heating the nanocrystals in a 70 μL alumina crucible (Mettler Toledo) from 25°C to 800°C at a heating rate of 20°C/min. The sample was then held at 800°C for 30 min. The measurements were performed under 50 mL/min nitrogen gas flow. The weight loss of ~40% corresponds to the loss of organic ligands.

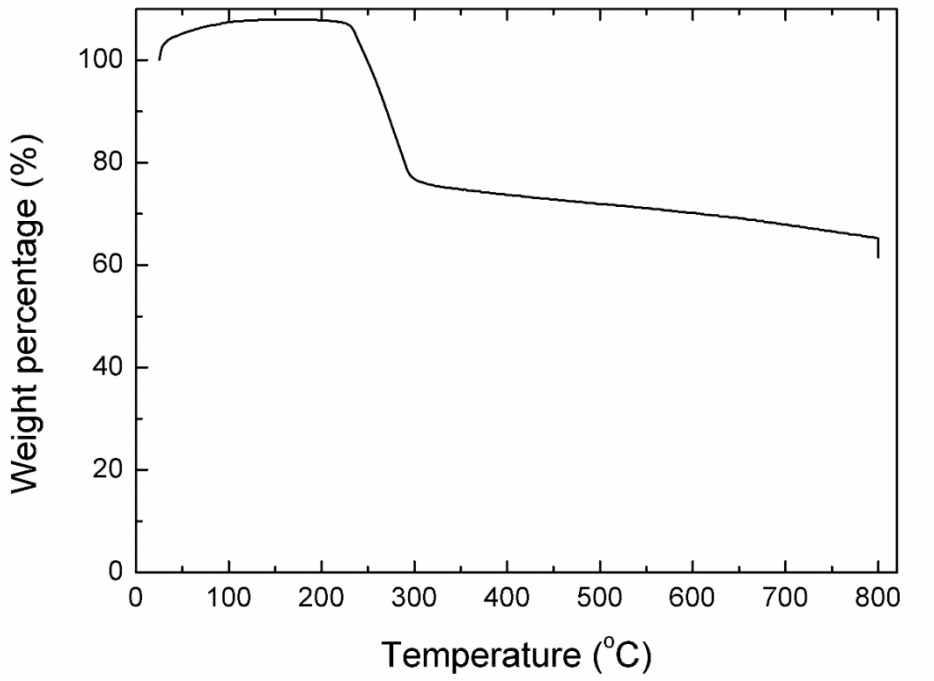

Figure 10.7: TGA of size-selected octadecanethiol-capped Au nanocrystals (average diameter of 1.66 ± 0.30 nm).

Figure 10.7 and 8 show TEM images of size-selected octadecanethiol-capped Au nanocrystal at low (Fig. 10.8) and high (Fig. 10.9) magnifications. The nanocrystals exhibit diameters less than 2 nm, consistent with sizing carried out by SAXS. Figure 10.10 shows TEM images of octadecanethiol-capped Au nanocrystals prior to size-selective precipitation. The particle size distribution is noticeably broader.

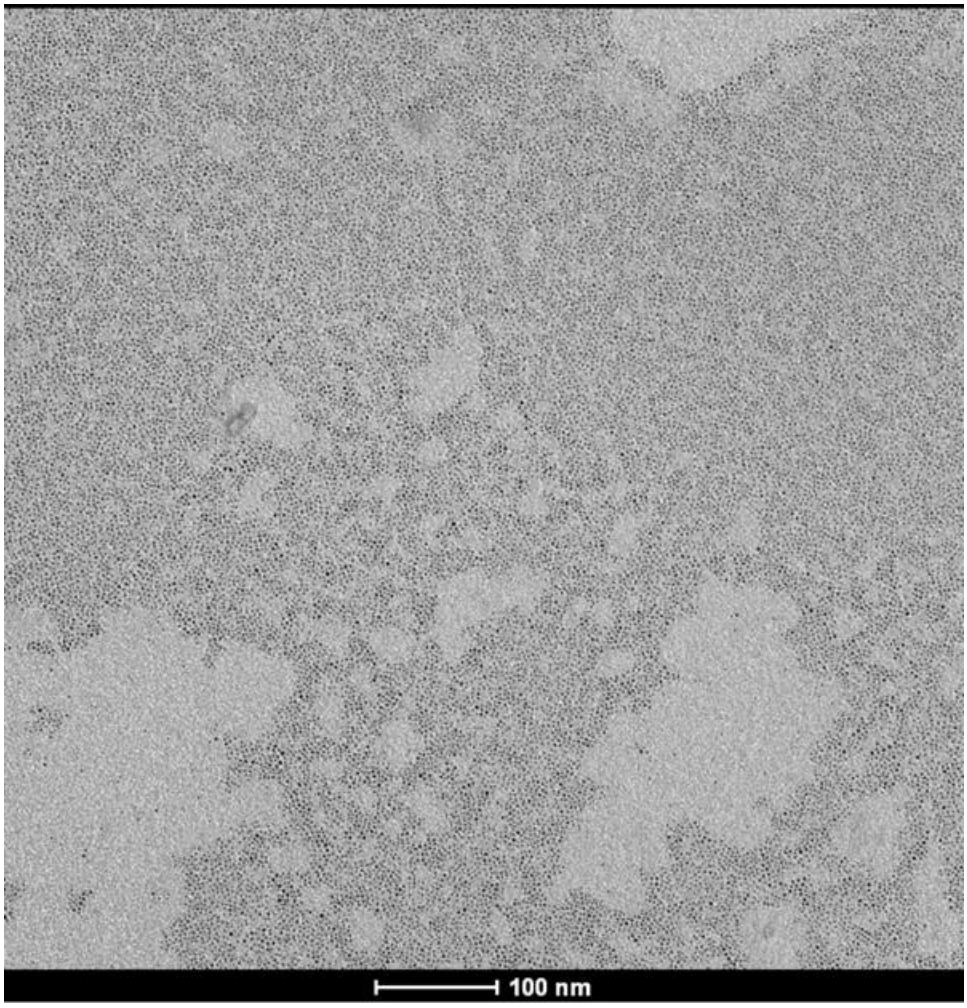

Figure 10.8: TEM image of size-selected octadecanethiol-capped Au nanocrystals.

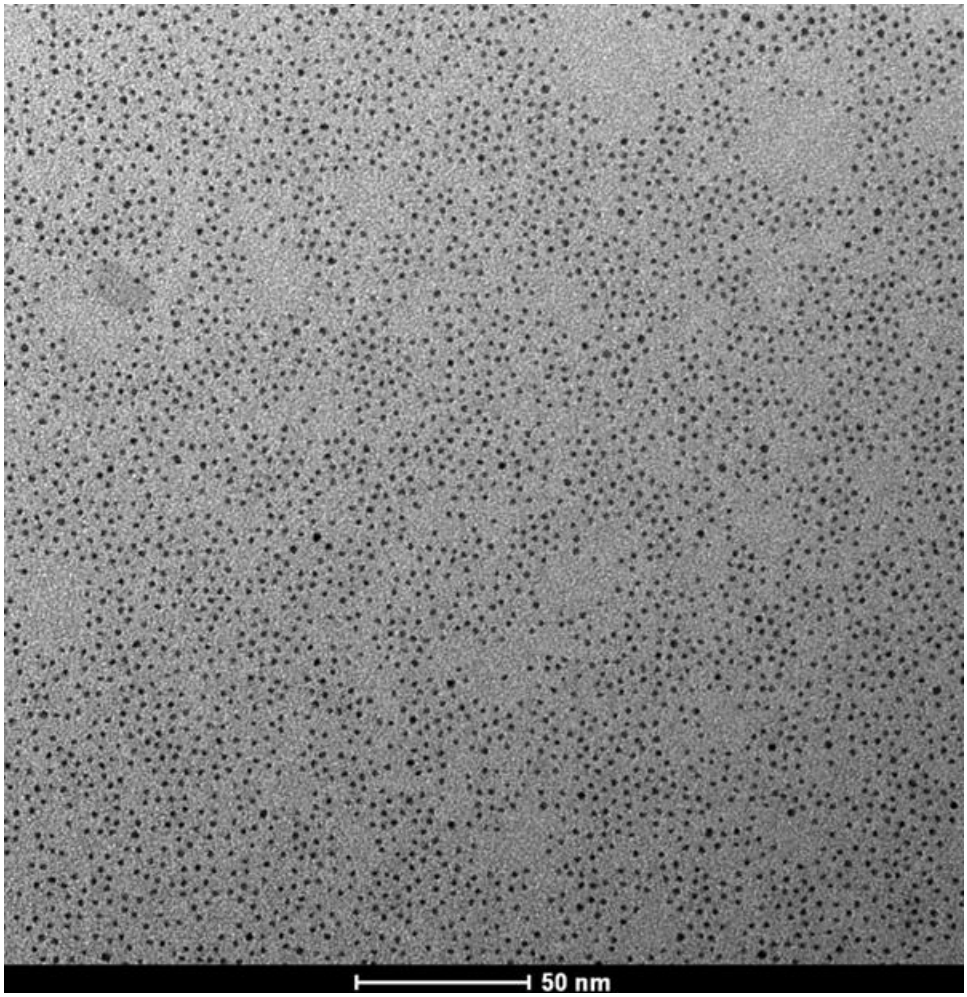

Figure 10.9: TEM image of size-selected octadecanethiol-capped Au nanocrystals.

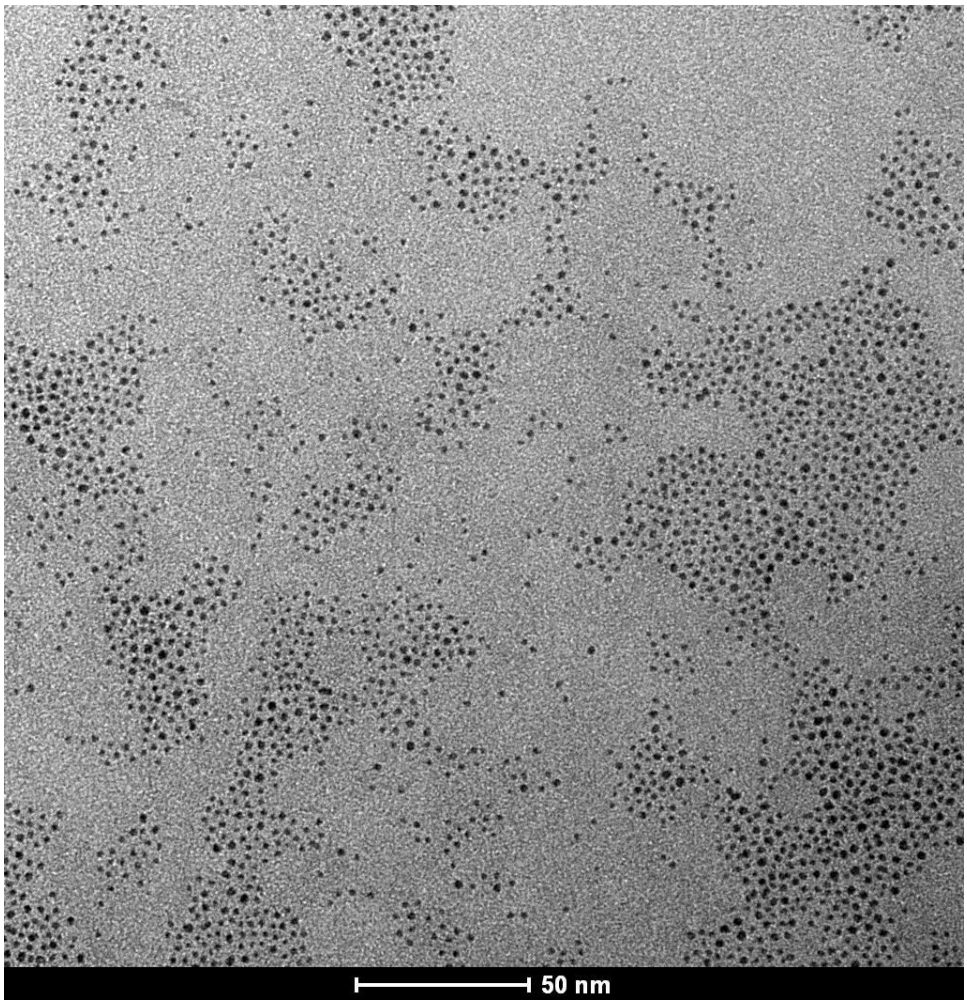

Figure 10.10: TEM image of size-selected octadecanethiol-capped Au nanocrystals.

Structure factor, S(q), could be calculated from scattering profile I (q) and form factor P(qR) determined in solution SAXS:

$$I(q) = n * P(qR) * S(q),$$

hence, $$S(q) = {I(q)}/{n * P(qR)}.$$

The Normalization factor n, is determined using the factor that

$$\langle S(q)\rangle = N^{-1} * \sum_{j,k}^{N} \langle e^{-iq(R_j - R_k)}\rangle$$

approaches a value of 1 at high q. In this work, we normalize our S(q) by assuming $S(q_{max})=1$. Figure 10.11 shows structure factors of Au nanocrystal superlattice during one heating-cooling cycle, plotted in 3d fashion.

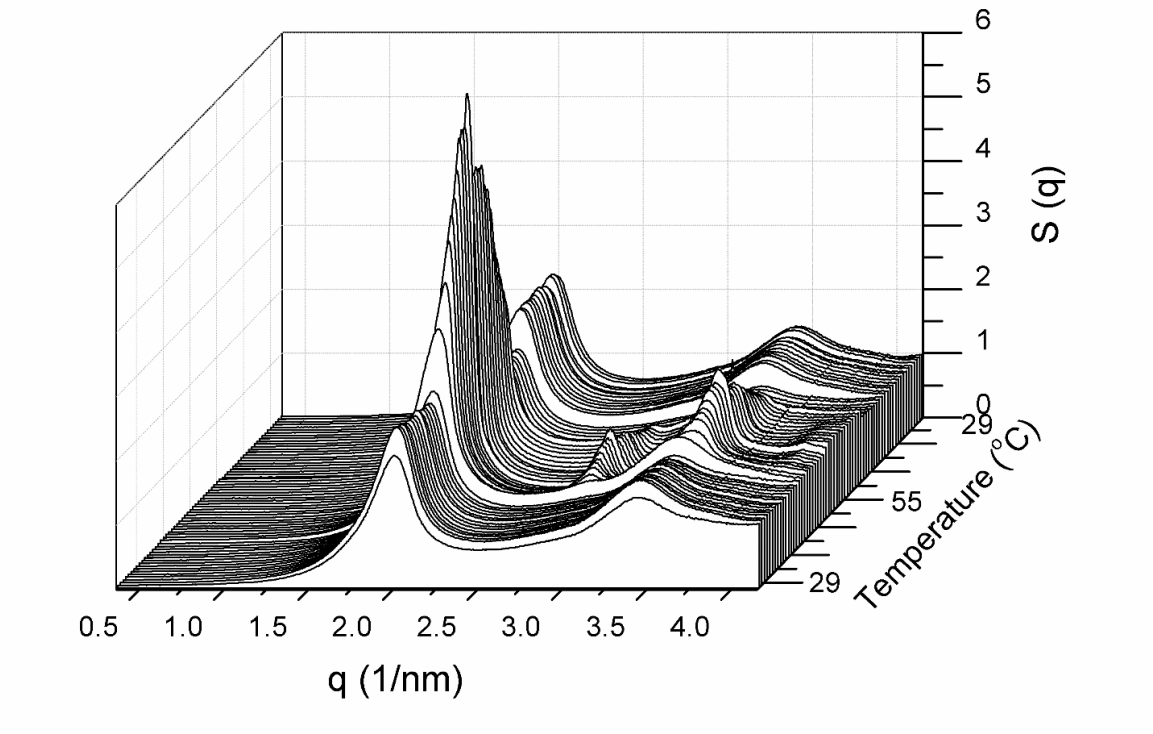

Figure 10.11: Structure factors of Au nanocrystal superlattice in a heating-cooling cycle.

10.4 CONCLUSION

Assemblies of very small, 1.66 nm diameter, octadecanethiol-capped Au nanocrystals with a reasonably polydisperse size distribution (σ=18.3%) undergo an ordering transition when heated. At room temperature, the assemblies are predominantly disordered, with only a slight evidence of short-range bcc order in the 2D GISAXS pattern. Once heated above 45-55^{o}C, the nanocrystals order into a well-defined bcc superlattice. Qualitatively, this heat-induced disorder-to-order transition is similar to inverse melting, in which the crystalline state occurs at higher temperature than the amorphous or liquid state.[34] DSC also showed an endotherm and exotherm associated with the disorder-to-order transition upon heating and the order-to-disorder structural transition upon cooling, as would be expected for an inverse melting transition.[31,49] These thermal features are also related to the melting and solidification of the octadecanethiol capping ligands. It appears that the capping ligands compensate for the Au core polydispersity when heated above the melting point of octadecanethiol.

This is the first *reversible* structural transition to be observed in a heated nanocrystal superlattice. The relatively mild transition temperature does not destroy the integrity of the nanocrystals. In all cases to date in which structure transitions in alkanethiol-capped Au nanocrystals have been observed with heating, the transitions have been irreversible due to ligand desorption and resulting changes in nanocrystal size.[26,50-57] This study provides new motivation to seek reversible structure transitions in nanocrystal superlattices, either through changes in temperature, pressure, or solvent vapor annealing and to seek systems with more robust ligand bonding, like alkyl-capped silicon

nanocrystals for example.[48] More robust nanocrystals should provide even more interesting model systems to study superlattice structure transitions—especially those that are reversible—perhaps with the possibility of finally observing a true melting transition in a nanocrystal superlattice.

10.5 REFERENCES

(1) Brust, M.; Walker, M.; Bethell, D.; Schiffrin, D. J.; Whyman, R. Synthesis of Thiol-Derivatised Gold Nanoparticles in a Two-Phase Liquid-Liquid System. *Chem. Commun.* **1994**, 801-802.

(2) Saunders, A. E.; Sigman, M. B.; Korgel, B. A. Growth Kinetics and Metastability of Monodisperse Tetraoctylammonium Bromide Capped Gold Nanocrystals. *J. Phys. Chem. B* **2004**, *108*, 193-199.

(3) Whetten, R. L.; Shafigullin, M. N.; Khoury, J. T.; Schaaff, T. G.; Vezmar, I.; Alvarez, M. M.; Wilkinson, A. Crystal Sreuctures of Molecular Gold Nanocrystal Arrys. *Acc. Chem. Res.* **1999**, *32*, 397-406.

(4) Santhanam, V.; Liu, J.; Agarwal; R.; Andres, R. P. Self-Assembly of Uniform Monolayer Arrays of Nanoparticles. *Langmuir*, **2003**, *19*, 7881-7887.

(5) Bigioni, T. P.; Lin, X.-M.; Nguyen, T. T.; Corwin, E. I.; Witten, T. A.; Jaeger, H. M. Kinetically Driven Self Assembly of Highly Ordered Nanoparticle Monolayer. *Nat. Mater.* **2006**, *5*, 265-270.

(6) Prasad, B. L.; Sorensen, C. M.; Klabunde, K. J. Gold Nanoparticle Superlattice. *Chem. Soc. Rev.* **2008**, *37*, 1871-1883.

(7) Ge, G.; Brus, L. Evidence for Spinodal Phase Separation in Two-Dimensional Nanocrystal Self-Assembly. *J. Phys. Chem. B* **2000**, *104*, 9573-9575.

(8) Stowell, C.; Korgel, B. A. Self-Assembled Honeycomb Networks of Gold Nanocrystals. *Nano Lett.* **2001**, *1*, 595-600.

(9) Smith, D. K.; Goodfellow, B. W.; Smilgies, D.-M.; Korgel B. A. Self-Assembled Simple Hexagonal AB_2 Binary Nanocrystal Superlattices: SEM, GISAXS, and Defects. *J. Am. Chem. Soc.* **2009**, *131*, 3281-3290.

(10) Ohara, P. C.; Heath, J. R.; Gelbart, W. M. Self-Assembly of Submicrometer Rings of Particles from Solution of Nanoparticles. *Angew. Chem. Intl. Ed.* **1997**, *36*, 1078-1080.

(11) Saunders, A. E.; Shah, P. S.; Sigman, M. B.; Hanrath, T.; Hwang, H. S.; Lim, K. T.; Johnston, K. P.; Korgel, B. A. Inverse Opal Nanocrystal Superlattice Films. *Nano Lett.* **2004**, *4*, 1943-1948.

(12) Lin, X. M.; Jaeger, H. M.; Sorensen, C. M.; Klabunde, K. J. Formation of Long-Range-Ordered Nanocrystal Superlattices on Silicon Nitride Substrates. *J. Phys. Chem. B* **2001**, *105*, 3353-3357; Goubet, N.; Pileni, M.-P. Negative Supracrystals

Inducing FCC-BCC Transition in Gold Nanocrystal Superlattices. *Nano Res.* **2014**, *7*, 171-179.
(13) Rabani, E.; Reichman, D. R.; Geissler, P. L.; Brus, L. E. Dring-Mediated Self-Assembly of Nanoparticles. *Nature*, **2003**, *426*, 271-274.
(14) Korgel, B. A.; Fitzmaurice, D.; Condensation of Ordered Nanocrystal Thin Films. *Phys. Rev. Lett.* **1998**, *80*, 3531-3534.
(15) Sigman, M. B.; Saunders, A. E.; Korgel, B. A. Metal Nanocrystal Superlattice Nucleation and Growth. *Langmuir* **2004**, *20*, 978-983.
(16) Pusey, P. N.; Zaccarelli, E.; Valeriani, C.; Sanz, E.; Poon, W. C. K.; Cates, M. E. Hard Spheres: Crystalline and Glass Formation. *Phil. Trans. R. Soc. A* **2009**, *367*, 4993-5011.
(17) Pusey, P. N.; van Megen, W. Phase Behaviors of Concentrated Suspensions of Nearly Hard Colloidal Spheres. *Nature* **1986**, *320*, 340-342.
(18) Sastry, S.; Truskett, T. M.; Debenedetti, P. G.; Torquato, S.; Stillinger, F. H. Free Volume in the Hard Sphere Liquid. *Molecular Phys.* **1998**, *95*, 289-297.
(19) Löwen, H.; Palberg, T.; Simon, R. Dynamical criterion for freezing of colloidal liquids. *Phys. Rev. Lett.* **1993**, *70*, 1557-1560.
(20) Torquato, S.; Stillinger, F. H. Jammed hard-particle packings: from Kepler to Bernal and beyond. *Rev. Mod. Phys.* **2010**, *82*, 2633-2672.
(21) Woodcock, L. V. Entropy difference between the face-centered cubic and hexagonal close-packed crystal structures. *Nature* **1997**, *385*, 141-143.
(22) Bodnarchuk, M. I.; Kovalenko, M. V.; Heiss, W.; Talapin, D. V. Energetic and entropic contributions to self-assembly of binary nanocrystal superlattices: temperature as the structure-directing factor. *J. Am. Chem. Soc.* **2010**, *132*, 11967-11977.
(23) Geyer, T.; Born, P.; Kraus, T. Switching between crystallization and amorphous agglomeration of alkyl thiol-coated gold nanoparticles. *Phys. Rev. Lett*. **2012**, *109*, 128302.
(24) Saunders, A. E.; Korgel, B. A. Growth Kinetics and Metastability of Monodisperse Tetraoctylammonium Bromide Capped Gold Nanocrystals. *J. Phys. Chem. B* **2004**, *108*, 16732-16738.
(25) Luedtke, W. D.; Landman, U. Structure, Dynamics, and Thermodynamics of Passivated Gold Nanocrystallites and Their Assemblies. *J. Phys. Chem.* **1996**, *100*, 13323-13329.
(26) Goodfellow, B. W.; Rasch, M. R.; Hessel, C. M.; Patel, R. N.; Smilgies, D.-M.; Korgel, B. A. Ordered structure rearrangements in heated gold nanocrystal superlattices. *Nano Lett.* **2013**, *13*, 5712-5714.
(27) Bian, K.; Choi, J. J.; Kaushik, A.; Clancy, P.; Smilgies, D.-M.; Hanrath, T. Shape-Anisotropy Driven Symmetry Transformations in Nanocrystal Superlattice Polymorphs. *ACS Nano* **2011**, *5*, 2815-2823.
(28) Goodfellow, B. W.; Korgel, B. A. Reversible Solvent Vapor-Mediated Phase Changes in Nanocrystal Superlattices. *ACS Nano* **2011**, *5*, 2419-2424.

(29) Hanrath, T. Colloidal Nanocrystal Quantum Dot Assemblies as Artificial Solids *J. Vac. Sci. Tech. A,* **2012**, *30*, 030802.
(30) Dobbs, E. R. Helium three, *Oxford University Press, Oxford*, **2002**.
(31) Rastogi, S.; Newman, M.; Keller, A. Unusual pressure-induced phase behavior in crystalline poly-4-methyl-pentene-1. *J. Poly. Sci. B* **1993**, *31*, 125-139.
(32) van Hooy-Corstjens, C. S. J.; Höhne, G. W. H.; Rastogi, S. Inverse melting in syndiotactic polystyrene. *Macromole.* **2005**, *38*, 1814-1821.
(33) Feeney, M. R.; Debenedetti, P. G.; Stillinger, F. H. A statistical mechanical model for inverse melting. *J. Chem. Phys.* **2003**, *119*, 4582-4591.
(34) Stillinger, F. H.; Debenedetti, P. G. Phase transitions, Kauzmann curves, and inverse melting. *Biophys. Chem.* **2003**, *105*, 211-220.
(35) Rasch, M. R.; Rossinyol, E.; Hueso, J. L.; Goodfellow, B. W.; Arbiol, J.; Korgel, B. A. Hydrophobic Gold Nanoparticle Self-Assembly with Phosphatidylcholine Lipid: Membrane-Loaded and Janus Vesicles. *Nano Lett.* **2010**, *10*, 3733-3739.
(36) Korgel, B. A.; Fullam, S.; Connolly, S.; Fitzmaurice, D. Assembly and Self-Organization of Silver Nanocrystal Superlattices: Ordered "Soft Spheres" *J. Phys. Chem. B* **1998**, *102*, 8379-8388.
(37) Smilgies, D.-M.; and Blasini, D. R. Indexation scheme for oriented molecular thin films studied with grazing-incidence reciprocal-space mapping. *J. Appl. Cryst.* **2007**, *40*, 716-718.
(38) Heitsch, A. T.; Patel, R. N.; Goodfellow, B. W.; Smilgies, D.-M.; Korgel, B. A. GISAXS Characterization of Order in Hexagonal Monolayers of FePt Nanocrystals. *J. Phys. Chem. C* **2010**, *114*, 14427-14432.
(39) Smilgies, D.-M.; Heitsch, A. T.; Korgel, B. A. Stacking of Hexagonal Nanocrystal Layers during Langmuir-Blodgett Deposition. *J. Phys. Chem. B*, **2012**, *116*, 6017-6026.
(40) Goodfellow, B. W.; Patel, R. N.; Panthani, M. G.; Smilgies, D.-M.; Korgel, B. A. Melting and sintering of a body-centered cubic superlattice of PbSe nanocrystals followed by small angle X-ray scattering. *J. Phys. Chem. C* **2011**, *115*, 6397-6404.
(41) Sheng, H. W.; Liu, H. Z.; Cheng, Y. Q.; Wen, J.; Lee, P. L.; Luo, W. K.; Shastri, S. D.; Ma, E. Polymorphism in a Metallic Glass. *Nature Mater.*, **2007**, *6*, 192-197.
(42) Harris, J. T.; Hueso, J. L.; Korgel, B. A. Hydrogenated Amorphous Silicon (a-Si:H) Colloids. *Chem. Mater.* **2010**, *22*, 6378-6383.
(43) Pell, L. E.; Schricker, A. D.; Mikulec, F. V.; Korgel, B. A. Synthesis of Amorphous Silicon Colloids by Trisilane Thermolysis in High Temperature Supercritical Solvents. *Langmuir* **2004**, *20*, 6546-6548.
(44) Hansen, J.-P.; Verlet, L. Phase transitions of the Lennard-Jones system. *Phys. Rev.* **1969**, *184*, 151-161.
(45) Saunders, A. E.; Shah, P. S.; Park, E. J.; Lim, K. T.; Johnston, K. P.; Korgel, B. A. Solvent Density-Dependent Steric Stabilization of Perfluoropolyether-Coated Nanocrystals in Supercritical Carbon Dioxide. *J. Phys. Chem. B* **2004**, *108*, 15969-15975.

(46) Badia, A.; Singh, S.; Demers, L.; Cuccia, L.; Brown, G. R.; Lennox, R. B. Self-assembled monolayers on gold nanoparticles. *Chem. Eur. J.* **1996**, *2*, 359-363.
(47) Phan, S.-E.; Russel, W. B.; Zhu, J.; Chaikin, P. M. Effects of polydispersity on hard sphere crystals. *J. Chem. Phys.* **1998**, *108*, 9789-9795.
(48) Yu, Y.; Bosoy, C. A.; Hessel, C. M.; Smilgies, D.-M.; Korgel, B. A. Silicon Nanocrystal Superlattice. *ChemPhysChem* **2013**, *14*, 84-87.
(49) Rastogi, S.; Höhne, G. W. H. A. Keller, Unusual Pressure-Induced Phase Behavior in Crystalline Poly(4-methylpentene-1): Calorimetric and Spectroscopic Results and Further Implications. *Macromolecules*, **1999**, *32*, 8897-8909.
(50) Korgel, B. A.; Zaccheroni, N.; Fitzmaurice, D. "Melting transition" of a quantum dots solid: collective interactions influence the thermally-induced order-disorder transition of a silver nanocrystal superlattice. *J. Am. Chem. Soc.* **1999**, *121*, 3533-3534.
(51) Yu, Y.; Bosoy, C. A.; Smilgies, D.-M.; Korgel, B. A. Self-assembly and thermal stability of binary superlattice of gold and silicon nanocrystals. *J. Phys. Chem. Lett.* **2013**, *4,* 3677-3682.
(52) Korgel, B. A. Correlated membrane fluctuations in nanocrystal superlattices. *Phys. Rev. Lett.* **2001**, *86*, 127-130.
(53) Goodfellow, B. W.; Patel, R. N.; Panthani, M. G.; Smilgies, D.-M.; Korgel, B. A. Melting and sintering of a body-centered cubic superlattice of PbSe nanocrystals followed by small angle X-ray scattering. *J. Phys. Chem. C* **2011**, *115*, 6397-6404.
(54) Courty, A.; Henry, A.-I.; Goubet, N.; Pileni, M.-P. Large Triangular Single Crystals Formed by Mild Annealing of Self-Organized Silver Nanocrystals. *Nature Mater.* **2007**, *6*, 900-907.
(55) Ingham, B.; Lim, T. H.; Dotzler, C. J.; Henning, A.; Toney, M. F.; Tilley, R. D. How Nanoparticle Coalesce: An in situ Study of Au Nanoparticle Aggregation and Grain Growth. *Chem. Mater.* **2011**, *23*, 3312-3317.
(56) Lee, B.; Podsiadlo, P.; Rupich, S.; Talapin, D. V.; Rajh, T.; Shevchenko, E. V. Comparison of Structural Behavior of Nanocrystals in Randomly Packed Films and Long-Range Ordered Superlattices by Time-Resolved Small Angle X-ray Scattering. *J. Am. Chem. Soc.* **2009**, *131*, 16386-16388.
(57) Ellis, A. V.; D'Arcy-Gall, J.; Vijayamohanan, K.; Goswami, R.; Ganesan, P. G.; Ryu, C.; Ramanath, G. Phase Transitions in Octanethiol-Capped Ag Nanocluster Microfilm Assemblies. *Themochimica Acta* **2005**, *426*, 207-212.

Chapter 11: Conclusions and Future Work Directions

Silicon nanocrystal combines the quantum confinement of semiconductor nanocrystal or quantum dots and the abundant and nontoxic nature of silicon to form a new generation of functional materials. Silicon nanocrystal exhibits size-tunable band gap and fluorescence color, and is eligible for low cost solution process, such as drop casting, spin coating, and doctor blading. Compare to other quantum dots, i.e. CdSe, CdS, PbSe, PdS, and InAs, silicon nanocrystal is environmentally friendly, nontoxic, biocompatible, and biodegradable. Silicon nanocrystals have applications in bioimaging, photodynamic and photothermal therapies, memory devices, photovoltaic, and light-emitting devices.

Unlike ionic semiconductor nanocrystals which could be synthesized in solutions, silicon is a covalent crystal, and as far as I know, typically requires a gas- or solid-state synthesis, leading to a broad size distribution. The covalent nature of silicon also adds difficulties to its surface functionalization. For example, epitaxy growth a wide band gap semiconductor on silicon nanocrystal has never been achieved. The lack of monodisperse silicon nanocrystals and means of surface functionalization are the main issues with silicon nanocrystal, which are also the reasons why silicon nanocrystals are way under developed comparing to CdSe.

This dissertation is dedicated in promoting silicon nanocrystal by solving these problems. On one hand, various chemistries are discovered and studied based on the specific applications; on the other hand, monodisperse silicon nanocrystals are obtained through a modified size-selective precipitation, and assembled to superlattices. Finally, as a side project, fundamentals of nanocrystal superlattices are studied by using sub-2 nm gold nanocrystal superlattices as model systems.

11.1 CONCLUSIONS

11.1.1 Silicon Nanocrystal Surface Chemistry

Room temperature hydrosilylation allows functionalization of silicon nanocrystals with carboxylic acid without involving any heating, UV irradiation, or additional catalyst. It minimizes potential silicon nanocrystal surface corrosion, mostly through oxidization, and generates silicon nanocrystals with high ligand coverage. 10-undecenoic acid capped 2.7 nm diameter silicon nanocrystal can disperse in water at a concentration of 10 mg/mL. Upon dispersed in water, the carboxylic acid groups are partially deprotonated to generate surface charges to stabilize nanocrystals in water. Silicon nanocrystals are slowly oxidized in water, leading to a blue shift in the photoluminescence and a decrease in the absorbance. However, the photoluminescence quenching is extremely slow, less than 10% in a month. Large silicon nanocrystal (up to 11 nm in diameter) could also be dispersed in water.

Hydrosilylation at room temperature also provides an approach to functionalize silicon nanocrystal with temperature sensitive ligands, such as styrene. Compared to the thermally or UV-initiated hydrosilylation that result in silicon nanocrystals embedded in polystyrene matrix, room temperature hydrosilylation generates styrene monolayer-functionalized silicon nanocrystals. The styrene monolayer facilates efficient charge carrier injection to silicon nanocrystal, which is crucial for enhancing the power efficiency of light emitting devices.

Room temperature hydrosilylation was also demonstrated to covalently conjugate silicon nanocrystal to iron oxide nanocrystal with a bifunctional ligand, 10-undecenoic acid. Iron oxide nanocrystal appeared to be in the center of the "supernanocrystal", and was surrounded by silicon nanocrystals, which generates dispersibility in polar organic solvents and aqueous solutions.

Besides hydrosilylation, thiolation was also found to be an effective way to passivate silicon nanocrystals. Under heating in nitrogen gas atmosphere, alkane thiol reacted with hydride-terminated silicon nanocrystals to form Si-S bonds. Thiol terminated silicon nanocrystal surface can undergo a ligand exchange to form a Si-C terminated surface, while the opposite ligand exchange does not exist. Si-S bonds are sensitive to moisture, leading to an extremely sensitive photoluminescence of thiol passivated silicon nanocrystals. 20 ppm of water was sufficient to immediately and completely quench the photoluminescence of thiol passivated 2.5 nm diameter silicon nanocrystals.

11.1.2 Silicon Nanocrystal Superlattice

Colloidal silicon nanocrystal superlattices were formed for the first time. Dodecene-capped silicon nanocrystals were size-selected through a multistep size-selective precipitation and drop casted from chloroform to form a superlattice. The superlattice typically has a face-centered-cubic (FCC) structure with its (111) planes oriented on the substrate. Silicon nanocrystal superlattices have ultra-high thermal stability, which can be attributed to the Si-C bonding on the nanocrystal surface.

Dodecene-capped 5.4 nm diameter Silicon nanocrystals tended to form FCC superlattice and dodecanethiol-capped 1.9 nm diameter gold nanocrystals tended to form body-centered cubic (BCC) superlattice, while a mixture of those two types of nanocrystals would form a simple hexagonal AlB_2 binary superlattice to maximize the packing density. Such binary superlattice had a lattice constant of 6.7 nm with 3.7% of lattice constant along the z-direction and oriented on the substrate with (001) planes. Upon heating to 200^{o}C in air, the gold nanocrystal became unstable due to the oxidation of thiol and started to coalesce, while silicon nanocrystal showed no response to this temperature. As a result of the two completely difference responses to heating of gold and silicon nanocrystals, the gold nanocrystals coherently migrate out of the binary superlattice and coalesce on its surface, leaving silicon nanocrystals be kinetically trapped in a thermodynamic unstable simple hexagonal superlattice.

11.1.3 Gold Nanocrystal Superlattice Phase Transitions

The surface of dodecanethiol-capped gold nanocrystal became unstable at elevated temperature due to the thiol oxidation, and as a result, Oswald ripening occurs, leading to nanocrystal growth and coalescence. Halide ion impurities, i.e. tetraoctylphosphonium bromide (TOPB), can further decrease the thermal stability of gold nanocrystals, allowing the superlattice to exhibit a series of order-to-order structural rearrangements. A typical structural rearrangement route was: BCC to ico-AB_{13} binary superlattice, to simple hexagonal AlB_2 binary superlattice, to simple hexagonal, to FCC, and finally to coalesced phase. In contrast, gold nanocrystal superlattice without halide

ions showed no Oswald ripening and related structural rearrangements before coalescence. A nucleate-and-growth behavior was also found for superlattice structural rearrangement.

Nature solids and artificial solids (nanocrystal superlattice) typical exhibit order to disorder transition upon increasing temperature, i.e. ice melts to water, polymers turn from crystalline to glass phase, and nanocrystal superlattice coalescence. Nanocrystal superlattice consist of hard inorganic core and flexible organic capping ligands, which could create additional internal freedom and generate usual phase transitions controlled by thermodynamics, similar to the case of inverse melting of liquid helium. Octedecanethiol-capped 1.66 nm diameter gold nanocrystals forms a BCC superlattice, in which the capping ligands occupies 94.4% of the space and plays an important role in determining the superlattice structure. Such nanocrystal formed amorphous ensemble at room temperature, turn to BCC superlattice if heated to temperature above 55^{o}C, and return to amorphous once cooled back to room temperature. Such phase transition is reversible, suggesting the transition is control by thermodynamics instead of kinetics. DSC study revealed that the amorphous-to-crystalline and crystalline-to-amorphous transition of superlattice occurred at a similar temperature of capping ligand melting and solidification transitions, respectively. This leads to a conclusion that the usual ordering upon heating transition of nanocrystal superlattice is a result of capping ligand melting, which created a isotropic inter-particle potential and favored order superlattice. At room temperature, capping ligands solidified and bundled, generating an anisotropic potential around the particle, for which amorphous phase is thermodynamically stable.

11.2 FUTURE WORK DIRECTIONS

11.2.1 Bioconjugation of Bioactive Molecules to Silicon Nanocrystal Surface

In order to specifically target certain types of cells, i.e. cancer cells, silicon nanocrystals have to be functionalized with bioactive molecules[1] with specific targeting abilities, such as a single strand of peptides and antibodies. Start with carboxylic acid-terminated silicon nanocrystals which have high aqueous dispersibility, EDC/NHS coupling[2] could be used to conjugate bioactive molecules to nanocrystals, by taking advantage of the reaction between COOH and the primary amine group NH_2 on the biomolecules. For instance, COOH on silicon nanocrystal reacts with NH_2 on the heavy chain of antibody. EDC/NHS coupling is widely used in the biochemistry field, but is not trivial to apply to the bioconjugation on silicon nanocrystal surface, due to the narrow pH window of dispersing silicon nanocrystal and activing EDC and NHS. The second challenge is to definitive characterizatize the biomolecule/silicon nanocrystal conjugates, which has not been shown in literature.

To approach a success in bioconjugation between bioactive molecules and silicon nanocrystals, EDC/NHS coupling of amine-PEG and silicon nanocrystal can be used as a model system to optimize the reaction parameters. An alternative way is to create a Si/ZnS core/shell nanocrystals and then apply the well-studied conjugation between ZnS and bioactive molecules, which was developed for CdSe/ZnS nanocrystals.

11.2.2 Si/ZnS core/shell Nanocrystals

Core/shell semiconductor nanocrystals exhibit enhanced fluorescence properties than a "naked" nanocrystals (still capped with organic ligands). A wider band gap shell can providing further quantum confinement for excitons, leading to a higher photoluminescence quantum yield and a suppressed emission intermittency.[3] Silicon nanocrystal can easily form a Si/SiO_2 core/shell structure, but the SiO_2 shell is typically amorphous. Even through SiO_2 shell is crystallized, there is a huge lattice mismatch on the Si/SiO_2 interface, leading to interface defects. ZnS has a zincblende crystalline structure with a lattice constant of 5.420 Å, which almost perfectly matches silicon crystal which has a diamond cubic structure with a lattice constant of 5.431 nm. ZnS also has a band gap of 3.54 eV which will form a type I heterojunction with silicon. More importantly, a ZnS shell would allow us to directly apply well-developed surface chemistry of ZnS.

In order to epitaxy deposit a shell of ZnS on silicon nanocrystals, the nanocrystals should first form a colloidal dispersion in solvent without any aggregation. It requires capping ligands on nanocrystal surface prior to ZnS coating. However, typical Si-C capped surface is highly stable and does not allow any ligand exchange, which makes ZnS coating impossible. The thiol capped silicon nanocrystal has Si-S bonds on its surface, which is exactly the bonding that ZnS coating requires. What's more, the thiol capped silicon nanocrystal has been shown to be able to undergo ligand exchange, presenting a promising opportunity to finally synthesis Si/ZnS core/shell nanocrystals.

11.2.3 Singlet Oxygen Generation by Silicon Nanocrystals

Oxygen is one of the special molecules that have a triplet ground state and singlet excited state. Singlet oxygen is highly reactive and toxic to cellular systems, mostly membrane systems, and hence presents high cytotoxicity. Singlet oxygen can find application in photodynamic therapy, which uses singlet oxygen to kill bacterias or cancer cells. The diffusion length of singlet oxygen in tissue is less than 20 nm, indicating that the cellular damage is highly localized to a specific region, such as tumors.

It requires 1.63 eV, corresponding to 758 nm light, to excite oxygen from the triple ground state to the singlet excited state. However, direct excitation is spin forbidden. Photodynamic therapy requires a photosensitizer, which absorbs light and transfers the energy to the triplet oxygen through a spin flip energy transfer,[4] generating singlet oxygen. This energy transfer has a rate corresponding to a lifetime of several microseconds, which post a requirement that the exciton or excited state in the photosensitizer should has a lifetime longer than this. Silicon nanocrystal, due to the indirect band gap, has an exciton life of tens or hundreds of microseconds, and hence can be an excellent candidate for photosensitizers in the photodynamic therapy.

11.2.4 Large Scale synthesis of Silicon Nanocrystals

The synthesis of silicon nanocrystal is difficult and energy consuming, due to its covalent nature. My synthesis involves thermal decomposition of hydrogen silsesquiloxane (HSQ), which the packaging material for integrated circuits. It is an expensive commercially available material. 2g of silicon nanocrystals requires 20g of

HSQ, which typically cost $900. A cheaper precursor is desired for low cost synthesis of silicon nanocrystals.

11.3 REFERENCE

(1) Medintz, I. L.; Uyeda, H. T.; Goldman, E. R. Mattoussi, H. Quantum Dot Bioconjugates for Imaging, Labeling and Sensing. *Nat. Mater.* **2005**, *4*, 435-446.

(2) Tengvall, P. Jansson, E.; Askendal, A.; Thomsen, P.; Gretzer, C. Preparation of Multilayer Plasma Protein Films on Silicon by EDC/NHS Coupling Chemistry. *Col. Surf. B* **2003**, *4*, 261-272.

(3) Chen, O. Zhao, J.; Chauhan, V. P.; Cui, J. Wong, C.; Harris, D. K.; Wei, H.; Han, H.-S.; Fukumura, D.; Jain, R. K.; Bawendi, M. G.; Compact High-Quality CdSe-CdS Core-Shell Nanocrystals with Narrow Emission Linewidths and Suppressed Blinking. *Nat. Mater.* **2013**, *12*, 445-451.

(4) Goller, B.; Polisski, S.; Kovalev, D. Spin-Flip Excitation of Molecules Mediated by Photoexcited Silicon Nanocrystals. *Phys. Rev. B* **2007**, *75*, 073403.

Bibliography

Aldana, J.; Wang, Y. A.; Peng, X. Photochemical Instability of CdSe Nanocrystals Coated by Hydrophilic Thiols. *J. Am. Chem. Soc.* **2001**, *123*, 8844-8850.

Alivisatos, A. P. Perspectives on the physical chemistry of semiconductor nanocrystals, *J. Phys. Chem.* **1996**, *100*, 13226-13239.

Alivisatos, A. P. Semiconductor Clusters, Nanocrystals, and Quantum Dots. *Science* **1996**, *271*, 933-937.

Ang, C. Y.; Giam, L.; Chan, Z. M.; Lin, A. W. H.; Devlin, H. Gu, E.; Papaefthymiou, G. C.; Selvan, S. T.; Ying, J. Y. Facile Synthesis of Fe2O3 Nanocrystals without Fe(CO)5 Precursor and One-Pot Synthesis of Highly Fluorescent Fe2O3–CdSe Nanocomposites. *Adv. Mater.* **2009**, *21*, 869-873.

Armstrong, D. A.; Wilkening, V. G. Effects of pH in the γ-Radiolysis of Aqueous Solutions of Cysteine and Methyl Mercaptan. *Can. J. Chem.* **1964**, *42*, 2631-2635.

Badia, A.; Singh, S.; Demers, L.; Cuccia, L.; Brown, G. R.; Lennox, R. B. Self-assembled monolayers on gold nanoparticles. *Chem. Eur. J.* **1996**, *2*, 359-363.

Bae, Y.; Lee, D. C.; Rhogojina, E. V.; Jurbergs, D. C.; Korgel, B. A.; Bard, A. J. Electrochemistry and Electrogenerated Chemiluminescence of Films of Silicon Nanoparticles in Aqueous Solution *Nanotechnology* **2006***, 17,* 3791-3797.

Bartlett, P.; Ottewill, R. H.; Pusey, P. N. Superlattice formation in binary mixture of hard-sphere colloids. *Phys. Rev. Lett.* **1992**, *68*, 3801−3804.

Bateman, J. E.; Eagling, R. D.; Worrall, D. R.; Horrocks, B. R.; Houlton, A. Alkylation of Porous Silicon by Direct Reaction with Alkenes and Alkynes. *Angew. Chem. Int. Ed.* **1998**, *37*, 2683-2685.

Bawendi, M. G.; Steigerwald, M. L.; Brus, L. E. The quantum mechanics of larger semiconductor clusters (“quantum dots") *Auun. Rev. Phys. Chem.* **1990**, *41*, 477-496.

Beard, M. C.; Knutsen, K. P.; Yu, P.; Luther, J. M.; Song, Q.; Metzger, W. K.; Ellingson, R. J.; Nozik, A. J. Multiple Exciton General in Colloidal Silicon Nanocrystals. *Nano Lett.* **2007**, *7*, 2506-2512.

Ben-Simon, A.; Eshet, H.; Rabani, E. On the Phase Behavior of Binary Mixtures of Nanoparticles. *ACS Nano* **2013**, *7*, 978-986.

Bian, K.; Choi, J. J.; Kaushik, A.; Clancy, P.; Smilgies, D.-M.; Hanrath, T. Shape-Anisotropy Driven Symmetry Transformations in Nanocrystal Superlattice Polymorphs. *ACS Nano* **2011**, *5*, 2815-2823.

Bigioni, T. P.; Lin, X.-M.; Nguyen, T. T.; Corwin, E. I.; Witten, T. A.; Jaeger, H. M. Kinetically Driven Self Assembly of Highly Ordered Nanoparticle Monolayer. *Nat. Mater.* **2006**, *5*, 265-270.

Bishop, K. J. M.; Chevalier, N. R.; Grzybowski, B. A. When and Why Like-Sized, Oppositely Charged Particles Assemble into Diamond-like Crystals. *J. Phys. Chem. Lett.* **2013**, *4*, 1507-1511.

Biteen, J. S.; Pacifici, D.; Lewis, N. S.; Atwater, H. A. Enhanced Radiative Emission Rate and Quantum Efficiency in Coupled Silicon nanocrystal-Nanostructured Gold Emitters. *Nano Lett.* **2005**, *5*, 1768-1773.

Bodnarchuk, M. I.; Kovalenko, M. V.; Heiss, W.; Talapin, D. V. Energetic and entropic contributions to self-assembly of binary nanocrystal superlattices: temperatures as the structure-directing factor, *J. Am. Chem. Soc.* **2010**, *132*, 11967-11977.

Bosworth, J. K.; Paik, M. Y.; Ruiz, R.; Schwartz, E. L.; Huang, J. Q.; Ko, A. W.; Smilgies, D. M., Black, C. T.; Ober C. K. Control of Self-Assembly of Lithographically Patterned Block Copolymer Films. *ASC Nano* **2008**, *2*, 1396-1402.

Boukherroub, R.; Morin, S.; Wayner, D. D. M.; Bensebaa, F.; Sproule, G. I.; Baribeau, J.-M.; Lockwood, D. J. Ideal Passivation of Luminescent Porous Silicon by

Thermal, Noncatalytic Reaction with Alkenes and Aldehydes. *Chem. Mater.* **2001**, *13*, 2002-2011.

Boukherroub, R.; Wayner, D. D. M. Controlled Functionalization and Multistep Chemical Manipulation of Covalently Modified Si(111) Surfaces. *J. Am. Chem. Soc.* **1999**, *121*, 11513-11515.

Bourg, M.-C.; Badia, A.; Lennox, R. B. Gold-Sulfur Bonding in 2D and 3D Self-Assembled Monolayers: XPS Characterization. *J. Phys. Chem. B* **2000**, *104*, 6552-6567.

Bredig, M. A. The Polymorphism of Calcium Carbide *J. Phys. Chem.* **1942**, *46*, 801-819.

Brus, L. Luminescence of Silicon Materials: Chains, Sheets, Nanocrystals, Nanowires, Microcrystals, and Porous Silicon. *J. Phys. Chem.* **1994**, *98*, 3575-3581.

Brust, M.; Walker, M.; Bethell, D.; Schiffrin, D. J.; Whyman, R. Synthesis of Thiol-Derivatised Gold Nanoparticles in a Two-Phase Liquid-Liquid System. *J. Chem. Soc., Chem. Commun.* **1994**, 801-802.

Buriak, J. M. Organometallic Chemistry on Silicon and Germanium Surfaces. *Chem. Rev.* **2002**, *102*, 1271-1308.

Buriak, J. M.; Allen, M. J. Lewis Acid Mediated Functionalization of Porous Silicon with Substituted Alkenes and Alkynes. *J. Am. Chem. Soc.* **1998**, *120*, 1339-1340.

Cannon, W. R.; Danforth, S. C.; Flint, J. H.; Haggerty, J. S.; Marra, R. A. Sinterable Ceramic Powders from Laser-Driven Reactions: I, Process Description and Modeling. *J. Am. Ceram. Soc.* **1982**, *65*, 324-330.

Cannon, W. R.; Danforth, S. C.; Haggerty, J. S.; Marra, R. A. Sinterable Ceramic Powders from Laser-Driven Reactions: II, Powder Characteristics and Process Variables. *J. Am. Ceram. Soc.* **1982**, *65*, 330-335.

Casey, K. G.; Quitevis, E. L. Effect of Solvent Polarity on Nonradiative Processes in Xanthene Dyes: Rhodamine B in Normal Alcohols. *J. Phys. Chem.* **1988**, *92*, 6590-6594.

Castner, D. G. X-ray Photoelectron Spectroscopy Sulfur 2p Study of Organic Thiol and Disulfide Binding Interactions with Gold Surfaces. *Langmuir* **1996**, *12*, 5083-5086.

Castro, E. G.; Salvatierra, R. V.; Schreiner W. H.; Oliveira, M. M.; Zarbin, A. J. G. Dodecanethiol-Stabilized Platinum Nanoparticles Obtained by a Two-Phase Method: Synthesis, Characterization, Mechanism of Formation, and Electrocatalytic Properties. *Chem. Mater*. **2010**, *22*, 360-370.

Chen, O. Zhao, J.; Chauhan, V. P.; Cui, J. Wong, C.; Harris, D. K.; Wei, H.; Han, H.-S.; Fukumura, D.; Jain, R. K.; Bawendi, M. G.; Compact High-Quality CdSe-CdS Core-Shell Nanocrystals with Narrow Emission Linewidths and Suppressed Blinking. *Nat. Mater.* **2013**, *12*, 445-451.

Chen, Z.; Moore, J.; Radtke, G.; Sirringhaus, H.; O'Brien, S. Binary Nanoparticle Superaltticesin the Semiconductor-Semiconductor System: CdTe and CdSe. *J. Am. Chem. Soc.* **2007**, *129*, 15702-15709.

Cheng, K.-Y.; Anthony, R.; Kortshagen, U. R.; Holmes, R. J. High-Efficiency Silicon Nanocrystal Light-Emitting Devices. *Nano Lett.* **2011**, *11*, 1952-1956.

Cheng, K.-Y.; Anthony, R.; Kortshagen, U. R.; Holmes, R. J. Hybride Silicon Nanocrystal-Organic Light-Emitting Devices for Infrared Electroluminescence. *Nano Lett.* **2010**, *10*, 1154-1157.

Cherepy, N. J.; Liston, D. B.; Lovejoy, J. A.; Mei, H.; Zhang, J. Z. Ultrafast Studies of Photoexcited Electron Dynamics in γ- and α-Fe_2O_3 semiconductor Nanoparticles. *J. Phys. Chem. B* **1998**, *102*, 770-776.

Choi, H. S.; Liu, W.; Misra, P.; Tanaka, E.; Zimmer, J. P.; Ipe, B. I.; Bawendi, M. G.; Frangioni, J. V. Renal Clearance of Quantum Dots. *Nat. Biotech.* **2007**, *25*, 1165-1170.

Clark, R. J.; Dang, M. K. M.; Veinot, J. G. C. Exploration of Organic Acid Chain Length on Water-Soluble Silicon Quantum Dot Surfaces. *Langmuir* **2010**, *26*, 15657-15664.

Collier, C. P.; Vossmeyer, T.; Heath, J. R. Nanocrystal superlattices, *Annu. Rev. Phys. Chem.* **1998**, *49*, 371-404.

Corr, S. A.; Rakovich, Y. P.; Gun'ko, Y. K. Multifunctional Magnetic-fluorescent Nanocomposites for Biomedical Applications. *Nanoscale Rev. Lett.* **2008**, *3*, 87-104.

Courty, A.; Henry, A.-I.; Goubet, N.; Pileni, M.-P. Large Triangular Single Crystals Formed by Mild Annealing of Self-Organized Silver Nanocrystals. *Nature Mater.* **2007**, *6*, 900-907.

Coutts, M. J.; Cortie, M. B.; Ford, M. J.; McDonagh, A. M. Rapid and Controllable Sintering of Gold Nanoparticles Inka at Room Temperature Using a Chemical Agent. *J. Phys. Chem. C.* **2009**, *113*, 1325-1328.

Daniel, M-C; Astruc, D. Gold Nanoparticles: Assembly, Supramolecular Chemistry, Quantum-Size-Related Properties, and Applications toward Biology, Catalysis, and Nanotechnology, *Chem. Rev.* **2004**, *104*, 293-346.

Dasog, M.; De los Reyes, G. B.; Titova, L. V.; Hegmann, F. A.; Veinot, J. G. C. Size vs Surface: Tuning the Photoluminescence of Freestanding Silicon Nanocrystals across the Visible Spectrum via Surface Groups. *ACS Nano* **2014**, *8*, 9636-9648.

Dasog, M.; Scott, R. W. J. Understanding the oxidative stability of gold monolayer-protected clusters in the presence of halide ions under ambient conditions, *Langmuir* **2007**, *23*, 3381-3387.

Dasog, M.; Veinot, J. G. C. Size Independent Blue Luminescence in Nitrogen Passivated Silicon Nanocrystals. *Phys. Stat. Sol. A* **2012**, *209*, 1844-1846.

Dasog, M.; Yang, Z.; Regli, S.; Atkins, T. M.; Faramus, A.; Singh, M. P.; Muthuswamy, E.; Kauzlarich, S. M.; Tilley, R. D.; Veinot, J. G. C. Chemical Insight into the

Origin of Red and Blue Photoluminescence Arising from Freestanding Silicon Nanocrystals. *ACS Nano* **2013**, *7*, 2676-2685.

Desireddy, A.; Conn, B. E.; Guo, J.; Yoon, B.; Barnett, R. N.; Monahan, B. M.; Kirschbaum,K. Griffith, W. P.; Whetten, R. L.; Landman, U.; Bigioni, T. P. Ultrastable Silver Nanoparticles. *Nature* **2013**, *501*, 399-402.

Dobbs, E. R. Helium three, *Oxford University Press, Oxford*, **2002**.

Dong, A.; Ye, X.; Chen, J.; Murray, C. B. Two-Dimensional Binary and Ternary Nanocrystal Superlattices: The Case of Monolayers and Bilayers. *J. Am. Chem. Soc.* **2011**, *11*, 1804-1809.

Doty, R. C.; Bonnecaze, R. T.; Korgel, B. A. Kinetic Bottleneck to the Self-Organization of Bidisperse Hard Disk Monolayers Formed by Random Sequential Adsorption. *Phys. Rev. E* **2002**, *65*, 061503.

Dylla, R. J.; Korgel, B. A. Temporal Organization of Nanocrystal Self-Assembly Directed by a Chemical Oscillator. *ChemPhysChem* **2001**, *1*, 61-64.

Ellis, A. V.; D'Arcy-Gall, J.; Vijayamohanan, K.; Goswami, R.; Ganesan, P. G.; Ryu, C.; Ramanath, G. Phase Transitions in Octanethiol-Capped Ag Nanocluster Microfilm Assemblies. *Themochimica Acta* **2005**, *426*, 207-212.

English, D. S.; Pell, L. E.; Yu, Z.; Barbara, P. F.; Korgel, B. A. Size Tunable Visible Luminescence from Individual Organic Monolayer Stabilized Silicon Nanocrystal Quantum Dots. *Nano Lett.* **2002**, *2*, 681-685.

Erogbogbo, F.; Tien, C.-A.; Chang, C.-W.; Yong, K.-T.; Law, W.-C.; Ding, H.; Roy, I.; Swihart, M. T.; Prasad, P. N. Bioconjugation of Luminescent Silicon Quantum Dots for Selective Uptake by Cancer Cells. *Bioconjugate Chem.* **2011**, *22*, 1081-1088.

Erogbogbo, F.; Yong, K.-T.; Hu, R.; Law, W.-C.; Ding, H.; Chang, C.-W.; Prasad, P. N.; Swihart, M. T. Biocompatible Magnetofluorescent Probes Luminescent Silicon

Quantum Dots Couple with Superparamagnetic Iron III Oxide. *ACS Nano* **2010**, *4*, 5131-5138.

Erogbogbo, F.; Yong, K.-T.; Roy, I.; Xu, G.; Prasad, P. N.; Swihart, M. T. Biocompatible Luminescent Silicon Quantum Dots for Imaging of Cancer Cells. *ACS Nano* **2008**, *2*, 873-878.

Evers, W. H.; De Nijs, B.; Filion, L.; Castillo, S.; Dijkstra, M.; Vanmaekelbergh, D. Entropy-Driven Formation of Binary Semiconductor-Nanocrystal Superlattices. *Nano Lett.* **2010**, *10*, 4235-4241.

Evers, W. H.; Friedrich, H.; Filion, L.; Dijkstra, M.; Vanmaekelbergh, D. Observation of a Ternary Nanocrystal Superlattice and Its Structural Characterization by Electron Tomography. *Angew. Chem. Intl. Ed.* **2009**, *48*, 9655-9657.

Feeney, M. R.; Debenedetti, P. G.; Stillinger, F. H. A statistical mechanical model for inverse melting. *J. Chem. Phys.* **2003**, *119*, 4582-4591.

Feng, W.; Miller, B. Self-Assembly and Characterization of Fullerence Monolayers on Si(100) Surfaces. *Langmuir* **1999**, *15*, 3152-3156.

Finklea, H. O.; Avery, S.; Lynch, M. Blocking Oriented Monolayer of Alkyl Mercaptans on Gold Electrodes. *Langmuir* **1987**, *3*, 409-413.

Froner, E.; Amato, E. D.; Adamo, R.; Prtljaga, N.; Larcheri, S.; Pavesi, L.; Rigo, A.; Potrich, C.; Scarpa, M. Deoxycholate as an Efficient Coating Agent for Hydrophilic Silicon Nanocrystals. *J. Coll. Interf. Sci.* **2011**, *358*, 86-92.

Ge, G.; Brus, L. Evidence for Spinodal Phase Separation in Two-Dimensional Nanocrystal Self-Assembly. *J. Phys. Chem. B* **2000**, *104*, 9573-9575.

Geyer, T.; Born, P.; Kraus, T. Switching between crystallization and amorphous agglomeration of alkyl thiol-coated gold nanoparticles. *Phys. Rev. Lett*. **2012**, *109*, 128302.

Girifalco, L. A. Statistical Mechanics of Solids. *Oxford University Press: Oxford,* **2003**.

Goller, B.; Polisski, S.; Kovalev, D. Spin-Flip Excitation of Molecules Mediated by Photoexcited Silicon Nanocrystals. *Phys. Rev. B* **2007**, *75*, 073403.

Goller, B.; Polisski, S.; Wiggers, H.; Kovalev, D. Silicon Nanocrystals Dispersed in Water: Photosensitizers for Molecular Oxygen. *Appl. Phys. Lett.* **2010**, *96*, 211901.

Goodfellow B. W.; Patel R. N.; Panthani M. G.; Smilgies D. M.; Korgel B. A. Melting and Sintering of a Body-Centered Cubic Superlattice of PbSe Nanocrystals Followed by Small Angle X-ray Scattering. *J. Phy. Chem. C* **2011**, *115*, 6397-6404.

Goodfellow, B. W.; Korgel, B. A. Reversible Solvent Vapor-Mediated Phase Changes in Nanocrystal Superlattices. *ACS Nano* **2011**, *5*, 2419-2424.

Goodfellow, B. W.; Rasch, M. R.; Hessel, C. M.; Patel, R. N.; Smilgies, D.-M.; Korgel, B. A. Ordered structure rearrangements in heated gold nanocrystal superlattices, *Nano Lett.* **2013**, *13*, 5710-5714.

Goubet, N.; Richardi, J.; Albouy, P. A.; Pileni, M. P. How to Predict the Growth Mechanism of Supracrystals from Gold Nanocrystals. *J. Phys. Chem. Lett.* **2011**, *2*, 417-422.

Gu, L.; Hall, D. J.; Qin, Z.; Anglin, E.; Joo, J.; Mooney, D. J.; Howell, S. B.; Sailor, M. J. In vivo Time-Gated Fluorescence Imaging with Biodegradable Luminescent Porous Silicon Nanoparticles. *Nat. Commun.* **2012**, *4*, 2326.

Guo, L.; Leobandung, E.; Chou, S. Y. A Silicon Single-Electron Transistor Memory Operating at Room Temperature. *Science* **1997**, *275*, 649-651.

Guo, L.; Park, J.-H.; Duong, K. H.; Ruoslahti, E.; Sailor, M. J. Magnetic Luminescent Porous Silicon Microparticles for Localized Delivery of Molecular Drug Payloads. *Small* **2010**, *6*, 2546-2552.

Gur, I.; Fromer, N. A.; Geier, M. L.; Alivisatos, A. P. Air-Stable All-Inorganic Nanocrystal Solar Cells Processed From Solution. *Science* **2005**, *310*, 462-466.

Haas, A. The Chemistry of Silicon-Sulfur Compounds. *Angew. Chem. Int. Ed.* **1965**, *4*, 1014-1023.

Hamaker, H. C. The London-van der Waals Attraction between Spherical Particles. *Physica IV* **1937**, *10*, 1058-1072.

Hanrath, T. Colloidal Nanocrystal Quantum Dot Assemblies as Artificial Solids *J. Vac. Sci. Tech. A,* **2012**, *30*, 030802.

Hansen, J.-P.; Verlet, L. Phase transitions of the Lennard-Jones system. *Phys. Rev.* **1969**, *184,* 151-161.

Harris, J. T.; Hueso, J. L.; Korgel, B. A. Hydrogenated Amorphous Silicon (a-Si:H) Colloids. *Chem. Mater.* **2010**, *22*, 6378-6383.

Hayashi, S.; Nagareda, T.; Kanzawa, Y.; Yamamoto, K. Photoluminescence of Si-Rich SiO_2 Films: Si Cluster as Luminescent Centers. Jpn, J. Appl. Phys. 1993, 32, 3840.

Heitmann, J.; Müller, F.; Zacharias, M.; Gösele, U. Silicon Nanocrystal: Size Matters. *Adv. Mater.* **2005**, *17*, 795-803.

Heitsch, A. T.; Akhavan, V. A.; Korgel, B. A. Rapid SFLS Synthesis of Si Nanowires Using Trisilane with in situ Alkyl-Amine Passivation. *Chem. Mater.* **2011**, *23*, 2697-2699.

Heitsch, A. T.; Hessel, C. M.; Akhavan, V. A.; Korgel, B. A. Colloidal Silicon Nanorod Synthesis. *Nano Lett.* **2009**, *9*, 3042-3047.

Heitsch, A. T.; Patel, R. N.; Goodfellow, B. W.; Smilgies, D.-M.; Korgel, B. A. GISAXS Characterization of Order in Hexagonal Monolayers of FePt Nanocrystals. *J. Phys. Chem. C* **2010**, *114*, 14427-14432.

Hessel, C. M.; Rasch, M. R.; Hueso, J. L.; Goodfellow, B. W.; Akhavan, V. A.; Puvanakrishnan, P.; Tunnel, J. W.; Korgel, B. A. Alkyl Passivation and Amphiphilic Polymer Coating of Silicon Nanocrystals for Diagnostic Imaging. *Small* **2010**, *6*, 2026-2034.

Hessel, C. M.; Henderson E. J.; Veinot, J. G.C. Hydrogen Silsesquioxane: A Molecular Precursor for Nanocrystalline Si-SiO2 Composites and Freestanding Hydride-Surface-Terminated Silicon Nanoparticles. *Chem. Mater.* **2006**, *18*, 6139-6146.

Hessel, C. M.; Reid, D.; Panthani, M .G.; Rasch, M. R.; Goodfellow, B. W.; Wei, J.; Fujii, H.; Akhavan, V.; Korgel, B. A. Synthesis of Ligand-Stabilized Silicon Nanocrystals with Size-Dependent Photoluminescence Spanning Visible to Near-Infrared Wavelengths. *Chem. Mater.* **2012**, *24*, 393-401.

Holmberg, V. C.; Korgel, B. A. Corrosion resistance of thiol- and alkene-passivated germanium nanowires. *Chem. Mater.* **2010**, *22*, 3698-3703.

Hostetler, M. J.; Wingate, J. E.; Zhong, C.-J.; Harris, J. E.; Vachet, R. W.; Clark, M. R. Londono, J. D.; Green, S. J.; Stokes, J. J.; Wignall, G. D.; Glish, G. L.; Porter, M. D.; Evans, N. D.; Murray, R. W. Alkanethiolate Gold Cluster Molecules with Core Diameters from 1.5 to 5.2 nm: Core and Monolayer Properties as a Function of Core Size. *Langmuir* **1998**, *14*, 17-30.

Hou, W.; Dasog, M.; Scott, R. W. J. Probing the relative stability of thiolate- and dithiolate-protected Au monolayer-protected clusters, *Langmuir* **2009**, *25*, 12954-12961.

Howes, P.; Green, M.; Bowers, A.; Parker, D.; Varma, G.; Kallumadil, M.; Hughes, M.; Warley, A.; Brain, A.; Botnar, R. Magnetic Conjugated Polymer Nanoparticles as Bimodal Imaging Agents. *J. Am. Chem. Soc.* **2010**, *132*, 9833-9842.

Hu, H.; Zheng, R.; Zhang, X.; Xu, B. Facile One-Pot Synthesis of Bifunctional Heterodimers of Nanoparticles A Conjugate of Quantum Dot and Magnetic Nanoparticles. *J. Am. Chem. Soc.* **2004**, *126*, 5664-5665.

Hua, F.; Mark T. Swihart, M. T.; Ruckenstein, E. Efficient Surface Grafting of Luminescent Silicon Quantum Dots by Photoinitiated Hydrosilylation. *Langumir* **2005**, *21*, 6054-6062.

Huh, C.; Choi, C.-J.; Kim, W.; Kim, B. K.; Park, B.-J.; Jang, E.-H.; Kim, S.-H.; Sung, G. Y. Enhancement in Light Emission Efficiency of Si Nanocrystal Light-Emitting Diodes by Surface Plasmon Coupling. *Appl. Phys. Lett.* **2012**, *100*, 181108.

Ingham, B.; Lim, T. H.; Dotzler, C. J.; Henning, A.; Toney, M. F.; Tilley, R. D. How Nanoparticle Coalesce: An in situ Study of Au Nanoparticle Aggregation and Grain Growth. *Chem. Mater.* **2011**, *23*, 3312-3317.

Insin, N.; Tracy, J. B.; Lee, H.; Zimmer, J. P.; Weatervelt, R. M.; Bawendi, M. G. Incorporation of Iron Oxide Nanoparticles and Quantum Dots into Silica Microspheres. *ACS Nano* **2008**, *2*, 197-202.

Israelachvili, J. *Intermolecular & Surface Forces,* 2nd ed.; Academic Press: San Diego, CA, 1992.

Jiang, C.-W.; Green, M. A. Silicon Quantum Dot Superlattices: Modeling of Energy Bands, Densities of States, and Mobilities for Silicon Tandem Solar Cell Applications. *J. Appl. Phys.* **2006**, *99*, 114902.

Jiang, W.; Kim, B. Y. S.; Rutka, J. T.; Chan, W. C. W. Nanoparticles-Mediated Cellular Response is Size-Dependent. *Nat. Nanotechnol.* **2008**, *3*, 145-150.

Joseph, Y.; Besnard, I.; Rosenberger, M.; Guse, B.; Nothofer, H.-G.; Wessels, J. M.; Wild, U.; Knop-Gericke, A.; Su, D.; Schlögl, R.; Yasuda, A.; Vossmeyer, T. Self-Assembled Gold Nanoparticle/Alkanethiol Films: Preparation, Electron Microscopy, XPS-Analysis, Charge Transport, and Vapor-Sensing Properties. *J. Phys. Chem. B* **2003**, *107*, 7406-7413.

Jurgergs, D.; Rogojina, E.; Mangolini, L.; Kortshagen, U. Silicon Nanocrystals with Ensemble Quantum Yields Exceeding 60%. *App. Phys. Lett.* **2006**, *23*, 233116.

Juzenas, P.; Chen, W.; Sun, Y.-P.; Coelho, M. A. N.; Generalov, R.; Generalov, N.; Christensen, I. L. Quantum Dots and Nanoparticles for Photodynamic and Radiation Therapies for Cancer. *Adv. Drug Deliv Rev.* **2008**, *60*, 1600-1614.

Katz, E.; Willner, I. Integrated Nanoparticle-Biomolecule Hybrid Systems: Synthesis, Properties, and Applications. *Angew. Chem. Int. Ed.* **2004**, *43*, 6042-6108.

Kelly, J. A.; Henderson, E. J.; Clark, R. J.; Hessel, C. M.; Cavell, R. G.; Veinot, J. G. C. X-ray Absorption Spectroscopy of Functionalized Silicon Nanocrystals. *J. Phys. Chem. C* **2010**, *114*, 22519-22525.

Kelly, J. A.; Shukaliak, A. M.; Fleischauer, M. D.; Veinot, J. G. C. Size-Dependent Reactivity in Hydrosilylation of Silicon Nanocrystals *J. Am. Chem. Soc.* **2011**, *133*, 9564-9571.

Kelly, J. A.; Veinot, J. G. C. An Investigation into Near-UV Hydrosilylation of Freestanding Silicon Nanocrystals. *ACS Nano* **2010**, *8*, 4645-4656.

Ketelaar, J. A. A. The crystal structure of alloys of zinc with the alkali and alkaline earth metals and of cadmium with potassium, *J. Chem. Phys.* **1937**, *5*, 668.

Khuong, K. S.; Jones, W. H.; Pryor, W. A.; Houk, K. N. The Mechanism of the Self-Initiated Thermal Polymerization of Styrene. Theoretical Solution of a Classic Problem. J. *Am. Chem. Soc.* **2005**, *127*, 1265-1277.

Kim, D. H.; Hwang, Y. J.; Ryou, J.; Kim, S.; Hong, S. Atomic and Electronic Structure of Styrene on Ge(100). *Surf. Sci.* **2011**, *605*, 1438-1444.

Kim, N. Y.; Laibinis, P. E. Derivatization of Porous Silicon by Grignard Reagents at Room Temperature. *J. Am. Chem. Soc.* **1998**, *120*, 4516-4517.

Kirczenow, G. Linear Chains of Styrene and Methylstyrene Molecules and their Heterojunctions on Silicon: Theory and Experiment. *Phys. Rev. B* **2005**, *72*, 245306.

Koole, R.; Liljeroth, P.; Donegá, C. de M.; Vanmaekelbergh, D.; Meijerink, A. Electronic coupling and exciton energy transfer in CdTe quantum-dot molecules, *J. Am. Chem. Soc.* **2006**, *128*, 10436-10441.

Korgel, B. A. Correlated membrane fluctuations in nanocrystal superlattices. *Phys. Rev. Lett.* **2001**, *86*, 127-130.

Korgel, B. A.; Fitzmaurice, D. Small-angle X-ray-Scattering Study of Silver-Nanocrystal Disorder-Order Phase Transitions. *Phys. Rev. B* **1999**, *59*, 14191-14201.

Korgel, B. A.; Fitzmaurice, D.; Condensation of Ordered Nanocrystal Thin Films. *Phys. Rev. Lett.* **1998**, *80*, 3531-3534.

Korgel, B. A.; Fullam, S.; Connolly, S.; Fitzmaurice, D. Assembly and Self-Organization of Silver Nanocrystal Superlattice: Ordered "Soft Spheres" *J. Phys. Chem. B* **1998**, *102*, 8379-8388.

Korgel, B. A.; Zaccheroni, N.; Fitzmaurice, D. "Melting Transition" of a Quantum Dot Solid: Collective Interactions Influence the Thermally-Induced Order-Disorder Transition of a Silver Nanocrystal Superlattice. *J. Am. Chem. Soc.* **1999**, *121*, 3533-3534.

Kovalenko, M. V.; Spokoyny, B.; Lee, J.-S.; Scheele, M.; Weber, A.; Perera, S.; Landry, D.; Talapin, D. V. Semiconductor Nanocrystals Functionalized with Antimony Telluride Zintl Ions for Nanostructure Thermoelectrics. *J. Am. Chem. Soc.* **2010**, *132*, 6686-6695.

Kovalev, D.; Fujii, M. Silicon Nanocrystals: Photosensitizers for Oxygen Molecules. *Adv. Mater.* **2005**, *17*, 2531-2544.

Krull, L.H.; Friedman, M. Reduction of Protein Disulfide Bonds by Sodium Hydride in Dimethyl Sulfoxide. *Biochem. Biophys. Res. Commun.* **1967**, *29*, 373-375.

Kwon, K.-W.; Shim, M. γ -Fe2O3II-VI Sulfide Nanocrystal Heterojunctions. *J. Am. Chem. Soc.* **2005**, *127*, 10269-10275.

Lai, Y.-H.; Yeh, C.-T.; Lin, Y.-H.; Hung, W.-H. Adsorption and thermal decomposition of H2S on Si(100). *Surf. Sci.* **2002**, *519*, 150-156.

Lee, B.; Podsiadlo, P.; Rupich, S.; Talapin, D. V.; Rajh, T.; Shevchenko, E. V. Comparison of Structural Behavior of Nanocrystals in Randomly Packed Films and Long-Range Ordered Superlattices by Time-Resolved Small Angle X0ray Scattering. *J. Am. Chem. Soc.* **2009**, *131*, 16386-16388.

Lee, D. C.; Smith, D. K.; Heitsch, A. T.; Korgel, B. A. Colloidal Magnetic Nanocrystals: Synthesis, Properties and Applications. *Annu. Rep. Prog. Chem., Sect. C: Phys. Chem.* **2007**, *103*, 351-402.

Lepage, H.; Kaminski-Cachopo, A.; Poncet, A.; le Carval, G. Simulation of Electron Transport in Silicon Nanocrystal Solids. *J. Phys. Chem. C* **2012**, *116*, 10873-10880.

Li, X.; He, Y.; Swihart, M. T. Surface Functionalization of Silicon Nanoparticles Produced by Laser-Driven Pyrolysis of Silane Followed by HF-HNO_3 Etching. *Langmuir* **2004**, *20*, 4720-4727.

Li, X.; He, Y.; Talukdar, S. S.; Swihart, M. T. Process for Preparing Macroscopic Quantities of Brightly Photoluminescent Silicon Nanoparticle with Emission Spanning the Visible Spectrum. *Langmuir* **2003**, *19*, 8490-8496.

Li, Y.; Huang, J.; McIver, R. T. Jr.; Hemminger, J. C. Characterization of thiol self-assembled films by laser desorption Fourier transform mass spectrometry, *J. Am. Chem. Soc.* **1992**, *114*, 2428-2432.

Li, Z. F.; Ruchenstein, E. Water-Soluble Poly(acrylic acid) Grafted Luminescent Silicon Nanoparticles and Their Use as Fluorescent Biological Staining Labels. *Nano Lett.* **2004**, *4*, 1463-1467.

Liang, L.; Pandey, A.; Werder, D. J.; Khanal, B. P.; Pietryga, J. M.; Klimov, V. I. Efficient Synthesis of Highly Luminescent Copper Indium Sulfide-Based Core/Shell Nanocrystals with Surprisingly Long-Lived Emission. *J. Am. Chem. Soc.* **2011**, *133*, 1176-1179.

Lin, X. M.; Jaeger, H. M.; Sorensen, C. M.; Klabunde, K. J. Formation of Long-Range-Ordered Nanocrystal Superlattices on Silicon Nitride Substrates. *J. Phys. Chem. B* **2001**, *105*, 3353-3357; Goubet, N.; Pileni, M.-P. Negative Supracrystals Inducing FCC-BCC Transition in Gold Nanocrystal Superlattices. *Nano Res.* **2014**, *7*, 171-179.

Linford, M. R.; Chidsey, C. E. D. Alkyl Monolayers Covalently Bonded to Silicon Surfaces. *J. Am. Chem. Soc.* **1993**, *115*, 12631-12632.

Liu, J.; Zhang, Y.; Yan, C.; Wang, C.; Xu, R.; Gu, N. Synthesis of MagneticLuminescent Alginate-Templated Composite Microparticles with Temperature-Dependent Photoluminescence under High-Frequency Magnetic Field. *Langmuir* **2010**, *26*, 19066-19072.

Liu, Y.; Yamazaki, S.; Yamaba, S.; Nakato, Y. A mild and efficient Si (111) Surface Modification via Hydrosilylation of Activated Alkynes. *J. Mater. Chem.* **2005**, *15*, 4906-4913.

Liu, Y.; Yamazaki, S.; Yamabe, S. Modification and Chemical Transformation of Si(111) Surface. *J. Org. Chem.* **2005**, *70*, 556-561.

Locritani, M.; Yu, Y.; Bergamini, G.; Baroncini, M.; Molloy, J. K.; Korgel, B. A.; Ceroni, P. Silicon Nanocrystals Functionalized with Pyrene Units: Efficient-Harvesting Antennae with Bright Near-Infrared Emission. *J. Phys. Chem. Lett.* **2014**, *5*, 3325-3329.

Löwen, H.; Palberg, T.; Simon, R. Dynamical criterion for freezing of colloidal liquids. *Phys. Rev. Lett.* **1993**, *70*, 1557-1560.

Lu, C.; Chen, Z.; O'Brien, S. Optimized Conditions for the Self-Organization of CdSe-Au and CdSe-CdSe Binary Nanoparticle Superlattices. *Chem. Mater.* **2008**, *20*, 3594-3600.

Lu, C.-W.; Hung, Y.; Hsiao, J.-K.; Yao, M.; Chung, T.-H.; Yang, Y.-S.; Huang, D.-M.; Chen, Y.-C. BifunctionalMagnetic Silica Nanoparticles for Highly Efficient Human Stem Cell Labelling. *Nano Lett.* **2007**, *7*, 149-154.

Lu, X.; Hessel, C. M.; Yu, Y.; Bogart, T. D.; Korgel, B. A. Colloidal Luminescent Silicon Nanorods. *Nano Lett.* **2013**, *13*, 3101-3105.

Lu, X.; Korgel, B. A. A Single-Step Reaction for Silicon and Germanium Nanorods. *Chem. Euro. J.* **2014**, *20*, 5874-5879.

Lu, Z. H.; Lockwood, D. J.; Baribeau, J.-M. Quantum Confinement and Light Emission in SiO_2/Si Superlattice. *Nature* **1995**, *378*, 258-260.

Lucovsky, G.; Nemanich, R. J.; Knights, J. C. Structural interpretation of the vibrational spectra of a-Si:H alloys. *Phys. Rev. B* **1979**, *19*, 2064-2073.

Luedtke, W. D.; Landman, U. Structure, Dynamics, and Thermodynamics of Passivated Gold Nanocrystallites and Their Assemblies. *J. Phys. Chem.* **1996**, *100*, 13323-13329.

Macfarlane, R. J.; Jones, M. R.; Lee, B.; Auyeung, E.; Mirkin, C. A. Topotactic Interconversion of Nanoparticle Superlattices. *Science* **2013**, *341*, 1222-1225.

Maier-Flaig, F.; Rinck, J.; Stephan, M.; Bocksrocker, T.; Bruns, M.; Kübel, C.; Powell, A. K.; Ozin, G. A.; Lemmer, U. Multicolor Silicon Light-Emitting Diodes (SiLEDs). *Nano Lett.* **2013**, *13*, 475-480.

Mangin, D.; Puel, F.; Veesler,S. Polymorphism in Processes of Crystallization in Solution: A Practical Review *Org. Process Res. Dev.* **2009**,*13*,1241-1253.

Mangolini, L.; Kortshagen, U. Plasma-Assisted Synthesis of Silicon Nanocrystal Inks. *Adv. Mater.* **2007**, *19*, 2513-2519.

Mangolini, L.; Thimsen, E.; Kortshagen, U. High-Yield Plasma Synthesis of Luminescent Silicon Nanocrystals. *Nano Lett.* **2005**, *5*, 655-659.

Mastronardi, M .L.; Maier-Flaig, F.; Faulkner, D.; Henderson, E. J.; Kübel, C.; Lemmer, U.; Ozin, G. A. Size-Dependent Absolute Quantum Yields for Size-Separated Colloidally-Stable Silicon Nanocrystals. *Nano Lett.* **2012**, *12*, 337-342.

Mastronardi, M. L.; Henderson, E. J.; Puzzo, D. P.; Chang, Y.; Wang, Z. B.; Helander, M. G.; Jeong, J.; Kherani, N. P.; Lu, Z.; Ozin, G. A. Silicon Nanocrystal OLEDs: Effect of Organic Capping Group on Performance. *Small* **2012**, *8*, 3647-3654.

Medintz, I. L.; Tetsuouyeda, H.; Goldman, E. R.; Mattoussi, H. Quantum Dot Bioconjugates for Imaging, Labelling and sensing. *Nat. Mater.* **2005**, *4*, 435-446.

Medintz, I. L.; Uyeda, H. T.; Goldman, E. R. Mattoussi, H. Quantum Dot Bioconjugates for Imaging, Labeling and Sensing. *Nat. Mater.* **2005**, *4*, 435-446.

Miller, J. B.; Van Sickle, A. R.; Anthony, R. J.; Kroll, D. M., Kortshagen, U. R.; Hobbie E. K. Ensemble Brightening and Enhanced Quantum Yield in Size-Purified Silicon Nanocrystals. *ACS Nano* **2012**, *6*, 7389-7396.

Miszta, K.; de Graaf, J.; Bertoni, G.; Dorfs, D.; Brescia, R.; Marras, S.; Ceseracciu, L.; Cingolani, R.; van Roij, R.; Dijkstra, M.; Manna, L. Hierarchical Self-Assembly of Suspended Branched Colloidal Nanocrystals into Superlattice Structures. *Nature Mater.* **2011**, *10*, 872-876.

Mnyukh, Y. *Fundamentals of solid-state phase transitions, ferromagnetism and ferroelectricity.* DirectScientific Press, 2010.

Moan, J. On the Diffusion Length of Singlet Oxygen in Cells and Tissues. *J. Photochem. Photobiol. B: Biol* **1990**, *6*, 343-347.

Murray, C. B.; Kagan, C. R.; Bawendi, M. G. Self-Organization of CdSe Nanocrystallites into Three-Dimensional Quantum Dot Superlattices. *Science* **1995**, *270*, 1335-1338.

Murray, C. B.; Kagan, C. R.; Bawendi, M. G. Synthesis and Characterization of Monodisperse Nanocrystals and Close-Packed Nanocrystal Assemblies. *Annu. Rev. Mater. Sci.* **2000**, *30*, 545-610.

Murray, M. J.; Sanders, J. V. Close-packed structures of spheres of two different sizes II. The packing densities of likely arrangements. *Philos. Mag. A* **1980**, *42*, 721−740.

Nosaka, Y.; Yamaguchi, K.; Miyama, H.; Hayashi, H. Preparation of Size-Controlled CdS Colloids in Water and Their Optical Properties. *Chem. Lett.* **1988**, *17*, 605-608.

Őğüt, S.; Chelikowsky, J. R.; Louie, S. G. Quantum Confinement and Optical Gaps in Si Nanocrystals. *Phys. Rev. Lett.* **1997**, *79*, 1770-1773.

Ohara, P. C.; Heath, J. R.; Gelbart, W. M. Self-Assembly of Submicrometer Rings of Particles from Solution of Nanoparticles. *Angew. Chem. Intl. Ed.* **1997**, *36*, 1078-1080.

Ohshima, H. Diffuse double layer interaction between two spherical particles with constant surface charge density in an electrolyte solution. *Colloid & Polymer Sci.* **1975**, *253*, 158-163.

Okamoto, H. *Desk handbook: Phase diagrams for binary alloys,* 1st ed., *ASM international: Materials Park, OH,* **2000**.

Osaki, F.; Kanamori, T.; Sando, S.; Sera, T.; Aoyama, Y. A Quantum Dot Conjugated Sugar Ball and Its Cellular Uptake. On the Size Effects of Endocytosis in the Subviral Region. *J. Am. Chem. Soc.* **2004**, *126*, 6520-6521.

Overgaag, K.; Evers, W.; Nijs, B.; Koole, R.; Meeldijk, J.; Vanmaekelbergh, D. Binary Superlattice of PbSe and CdSe Nanocrystals. *J. Am. Chem. Soc.* **2008**, *130*, 7833-7835.

Panthani, M. G.; Hessel, C. M.; Reid, D.; Casillas, G.; Jose-Yacaman, M.; Korgel, B. A. Graphene-Supported High-Resolution TEM and STEM Imaging of Silicon Nanocrystals and their Capping Ligands. *J. Phys. Chem. C* **2012**, *116*, 22463-22468.

Park, J.-H.; Gu, L.; von Maltzahn, G.; Ruoslahti, E.; Bhatia, S. N.; Sailor, M. J. Biodegradable luminescent porous silicon nanoparticles for in vivo applications *Nat. Mater.* **2009**, *8*, 331-336.

Park, J.-H.; von Maltzahn, G.; Ruoslahti, E.; Bhatia, S. N.; Sailor, M. J. Micellar Hybrid Nanoparticles for Simultaneous Magnetofluorescent Imaging and Drug Delivery. *Angew. Chem. Int. Ed.* **2008**, *47*, 7284-7288.

Patai, S. The Chemistry of the Thiol Group. *John Wiley & Sons London,* **1974**.

Pavesi, L.; Dal Negro, L.; Mazzoleni, C.; Franzò, G.; Priolo, F. Optical Gain in Silicon Nanocrystals. *Nature* **2000**, *408*, 440-444.

Pavesi, L; Turan, R., Eds. Silicon Nanocrystals: Fundamentals, Synthesis and Applications*, Wiley-VCH, Germany*, **2010**.

Pell, L. E.; Schricker, A. D.; Mikulec, F. V.; Korgel, B. A. Synthesis of Amorphous Silicon Colloids by Trisilane Thermolysis in High Temperature Supercritical Solvents. *Langmuir* **2004**, *20*, 6546-6548.

Pereira, R. N.; Niesar, S.; You, W. B.; da Cunha, a. F.; Erhard, N.; Stegner, A. R.; Wiggers, H.; Willinger, M.-G.; Stutzmann, M.; Brandt, M. S. Solution-Processed Networks of Silicon Nanocrystals: The Role of Internanocrystal Medium on Semiconducting Behavior. *J. Phys. Chem. C* **2011**, *115*, 20120-20127.

Peter, K.; Vollhardt, C.; Schore, N. E. *Organic Chemistry: Structure and Function*, W. H. Freeman and Company, New York, **2002**, 864-879.

Phan, S.-E.; Russel, W. B.; Zhu, J.; Chaikin, P. M. Effects of polydispersity on hard sphere crystals. *J. Chem. Phys.* **1998**, *108*, 9789-9795.

Polito, L.; Colombo, M.; Monti, D.; Melato, S.; Caneva, E.; Prosperi, D. Resolving the Structure of Ligands Bound to the Surface of Superparamagnetic Iron Oxide Nanoparticles by High-Resolution Magic-Angle Spinning NMR Spectroscopy. *J. Am. Chem. Soc.* **2008**, *130*, 12712-12724.

Porter, M. D.; Bright, T. B.; Allara, D. L.; Chidsey, C. E. D. Spontaneously Organized Molecular Assemblies. 4. Structural Characterization of n-Alkyl Thiol Monolayers on Gold by Optical Ellipsometry, Infrared Spectrosopy, and Electrochemistry. *J. Am. Chem. Soc.* **1987**, *109*, 3559-3568.

Prasad, B. L.; Sorensen, C. M.; Klabunde, K. J. Gold Nanoparticle Superlattice. *Chem. Soc. Rev.* **2008**, *37*, 1871-1883.

Priolo, F.; Gregorkiewicz, T.; Galli, M.; Krauss, T. F. Silicon Nanostructure for Photonics and Photovoltaics. *Nature Nanotech.* **2014**, *9*, 19-32.

Profio, G. D.; Tucci, S.; Curcio, E.; Drioli, E. Controlling Polymorphism with Membrane-Based Crystallizers: Application to Form I and II of Paracetamol *Chem. Mater.* **2007**, *19*, 2386-2388.

Proot, J. P.; Delerue, C.; Allan, G. Electronic Structure and Optical Properties of Silicon Crystallites: Application to Porous Silicon. *App. Phys. Lett.* **1992**, *61*, 1948-1950.

Pusey, P. N.; van Megen, W. Phase Behaviors of Concentrated Suspensions of Nearly Hard Colloidal Spheres. *Nature* **1986**, *320*, 340-342.

Pusey, P. N.; Zaccarelli, E.; Valeriani, C.; Sanz, E.; Poon, W. C. K.; Cates, M. E. Hard Spheres: Crystalline and Glass Formation. *Phil. Trans. R. Soc. A* **2009**, *367*, 4993-5011.

Puzzo, D. P.; Henderson, E. J.; Helander, M. G.; Wang, Z.; Ozin, G. A.; Lu, Z. Visiblle Colloidal Nanocrystal Silicon Light-Emitting Diode. *Nano Lett.* **2011**, *11*, 1585-1590.

Quiros, I.; Yamada, M.; Kubo, K.; Mizutani, J.; Kurihara, M.; Nishihara, H. Preparation of Alkanethiolate-Protected Palladium Nanoparticles and Their Size Dependence on Synthetic Conditions. *Langmuir* **2002**, *18*, 1413-1418.

Rabani, E.; Reichman, D. R.; Geissler, P. L.; Brus, L. E. Dring-Mediated Self-Assembly of Nanoparticles. *Nature*, **2003**, *426*, 271-274.

Rasch, M. R.; Rossinyol, E.; Hueso, J. L.; Goodfellow, B. W.; Arbiol, J.; Korgel, B. A. Hydrophobic Gold Nanoparticle Self-Assembly with Phosphatidylcholine Lipid: Membrane-Loaded and Janus Vesicles. *Nano Lett.* **2010**, *10*, 3733-3739.

Rasch, M. R.; Yu, Y.; Bosocy, C.; Goodfellow, B. W.; Korgel, B. A. Chloroform-Enhanced Incorporation of Hydrophobic Gold Nanocrystals into Dioleoylphosphatidylcholine (DOPC) Vesicle Membranes. *Langmuir* **2012**, *28*, 12971-12981.

Rastogi, S.; Höhne, G. W. H. A. Keller, Unusual Pressure-Induced Phase Behavior in Crystalline Poly(4-methylpentene-1): Calorimetric and Spectroscopic Results and Further Implications. *Macromolecules*, **1999**, *32*, 8897-8909.

Rastogi, S.; Newman, M.; Keller, A. Unusual pressure-induced phase behavior in crystalline poly-4-methyl-pentene-1. *J. Poly. Sci. B* **1993**, *31*, 125-139.

Ratchford, D.; Shafiei, F.; Kim, S.; Gray, S. K.; Li X. Manipulating Coupling between a Single Semiconductor Quantum Dot and Single Gold Nanoparticle. *Nano Lett.* **2011**, *11*, 1049-1054.

Redl, F. X.; Cho, K.-S.; Murray, C. B.; O'Brien, S. Three-Dimensional Binary Superlattices of Magnetic Nanocrystals and Semiconductor Quantum Dots. *Nature* **2003**, *423*, 968-971.

Rogozhina, E. V.; Eckhoff, D. A.;Gratton, E.; Braun, P. V. Carboxyl Functionalization of Ultrasmall Luminescent Silicon Nanoparticles Through Thermal Hydrosilylation. *J. Mater. Chem*. **2006**, *16*, 1421-1430.

Rosi, N. L.; Mirkin, C. A. Nanostructure in Biodiagnostics. *Chem. Rev.* **2005**, *105*, 1547-1562.

Ruland, W.; Smarsly, B. M. Two-Dimensional Small-Angle X-Ray Scattering of Self-Assembled Nanocomposite Films with Oriented Arrays of Spheres: Determination of Lattice Type, Preferred Orientation, Deformation and Imperfection. *J. Appl. Cryst.* **2007**, *40*, 409-417.

Sailor, M. J.; Park, J.-H. Adv. Mater., Hybrid Nanoparticles for Detection and Treatment. *2012*, **24**, 3779-3802.

Santhanam, V.; Liu, J.; Agarwal; R.; Andres, R. P. Self-Assembly of Uniform Monolayer Arrays of Nanoparticles. *Langmuir*, **2003**, *19*, 7881-7887.

Sardar, R.; Funston, A. M.; Mulvaney, P.; Murray, R. W. Gold Nanoparticles: Past, Present, and Future. *Langmuir* **2009**, *25*, 13840-13851.

Sastry, S.; Truskett, T. M.; Debenedetti, P. G.; Torquato, S.; Stillinger, F. H. Free Volume in the Hard Sphere Liquid. *Molecular Phys.* **1998**, *95*, 289-297.

Sato, K.; Yokosuka, S.; Takigami, Y.; Hirakuri, K.; Fujioka, K.; Manome, Y.; Sukegawa, H.; Iwai, H.; Fukata, N. Size-Tunable Silicon/Iron Oxide Hybrid Nanoparticles with Fluorescence, Superparamagnetism, and Biocompatibility. *J. Am. Chem. Soc.* **2011**, *133*, 18626-18633.

Sato, S.; Swihart, M. T. Propionic-Acid-Terminated Silicon Nanocrystals: Synthesis and Optical Characterization. *Chem. Mater.* **2006**, *18*, 4083-4088.

Saunders, A. E.; Korgel, B. A. Growth Kinetics and Metastability of Monodisperse Tetraoctylammonium Bromide Capped Gold Nanocrystals. *J. Phys. Chem. B* **2004**, *108*, 16732-16738.

Saunders, A. E.; Korgel, B. A. Observation of an AB phase in bidisperse nanocrystal superlattices. *ChemPhysChem* **2005**, *6*, 61-65.

Saunders, A. E.; Shah, P. S.; Park, E. J.; Lim, K. T.; Johnston, K. P.; Korgel, B. A. Solvent Density-Dependent Steric Stabilization of Perfluoropolyether-Coated Nanocrystals in Supercritical Carbon Dioxide. *J. Phys. Chem. B* **2004**, *108*, 15969-15975.

Saunders, A. E.; Shah, P. S.; Sigman, M. B.; Hanrath, T.; Hwang, H. S.; Lim, K. T.; Johnston, K. P.; Korgel, B. A. Inverse Opal Nanocrystal Superlattice Films. *Nano Lett.* **2004**, *4*, 1943-1948.

Saunders, A. E.; Sigman, M. B.; Korgel, B. A. Growth Kinetics and Metastability of Monodisperse Tetraoctylammonium Bromide Capped Gold Nanocrystals. *J. Phys. Chem. B* **2004**, *108*, 193-199.

Scholz, F. Electroanalytical Methods Guide to Experiments and Applications. *Springer: New York*, **2002**.

Schwartz, M. P.; Ellison, M. D.; Coulter, S. K.; Hovis, J. S.; Hamers, R. J. Interaction of π-Conjugated Organic Molecules with π-Bonded semiconductor Surfaces: Structure, Selectivity, and Mechanistic Implications. *J. Am. Chem. Soc.* **2000**, *122*, 8529-8538.

Selvan, S. T.; Patra, P. K.; Ang, C. Y.; Ying, J. Y. Synthesis of Silica-Coated Semiconductor and Magnetic Quantum Dots and Their Use in the Imaging of Live Cells. *Angew. Chem. Int. Ed.* **2007**, *46*, 2448-2452.

Sheng, H. W.; Liu, H. Z.; Cheng, Y. Q.; Wen, J.; Lee, P. L.; Luo, W. K.; Shastri, S. D.; Ma, E. Polymorphism in a Metallic Glass. *Nature Mater.*, **2007**, *6*, 192-197.

Sherman, D. M.; Waite, T. D. Electroic Spectra of Fe^{3+} Oxides and Oxide Hydroxides in the Near IR to Near UV. *Am. Mineral*, **1985**, *70*, 1262-1269.

Shevchenko, E. V.; Kortright, J. B.; Talapin, D. V.; Aloni, S.; Alivisatos, A. P. Quasi-Ternary Nanoparticle Superlattice Through Nanoparticle Design. *Adv. Mater.* **2007**, *19*, 4183-4188.

Shevchenko, E. V.; Talapin, D. V.; Kotov, N. A.; O'Brien, S.; Murray, C. B.; Structural Diversity in Binary Nanoparticles Superlattice. *Nature* **2006**, *439*, 55-59.

Shevchenko, E. V.; Talapin, D. V.; Murray, C. B.; O'Brien, S. Structural Characteriztion of Self-Assembled Multifunctional Binary Nanoparticle Superlattices. *J. Am. Soc. Chem.* **2006**, *128*, 3620-3637.

Shevchenko, E. V.; Talapin, D. V.; O'Brien, S.; Murray, C. B. Polymorphism in AB_{13} nanoparticle superlattices: an example of semiconductor-metal metamaterials, *J. Am. Chem. Soc.* **2005**, *127*, 8741-8747.

Shevchenko, E. V.;Ringler, M.; Schwemer, A.; Talapin, D. V.; Klar, T. A.; Rogach, A. L.; Feldmann, J.; Alivisatos, A. P. Self-Assembled Binary Superlattices of CdSe and Au nanocrystals and Their Fluorescence Properties. *J. Am. Soc. Chem.* **2008**, *130*, 3274-3275.

Shimizu, T.; Teranishi, T.; Hasegawa, S.; Miyaka, M. Size evolution of alkanethiol-protected gold nanoparticles by heat treatment in the solid state, *J. Phys. Chem. B* **2003**, *107*, 2719-2724.

Shipway, A. N.; Katz, E.; Willner, I. Nanoparticle Arrays on Surface for Electronic, Optical, and Sensors Applications. *ChemPhysChem* **2000**, *1*, 18-52.

Shirley, D. A. High-Resolution X-Ray Photoemission Spectrum of the Valence Bands of Gold. *Phy. Rev. B* **1972**, *5*, 4709-4714.

Shoemaker, D. P.; Marsh, R. E.; Ewing, F. J.; Pauling, L. Interatomic distances and atomic valences in $NaZn_{13}$, *Acta Cryst.* **1952**, *5*, 637-644.

Sieval, A. B.; Demirel, A. L.; Nissink, J. W. M.; Linford, M. R.; Van der Maas, J. H.; de Jeu, W. H.; Zuilhof, H.; Sudholter, E. J. R. Highly Stable Si-C Linked Functionalized Monolayers on the Silicon (100) Surface. *Langmuir* **1998**, *14*, 1759-1768.

Sigman, M. B.; Saunders, A. E.; Korgel, B. A. Metal Nanocrystal Superlattice Nucleation and Growth. *Langmuir* **2004**, *20*, 978-983.

Singh, V.; Yu, Y.; Sun, Q.-C.; Korgel, B. A.; Nagpal, P. Pseudo-Direct Bandgap Transitions in Silicon Nanocrystals: Effect on Optoelectronics and Thermoelectrics. *Nanoscale* **2014**, *6*, 14643-14647.

Smilgies, D.-M.; and Blasini, D. R. Indexation scheme for oriented molecular thin films studied with grazing-incidence reciprocal-space mapping. *J. Appl. Cryst.* **2007**, *40*, 716-718.

Smilgies, D.-M.; Heitsch, A. T.; Korgel, B. A. Stacking of Hexagonal Nanocrystal Layers during Langmuir-Blodgett Deposition. *J. Phys. Chem. B*, **2012**, *116*, 6017-6026.

Smith, D. K.; Goodfellow, B.; Smilgies, D.-M.; Korgel, B. A. Self-Assembled Simple Hexagonal AB_2 Binary Nanorystal Superlattices: SEM, GISAXS, and Defects. *J. Am. Soc. Chem.* **2009**, *131*, 3281-3290.

Socrates, G. *Infrared Characteristic Group Frequencies: Tables and Charts.* John Wiley & Sons, New York, **1994**, 34-189.

Sommer, L. H.; McLick, J. Stereochemistry of Asymmetric Silicon. IX. The Silicon-Sulfur Bond. *J. Am. Chem. Soc.* **1967**, *89*, 5806-5812.

Son, J. S.; Lee, J.-S.; Shevchenko, E. V.; Talapin, D. V. Magnet-in-the-Semiconductor Nanomaterials: High Electron Mobility in All-Inorganic Arrays of FePt/CdSe and FePt/CdS Core-Shell Heterostructures. *J. Phys. Chem. Lett.* **2013**, *4*, 1918-1923.

Song, J. H.; Sailor, M. J. Functionalization of Nanocrystalline Porous Silicon Surfaces with Aryllithium Reagents: Formation of Silicon-Carbon Bonds by Cleavage of Silicon-Silicon Bonds. *J. Am. Chem. Soc.* **1998**, *120*, 2376-2381.

Steigerwald, M. L.; Alivisatos, A. P.; Gibson, J. M.; Harris, T. D.; Kortan, R.; Muller, A. J.; Thayer, A. M.; Duncan, T. M.; Douglass, D. C.; Brus, L. E. Surface Derivatization and Isolation of Semiconductor Cluster Molecules. *J. Am. Chem. Soc.* **1988**, *110*, 3046-3050.

Stillinger, F. H.; Debenedetti, P. G. Phase transitions, Kauzmann curves, and inverse melting. *Biophys. Chem.* **2003**, *105*, 211-220.

Stowell, C.; Korgel, B. A. Self-Assembled Honeycomb Networks of Gold Nanocrystals. *Nano Lett.* **2001**, *1*, 595-600.

Streetman, B.; Banerjee, S. Solid State Electronic Devices, 7th Edition, *Prentice Hall, USA,* **2015**.

Suganuma, Y.; Trudeau, P.-E.; Dhirani, A.-A. Multi-Valued Analogue Information Storage Using Self-Assembled Nanoparticle Films. *Nanotechnology* **2005**, *16*, 1196-1203.

Sykora, M.; Mangolini, L.; Schaller, R. D.; Kortshagen, U.; Jurbergs, D.; Klimov, V. I. Size-Dependent Intrinsic Radiative Decay Rates of Silicon Nanocrystals at Large Confinement Energies, *Phy. Rev. Lett*. **2008**, *100*, 067401.

Takeda, E.; Nakamura, T.; Fujii, M.; Miura, S.; Hayashi, S. Surface Plasmon Polarity Mediated Photoluminescence from Excitons in Silicon Nanocrystals. *Appl. Phys. Lett.* **2006**, *89*, 101907.

Talapin, D. V.; Murray, C. B. PbSe Nanocrystal Solids for n- and p-Channel Thin Film Field-Effect Transistors. *Science* **2005**, *310*, 86-89.

Talapin, D. V.; Shevchenko, E. V.; Murray, C. B.; Titov, A. V.; Král, P. Dipole-Dipole Interactions in Nanocrystal Superlattices. *Nano Lett.* **2007**, *7*, 1213-1219.

Tengvall, P. Jansson, E.; Askendal, A.; Thomsen, P.; Gretzer, C. Preparation of Multilayer Plasma Protein Films on Silicon by EDC/NHS Coupling Chemistry. *Col. Surf. B* **2003**, *4*, 261-272.

Teranishi, T.; Hasegawa, S.; Shimizu, T.; Miyaka, M. Heat-induced size evolution of gold nanoparticles in the solid state, *Adv. Mater.* **2001**, *12*, 1699-1701.

Thakur, D.; Deng, S.; Baldet, T.; O Winter, pH Sensitive CdS-Iron Oxide Fluorescent-Magnetic Nanocomposites. *Nanotechnol.* **2009**, *20*, 485601.

Torquato, S.; Stillinger, F. H. Jammed hard-particle packings: from Kepler to Bernal and beyond. *Rev. Mod. Phys.* **2010**, *82*, 2633-2672.

Tsybeskov, L.; Hirschman, K. D.; Duttagupta, S. P.; Zacharias, M.; Fauchet, P. M.; McCaffrey, J. P.; Lockwood, D. J. Nanocrystalline-Silicon Superlattice Produced by controlled Recrystallization. *Appl. Phys. Lett.* **1998**, *72*, 43-45.

Tu, C.; Ma, X.; Pantazis, P.; Kauzlarich, S. M.; Louie, A. Y. Paramagnetic, Silicon Quantum Dots for Magnetic Resonance and Two-Photon Imaging of Macrophages. *J. Am. Chem. Soc.* **2010**, *132*, 2016-2023.

Tu, C.-C.; Zhang, Q.; Lin, L. Y.; Cao, G. Brightly Photoluminescence Phosphor Materials Based on Silicon Quantum Dots with Oxide Shell Passivation. *Optics Express* **2012**, *20*, A69-A74.

Urban, J. J.; Talapin, D. V.; Shevchenko, E. V.; Kagan, C. R.; Murray, C. B. Synergism in Binary Nanocrystal Superlattices Leads to Enhanced p-Type Conductivity in Self-Assembled PbTe/Ag_2Te Thin Films. *Nat. Mater.* **2007**, *6*, 115-121.

van Hooy-Corstjens, C. S. J.; Höhne, G. W. H.; Rastogi, S. Inverse melting in syndiotactic polystyrene. *Macromole.* **2005**, *38*, 1814-1822.

Vial, J. C.; Bsiesy, A.; Gaspard, F.; Hérino, R.; Ligeon, M.; Muller, F.; Romestain, R. Mechanisms of Visible-Light Emission from Electro-Oxidized Porous Silicon. *Phys. Rev. B* **1992**, *45*, 14171-14176.

Vollath, D. Bifunctional Nanocomposites with Magnetic and Luminescence Properties. *Adv. Mater.* **2010**, *22*, 4410-4415.

Wall, J. S. Disulfide Bonds: Determination, Location, and Influences on Molecular Properties of Proteins. *Agricultural and Food Chem.* **1971**, *19*, 619-625.

Wang, B.; Hai, J.; Wang, Q.; Li, T.; Yang, Z. Coupling of Luminescent Terbium Complexes to Fe3O4 Nanoparticles for Imaging Applications. *Angew. Chem. Int. Ed.* **2011**, *50*, 3063-3066.

Wang, D.; He, J.; Rosenzweig, N.; Rosenzweig, Z. Superparamagnetic Fe2O3 Beads−CdSe ZnS Quantum Dots Core-Shell Nanocomposite Particlesfor Cell Separation. *Nano Lett.* **2004**, *4*, 409-413.

Wang, L.; Yang, Z.; Zhang, Y.; Wang, L. Bifunctional Nanoparticles with Magnetization and Luminescence. *J. Phys. Chem. C* **2009**, *113*, 3955-3959.

Warner, J. H.; Hoshino, A.; Yamamoto, K.; Tilley, R. D. Water-Soluble Photoluminescent Silicon Quantum Dots. *Angew. Chem. Int. ed.* **2005**, *44*, 4550-4554.

Whetten, R. L.; Shafigullin, M. N.; Khoury, J. T.; Schaaff, T. G.; Vezmar, I.; Alvarez, M. M.; Wilkinson, A. Crystal Sreuctures of Molecular Gold Nanocrystal Arrys. *Acc. Chem. Res.* **1999**, *32*, 397-406.

Wilson, W. L.; Szajowski, P. F.; Brus, L. E. Quantum Confinement in Size-Selected, Surface-Oxidized Silicon Nanocrystals. *Science* **1993**, *262*, 1242-1244.

Woodcock, L. V. Entropy difference between the face-centered cubic and hexagonal close-packed crystal structures. *Nature* **1997**, *385*, 141-143.

Xiao, L.; Gu, L.; Howell, S. B.; Sailor, M. J. Porous Silicon Nanoparticle Photosensitizers for Singlet Oxygen and Their Phototoxicity against Cancer Cells. *ACS Nano* **2011**, *5*, 3651-3659.

Xu, H.; Cheng, L.; Wang, C.; Ma, X.; Li, Y.; Liu, Z. Polymer encapsulated upconversion nanoparticleiron oxide nanocomposites for multimodal imaging and magnetic targeted drug delivery. *Biomater*. **2011**, *32*, 9364-9373.

Yang, Z.; Dasog, M.; Dobbie, A. R.; Lockwood, R.; Zhi, Y.; Meldrum, A.; Veinot, J. G. C. Highly Luminescent Covalently Linked Silicon Nanocrystal/Polystyrene Hybrid Functional Materials: Synthesis, Properties, and Processability. *Adv. Funct. Mater.* **2013,** DOI: 10.1002/adfm.201302091.

Yang, Z.; Iabal, M.; Dobbie, A. R.; Veinot, J. G. C. Surface-Induced Alkene Oligomerization: Does Thermal Hydrosilylation Really Lead to Monolayer Protected Silicon Nanocrystals? *J. Am. Chem. Soc.* **2013**, *135*, 17595-157801.

Ye, X.; Chen, J.; Murray, C. B. Polymorphism in self-assembled AB_6 binary nanocrystal superlattices, *J. Am. Chem. Soc.* **2011**, *133*, 2613-2620.

Yilmaz, D. On the Strain in Silicon Nanocrystals. Ph.D. Thesis, Bilkent University, Ankara, *Turkey*, **2009**.

Yu, Y.; Bosoy, C. A.; Hessel, C. M.; Smilgies, D.-M.; Korgel, B. A. Silicon Nanocrystal Superlattices. *ChemPhyChem* **2013**, *14*, 84-87.

Yu, Y.; Bosoy, C. A.; Smilgies, D.-M.; Korgel, B. A. Self-assembly and thermal stability of binary superlattices of gold and silicon nanocrystals. *J. Phys. Chem. Lett.* **2013**, *4*, 3677-3682.

Yu, Y.; Hessel, C. M.; Bogart, T. D.; Panthani, M. G.; Rasch, M. R.; Korgel, B. A. Room Temperature Hydrosilylation of Silicon Nanocrystals with Bifunctional Terminal Alkenes. *Langmuir* **2013**, *29*, 1533-1540.

Zaborovskiy, A. B.; Lutsyk, D. S.; Prystansky, R. E.;Kopylets, V. I.; Timokhin, V. I.; Chatgilialoglu, C. A Mechanistic Investigation of $(Me_3Si)_3SiH$ Oxidation *J. Organomet. Chem.* **2004**, *689*, 2912-2919.

Zacharias, M.; Heitmann, J.; Scholz, R.; Kahler, U.; Schmidt, M.; Bläsing, J. Size-Controlled Highly Luminescent Silicon Nanocrystals: A SiO/SiO_2 superlattice approach. *Appl. Phys. Lett.* **2002**, *80*, 661-663.

Zazzera, L. A.; Evans, J. F.; Deruelle, M.; Tirrell, M.; Kessel, C. R. Bonding Organic Molecules to Hydrogen-Terminated Silicon Wafers. *J. Electrochem. Soc.* **1997**, *144*, 2184-2189.

Zhang, S.; Li, J.; Lykotrafitis, G.; Bao, G.; Suresh S. Size-Dependent Endocytosis of Nanoparticles. *Adv. Mater.* **2009**, *21*, 419-424.

Zhang, X.; Brynda, M.; Britt, R. D.; Carroll, E. C.; Larsen, D. S.; Louie, A. Y.; Kauzlarich, S. M. Synthesis and Characterization of Manganese-Doped Silicon Nanoparticles: Bifunctional Paramagnetic-Optical Nanomaterial. *J. Am. Chem. Soc.* **2007**, *129*, 10668-10669.

Zhelev, Z.; Jose, R.; Nagase, T.; Ohba, H.; Bakalova, R.; Ishikawa, M.; Baba, Y. Enhancement of the Photoluminescence of CdSe Quantum Dots during Long-Term UV-Irradiation: Privilege or Fault in Life Science Research? *J. Photochem. Photobiol. B: Biol.* **2004**, *75*, 99-105.

Zipoli, F.; Bernasconi, M. Ab initio Simulation of the Grafting of Phenylacetylene on Hydrogenated Surfaces of Crystalline Silicon Catalyzed by a Lewis Acid, *J. Phys. Chem. B* **2006**, *110*, 23403-23409.

Vita

Yixuan Yu, email address: yixuanyu@gmail.com, was born in Maanshan, Anhui province of China, and lived a worryless life in a little town called Xinshi until he left his home to go to high school at the age of 13. He went to attend Tsinghua University, Beijing, in 2003. Four years later, he graduated with a Bachelor degree of Science in Materials Science and Engineering, and went on to pursue a Master of Science degree in the same discipline, which cost him three years. In 2010, he enrolled at The University of Texas at Austin as a Ph.D. student in Chemical Engineering to study the surface chemistry and self-assembly of silicon nanocrystals under the supervision of Dr. Brian Korgel. This dissertation is typed by the author.